JST-SPH: A TOTAL LAGRANGIAN, STABILISED MESHLESS METHODOLOGY FOR MIXED SYSTEMS OF CONSERVATION LAWS IN NONLINEAR SOLID DYNAMICS

GIORGIO GRETO

Submitted in partial fulfilment of
the requirements for the degree of

Doctor of Philosophy

School of Engineering

Cardiff University

– October 2018 –

DECLARATION

This work has not been submitted in substance for any other degree or award at this or any other university or place of learning, nor is being submitted concurrently in candidature for any degree or other award.

Signed …… (candidate) Date ……

STATEMENT 1

This thesis is being submitted in partial fulfillment of the requirements for the degree of ……(insert MCh, MD, MPhil, PhD etc, as appropriate).

Signed …… (candidate) Date ……

STATEMENT 2

This thesis is the result of my own independent work/investigation, except where otherwise stated, and the thesis has not been edited by a third party beyond what is permitted by Cardiff University's Policy on the Use of Third Party Editors by Research Degree Students. Other sources are acknowledged by explicit references. The views expressed are my own.

Signed …… (candidate) Date ……

STATEMENT 3

I hereby give consent for my thesis, if accepted, to be available online in the University's Open Access repository and for inter-library loan, and for the title and summary to be made available to outside organisations.

Signed …….. (candidate) Date ……

ABSTRACT

The combination of linear finite elements space discretisation with Newmark family time-integration schemes has been established as the de-facto standard for numerical analysis of fast solid dynamics. However, this set-up suffers from a series of drawbacks: mesh entanglements and elemental distortion may compromise results of high strain simulations; numerical issues, such as locking and spurious pressure oscillations, are likely to manifest; and stresses usually reach a reduced order of accuracy than velocities.

Meshless methods are a relatively new family of discretisation techniques that may offer a solution to problems of excessive distortion experienced by linear finite elements. Amongst these new methodologies, smooth particles hydrodynamics (SPH) is the simplest in concept and the most straightforward to numerically implement. Yet, this simplicity is marred by some shortcomings, namely (i) inconsistencies of the SPH approximation at or near the boundaries of the domain; (ii) spurious hourglass-like modes caused by the rank deficiency associated with nodal integration, and (iii) instabilities arising when sustained internal stresses are predominantly tensile.

To deal with the aforementioned SPH-related issues, the following remedies are hereby adopted, respectively: (i) corrections to the kernel functions that are fundamental to SPH interpolation, improving consistency at and near boundaries; (ii) a polyconvex mixed-type system based on a new set of unknown variables ($\mathbf{p}$, $\mathbf{F}$, $\mathbf{H}$ and J) is used in place of the displacement-based equation of motion; in this manner, stabilisation techniques from computational fluid dynamics become available; (iii) the analysis is set in a total Lagrangian reference framework.

Assuming polyconvex variables as the main unknowns of the set of first order conservation laws helps to establish the existence and uniqueness of analytical solutions. This is a key reassurance for a robust numerical implementation of simulations. The resulting system of hyperbolic first order conservation laws presents analogies to the Euler equations in fluid dynamics. This allows the use of a well-proven stabilisation technique in computational fluid dynamics, the Jameson Schmidt Turkel (JST) algorithm. JST is very effective in damping numerical oscillations, and in capturing discontinuities in the solution that would otherwise be impossible to represent.

Finally, we note that the JST-SPH scheme so defined is employed in a battery of numerical tests, selected to check its accuracy, robustness, momentum preservation capabilities, and its viability for solving larger scale, industry-related problems.

LIST OF PUBLICATIONS

INTERNATIONAL JOURNALS

[1] C.H. Lee, A. Gil, G. Greto, S. Kulasegaram and J. Bonet. A new JST Smooth Particle Hydrodynamics algorithm for large strain explicit fast dynamics. In: *Computer Methods in Applied Mechanics and Engineering* **311** (2016), pp. 71–111.

[2] G. Greto, S. Kulasegaram, C.H. Lee and A. Gil. *The JST-SPH Method: Applications in Metal Plasticity*. In preparation. 2018.

CONFERENCE PROCEEDINGS

[1] G. Greto, S. Kulasegaram, C.H. Lee, A. Gil and J. Bonet. A first order mixed formulation for fast solid dynamics using Smooth Particle Hydrodynamics. In: *Proceedings of the 23rd UK Conference of the Association for Computational Mechanics in Engineering*. 8–10 April 2015, pp. 395–398.

[2] G. Greto, S. Kulasegaram, C.H. Lee, A. Gil and J. Bonet. A stabilised Total Lagrangian Corrected Smooth Particle Hydrodynamics (CSPH) in large strain explicit solid dynamics. In: *Proceedings of the 24th UK Conference of the Association for Computational Mechanics in Engineering*. 31 March–1 April 2016, pp. 201–204.

[3] G. Greto, S. Kulasegaram, C.H. Lee, A. Gil and J. Bonet. A stabilised Total Lagrangian Corrected Smooth Particle Hydrodynamics technique in large strain explicit fast solid dynamics. In: *ECCOMAS Congress 2016 - Proceedings of the 7th European Congress on Computational Methods in Applied Sciences and Engineering*. Vol. 4. 5–10 June 2016, pp. 8231–8240.

[4] G. Greto, S. Kulasegaram, C.H. Lee, A. Gil and J. Bonet. A new, meshless approach to fast solid dynamics: applications in metal plasticity. In: *Proceedings of the 25th UKACM Conference on Computational Mechanics*. 12–13 April 2017, pp. 201–204.

OTHERS

[1] G. Greto. "Computer-aided Modelling of Fast Dynamics in Engineering: an Alternative Approach". In: "*Speaking of Science*", student-led postgraduate conference. Cardiff University, 6 May 2016.

CONTENTS

LIST OF FIGURES

LIST OF TABLES

LIST OF ALGORITHMS

ACRONYMS

ADT	alternating digital tree
BC	boundary condition
BCs	boundary conditions
CFD	computational fluid dynamics
CFL	Courant Friedrichs Lewy
CSM	computational solid mechanics
DEM	diffuse element method
d.o.f.	degree of freedom
ECAE	equal channel angular extrusion
EFG	element free Galerkin
EFGM	element free Galerkin method
FD	finite differences
FDM	finite differences method
FE	finite elements
FEM	finite elements method
FV	finite volumes
h.o.t.	higher order terms
ICs	initial conditions
JST	Jameson Schmidt Turkel
LAE	linear advection equation

LBB	Ladyzenskaja Babushka Brezzi
LHS	left hand side
Max-Ent	maximum entropy
MLPG	meshless local Petrov-Galerkin
MLS	moving least squares
ODE	ordinary differential equation
ODEs	ordinary differential equations
PDE	partial differential equation
PDEs	partial differential equations
p.p.s.	particles per side
RA	real analysis
RHS	right hand side
RK	Runge Kutta
RKPM	reproducing kernel particle method
RPIM	radial point interpolation method
SPH	smooth particles hydrodynamics
TVD	total variation diminishing
TVD-RK	total variation diminishing, Runge Kutta
VMS	variational multiscale stabilisation

NOMENCLATURE

Symbols are followed by their description and a link to the page of first appearance.

MATHEMATICAL OPERATORS AND OPERATIONS

$\delta(\mathbf{x})$ Dirac delta function, p. 105

δ_{ij} Kronecker delta function, p. 94

$\|\cdot\|$ Norm of a functional space, p. 91

$\mathcal{E}_{ijk}$ Levi-Civita permutation tensor, p. 22

$\mathcal{O}(\cdot^n)$ Polynomial terms from order n upwards become small enough to be negligible in a series expansion, p. 111

Φ Phase angle of a complex number, p. 169

$\mathcal{A}(\cdot)$ Generic differential operator, p. 89

$\mathcal{I}[\cdot]$ Interpolant operator on function $f(\mathbf{x})$, p. 104

$\mathcal{I}$ Identity tensor, p. 77

$\mathbf{M}_{\mathbf{F}|i,j}$ Minor of the i^{th} row- and j^{th} column-component of matrix $\mathbf{F}$, p. 26

$\mathbf{Q}_{rot}$ Rotation matrix in $\mathbb{R}^3$, p. 35

H_f Hessian matrix of a function $f(\mathbf{x})$, p. 67

$I\,[=\sqrt{-1}]$ Imaginary unit, p. 169

$\cdot$ Scalar product, p. 23

$:$ Double contraction, p. 23

$\times$ Vector product, p. 23

$\mathbf{\times}$ Tensorial cross product, p. 22

$\otimes$ Tensor product, p. 23

∇ Spatial vector differential operator, p. 22

∇_0 Material vector differential operator, p. 22

$(\cdot)^T$ Transpose vector/matrix, p. 20

$\det(\cdot)$ Determinant of a matrix, p. 23

$\mathrm{tr}(\cdot)$ Trace of a matrix, p. 23

$\mathrm{cof}(\cdot)$ Cofactors matrix, p. 24

$(\cdot)'$ Deviatoric part of a stress tensor, p. 56

$D\mathbf{A}[\delta\mathbf{x}]$ Gateaux (directional) derivative of tensor $\mathbf{A}$ in direction $\mathbf{x}$, p. 61

$(\cdot)^{-/+}$ Values of a variable at either side of a discontinuity, p. 27

$\mathfrak{I}(\cdot)$ Imaginary part of a complex number, p. 170

$\mathfrak{R}(\cdot)$ Real part of a complex number, p. 169

OTHER MATHEMATICAL OBJECTS

$(\cdot,\cdot)$ Scalar product on a vector space, p. 91

λ_i i^{th} eigenvalue of a matrix, p. 34

λ_{wl} wavelength of a harmonic, p. 169

$\boldsymbol{\mathcal{F}}_1$, $\boldsymbol{\mathcal{F}}_2$, $\boldsymbol{\mathcal{F}}_3$ Vector of flux terms projected on $\{\boldsymbol{e}_1, \boldsymbol{e}_2, \boldsymbol{e}_3\}$, p. 74

$\boldsymbol{\mathcal{A}}_{I=1,2,3}$ System matrix of the quasi-linear mixed system of conservation laws, p. 74

$\boldsymbol{\mathcal{F}} = (f_1 \cdots f_n)^T$ Vector of fluxes of conserved variables, p. 26

$\boldsymbol{\mathcal{F}}_m$ Flux matrix in direction $\mathbf{m}$, p. 27

$\boldsymbol{\mathcal{R}}(\boldsymbol{\mathcal{U}}_a)$ Vector of residuals, p. 132

$\boldsymbol{\mathcal{S}} = (s_1 \cdots s_n)^T$ Vector of source terms, p. 26

$\boldsymbol{\mathcal{U}} = (u_1 \cdots u_n)^T$ Vector of conserved variables, p. 26

$\mathbf{R}_i$ i^{th} eigenvector of a matrix, p. 34

$a(\cdot,\cdot)$ Bilinear form on a vector space, p. 91

$H^k(\boldsymbol{\mathcal{B}})$ Sobolev space (of functions bounded by a constant) in $\boldsymbol{\mathcal{B}}$, p. 90

k_i Wave number of a Fourier harmonic, p. 169

$L^2(\boldsymbol{\mathcal{B}})$ Space of square-integrable functions in $\boldsymbol{\mathcal{B}}$, p. 90

z_P Numerical amplification factor of a time integration scheme, p. 170

GEOMETRIC DESCRIPTION

$\delta\mathbf{u}$ Virtual displacements field, p. 61

Γ_D Boundary tract of $\boldsymbol{\mathcal{B}}$ where Dirichlet BCs apply, p. 89

Γ_N Boundary tract of $\boldsymbol{\mathcal{B}}$ where Neumann BCs apply, p. 89

$\mathbb{R}^3$ Three dimensional real vector space, p. 20

$\boldsymbol{\mathcal{B}}(t)$ Continuum body in $\mathbb{R}^3$, current configuration at instant t, p. 29

$\boldsymbol{\mathcal{B}}$ Continuum body in space as an open set in $\mathbb{R}^3$, p. 20

$\boldsymbol{\mathcal{B}}_0$ Continuum body in $\mathbb{R}^3$, reference configuration, p. 29

ν Poisson's ratio, p. 5

∂V Volume boundary, p. 29

$\Phi(\mathbf{X}, t)$ Mapping of motion, p. 20

v Velocity vector, p. 22

$\mathbf{A}$ Reference/material area vector, p. 29

$\mathbf{a}$ Current/spatial area vector, p. 29

$\mathbf{c}_{\text{disc}}$ Velocity of a discontinuity, p. 27

$\mathbf{e}_1$, $\mathbf{e}_2$, $\mathbf{e}_3$ Cartesian coordinate directions, p. 74

$\mathbf{N}$ Reference/material surface normal vector, p. 26

$\mathbf{n}$ Current/spatial surface normal vector, p. 26

$\mathbf{N}_{\text{disc}}$ Normal of a discontinuity surface, p. 27

$\mathbf{X} = (X_1, X_2, X_3)^T$ Reference/material position vector in $\mathbb{R}^3$, p. 20

$\mathbf{x} = (x_1, x_2, x_3)^T$ Current/spatial position vector in $\mathbb{R}^3$, p. 20

$\mathbf{Z}$ Direction vector in $\mathbb{R}^3$, p. 34

$C^n(\mathbb{R}^3)$ Space of functions in $\mathbb{R}^3$ continuous and differentiable up to the n^{th} order, p. 29

$d\mathbf{A}$ Reference/material area vector, p. 26

$d\mathbf{a}$ Current/spatial area vector, p. 26

$d\mathbf{X}$ Material fibre, p. 24

$d\mathbf{x}$ Spatial fibre, p. 24

dA Reference/material elemental area, p. 26

da Current/spatial elemental area, p. 26

dV Reference/material elemental volume, p. 25

dv Current/spatial elemental volume, p. 25

t Time instant, p. 20

V Reference/material control volume, p. 26

v Current/spatial control volume, p. 27

$(\cdot)_0$ Physical quantity or mathematical operator referring to the initial configuration, p. 132

α_i, μ_i $i = 1, \ldots, N$ Ogden hyperelastic material model parameters, p. 47

$\bar{\varepsilon}_p$ Plastic strain, p. 56

$\bar{\sigma}_y$ Yield stress measure, p. 57

$\bar{\sigma}_y^0$ Initial yield stress measure, p. 57

$\delta\mathcal{W}_{ext}$ Virtual work performed by external forces, p. 133

$\delta\mathcal{W}_{int}$ Virtual work performed by internal stresses, p. 133

$\dot{\varepsilon}_p$ Plastic multiplier, p. 59

$\dot{\mu}$ Internal dissipation rate, p. 42

$\hat{\lambda}_1$, $\hat{\lambda}_2$, $\hat{\lambda}_3$ Principal stretches isochoric (distortional) part, p. 47

$\hat{\lambda}_{e,1}$, $\hat{\lambda}_{e,2}$, $\hat{\lambda}_{e,3}$ Principal stretches of $\mathbf{F}'_e$, p. 58

$\hat{\varsigma}$ Eigenvalues of the distortional stress tensor $\hat{\mathbf{S}}$, p. 48

$\hat{\mathbf{S}}$ Second Piola-Kirchhoff stress tensor, distortional (isochoric) part, p. 48

$\hat{I}_1$, $\hat{I}_2$ First two invariants of the distortional deformation tensor $\hat{\mathbf{C}}$, p. 44

κ Bulk modulus, p. 45

λ_1, λ_2, λ_3 Principal stretches, p. 37

$\lambda_{e,1}$, $\lambda_{e,2}$, $\lambda_{e,3}$ Principal stretches of $\mathbf{F}_e$, p. 58

$\mathcal{C}$ Material elasticity 4^{th} order tensor, p. 39

μ Shear modulus, p. 44

μ_1, μ_2 Hyperelastic material model shear parameters, p. 44

Ψ Elastic potential strain energy, p. 35

ρ Spatial density/Density in case $\rho = \text{const}$, p. 27

ρ_0 Material density, p. 22

σ_1, σ_2, σ_3 Principal stresses of stress tensor $\boldsymbol{\sigma}$, p. 57

σ_{eq} Equivalent deviatoric stress measure in yield criterion, p. 56

θ Temperature, p. 41

$\mathcal{U}_\alpha^R = \{\mathbf{p}_\alpha^R, \mathbf{F}_\alpha^R, \mathbf{H}_\alpha^R, J_\alpha^R\}$ Right eigenvector of deformation mode α of an elastic medium, p. 77

$\boldsymbol{\nu}$ Normal to the plastic yield surface at load point, in $\{\sigma_1, \sigma_2, \sigma_3\}$ space, p. 60

$\boldsymbol{\sigma}$ Cauchy stress tensor, p. 28

$\boldsymbol{\Sigma}_F$, $\boldsymbol{\Sigma}_H$ Σ_J Polyconvex stress work conjugates to polyconvex strain measures $\mathbf{F}$, $\mathbf{H}$, J, p. 60

$\boldsymbol{\tau}'$ Deviatoric part of the Kirchhoff stress tensor, p. 60

$\mathbf{b}$ Left Cauchy-Green deformation tensor, p. 46

$\mathbf{b}_F$ Body force vector, p. 29

$\mathbf{C}$ Right Cauchy-Green deformation tensor, p. 43

$\mathbf{F}$ Deformation gradient tensor, p. 24

$\mathbf{F}_e$, $\mathbf{C}_e$, $\mathbf{b}_e$ Elastic part of the deformation tensors, p. 55

$\mathbf{F}_p$, $\mathbf{C}_p$, $\mathbf{b}_p$ Plastic part of the deformation tensors, p. 55

$\mathbf{H}$ Matrix of cofactors of $\mathbf{F}$, p. 25

$\mathbf{l}$ Rate of deformation vector, p. 56

$\mathbf{l}_p$ Rate of plastic deformation vector, p. 56

$\mathbf{P}$ First Piola-Kirchhoff stress tensor, p. 28

$\mathbf{p}$ Linear momentum vector, p. 22

$\mathbf{P}_{dev}$ Deviatoric part of the material stress tensor, p. 42

$\mathbf{P}_{vol}$ Volumetric part of the material stress tensor, p. 42

$\mathbf{Q}$ Heat flux vector, p. 31

$\mathbf{S}$ Second Piola-Kirchhoff stress tensor, p. 30

$\mathbf{t}$ Traction force vector, p. 28

$\mathbf{t}_{\partial V\|}$ Projection of $\mathbf{t}_{\partial V}$ on the boundary surface, p. 75

$\mathbf{t}_{\partial V}$ Traction force vector imposed on the boundary, p. 75

A Helmholtz free energy potential, p. 41

c_{00}, c_{01}, c_{10}, c_{11} Hyperelastic material model parameters, p. 44

c_α Wave speed of deformation mode α of an elastic medium, p. 77

E Total energy, p. 31

e Total energy per unit volume, p. 32

$h(\bar{\varepsilon}_p)$ Plastic hardening function, p. 57

I_1, I_2, I_3 Invariants of deformation tensor $\mathbf{C}$, p. 43

J Jacobian of the deformation, p. 24

m Mass, p. 27

p Hydrostatic pressure, p. 42

s Entropy function, p. 35

s_Q Heat source, p. 31

GALERKIN METHODS AND FINITE ELEMENTS

$\beta_{i=1,\dots,N}$ Shape functions, p. 92

$\Delta t^n = t^{n+1} - t^n$ Time step size, p. 140

$\hat{\mathbf{u}}$ Approximated solution vector, p. 94

$\mathcal{U}_h$ Vector space of test functions, p. 92

$\mathcal{V}_h$ Vector space of trial functions, p. 92

F_j External force component for node j, p. 93

K_{ij} Stiffness matrix component for nodes i and j, p. 93

N_{RK} End of step evaluation obtained with Runge-Kutta time integration scheme, p. 163

σ_{CFL} CFL number, p. 141

$\upsilon_{i=1,\dots,M}$ Basis functions, p. 92

Γ_a^η Arm length of angular moment at particle a and Runge-Kutta temporal stage $\eta = \{n, *\}$, p. 151

$\mathcal{D}_{a|JST}^\eta$ JST dissipation term at particle a and Runge-Kutta temporal stage $\eta = \{n, *\}$, p. 151

$\mathcal{U}_a^*, \mathcal{U}_a^{**}, \mathcal{U}_a^{n+1}$ Subsequent stages in the Runge-Kutta time-marching scheme, p. 145

v Test functions, p. 92

$\mathbf{F}$ External force vector, p. 94

$\mathbf{K}$ Stiffness matrix, p. 94

σ_ν Artificial viscosity additional stress term, p. 114

$\mathbf{T}_a^\eta$ Internal forces vector at particle a and Runge-Kutta temporal stage $\eta = \{n, *\}$, p. 150

$\mathbf{u}_h$ Trial functions, p. 92

x_{int} Integration point, p. 95

$\widehat{\mathcal{D}}_{J|a}$ Momentum-preserving modified JST dissipation term for the Jacobian at particle a, p. 153

$\widehat{\mathcal{D}}_a$ Momentum-preserving modified JST dissipation term at particle a, p. 152

$\widehat{\mathbf{T}}_a$ Momentum-preserving modified internal force at particle a, p. 152

T Final instant of the simulation, p. 140

t^0 Initial instant of the simulation, p. 140

U_{int} Total internal energy, p. 229

$W_{(JST)}$ JST artificial dissipation, p. 229

$W_{(p)}$ Total plastic dissipation, p. 229

ϵ_S Smoothing error, p. 110

ϵ_T Truncation error, p. 112

ε_ϕ Dispersion error, p. 188

ε_D Dissipation error, p. 188

REPRODUCING KERNEL AND SPH

α Kernel normalising factor, p. 119

α_h Constant determining the smoothing length h as $h = \alpha_h|x_a - x_b|$, p. 197

$\Delta\mathbf{x} = \|\mathbf{x}_a - \mathbf{x}_b\|$ Distance between two particles a and b, p. 117

$\kappa^{(2)/(4)}$ JST parameters, p. 137

Λ_a set of neighbouring particles that fall in the compact support around target particle a, p. 137

$\langle \mathbf{f}(\mathbf{x}) \rangle$ Reproducing kernel approximation of function $\mathbf{f}(\mathbf{x})$, p. 105

Ω Computational domain, p. 101

Ω_i Support domain for particle i, p. 101

$\Psi(\mathbf{x}) = f(\alpha(\mathbf{x}), \boldsymbol{\beta}(\mathbf{x}))$ Corrective function for SPH kernels, depending on parameters $\alpha(\mathbf{x})$ and $\boldsymbol{\beta}(\mathbf{x})$, p. 123

θ_{ab} JST weighting coefficients between particles a and b, p. 137

$\upsilon_b(\mathbf{x})$ SPH shape function for target $\mathbf{x}$ at neighbour B, p. 109

$\Upsilon_{a|FV}$ JST normalised second order difference detector for element a as used in finite volumes, p. 137

$\Upsilon_{a|SPH}$ JST normalised second order difference detector for particle a as used in SPH, p. 137

$\varepsilon^{(2)/(4)}(\mathbf{x})$ JST discontinuity switches, p. 137

$\mathcal{D}_{2,4}(\mathcal{U})$ JST dissipation second or fourth order term, p. 136

$\mathcal{D}_{JST}(\mathcal{U})$ JST dissipation overall term, p. 136

$\mathcal{L}_{FV}(\cdot)$ Undivided Laplacian operator used in JST terms, p. 137

$\mathbf{D}$ SPH discretisation operator matrix, p. 168

$\mathbf{a}(\mathbf{x})$ Vector of RKPM corrective parameters, p. 254

$\mathbf{L}_a$ Correction matrix for the corrected gradient $\widetilde{\nabla}W(\mathbf{x})$ at particle a, p. 125

$\mathbf{P}(\mathbf{x})$ Vector of RKPM test function polynomials, p. 254

$\mathbf{r}$ Support radius, p. 101

$\mathbf{r}_{ij} = \|\mathbf{x}_i - \mathbf{x}_j\|$ Distance between two particles i and j, p. 115

$\mathbf{u}^h$ Approximated (interpolated) field variable, p. 102

$\mathbf{x}_a$ Target particle position, p. 102

$\mathbf{x}_b$ Neighbouring particle position, p. 102

$\widetilde{\nabla}W(\mathbf{x}-\mathbf{x}_b, \mathbf{x}, h)$ Corrected gradient of kernel, p. 125

$\widetilde{\nabla}^2W(\mathbf{x}-\mathbf{x}_b, \mathbf{x}, h)$ Corrected Laplacian of kernel, p. 127

$\widetilde{W}(\mathbf{x}-\mathbf{x}_b, \mathbf{x}, h)$ Corrected SPH kernel function, p. 123

$C_{RKPM}(\mathbf{x}-\mathbf{x}_b, \mathbf{x})$ RKPM correction function, p. 253

h Smoothing length, p. 105

$N_b(\mathbf{x}_a)$ Shape function for target particle in $\mathbf{x}_a$ evaluated at neighbouring particle in $\mathbf{x}_b$, p. 102

$W(\mathbf{x}-\mathbf{x}_b, \mathbf{x}, h)$ SPH kernel function, p. 105

$W_{RKPM}(\mathbf{x}-\mathbf{x}_b, \mathbf{x}, h)$ RKPM kernel function, p. 253

1 INTRODUCTION

1.1 BACKGROUND

Any physical problem of interest to human applications can usually be expressed mathematically through systems of partial differential equations (PDEs) to yield the desired field variables. Nonetheless, it is very rare for those systems of differential equations to have closed-form solutions; when that is the case, they are generally determined only for linearised versions of considerably simplified problems.

For the wider variety of real world applications, where nonlinear effects are prevalent, it is therefore necessary to seek approximate solutions via numerical methods. The momentous increase in computational power of the past four decades, due to advances in computer hardware technology, and in data transmission with the advent of the world wide web, has produced a growing interest in industry for the development of novel – and the enhancement of older – numerical techniques, with the aim of tackling problems deemed untreatable before, due to their complexity, or due to the level of detail required to obtain meaningful results.

Fast dynamics analyses, in particular, are very expensive to validate with campaigns of experimental tests, both in terms of time and resources. Industry relevant examples include collision and impact tests, vehicles crashes, sub-, super- and hypersonic ballistics, earthquake shaking table tests on structural models (see fig. 1.1).

Numerical procedures based on continuum domain discretisation, such as finite elements (FE) or the finite volumes (FV) method, can ideally be set up either from the displacement method, or from the method of forces, respectively known also as the stiffness and flexibility methods [255]; these two techniques offer alternative ways to obtain the current state of stress and strain across a continuum in linear solid mechanics.

(a) Automotive crash test

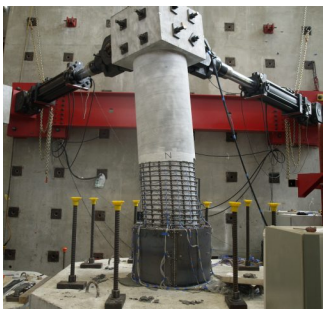

(b) Earthquake safety test

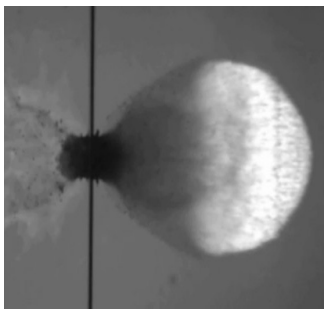

(c) Hypersonic ballistic test

Figure 1.1: some examples of industry-related real physics test modelling that can be alternatively performed with nonlinear solid dynamics numerical applications.

By far the most widely used of the two is the displacement method, conceptually more straightforward, and easier to implement in computer codes due to its repetitive, mechanical nature. It is also easier to extend this approach for nonlinear cases [22].

For nonlinear solid dynamics problems, the differential form of the displacement-based governing equation, to be verified locally at each space point of the domain, is

$$\rho \ddot{\mathbf{x}} = \nabla \cdot \boldsymbol{\sigma}(\mathbf{x}) + \mathbf{f} \tag{1.1}$$

where ρ is the material density, $\ddot{\mathbf{x}}$ is the local current acceleration, $\nabla \cdot \boldsymbol{\sigma}(\mathbf{x})$ represents the divergence of local stresses, and $\mathbf{f}$ generically refers to external forces.

The equation of motion (1.1) should be complemented with proper boundary values for displacements $\mathbf{x}$ and/or stresses $\boldsymbol{\sigma}$, and initial conditions (ICs) for both positions $\mathbf{x}$, and velocities $\dot{\mathbf{x}}$.

FE formulations employ the weak version of (1.1), obtained through the time rate of the principle of virtual work [39, 196, 262]:

$$\int_{\Omega} \rho \ddot{\mathbf{x}} \cdot \delta \boldsymbol{w} \, d\Omega + \int_{\Omega} \boldsymbol{\sigma}(\mathbf{x}) : \delta \mathbf{d} \, d\Omega = \int_{\partial\Omega} \mathbf{t} \cdot \delta \boldsymbol{w} \, d\partial\Omega + \int_{\Omega} \mathbf{f} \cdot \delta \boldsymbol{w} \, d\Omega \tag{1.2}$$

In (1.2), the traction force vector $\mathbf{t}$ is obtained by applying integration by parts and the divergence theorem to the term $\nabla \cdot \boldsymbol{\sigma}$ in (1.1), $\delta \boldsymbol{w}$ represents

virtual arbitrary velocities, and $\delta\mathbf{d}$ is the virtual rate of deformation tensor, defined as $\delta\mathbf{d} = {}^1/_2\left(\nabla\delta\boldsymbol{w} + \nabla\delta\boldsymbol{w}^{\mathrm{T}}\right)$.

The domain of interest Ω is firstly partitioned into a number of finite elements, across which equation (1.2) is then discretised. The integrals are computed numerically using quadrature rules; as a result, a global algebraic system including all elements is assembled and solved for the values of displacement at the elements nodes, through an implicit or explicit time-marching scheme, such as the Newmark method [115]. As a last step, displacement values at the nodes are used as starting points to interpolate displacement fields over the whole domain, with the help of assigned shape functions.

This procedure generally yields good results, acceptable even in the case of coarse meshes. Such robustness has made it possible to adopt linear finite elements, possessing a limited number of nodes and integration points with respect to higher order elements, as a preferred choice in nonlinear dynamics analyses by commercial FE packages (e. g. Adina, Abaqus or LS-Dyna), principally due to the considerable speed-up in simulation time. Other advantages of low order elements include simpler detection rules for interpenetration of opposite surfaces during analyses involving contact [103], and, more importantly, the availability of mesh generators based on Delaunay triangulation for 3D tetrahedral and 2D triangular elements, that are fast and can be automatised and adapted for complex geometries. In addition, these advanced mesh generators can guarantee elemental angles in the correct range, to avoid distorted and even unusable grid elements [142, 220, 254]. This robustness can be further enhanced by smoothing techniques, that act by relocating nodes in order to eliminate excessively distorted elements [78, 215]. This swift meshing capability is especially advantageous, given that a sizeable portion of the average analysis process seems to be spent on pre-processing, as can be readily noticed from fig. 1.2.

Thus, the combination of linear tetrahedral FE with a time integrator of the Newmark family forms a mature and convenient methodology, and as such it is widely used for fast dynamics simulations in academy and industry. Still, room is left for improvement, as the technique has (a) a glaring defect that affects all analyses, and, in addition, (b) it encounters serious difficulties when employed in solving a few specific classes of applications.

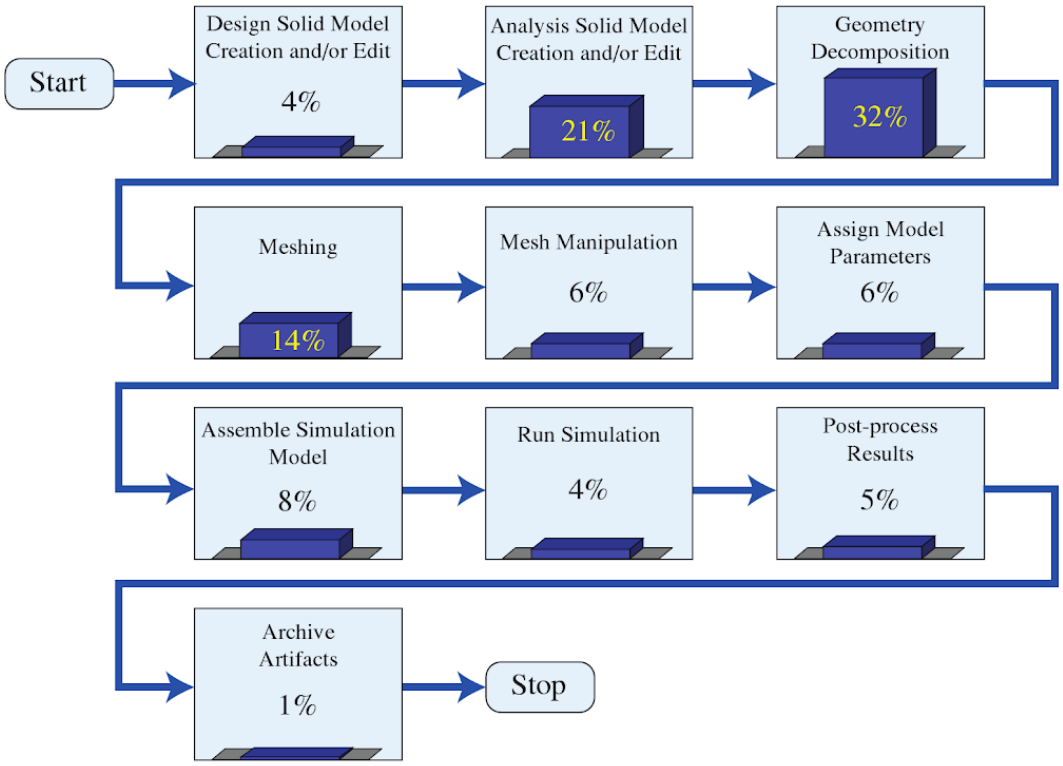

Figure 1.2: typical time allocation to the different stages of analysis for a solid mechanics numerical simulation. Data elaborated at Sandia National Laboratories, USA. (Source: [55])

a. ORDER OF ACCURACY: more to the point, the shortcoming mentioned above consists in a lower degree of accuracy (first order) that stresses and strains can achieve, in comparison to the second order reached by displacements and velocities. This obviously affects the quality of solutions, but also gives rise to other problems, in case internal bending moments are present.

In fact, in a bending scenario, linear tetrahedral finite elements cannot reproduce the deformed state correctly, because the number of nodes they possess is not enough to interpolate with sufficient accuracy the internal tensile stress associated with bending.*

This results in tensile stresses being underestimated when compared to shear stresses, whereas in a bending scenario it should work the other way around [16]. As a consequence, the structure will experi-

* It is said that they lack *polynomial consistency*.

ence smaller deformations than expected, exhibiting an overly stiff behaviour.

What just described is the so-called *shear locking* phenomenon, which can be overcome by increasing the number of elements in the simulation (*h*-refinement) [103], or by substituting the linear elements with higher order elements, with nodes located at the mid-edges, not just at the tetrahedral vertices (*p*-refinement). Both h- and p-refinement add to the computational burden of the simulation, with the latter also fundamentally altering the nature of the scheme.

b. ENFORCING INCOMPRESSIBILITY: in the particular scenarios of *constrained media* problems, involving incompressible (Poisson's ratio $\nu = 0.5$) and nearly-incompressible materials† ($\nu \to 0.5$), the Galerkin weak formulation as set up in (1.2) may not be able to suppress the volumetric dilation throughout the whole domain Ω. Failing to enforce the incompressibility condition leads to the development of the *volumetric locking* pathology. For the simple case of linear elasticity, volumetric locking can be explained as following: since $\nu \approx 0.5$, the material bulk modulus κ, dependent on ν, assumes very large values; as a consequence a pressure field (the portion of stress proportional to the volumetric strain via κ) will produce little deformation, resulting in overly stiff behaviour.

Volumetric locking cannot be rectified by h-refinement. One possible solution consists in performing p-refinement (adopting high order elements), and then in underintegrating the elements, that is, in reducing their number of integration points. Reduced integration elements perform considerably better than fully integrated high order elements, because the latter have more integration points than degrees of freedom available to satisfy the dilatation conditions [41], overconstraining the kinematically admissible displacement field. Hence, eliminating some of the quadrature points also eliminates these overconstraints, reducing the stiffness of the response and improving accuracy.

In any case, reduced integration is not available for basic linear finite elements, given that they have just one integration point.

† Real world examples of such materials: natural and synthetic rubbers, biological tissues.

In order to address the numerical issues caused by incompressibility, significant efforts have been made in the past to alter the original displacement-based problem (1.1), and to develop formulations where additional equations, with forces or force-like variables (e. g. pressure) as unknowns, are coupled as constraints to the balance of linear momentum, to be solved for the displacements. These alternative governing systems of equations, that have both forces and displacements as field unknowns, are termed *mixed methods*.

Problem (1.1) will have to be reformulated accordingly, and a solution space of forces (or pressures) will be prescribed along with the solution space of displacements, in order to define the Galerkin weak statement of the problem. Nodes intended for pressure interpolation will have then to be defined, in addition to those allocated for interpolating displacements [115].

Mixed formulations present a system matrix that is symmetric, but not positive-definite: zero-valued eigenvalues may appear, in the form of spurious *pressure modes* that will make the solution unstable.

The stability requirements of mixed formulation methods were investigated by Babushka [10] and Brezzi [45], leading to the fundamental Ladyzenskaja Babushka Brezzi (LBB) stability condition, an inf-sup requirement on the solutions function spaces, that in many practical cases demands their *enrichment*, i. e. the addition of further degrees of freedom in the model.

It has been proven [168] that certain types of mixed formulations, depending on the disposition of pressure nodes, end up yielding the same results as certain approaches to displacement-based reduced, or selective [169], integration. Nevertheless, the reverse is not necessarily true, i. e. there may not be a reduced integration technique for every possible mixed formulation conceivable, especially for meshes including different element types [29].

A technique that blends the concepts of mixed formulation and of reduced integration is the $\overline{\mathbf{B}}$-method proposed in [114]. In fact, this method has been proven in [235] to be equivalent to methods derived from Hu-Washizu three-field variational principles [39], such as the mean dilatation algorithm. In general, the three independent variables that define a Hu-Washizu-type of energy potential $W(\Phi, \mathbf{P}, \mathbf{F})$ are the spatial positions Φ, a complete stress field $\mathbf{P}$, and its associated deformations $\mathbf{F}$. The mean dilatation method, introduced in [188] assumes the spatial positions Φ, the hydrostatic pressure

p, and the volumetric deformation J as independent variables for W. Numerical integration of volumetric and distortional components is performed separately, and the integration rule is one order lower for the volumetric contribution, allowing it to relax some of the constraints under incompressible conditions. Thus, volumetric locking is overcome by performing reduced integration on just one component of the deformation. Much in the same way, and yielding the same results, the $\overline{\mathbf{B}}$-method underintegrates the volumetric component of the strain-displacement matrix $\mathbf{B}$. In the case of linear elements underintegrated to just one quadrature point for volumetric strain evaluation, a constant value $\overline{\mathbf{B}}$ is obtained over the element. This method has gained acknowledgement and widespread usage for its efficiency and reliability in treating (nearly-)incompressible material behaviours, and as such can function as benchmark to test and validate new methodologies.

The $\overline{\mathbf{F}}$-method [240, 241] directly modifies the deformation gradient $\mathbf{F}$ in order to meet the incompressibility condition just on a limited set of quadrature points, instead of enforcing it at every point. This procedure inhibits volumetric locking, and differs from the $\overline{\mathbf{B}}$-method, in that it introduces its corrections after the internal stress is obtained from the elastic potential energy through variational methods.

Unfortunately, neither the $\overline{\mathbf{B}}$-, nor the $\overline{\mathbf{F}}$-methods can be applied directly to simple linear elements (linear triangles in 2-D and tetrahedra in 3-D), because these elements are already at the lowest possible amount of quadrature points, that cannot be reduced further.

An effort to extend these constraint relaxation techniques to linear 3-D elements was made by Bonet et al. [30, 37] through the use of nodal integration. This technique however, itself a form of reduced integration, introduces rank deficiency in the system matrix, leading to the emergence of spurious modes [208] that produce excessive pressure oscillations, effectively spoiling the solution.

An ongoing attempt to stabilise nodally integrated tetrahedral elements by Scovazzi et al. [218, 222, 225] employs a stress(pressure)-velocity mixed formulation, in conjunction with the variational multiscale stabilisation (VMS) algorithm previously used in Lagrangian shock hydrodynamics [116, 221, 223, 224]. Results look promising for Lagrangian elastodynamics applications.

This summary is by no means exhaustive, as a considerable amount of research efforts has been poured into mixed formulation FE for nearly-incompressible elasticity over the years. At this juncture, it is worth noting further alternative investigations performed on nodally integrated tetrahedra by Puso and Solberg [209], and Dohrmann et al. [66, 85].

1.2 POLYCONVEX MIXED FORMULATION

One of the combinations of field variables proposed in the past as unknowns for mixed methods elastodynamics problems was that of $\mathbf{p}$, the linear momentum and $\mathbf{F}$, the deformation gradient. Trangenstein et al. [257, 259, 260] were the first in trying to reformulate the elastodynamics problem in terms of first order conservation laws with $\mathbf{p}$ and $\mathbf{F}$ as unknowns. This formulation gave rise to a hyperbolic system of PDEs analogous in its nature to the Euler equations widely used in computational fluid dynamics (CFD).

In the case of hyperbolic PDEs discontinuities may emerge in the solution over time‡, even in presence of smooth ICs [139, 258]. In CFD, hyperbolic systems are discretised either:

1. with a combination of a spatial second order centred scheme (FV or finite differences (FD)) with a *method-of-line* solver in time, such as one in the Runge Kutta (RK) family [107]. This scheme may require artificial viscosity to cure numerical oscillations that appear near discontinuities of the solution.

2. with upwind, shock-capturing methods in FV [147, 206].

The aforementioned works of Trangenstein et al. employ the second of the approaches listed above; however, they restrict their endeavours to the small deformations, linearly elastic regime, from an Eulerian point of view.

Recently, further attempts were made to tailor FV algorithms from gasdynamics to solid dynamics applications, especially under a Lagrangian point of view [48, 49, 132].

‡ Discontinuities go also by the name of "shocks" in gasdynamics literature, a real-physics reference to the acoustic loud bangs that develop when mathematical solutions lose their continuity.

The idea of Trangenstein and Colella, to avoid volumetric locking in elastodynamics by using a $\{\mathbf{p}, \mathbf{F}\}$ mixed formulation combined with FV fluid dynamics methodologies, has been lately picked up again by Bonet et al. [1, 129, 143, 144], who recognised that conservation of angular momentum needs to be enforced over the discretised system at each time step. They managed to achieve second order of accuracy for strains and stresses (ordinary displacement-based codes can only reach first order in these variables). Later, they have added a third conservation law for the volumetric strain measure J, the Jacobian of $\mathbf{F}$, in order to pursue the incompressible limit $\nu \to 0.5$ [86].

In [2, 31–33, 87, 99, 145, 146] they further refined their method by noting that an extended $\{\mathbf{p}, \mathbf{F}, \mathbf{H}, J\}$ mixed formulation – with an additional conservation law for the cofactors matrix of $\mathbf{F}$, $\mathbf{H}$ – would receive solid mathematical foundations from the theoretical framework of *polyconvexity* [13, 62, 231], which could provide for proof of existence and uniqueness of solutions, and hence offer the opportunity to systematise their approach for treating elastodynamics with CFD stabilisation techniques. At least, this will be true for material models with an internal potential energy that satisfies the polyconvexity requirements.

1.3 MESHLESS METHODS AND SPH

In the landscape of computational solid mechanics, FE formulations are by far the most widespread and well-known methodologies for obtaining numerical solutions to systems of PDEs. Many decades of research into the finite elements method (FEM) have made it a mature and reliable technology; code implementation into commercial computational software packages (employed to solve problems in almost every field of engineering), has contributed to its popularity amongst practitioners.

Meshless (meshfree) methods, on the other hand, have been introduced in the literature relatively recently, and are not currently available for commercial packages in anything but their most basic and uncomplicated features.

As an alternative discretisation technique to FE, meshfree methods present both similarities and differences with it.

Fundamentally, both approaches rely on the identification of a set of material points across the problem domain, that will serve as nodes for the interpolation of field variables. This interpolation is obtained through the use of basis functions, that in both cases will need to compose a *partition of unity* function space [11]. However, what sets the two apart, most noticeably, is the dependence of the FEM from the discretisation of the domain into a set of non-overlapping elements, that are in place to enable to perform the necessary numerical integrations, and to ensure the internal compatibility of the interpolation fields. On the contrary, in meshless techniques, there is no mesh to connect the nodal points between them[§].

The FEM enforces an internal compatibility of displacements that may not be robust enough when subject to large deformations; moreover, in simulations of explosions and fragmentations, the mesh topology bears an influence on crack propagation and separation patterns, that should not exist. Meshfree methods, instead, behave very well under the aforementioned conditions, due to nodal connectivity not being constrained by the presence of elements [153].

Other advantageous features of meshless methods with respect to the FEM are: (i) ease of implementation of high-order shape functions, that are necessary to discretise PDEs containing higher order derivatives (high rate elasto-plasticity, plates and shells[¶]); (ii) an efficient adaptive refinement capability in regions where more detailed analysis is needed, as particles can be freely added locally (remeshing in FE is computationally taxing, and can only be performed up to a certain point for complex geometries) [151].

Further, the task of structured meshing is far easier for meshless methods than for FE [190].

So far, the advantages displayed by meshless particle methods over FE would seem to suggest that a change in paradigm in computational mechanics, from the latter to the former, is nothing but inevitable. However, the decisive factors of speed, ease of implementation, and the support of mathe-

§ In partial exception to the general rule, many meshless techniques, such as the class of Galerkin meshfree methods, need a background set of (possibly overlapping) cells, in order to perform the integration of stresses through Gauss quadrature rules [23, 158].

¶ FE shape functions with higher regularity than $\mathcal{C}^0$ are in fact difficult to construct for complicated geometries [50].

matically sound and straightforward theory in favour of the FE method, all contribute to make this vaunted replacement very unlikely.

Most meshless methods are, as a matter of fact, quite elaborate in their implementation, often requiring their shape functions to be built locally (employing complicated procedures) at each time step in the simulation, as they lack the simple mapping procedures that allow the FE shape functions to be built just once in the reference space, and then pushed forward to the current configuration [190].

The first meshless method with a robust implementation to appear in literature is the smooth particles hydrodynamics (SPH) formulation [88, 166]. The method constitutes an exception amongst other meshfree techniques for its simplicity: its reproducing kernel mechanism, used for building local shape functions, is in fact rather straightforward to implement, even with regards to FE [177].

The simplicity of SPH comes useful when modelling multiscale computations, as SPH can go all the way down to simulate physical interactions at the microscale, where most other local approximations, such as FE, FV or Galerkin meshfree methods would break down, because of their need of a background mesh [153].

There exists a vast literature on SPH, given the wide variety of applications the method has been adapted to: originally devised for the fields of astrophysics and cosmology, it expanded to fluid dynamics (including simulation of breaking waves, breaking dams, sloshing tanks, liquid metal moulding), to large deformation (metal forming) [34] and to fragmentation problems [25, 26] in solid mechanics, where it really excels in comparison with FE [181].

Reviews of the state of the art of SPH at various stages in its development, each with focus on application in a particular discipline, are readily available [178, 181, 243, 265].

The main advantage of SPH – its simplicity of implementation – is based on the fact that it integrates over the field by *collocation*: a form of nodal integration, it does not need background cells.

Nodal integration, per se, is a lean and straightforward methodology. However, it can be partly associated with some drawbacks inherent in SPH, that strongly limit its application.

As noted in section 1.2, nodal integration is useful in avoiding locking numerical issues; however, oscillatory instabilities may still arise in the absence of proper stabilisation. Stabilisation should be introduced in the form of artificial viscosity or upwinding schemes, as also reported in section 1.2 with respect to FV.

Oscillatory instabilities arise when numerical integration of quantities of interest is not performed over Gaussian quadrature points: that is, when it does not follow proper optimal quadrature rules. In those cases, which include nodal (or equivalently, reduced) integration, not only does the unconventional integration introduce a truncation error due to its inherent inaccuracy, but it also decreases the rank of the local stiffness matrices, thus introducing spurious zero-energy modes, called mechanisms or *hourglass modes* [115]. Hourglassing modes are the reason for the oscillations in pressure values observed in non-stabilised solid dynamics SPH simulations.

This numerical issue can be addressed by introducing artificial dissipation as an additional term in the equation of motion, as proposed by Monaghan et al. [177, 184]. Later, Vidal et al. also recognised the need to add artificial dissipation in the context of their updated Lagrangian SPH model, in case instabilities were to develop over the long run [264]. Alternatively, Vignjevic et al. [266] developed a scheme where some particles are used for evaluating the velocities, while another set of particles is employed to compute stresses, similar to "quadrature points" in FE. Analogous approaches are followed by Belitschko et al. [20], Randles and Libersky [212], and Gray et al. [95]. Dyka et al. [71] attempted to treat zero-energy modes by scattering integration points in between particles, fundamentally altering the particle nature of SPH. Recently, Ganzenmüller tried to eliminate hourglass modes by minimising an error measure based on distances between particles, using a penalty force [82].

Another drawback of SPH is its lack of consistency at and near the boundaries of the computational domain. This means that SPH cannot even approximate constant values in regions adjacent to domain boundaries, because locally its shape functions do not constitute a partition of unity. The reason for this lies in the fact that shape functions, for particles at and near the boundaries, are built on a domain of influence that is partially truncated by the boundaries themselves, leaving it incomplete [153].

Several corrections to the SPH shape functions were proposed over the years to address this boundary incompleteness: ad-hoc modifications to the kernels underlying the SPH shape functions, for instance through a moving least squares (MLS) interpolant [65], or the corrections introduced by Liu et al. [159, 163], that in practice developed a new meshless method, the reproducing kernel particle method (RKPM). Johnson and Beissel treated high-speed problems in [126], and focused on a normalised formula for the velocities; Randles and Libersky [211] attempt something similar, by operating a double contraction over the internal stresses with a correction tensor weighted upon the current geometry. The corrections proposed by Bonet et al. [34, 36] will be discussed at length in chapter 3.

Lastly, many studies have been devoted to the issue of *tensile instability*, that affects SPH implementation in solid mechanics applications. This is a behaviour observed in presence of a tensile state of stress: when this is the case, the SPH nodal particles start accelerating towards each other, and form clumps of particles. Once inside one of such clumps, particles velocities decrease and turn into slow oscillatory motions. The occurrence of tensile instability in SPH has been analysed in a number of papers [20, 35, 64, 70, 71, 180, 248]; it was concluded by Swegle et al. [248] that tension instability develops as a consequence of the interaction between the SPH kernel functions and the SPH expression of internal stresses, as the particles move in and out of the domain of influence of each other.

Bonet and Kulasegaram proved in [35] that adopting a *total Lagrangian* approach, in which the particles' fields of influence are calculated based on the reference configuration, and are then kept constant during the rest of the simulation, can entirely eliminate the issue of tensile instability, as the particles' fields of influence are kept fixed throughout the simulation.

1.4 THE JST-SPH SCHEME

Earlier in this chapter, in section 1.1, we have briefly summarised the limitations of FE when performing nonlinear solid dynamics analyses. Afterwards, in section 1.3 we have reviewed the advantages that meshless methods have in conducting such analyses, that is, improved capability in handling

high-strain scenarios, higher-order shape functions consistency, efficient and flexible implementations of adaptivity.

SPH, in particular, was given special consideration and its obstacles were carefully noted, namely:

- Consistency problems at or near the boundaries: the issue is neutralised by incorporating corrections to the SPH kernel functions. ✓
- Tensile instability: this problem is easily prevented by adopting a total Lagrangian framework. ✓
- Spurious pressure oscillations: this is caused by rank deficiency of the system matrix due to nodal integration, inherent to SPH. Elimination of hourglass modes can be achieved by either (i) the introduction of artificial dissipation in the equation of motion, (ii) upwind schemes, or (iii) the introduction of a background set of stress-evaluating points. We are going to adopt one of the three aforementioned techniques.

The hourglassing issue with SPH, discussed above, has to be resolved in order to implement a nonlinear solid dynamics numerical solver able to harness all the advantages offered by SPH. Introduction of an artificial dissipation term of the kind presented by Monaghan [184] seems to be, out of the methods proposed above, the most straightforward to implement.

However, the most advantageous option turns out to be the adoption of the mixed formulation based on a polyconvex strain energy potential, as outlined in section 1.2. Expressing the problem in terms of a mixed $\{\mathbf{p}, \mathbf{F}, \mathbf{H}, J\}$ first order system of hyperbolic PDEs, in essence:

- ensures the existence and uniqueness of analytical solutions to the problem, the numerical solution can achieve;
- enhances the order of accuracy of derived variables (stresses and strains);
- enables the use of well-proven dissipation algorithms from CFD, an opportunity offered by the analogy that can be established between the Euler equations and the mixed $\{\mathbf{p}, \mathbf{F}, \mathbf{H}, J\}$ solid dynamics system.

  More precisely, a Jameson Schmidt Turkel (JST) artificial dissipation scheme [122] would allow a higher order of accuracy than the scheme

proposed in [184]. The JST scheme has already been tested in the context of the mixed $\{\mathbf{p}, \mathbf{F}\}$, $\{\mathbf{p}, \mathbf{F}, J\}$ and $\{\mathbf{p}, \mathbf{F}, \mathbf{H}, J\}$ formulations in solid dynamics, with promising results for FV [1, 2].

JST has the significant advantage of being composed of two terms: one built on the Laplacians of the solution variables to be stabilised, and the other made of Laplacians of Laplacians of those same variables. The former is switched on in case a discontinuity is detected, while the latter, instead, remains activated as long as the solution is continuous. Any discontinuity will then be smeared over a region of high-gradient that the scheme is able to capture, without generating oscillations on the opposite edges of the discontinuity.

1.5 AIM AND OBJECTIVES

The main objective of the research underlying this thesis, is to numerically solve nonlinear, fast solid dynamics problems by adopting a new methodology, that combines a spatial discretisation performed in the SPH meshless technique, with an explicit RK time-marching scheme.

Instead of employing the standard formulation made of a second order differential equation with displacements as the unknown variable, the fast solid dynamics problem is expressed mathematically as a set of conservation laws: a system of first order hyperbolic PDEs having the linear momentum and the fibre, areal, and volumetric strain measures as unknowns to solve for. In the FE literature, mixed formulation approaches are usually employed when dealing with volumetric or shear locking, in case reduced integration is not available (for instance, when employing linear elements for improved performance).

This pursuit is not trivial, as there are a few numerical difficulties to overcome, mostly stemming from local inconsistencies of the numerical scheme arising near the boundary of the domain, and the limited stability of the time integrator. A series of modifications to the scheme have to be introduced accordingly, including the addition of a much used tool in CFD, a JST dissipation term directly dependent on the undivided Laplacian of the field variables.

1.6 OUTLINE OF THE THESIS

Figure 1.3 graphically illustrates the implementation of the new meshless SPH mixed $\{\mathbf{p}, \mathbf{F}, \mathbf{H}, J\}$ formulation for nonlinear solid dynamics problems, as proposed in section 1.4.

This novel methodology should be free from locking and pressure oscillations issues, that are also observed for linear FE under the same conditions, and at the same time should avoid numerical problems inherent to SPH: specifically, inconsistency and incompleteness of the interpolation at or near the boundary regions, and tensile instability.

Description of the research effort undertaken to implement and test this JST-SPH numerical scheme constitutes the main objective of this thesis, which will, in its remaining chapters, be structured as follows:

- CHAPTER 2: a description of the principles behind hyperbolic systems of conservation laws, including the theoretical requirements that such systems must satisfy in order to exhibit existence and uniqueness of solutions.

  This is followed by a survey on the polyconvexity property a hyperelastic material may or may not enjoy, and how its being a stricter condition than ellipticity, implies it can serve as proof for existence and uniqueness of solution to the solid dynamics problem.

  Afterwards, calculations are performed that are necessary to show that a set of hyperelastic material models enjoy the property of polyconvexity, and a spectral study of the complete $\{\mathbf{p}, \mathbf{F}, \mathbf{H}, J\}$ mixed formulation for elastodynamics is attempted.

- CHAPTER 3: here, the implementation of the JST-SPH scheme is followed step by step. In addition, a brief overview of meshless methods, including SPH, is provided. Key equations employed in the SPH method are detailed, with relevant correction methods adopted to overcome boundary inconsistencies and tensile instability. Subsequently, a description of the JST dissipation term is presented, and is then used to develop a semidiscretised $\{\mathbf{p}, \mathbf{F}, \mathbf{H}, J\}$ mixed system.

  An explicit time-marching scheme of the two-stages RK family is employed to finally obtain the fully discretised $\{\mathbf{p}, \mathbf{F}, \mathbf{H}, J\}$ system.

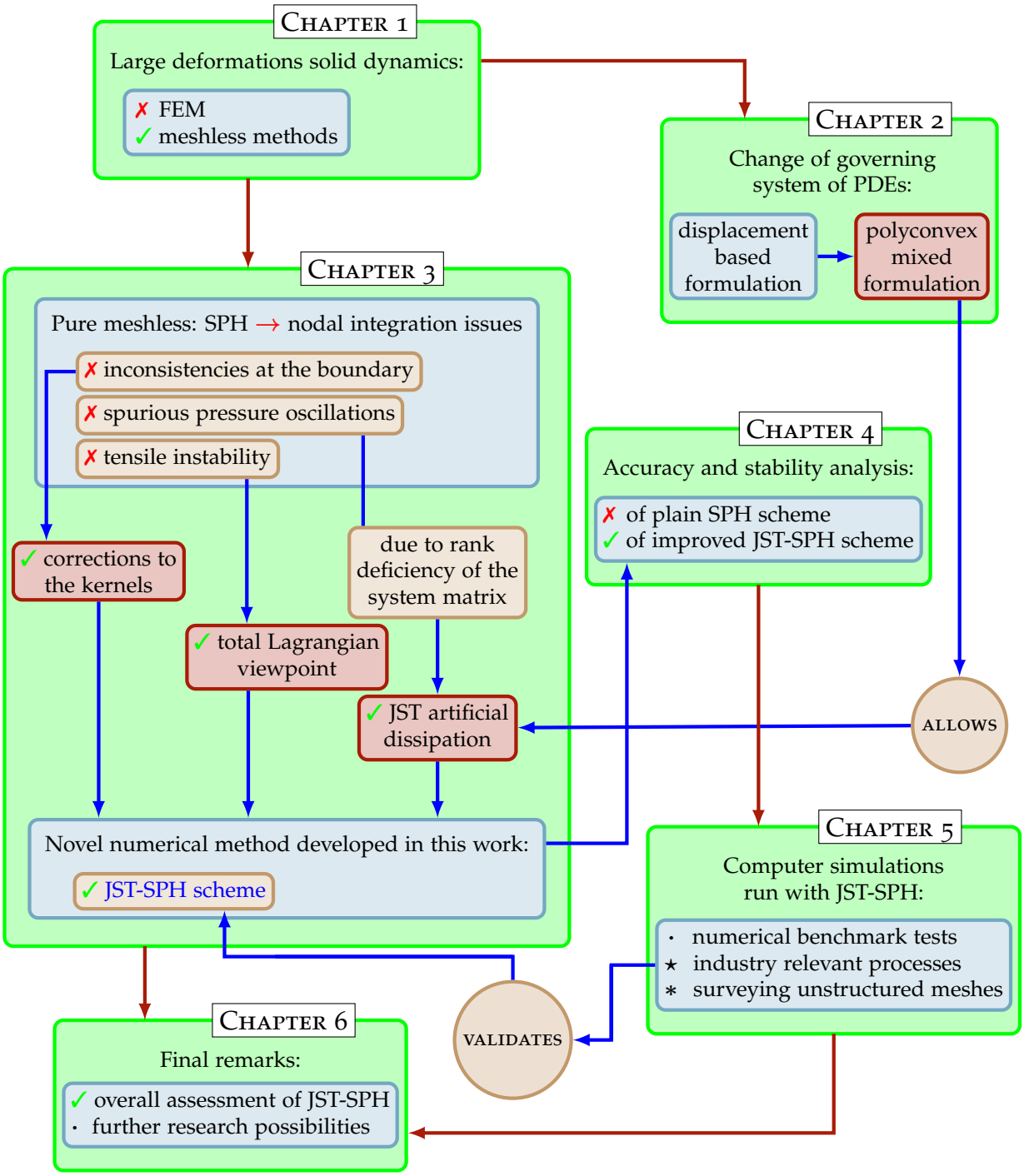

Figure 1.3: flowchart of contents of this thesis, showing correlations behind topics in blue lines, and the logical flow of chapters in red lines. Red blocks compose the main items of the JST-SPH scheme.

- CHAPTER 4: an accuracy and stability analysis is performed for a simple SPH unidimensional spatial discretisation of a linear partial differential equation (PDE) associated with the RK time-marching scheme previously described in chapter 3. The analysis includes a parametric study, with the number of neighbouring particles acting as the influencing factor. The JST dissipation is then introduced, to study its stabilising effects on the dispersion and diffusion errors of the scheme.

- CHAPTER 5: numerical applications ranging from simple elastic problems, carried out to verify the order of accuracy of the JST-SPH scheme, to nearly-incompressible and incompressible hyperelasticity high deformation problems, to impact tests and industry relevant high-strain metal extrusion processes performed in the nonlinear elasto-plastic regime. The chapter concludes by presenting some numerical simulations performed using unstructured grids of particles.

- CHAPTER 6: conclusions are drawn by highlighting main outcomes of the research reported in this thesis. Several possible avenues of future research are recommended.

2 GOVERNING EQUATIONS

The purpose of this chapter is to describe the mathematical model underlying the proposed research, and to clarify the strategy behind the chosen computational procedures.

The contents of this chapter are organised as follows. Brief remarks on geometry and kinematics in section 2.1 are useful to introduce the notation on which the rest of the chapter will build upon. Section 2.2 focuses on the definition and background of generalised *conservation laws* presented in the form of first order, hyperbolic PDEs. Following this, sections 2.3 to 2.6 elaborate the conservation laws for various relevant physical quantities of interest. Section 2.7 presents, in general terms, the nonclassical approach adopted to model finite elasticity as a system of PDEs involving multiple measures of strain, and the reasons that led to such a choice, that is, to ensure compliance to certain constitutive inequalities. The role these constitutive inequalities play on the physical plausibility, and on the uniqueness and regularity of solutions – by prescribing certain convexity conditions on the stored energy function – is the topic of section 2.8. In section 2.9, we are thus then able to select appropriate hyperelastic energy functions for the reversible part of the deformation. Furthermore, given that many of the examples in subsequent chapters will include large inelastic deformations, a necessary extension of these constitutive relations into the realm of plasticity is treated in section 2.10. In section 2.11, the hyperelastic elastic energy functions types previously considered are modified to become functions of all strain measures needed for polyconvex modelling; for this purpose, an alternative definition of the first Piola-Kirchhoff stress tensor is introduced. In so doing, we will need to associate conservation laws for such strain measures, and we will do that in section 2.12. The system of conservation laws governing the nonlinear elastodynamics problem can now be finally introduced with strong mathematical foundations in section 2.13. Some properties of this system – specifically, ancillary static conservation laws

(*involutions*), entropy function and boundary conditions (BCs) – will be the object of section 2.14. In section 2.15, study of the eigenstructure of the mixed system of conservation laws is attempted, to check that it possess real elastic wave speeds. It will then be shown how this fact leads to compliance with conditions prescribed in section 2.8, closing the loop on the subject. To cap off the chapter, in section 2.16 the eigenstructure problem so defined is set up in the case of an Ogden-type hyperelastic constitutive model. Finally, an overview of the chapter contents is offered in section 2.17.

For convenience, a graphical walk-through of the chapter is sketched in fig. 2.1.

2.1 INTRODUCTION: NOTATION, GEOMETRY, KINEMATICS

Let us now define our body of interest as an open set $\mathcal{B} \in \mathbb{R}^3$. Then, a *configuration* of $\mathcal{B}$ is a mapping $\Phi : \mathcal{B} \to \mathbb{R}^3$ that is sufficiently smooth, and invertible. A *motion* can then be introduced as the set of all configurations that exist in the time frame considered, and can be expressed as

$$\boldsymbol{x} = \Phi(\mathbf{X}, t)$$

Here, $\boldsymbol{x}^*$ represents a vector of positions the body occupies at a given time t, and is used to express the current configuration of that body at that instant, whereas $\mathbf{X}$ describes its starting positions in the reference configuration.

The rest of this dissertation will make use of the *Lagrangian (material) description* of motion, meaning that fields of physical properties will depend, at each point in time, on the initial configuration. With this approach, any physical property can be directly referred with respect to the initial configuration, and followed for the entire duration of the motion. In contrast, in the *Eulerian (spatial) description*, physical fields are direct functions of current positions. The difference between these descriptions can be formulated by identifying the body particles as the *material points* $\mathbf{X} = (X_1, X_2, X_3)^T$, and positions in $\mathbb{R}^3$ as the *spatial points* $\boldsymbol{x} = (x_1, x_2, x_3)^T$.

* Throughout this work scalar quantities will be denoted as a, in regular typeface; vectors in boldface as $\mathbf{a}$, and second order tensors in uppercase boldface as $\mathbf{A}$.

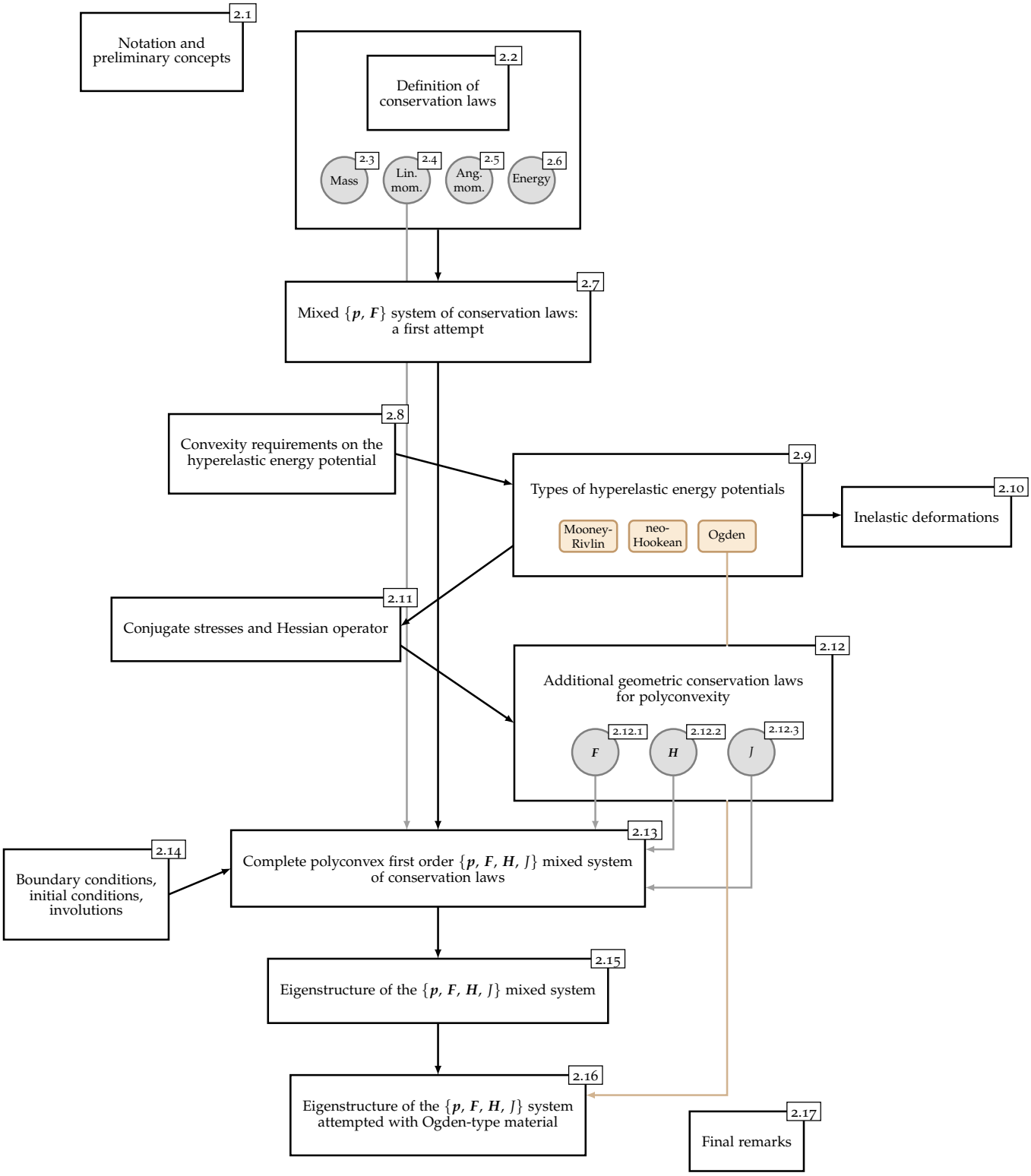

Figure 2.1: block diagram illustrating how individual sections of this chapter logically connect to each other.

In terms of notation, making a distinction between Lagrangian and Eulerian framework is important for kinematic quantities expressing positions or directions, and with regards to symbols employed to indicate differential field operators.

Following standard practice in nonlinear continuum mechanics [73], we will denote in upper case letters kinematic quantities when using a material description, while quantities in spatial description will be written in lower case letters.

In table 2.1 we compile a list of algebraic operations on vectors and tensors used throughout this work. The lesser known among those operations, the *tensorial cross product* $\times$, has been more extensively described in [31–33, 87]. As can be seen from table 2.1, the tensorial cross product can be between two second order tensors, or can involve a tensor and a vector. Its outcome will always be a second order tensor.

In addition, papers [31–33, 87] derive a number of useful properties valid for the tensorial cross product, reproduced in table 2.2 for convenience.

Differential field operators include gradient, divergence and curl; the nabla symbol ∇ will express them in spatial terms, while ∇_0 will be used for the material description.

Table 2.3 defines the differential operators used, and their notation.† In table 2.3, $\boldsymbol{\mathcal{E}}_{ijk}$ is the *Levi-Civita permutation tensor*, assuming value $+1$ in case ijk is an even permutation of the ordinal sequence $[1,2,3]$, and -1 in case is odd [148].

The material *velocity* $\boldsymbol{v}(\mathbf{X},t)$ is defined as the time derivative of the motion:

$$\boldsymbol{v}(\mathbf{X},t) = \frac{\partial \Phi(\mathbf{X},t)}{\partial t} \tag{2.1}$$

The *linear momentum* $\mathbf{p}(\mathbf{X},t)$ is then defined in terms of material *density* ρ_0 as

$$\mathbf{p}(\mathbf{X},t) = \rho_0\, \boldsymbol{v}(\mathbf{X},t) \tag{2.2}$$

The concept of *strain* allows to relate the initial material configuration and the current spatial configuration at time t. It does so through the kinematic

† In table 2.3, and everywhere else in this work, repeated subscript indices are meant to be summed.

Table 2.1: product operations involving vectors and tensors. Scalar quantities are denoted in normal font a, B; vectors in bold lowercase $\mathbf{a}$, $\mathbf{b}$; and second order tensors in bold uppercase $\mathbf{A}$, $\mathbf{B}$. Subscript indices range from 1 to 3 for the $\mathbb{R}^3$ domain. Functions $\operatorname{tr}\mathbf{A}$ and $\det\mathbf{A}$ stand respectively for trace and determinant of a matrix $\mathbf{A}$.

operation	representation	result
scalar (inner) product	$\mathbf{a}\cdot\mathbf{b} =$	$c = \sum_{i=1}^{3} a_i b_i$
vector product	$\mathbf{a}\times\mathbf{b} =$	$\mathbf{c} = \begin{pmatrix} a_2b_3 - a_3b_2 \\ a_3b_1 - a_1b_3 \\ a_1b_2 - a_2b_1 \end{pmatrix}$
tensor (outer) product	$\mathbf{a}\otimes\mathbf{b} =$	$\mathbf{C} = \begin{bmatrix} a_1b_1 & a_1b_2 & a_1b_3 \\ a_2b_1 & a_2b_2 & a_2b_3 \\ a_3b_1 & a_3b_2 & a_3b_3 \end{bmatrix}$
double contraction	$\mathbf{A} : \mathbf{B} =$	$c = \operatorname{tr}\left(\mathbf{A}^{\mathsf{T}}\mathbf{B}\right) = \sum_{i=1}^{3}\sum_{j=1}^{3} A_{ij}B_{ij}$
tensorial cross product	$\mathbf{a}\times\mathbf{A} =$	$\mathbf{C} = \begin{bmatrix} a_2A_{31} - a_3A_{21} & a_2A_{32} - a_3A_{22} & a_2A_{31} - a_3A_{21} \\ a_3A_{11} - a_1A_{31} & a_3A_{12} - a_1A_{32} & a_3A_{11} - a_1A_{31} \\ a_1A_{21} - a_2A_{11} & a_1A_{22} - a_2A_{12} & a_1A_{21} - a_2A_{11} \end{bmatrix}$
	$\mathbf{A}\times\mathbf{a} =$	$\mathbf{C} = \begin{bmatrix} A_{12}a_3 - A_{13}a_2 & A_{13}a_1 - A_{11}a_3 & A_{11}a_2 - A_{12}a_1 \\ A_{22}a_3 - A_{23}a_2 & A_{23}a_1 - A_{21}a_3 & A_{21}a_2 - A_{22}a_1 \\ A_{32}a_3 - A_{33}a_2 & A_{33}a_1 - A_{31}a_3 & A_{31}a_2 - A_{32}a_1 \end{bmatrix}$
	$\mathbf{A}\times\mathbf{B} =$	$\mathbf{C} = \begin{bmatrix} \det\begin{pmatrix} A_{22} & A_{23} \\ B_{32} & B_{33} \end{pmatrix} + \det\begin{pmatrix} B_{22} & B_{23} \\ A_{32} & A_{33} \end{pmatrix} & -\det\begin{pmatrix} A_{21} & A_{23} \\ B_{31} & B_{33} \end{pmatrix} - \det\begin{pmatrix} B_{21} & B_{23} \\ A_{31} & A_{33} \end{pmatrix} & \det\begin{pmatrix} A_{21} & A_{22} \\ B_{31} & B_{32} \end{pmatrix} + \det\begin{pmatrix} B_{21} & B_{22} \\ A_{31} & A_{32} \end{pmatrix} \\ -\det\begin{pmatrix} A_{12} & A_{13} \\ B_{32} & B_{33} \end{pmatrix} - \det\begin{pmatrix} B_{12} & B_{13} \\ A_{32} & A_{33} \end{pmatrix} & \det\begin{pmatrix} A_{11} & A_{13} \\ B_{31} & B_{33} \end{pmatrix} + \det\begin{pmatrix} B_{11} & B_{13} \\ A_{31} & A_{33} \end{pmatrix} & -\det\begin{pmatrix} A_{11} & A_{12} \\ B_{31} & B_{32} \end{pmatrix} - \det\begin{pmatrix} B_{11} & B_{12} \\ A_{31} & A_{32} \end{pmatrix} \\ \det\begin{pmatrix} A_{12} & A_{13} \\ B_{22} & B_{23} \end{pmatrix} + \det\begin{pmatrix} B_{12} & B_{13} \\ A_{22} & A_{23} \end{pmatrix} & -\det\begin{pmatrix} A_{11} & A_{13} \\ B_{21} & B_{23} \end{pmatrix} - \det\begin{pmatrix} B_{11} & B_{13} \\ A_{21} & A_{23} \end{pmatrix} & \det\begin{pmatrix} A_{11} & A_{12} \\ B_{21} & B_{22} \end{pmatrix} + \det\begin{pmatrix} B_{11} & B_{12} \\ A_{21} & A_{22} \end{pmatrix} \end{bmatrix}$

Table 2.2: list of properties of the tensorial cross product $\boldsymbol{\times}$. Constants are denoted in lowercase font as a, vectors in bold lowercase as $\mathbf{a}$, $\mathbf{b}$, and second order tensors in bold uppercase as $\mathbf{A}$, $\mathbf{B}$. Function $\operatorname{cof}\mathbf{A}$ represents the cofactors matrix associated to $\mathbf{A}$.

1.	$(\mathbf{a} \boldsymbol{\times} \mathbf{A})\,\mathbf{b} = \mathbf{a} \times (\mathbf{A}\mathbf{b})$
2.	$(\mathbf{A} \boldsymbol{\times} \mathbf{a})\,\mathbf{b} = \mathbf{A}\,(\mathbf{a} \times \mathbf{b})$
3.	$\mathbf{a} \cdot (\mathbf{A} \boldsymbol{\times} \mathbf{B})\,\mathbf{b} = (\mathbf{a} \boldsymbol{\times} \mathbf{A}) : (\mathbf{B} \boldsymbol{\times} \mathbf{b})$
4.	$\mathbf{A} \boldsymbol{\times} \mathbf{B} = \mathbf{B} \boldsymbol{\times} \mathbf{A}$
5.	$(\mathbf{A} \boldsymbol{\times} \mathbf{B})^{\mathsf{T}} = \mathbf{A}^{\mathsf{T}} \boldsymbol{\times} \mathbf{B}^{\mathsf{T}}$
6.	$\mathbf{A} \boldsymbol{\times} (\mathbf{B} + \mathbf{C}) = \mathbf{A} \boldsymbol{\times} \mathbf{B} + \mathbf{A} \boldsymbol{\times} \mathbf{C}$
7.	$a\,(\mathbf{A} \boldsymbol{\times} \mathbf{B}) = (a\,\mathbf{A}) \boldsymbol{\times} \mathbf{B} = \mathbf{A} \boldsymbol{\times} (a\,\mathbf{B})$
8.	$(\mathbf{A} \boldsymbol{\times} \mathbf{B}) : \mathbf{C} = (\mathbf{B} \boldsymbol{\times} \mathbf{C}) : \mathbf{A} = (\mathbf{A} \boldsymbol{\times} \mathbf{C}) : \mathbf{B}$
9.	$\mathbf{a} \boldsymbol{\times} (\mathbf{A} \boldsymbol{\times} \mathbf{b}) = (\mathbf{a} \boldsymbol{\times} \mathbf{A}) \boldsymbol{\times} \mathbf{b} = \mathbf{a} \boldsymbol{\times} \mathbf{A} \boldsymbol{\times} \mathbf{b}$
10.	$\mathbf{A} \boldsymbol{\times} (\mathbf{a} \otimes \mathbf{b}) = -\mathbf{a} \boldsymbol{\times} \mathbf{A} \boldsymbol{\times} \mathbf{b}$
11.	$\mathbf{A} \boldsymbol{\times} \mathbf{I} = \operatorname{tr}(\mathbf{A})\,\mathbf{I} - \mathbf{A}^{\mathsf{T}}$
12.	$(\mathbf{A} \boldsymbol{\times} \mathbf{A}) : \mathbf{A} = 6 \det(\mathbf{A})$
13.	$\operatorname{cof}(\mathbf{A}) = \frac{\mathbf{A} \boldsymbol{\times} \mathbf{A}}{2}$

functions $\mathbf{F}$, J and $\mathbf{H}$, each one following a specific geometric property through the deformation process.

The *deformation gradient* $\mathbf{F}$ is a second order tensor that acts on the material fibre $d\mathbf{X}$ to give back the spatial fibre $d\mathbf{x} = \mathbf{F}\,d\mathbf{X}$:

$$\mathbf{F}(\mathbf{X}, t) = \frac{\partial \Phi(\mathbf{X}, t)}{\partial \mathbf{X}} \tag{2.3}$$

From (2.3) follows that the deformation gradient can be understood as the derivative of the current configuration of the body with respect to the starting position.

The definition of the *Jacobian* J of the deformation is

$$J = \det \mathbf{F} \tag{2.4}$$

Table 2.3: summary of how differential operators (in rows) act with regards to the dimensionality of the object they apply to (in columns). Subscript indices range from 1 to n for the $\mathbb{R}^n$ domain. For material quantities, substitute ∇_0 for ∇, and X_i for x_i.

	scalar a	vector $\mathbf{a}$	2^{nd} order tensor $\mathbf{A}$
gradient	$(\nabla a)_i = \partial a/\partial x_i$	$(\nabla \mathbf{a})_{ij} = \partial a_i/\partial x_j$	$(\nabla \mathbf{A})_{ijk} = \partial A_{ij}/\partial x_k$
divergence	null	$\nabla \cdot \mathbf{a} = \partial a_i/\partial x_i$	$(\nabla \cdot \mathbf{A})_i = \partial A_{ij}/\partial x_j$
curl	null	$(\nabla \times \mathbf{a})_i = \boldsymbol{\mathcal{E}}_{ijk}\partial a_k/\partial x_j$	$(\nabla \times \mathbf{A})_{ij} = \boldsymbol{\mathcal{E}}_{jkl}\partial A_{il}/\partial x_k$

J in (2.4) is a measure of volumetric change during the deformation. In fact, once identified with dV the reference (material) elemental volume, and with dv the current (spatial) elemental volume, it is true that

$$dv = J\, dV \tag{2.5}$$

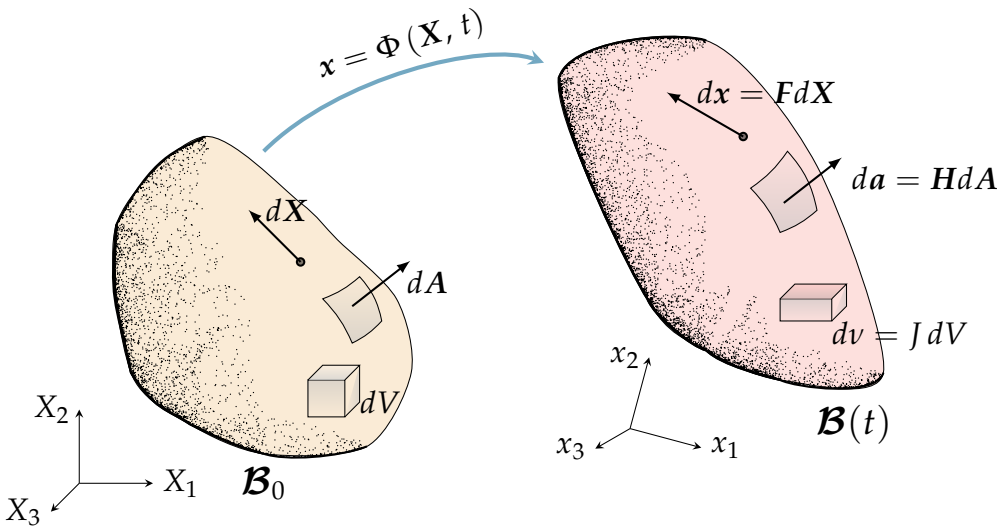

Figure 2.2: finite deformation process on a body in the continuum.

The second order tensor $\mathbf{H}$ is nothing else than the *matrix of cofactors* of $\mathbf{F}$, obtained as follows

$$\mathbf{H}(\mathbf{X}, t) = J\mathbf{F}^{-T} \tag{2.6}$$

Single entries in matrix $\mathbf{H}$ are the cofactors $H_{i,j}$, defined as

$$H_{i,j} = -1^{i+j} \det \mathbf{M}_{\mathbf{F}|i,j} \qquad \text{for } i,j = 1,2,3 \tag{2.7}$$

In (2.7), $\mathbf{M}_{\mathbf{F}|i,j}$ is the submatrix of $\mathbf{F}$ obtained by removing its i^{th} row and its j^{th} column.

The $\mathbf{H}$ tensor in (2.6) maps the reference element area vector, $d\boldsymbol{A} = \mathbf{N}dA$ (with $\mathbf{N}$ being the unit vector normal to the surface element dA) into the current element area vector $d\boldsymbol{a}$ as:

$$d\boldsymbol{a} = \mathbf{n}da = \mathbf{H}\, d\boldsymbol{A} \tag{2.8}$$

In (2.8), $\mathbf{n}$ is the unit vector normal to the spatial surface element da.

Tensors $\mathbf{F}$ and $\mathbf{H}$ can be characterised as *two-point* tensors, in that they map points from the referential, to the spatial point of view.

Figure 2.2 presents graphically some of the nomenclature just introduced in this section.

2.2 GENERAL DEFINITION OF CONSERVATION LAWS

Intuitive notions of conservation for a closed system – that certain physical quantities can neither be created nor destroyed, but rather only be redistributed throughout the system domain (the case of mass) and also turned from one form to another (the case of momentum and energy) [139] – are useful to understand the definition of *conservation laws*, as PDEs that track changes of the *conserved variables* $\boldsymbol{\mathcal{U}}$ in a control volume V [147]:

$$\frac{d}{dt}\int_V \boldsymbol{\mathcal{U}} dV + \int_{\partial V} \boldsymbol{\mathcal{F}}(\boldsymbol{\mathcal{U}}) dA = \int_V \boldsymbol{\mathcal{S}} dV \tag{2.9}$$

In (2.9), $\boldsymbol{\mathcal{F}}$ is the vector of the *fluxes* of the conserved variables in and out of the control volume, and $\boldsymbol{\mathcal{S}}$ are the source terms:

$$\boldsymbol{\mathcal{U}} = (u_1 \cdots u_n)^T, \quad \boldsymbol{\mathcal{F}}(\boldsymbol{\mathcal{U}}) = (f_1 \cdots f_n)^T, \quad \boldsymbol{\mathcal{S}} = (s_1 \cdots s_n)^T \tag{2.10}$$

As their name suggests, we can understand fluxes f_i as the amount of conserved variable u_i flowing in (if $f_i > 0$) or out (if $f_i < 0$) of the control volume V.

The integral form of the conservation laws expressed in (2.9) can also be stated in differential terms, provided that the set of $\boldsymbol{\mathcal{U}}$ be differentiable in time and the set of $\boldsymbol{\mathcal{F}}$ be differentiable in space:

$$\frac{\partial \boldsymbol{\mathcal{U}}}{\partial t} + \frac{\partial \boldsymbol{\mathcal{F}}(\boldsymbol{\mathcal{U}})}{\partial X} = \boldsymbol{\mathcal{S}} \tag{2.11}$$

In case $\boldsymbol{\mathcal{U}}$ are not continuous in the domain, *Rankine-Hugoniot conditions* have to be applied at the discontinuity, of normal $\mathbf{N}_{\text{disc}}$, that supposedly travels with velocity $\mathbf{c}_{\text{disc}}$:

$$\left(\mathbf{c}_{\text{disc}} \cdot \mathbf{N}_{\text{disc}}\right)\left(\boldsymbol{\mathcal{U}}^{+} - \boldsymbol{\mathcal{U}}^{-}\right) = \left(\boldsymbol{\mathcal{F}}^{+} - \boldsymbol{\mathcal{F}}^{-}\right)\mathbf{N}_{\text{disc}} \tag{2.12}$$

In (2.12), $\boldsymbol{\mathcal{U}}^{+}/\boldsymbol{\mathcal{U}}^{-}$ and $\boldsymbol{\mathcal{F}}^{+}/\boldsymbol{\mathcal{F}}^{-}$ express the values on one and the other side of a discontinuity. The reader who is interested can consult [107] for the full derivation of (2.12).

Fluxes terms in conservation laws (2.9) and (2.11) have to be referred, in a three dimensional domain, to a direction $\mathbf{m}$ so that the projection

$$\boldsymbol{\mathcal{F}} = \boldsymbol{\mathcal{F}}_{\mathbf{m}}\mathbf{m} \tag{2.13}$$

where $\boldsymbol{\mathcal{F}}_{\mathbf{m}}$ is the $n \times 3$ *flux matrix*, is obtained.

2.3 CONSERVATION OF MASS

Given the spatial density $\rho(\mathbf{x}, t)$ of a body $\boldsymbol{\mathcal{B}}$ with volume v in the current configuration, its *mass* will be $m = \int_v \rho dv$. The conservation of mass principle states that m is neither created nor destroyed during a motion $\Phi(\mathbf{X}, t)$:

$$\frac{d}{dt}\int_v dm = \frac{d}{dt}\int_v \rho(\mathbf{x}, t)\, dv = 0 \tag{2.14}$$

Noting that the current volume dv of a region in $\mathcal{B}$ is the scalar triple product $dv = |d\boldsymbol{x}_1 \cdot (d\boldsymbol{x}_2 \times d\boldsymbol{x}_3)|$, and that the spatial fibre vectors can be obtained from the deformation gradient as (see [97])

$$d\boldsymbol{x}_i = \mathbf{F}(\mathbf{X}, t)\, d\mathbf{X}_i = \frac{\partial \Phi(\mathbf{X}, t)}{\partial \mathbf{X}} \mathbf{N}_i dX_i = \frac{\partial \Phi(\mathbf{X}, t)}{\partial \mathbf{N}_i} dX_i$$

it can be seen that

$$dv = d\boldsymbol{x}_1 \cdot (d\boldsymbol{x}_2 \times d\boldsymbol{x}_3) = \underbrace{\frac{\partial \Phi}{\partial N_1} \cdot \left(\frac{\partial \Phi}{\partial N_2} \times \frac{\partial \Phi}{\partial N_3} \right)}_{\det \mathbf{F}} dX_1 dX_2 dX_3 =$$

$$= \det \mathbf{F}\, dV = J\, dV \tag{2.15}$$

This way, (2.14) can be alternatively put as

$$\int_v \rho(\boldsymbol{x}, t)\, dv = \int_V \rho(\boldsymbol{x}, t) J\, dV = \int_V \rho_0(\mathbf{X}, t)\, dV \tag{2.16}$$

Equation (2.16) can be more compactly put in differential form, provided $\Phi(\mathbf{X}, t)$ is sufficiently regular (no ripping or interpenetration taking place):

$$\frac{\rho_0}{\rho} = J \tag{2.17}$$

2.4 CONSERVATION OF LINEAR MOMENTUM

Let $\mathbf{t}(\boldsymbol{x}, t, \boldsymbol{n})$ be the *traction force*, defined as the force per unit area vector applied on an elemental surface of $\mathcal{B}$ having a normal pointed to the outside $\boldsymbol{n}$ in the spatial configuration. Then, the *Cauchy stress tensor* $\boldsymbol{\sigma}$ can be introduced as (see, for instance, [39])

$$\mathbf{t} = \boldsymbol{\sigma}\, \boldsymbol{n} \tag{2.18}$$

The *first Piola-Kirchhoff stress tensor* $\mathbf{P}$ is the two-point tensor that expresses the (current) force per unit of undeformed area

$$\mathbf{t} = \boldsymbol{\sigma}\, \boldsymbol{n} = J\, \boldsymbol{\sigma} \mathbf{F}^{-T} \mathbf{N} = \mathbf{P}\, \mathbf{N} \tag{2.19}$$

In (2.19), $\mathbf{N}$ represents the direction and orientation of unit vector $\mathbf{n}$ at the initial configuration.

We have derived equation (2.19) using the *Piola transform* rule, that, provided the motion $\Phi : \boldsymbol{\mathcal{B}}_0 \to \boldsymbol{\mathcal{B}}(t)$ is continuous and differentiable, allows to express the pull back of a vector field $\mathbf{a}$ – connected with measures of area or volume – from some configuration $\boldsymbol{\mathcal{B}}(t)$ to the reference state $\boldsymbol{\mathcal{B}}_0$ [196]:

$$\mathbf{A} = J\,\mathbf{F}^{-1}\mathbf{a} \tag{2.20}$$

Having defined the traction force $\mathbf{t}$ in terms of the reference area $d\mathbf{A} = \mathbf{N}\,dA$, and given the eventual presence of external body forces $\mathbf{b}_F$, it is easy to assemble the balance of system linear momentum in global form:

$$\frac{d}{dt}\int_V \mathbf{p}\,dV - \int_V \rho_0\mathbf{b}_F\,dV = \int_{\partial V}\mathbf{t}\,dA = \int_{\partial V}\mathbf{P}\,\mathbf{N}\,dA \tag{2.21}$$

Now, recalling the main statement of the *divergence theorem* for $C^1(\mathbb{R}^3)$ vector fields $\mathbf{a}$, on a compact volume V with a continuously differentiable boundary ∂V vector fields $\mathbf{a}$, as

$$\int_V \nabla_0 \cdot \mathbf{a}\,dV = \int_{\partial V}\mathbf{a}\cdot\mathbf{N}\,dA \tag{2.22}$$

we can put (2.21) in differential terms as following

$$\frac{\partial \mathbf{p}}{\partial t} - \nabla_0 \cdot \mathbf{P} = \rho_0\mathbf{b}_F \tag{2.23}$$

2.5 CONSERVATION OF ANGULAR MOMENTUM

In principle, the conservation of angular momentum can be summarised by stating that any torque acting on a system should be counterbalanced by an equal and opposite variation of the overall angular momentum for that same system [242].

This, however, does not result in a simple extension of the linear momentum conservation law, obtained by pre-multiplying each of the terms in (2.21) by the distance from a point chosen at will.

In fact, if we proceed by identifying the pivot point with the origin $(0,0,0)$ of the system of coordinates, proceeding as described just above will yield:

$$\int_V \mathbf{x} \times \frac{\partial \mathbf{p}}{\partial t}\, dV - \int_V \mathbf{x} \times \rho_0 \mathbf{b}_F\, dV = \int_{\partial V} \mathbf{x} \times (\mathbf{P}\,\mathbf{N})\; dA \tag{2.24}$$

Consider the following property of the vector product [233]

$$\mathbf{a} \times \mathbf{b}_F = \boldsymbol{\mathcal{E}} : (\mathbf{a} \otimes \mathbf{b}_F) \tag{2.25}$$

Using the divergence theorem on the right hand side (RHS) of (2.24) we get

$$\begin{aligned}
&\int_V \mathbf{x} \times \frac{\partial \mathbf{p}}{\partial t}\, dV - \int_V \mathbf{x} \times \rho_0 \mathbf{b}_F\, dV = \int_V \nabla_0 \cdot (\mathbf{x} \times \mathbf{P})\; dV = \\
&= \int_V \frac{\partial}{\partial X_i} \left(\boldsymbol{\mathcal{E}}_{jkl} x_k P_{li}\right)\; dV = \\
&\int_V \left[\mathbf{x} \times (\nabla_0 \cdot \mathbf{P}) + \boldsymbol{\mathcal{E}}_{jkl} F_{ki} P_{li}\right]\; dV
\end{aligned} \tag{2.26}$$

where $i, j, k, l = 1, 2, 3$.

The terms composing (2.23) can then be isolated on one side of (2.26) :

$$\int_V \mathbf{x} \times \left(\frac{\partial \mathbf{p}}{\partial t} - \nabla_0 \cdot \mathbf{P} - \rho_0 \mathbf{b}_F\right)\; dV = \int_V \boldsymbol{\mathcal{E}}_{jkl} F_{ki} P_{li}\, dV \tag{2.27}$$

thus obtaining

$$\int_V \boldsymbol{\mathcal{E}}_{jkl} F_{ki} P_{li}\, dV = \int_V \boldsymbol{\mathcal{E}} : \left(\mathbf{F}\mathbf{P}^T\right)\; dV = 0 \tag{2.28}$$

Now, we can observe that (2.28), expressed in local terms, yields the symmetry

$$\mathbf{F}\mathbf{P}^T = \mathbf{P}\mathbf{F}^T \tag{2.29}$$

In passing, it is useful to note that (2.29) leads to the definition of a material, symmetric stress tensor $\mathbf{S} = \mathbf{F}^{-1}\mathbf{P}$, the *second Piola-Kirchhoff stress*

tensor (the first Piola-Kirchhoff stress tensor $\mathbf{P}$ is a two-point tensor, and not necessarily symmetric).

2.6 CONSERVATION OF ENERGY

The first law of thermodynamics is, in essence, the statement that the rate of change in time of the total energy E of a system subject to a transformation process (that might be, amongst many others, a deformation) is equal to the quantity of energy exchanged by the system with the outer environment [76]. The first law of thermodynamics directly leads to a conservation law for the total energy of the system.

In continuum mechanics, the system coincides with a deformable body, and influence from the outside comes in the form of the rate of work exerted on the body by external traction, or volume forces; from heat exchange, through the presence of a heat flux with the outside; and, potentially, heat sources.

In absence of other forms of energy, conservation of mechanical energy is a renown fact in general mechanics. It leads to the definition of conservative force fields, as those that perform a fixed amount of work, that stays the same regardless of the path taken in moving matter between two definite positions.

The first law of thermodynamics on a continuum volume V can be expressed as

$$\frac{\partial}{\partial t}\int_V E\,dV = \underbrace{\int_{\partial V} \mathbf{t}\cdot\frac{\mathbf{p}}{\rho}\,dA + \int_V \mathbf{b}_F\cdot\mathbf{p}\,dV}_{\text{mechanical}} \underbrace{- \int_{\partial V}\mathbf{Q}\cdot\mathbf{N}\,dA + \int_V s_Q\,dV}_{\text{thermal}} \tag{2.30}$$

where $\mathbf{t}$ is the traction force defined in (2.18), $\mathbf{b}_F$ stands for body force, and $\mathbf{Q}$ and s_Q are the heat flux with the outside and a heating source, respectively. Equation (2.30) is valid when only mechanical and thermal exchanges with the outside are considered, disregarding other effects (such as changes of phase or electromagnetic interactions).

It is useful to introduce the *internal energy* per unit initial volume e as

$$e = E - \underbrace{\frac{1}{2}\frac{\mathbf{p}\cdot\mathbf{p}}{\rho}}_{\text{kinetic energy}} \tag{2.31}$$

In (2.31), e could be identified with the amount of potential energy available to the system.

Thanks to (2.31) and the divergence theorem, we can express (2.30) locally as a balance statement for the internal energy:

$$\frac{\partial e}{\partial t} + \frac{\mathbf{p}}{\rho}\cdot\frac{\partial \mathbf{p}}{\partial t} - \nabla_0\cdot\left(\mathbf{P}^T\frac{\mathbf{p}}{\rho}\right) = \mathbf{b}_F\cdot\mathbf{p} - \nabla_0\cdot\mathbf{Q} + s_Q \tag{2.32}$$

Substituting in (2.32) the local form of the conservation law of linear momentum (2.23):

$$\frac{\partial e}{\partial t} + \mathbf{p}\cdot\left(\frac{\nabla_0\cdot\mathbf{P}}{\rho} + \mathbf{b}_F\right) - \frac{\nabla_0\cdot\left(\mathbf{P}^T\mathbf{p}\right)}{\rho} = \mathbf{b}_F\cdot\mathbf{p} - \nabla_0\cdot\mathbf{Q} + s_Q \tag{2.33}$$

Given that

$$\nabla_0\cdot\left(\mathbf{P}^T\mathbf{p}\right) - \mathbf{p}\cdot(\nabla_0\cdot\mathbf{P}) = \mathbf{P}:\nabla_0\mathbf{p} \tag{2.34}$$

We can rewrite (2.33) as

$$\frac{\partial e}{\partial t} = \mathbf{P}:\frac{\nabla_0\mathbf{p}}{\rho} - \nabla_0\cdot\mathbf{Q} + s_Q \tag{2.35}$$

Observing that symmetry of second derivatives allows to write

$$\frac{\partial^2\mathbf{x}(\mathbf{X},t)}{\partial\mathbf{X}\,\partial t} = \frac{\partial\mathbf{F}}{\partial t} = \frac{\nabla_0\mathbf{p}}{\rho}$$

our final formulation of the conservation law of energy can be made dependent from $\mathbf{F}$ as

$$\frac{\partial e}{\partial t} = \mathbf{P}:\frac{\partial\mathbf{F}}{\partial t} - \nabla_0\cdot\mathbf{Q} + s_Q \tag{2.36}$$

The term $\mathbf{P} : \frac{\partial \mathbf{F}}{\partial t}$ on the RHS of (2.36) provides the relation between the laws of conservation of mechanical and thermodynamic energy.

In fact, the work done by internal stresses, $\mathbf{P}$, may be split in two parts: reversible, and irreversible. This provides the basis for the concept of entropy, and the second principle of thermodynamics [227]; how to address irreversibility effects when dealing with an elasto-plastic material model will be the object of section 2.10.

2.7 MIXED SYSTEM OF CONSERVATION LAWS: A FIRST ATTEMPT

We may already be able to describe the motion $\Phi(\mathbf{X}, t)$ in all its configurations in time by noting that, using the definition of deformation gradient as $\mathbf{F}(\mathbf{x}) = \nabla_0 \mathbf{x}$, the conservation of linear momentum (2.23) can be recast as a function of the current position $\mathbf{x}$:

$$\rho_0 \ddot{\mathbf{x}} = \nabla_0 \cdot \mathbf{P}(\mathbf{F}(\mathbf{x})) + \rho_0 \mathbf{b}_F \tag{2.37}$$

Equation (2.37) is solved for positions $\mathbf{x}$. When it is complemented with: (i) a material constitutive relation that explicitly expresses the dependence $\mathbf{P}(\mathbf{F})$, (ii) ICs describing the geometry of the reference configuration $\mathcal{B}_0$, and (iii) appropriate BCs on $\mathbf{x}$ or $\mathbf{P}$, equation (2.37) allows to completely determine the motion $\Phi(\mathbf{x}, t)$ in time.

In $\mathbb{R}^3$, equation (2.37) is a system of nonlinear second order hyperbolic PDEs in $\mathbf{x}$.

For this type of problem, a unique solution has been proven to exist only locally in time [124, 130, 172] even in the case of a system defined in open space, where prescribed BCs are not necessary.

Furthermore, existing solutions are limited by the conditions that $\mathbf{x} \in C^2(\mathcal{B})$ and $\dot{\mathbf{x}} \in C^1(\mathcal{B})$, in other words, without any discontinuity [62, 89, 172]. This restriction rules out the modelling of *shocks*, that is instead of great interest in applications, such as fracture, fragmentation or impacts [22].

In the past, the introduction of dissipative mechanisms of visco-elastic or thermo-diffusive nature in (2.37) was proposed to attain a proof of existence

for weaker solutions, by way of setting the added viscous or diffusive term to the limit of 0 [62].

All these attempts have involved the transformation of (2.37) into a system of first order conservation laws of the type [63, 140, 172]:

$$\frac{\partial p_i}{\partial t} - \frac{\partial P_{ij}}{\partial X_j} = 0 \tag{2.38a}$$

$$\frac{\partial F_{ij}}{\partial t} - \frac{\partial p_i}{\partial X_j} = 0 \qquad i,j = 1,2,3 \tag{2.38b}$$

We obtained system (2.38) by rearranging the unknowns in (2.37) to be $\mathcal{U} = (\mathbf{p}, \mathbf{F})$ instead of $\mathbf{x}$. The additional set of equations (2.38b) are a simple consequence of the commutative property of partial derivatives.

The source term $\mathbf{b}_F$ was eliminated in (2.38), as its presence is not required in what follows.

Now, proof of *hyperbolicity* for system (2.38) implies that its solutions can be expressed in a wave-like form of type [74, 139]

$$\mathcal{U} = f\left(\mathbf{X}\cdot\mathbf{Z} - \lambda_i(\mathbf{X})\, t\right)\mathbf{R}_i \qquad i = 1,2,3 \tag{2.39}$$

where $\mathbf{Z}$ is a direction of choice, λ_i is the wave velocity and an eigenvalue of the flux matrix, and $\mathbf{R}_i$ is the wave profile and the eigenvector of the flux matrix corresponding to λ_i.

System (2.38) is hyperbolic if its flux matrix has maximum rank, that is, if its eigenvalues are all real and distinct, and its eigenvectors are orthogonal to each other. Proof of hyperbolicity is key to ensure dependable and realistic solutions, because the eigenvalues λ_i are the mathematical counterpart to physical wave speeds travelling in the continuum during the motion [63].

One condition that guarantees hyperbolicity to a system of conservation laws is the existence of a *convex entropy* function associated with it [13, 14]. Intuitively, a convex function on a Cartesian plane can be identified as one having its curve always below the segment connecting any two of its points.

Entropy methods are generally utilised to gain information on solutions of nonlinear PDEs, by integrating their terms, and then investigating their boundedness. This way, non-increasing bound constraints help establishing inequalities similar to dissipative behaviour [75].

In order to be completely determined, system (2.38) has to refer to a *constitutive relation* $\mathbf{P}(\mathbf{F})$. A general hyperelastic formulation is given by

$$P_{ij}(F_{ij}) = \frac{\partial \Psi(F_{ij})}{\partial F_{ij}} \qquad i,j = 1,2,3 \tag{2.40}$$

In (2.40), Ψ can either be defined as the *elastic potential*, in the case of reversible elasticity, or the Helmholtz free energy, when dissipative processes are also present.

For simplicity, hereafter we will always assume to be under isothermal conditions.

A property of systems of conservation laws such as (2.38) consists in the fact that their state variables end up satisfying certain relations at the starting configuration, that are then guaranteed to hold for all time periods considered.

These additional, stationary conservation laws emerging from systems of PDEs similar to (2.38), are the so called *involutions*. Involutions for system (2.38) are provided by the following set of equations:

$$\frac{\partial F_{ij}}{\partial X_k} - \frac{\partial F_{ik}}{\partial X_j} = 0 \qquad i,j,k = 1,2,3 \tag{2.41}$$

Noticeably, (2.41) simply restates the definition of deformation gradient as $\mathbf{F} = \nabla_0 \mathbf{x}$ by taking advantage of the property of commutativity of partial derivatives. In vectorial notation, (2.41) can be written more succinctly as $\nabla_0 \times \mathbf{F} = \mathbf{0}$.

To system (2.38) we can associate an *entropy* function s:

$$s = \frac{p^2}{2\rho_0} + \Psi(\mathbf{F}) \tag{2.42}$$

There is, however, a conflict between the conditional requirements on entropy s as formulated in (2.42):

- reference frame *objectivity* for Ψ prescribes that the relation $\Psi(\mathbf{F}) = \Psi(\mathbf{Q}_{rot}\mathbf{F})$ has to be valid for any orthogonal rotation matrix $\mathbf{Q}_{rot}$;
- but, on the other hand, s has to be convex.

These two instances clash in all cases, except when Ψ is quadratic with respect to $\mathbf{F}$ [63]. This type of dependence, however, is not found for any of the most used hyperelastic material models (see [109]).

From a mathematical standpoint, it has been shown in [63] that limiting the convexity requirement to a reduced set of $\mathbf{F}$ (the so-called *involution cone*) is not incompatible with material frame indifference of s, and does produce realistic solutions.

From the numerical perspective, instead, framing the problem as a system of conservation laws allows to employ dissipation techniques from CFD that apply exclusively in case of hyperbolicity.

In light of these considerations, in the next section we will elaborate on the relation between convexity of the energy function, and hyperbolicity of the conservation laws, and on definitions further required to fulfil it.

More in particular, we shall see that introducing additional measures of strains as unknowns to the system – moving from the $\{\mathbf{p}, \mathbf{F}\}$ to the $\{\mathbf{p}, \mathbf{F}, \mathbf{H}, J\}$ set of variables – will be, in this regard, the key step to take.

2.8 CONVEXITY REQUIREMENTS ON THE HYPERELASTIC ENERGY POTENTIAL

The second law of thermodynamics is an example of a restriction that can be imposed on governing equations (2.38) in order to exclude possible mathematical solutions that are not coherent with reality. It states that the total entropy of an isolated system, accounting for all its components and their interactions, can only remain constant or increase [76].

Non-decreasing entropy prescribes that the system can only drift towards a more chaotic state or, at best, maintain its current level constant.

In order to reproduce real situations, further physical quantities, other than entropy, can be subjected to mathematical constraints that assume the form of inequalities.

Think, for instance, at the intuitive notion that internal stress increases after any kind of compatible strain is imposed. This empirical observation directly translates into a constraint on the hyperelastic formulation (expressed in (2.40)) of the elastic potential of the material.

The aforementioned constraint on the Ψ of the material can be expressed mathematically by noting that:

- in the simplest possible situation of tension being applied to a body in the three Cartesian directions, a straightforward way to define the potential energy consists in resorting to a symmetric function of the stretches in principal directions λ_1, λ_2 and λ_3, coinciding with the Cartesian directions:

$$\Psi = \Psi(\lambda_1, \lambda_2, \lambda_3) \tag{2.43}$$

- The deformation gradient $\mathbf{F}$ and the stress tensor $\mathbf{P}$ can be expressed as

$$\mathbf{F} = \begin{bmatrix} \lambda_1 & 0 & 0 \\ 0 & \lambda_2 & 0 \\ 0 & 0 & \lambda_3 \end{bmatrix} \qquad \mathbf{P} = \begin{bmatrix} \frac{\partial \Psi}{\partial \lambda_1} & 0 & 0 \\ 0 & \frac{\partial \Psi}{\partial \lambda_2} & 0 \\ 0 & 0 & \frac{\partial \Psi}{\partial \lambda_3} \end{bmatrix}$$

- Switching to the spatial description, and using (2.19), the Cauchy stress tensor assumes the form:

$$\boldsymbol{\sigma} = J^{-1}\mathbf{P}\mathbf{F}^T = \begin{bmatrix} \sigma_1 & 0 & 0 \\ 0 & \sigma_2 & 0 \\ 0 & 0 & \sigma_3 \end{bmatrix} = \frac{1}{J}\begin{bmatrix} \frac{\partial \Psi}{\partial \lambda_1}\lambda_1 & 0 & 0 \\ 0 & \frac{\partial \Psi}{\partial \lambda_2}\lambda_2 & 0 \\ 0 & 0 & \frac{\partial \Psi}{\partial \lambda_3}\lambda_3 \end{bmatrix} \tag{2.44}$$

A material inequality can be established by noting that if $\lambda_i > \lambda_j$, then by empirical observation it must follow that $\sigma_i > \sigma_j$, for $i, j = 1, 2, 3$, and therefore

$$(\sigma_i - \sigma_j)(\lambda_i - \lambda_j) > 0 \qquad i \neq j \tag{2.45}$$

from which

$$\frac{\frac{\partial \Psi}{\partial \lambda_i}\lambda_i - \frac{\partial \Psi}{\partial \lambda_j}\lambda_j}{\lambda_i - \lambda_j} > 0 \qquad i \neq j \tag{2.46}$$

Inequality (2.46) is one of the results obtained in [12]. It is equivalent to demand that the spatial stresses σ_i be *monotonic* in λ_i, since the first inequality above, (2.45), constitutes the definition of monotonicity.

Another basic concept drawn from real analysis (RA) that is useful to characterise the admissibility of an elastic potential function is that of *convexity*. A convex function $f(x)$ is defined as

$$f(\lambda a + (1-\lambda)b) \leqslant \lambda f(a) + (1-\lambda)f(b), \qquad a \neq b, \quad 0 < \lambda < 1 \tag{2.47}$$

Intuitively, (2.47) is equivalent to state that the line segment connecting the points $(a, f(a))$ and $(b, f(b))$ on a Cartesian plane will always lie above the graph of the function $f(x)$ itself. Analytically, this is equivalent to the condition

$$f''(x) \geqslant 0 \tag{2.48}$$

If (2.47) and (2.48) are intended as strong inequalities (i.e. substitute symbols $\lesseqgtr$ with $\lessgtr$), then function $f(x)$ is said to be *strictly* convex.

Figure 2.3 is a graphical representation of a convex function.

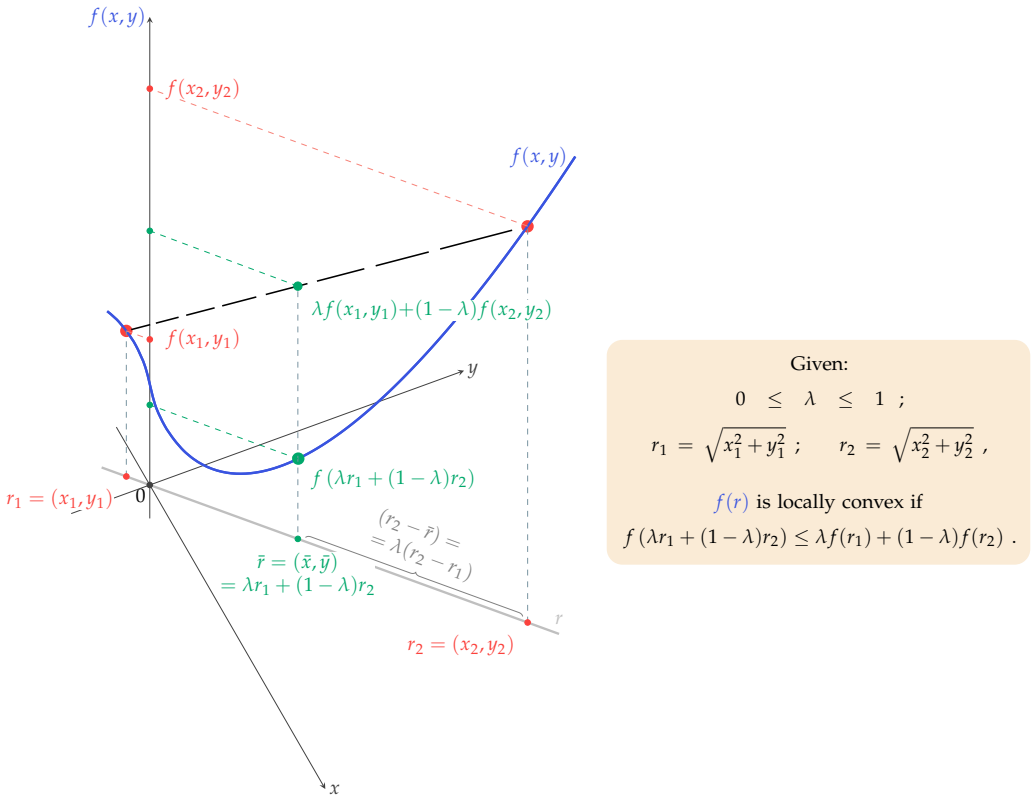

Figure 2.3: example of a convex function $f(x,y)$ in two variables. The function is presented lying on a plane of fixed inclination for simplicity.

Convex functions are of special interest because they possess only one minimum value on an open set. If strictly convex, they possess a unique minimum point.

Under suitable additional conditions, convex functions continue to satisfy such properties independently from the number of dimensions of the domain. As a result, they are widely employed as functionals in the field of calculus of variations [61]. This is interesting for our purposes because, at each instant in time, the solution of the elastic problem (2.37) also satisfies an associated variational problem [115, 125].

Strict convexity of a function $f(x)$ implies monotonicity of its first derivative $f'(x)$, meaning in our case that strict convexity of $\Psi(\lambda_1, \lambda_2, \lambda_3)$ leads to monotonicity of its first derivative with respect to the deformations, the stress tensor $\boldsymbol{\sigma}$ [172].

If we now shift our attention from the spatial to the material point of view, we may find [13] that, while the *Baker-Ericksen* condition (2.46) holds for any material, the monotonicity statement in (2.45) does not hold for $\mathbf{P}$, in the case of nearly incompressible hyperelastic materials.

As stated earlier in chapter 1, much of the research underlying this thesis is centred on the amelioration of numerical issues that arise in discretisations involving hyperelastic materials at or near the limit of incompressibility. We can now appreciate that these problems are related to the topic of mathematical admissibility of the potential elastic function underneath the equations to be discretised.

Convexity can be also imposed on the hyperelastic potential Ψ in the material frame, if $\mathbf{P}$ satisfies the following *strong ellipticity* condition:

$$(\boldsymbol{v} \otimes \boldsymbol{w}) : \boldsymbol{\mathcal{C}} : (\boldsymbol{v} \otimes \boldsymbol{w}) \geqslant \varepsilon \|\boldsymbol{v}\|^2 \|\boldsymbol{w}\|^2 \tag{2.49}$$

where $\boldsymbol{\mathcal{C}} = \frac{\partial \mathbf{P}}{\partial \mathbf{F}} = \frac{\partial^2 \Psi}{\partial \mathbf{F} \partial \mathbf{F}}$, and $\varepsilon > 0$. Inequality (2.49) has to hold for any vector $\boldsymbol{v}, \boldsymbol{w} \in \mathbb{R}^3$.

Strong ellipticity leads to three important developments:

1. the *Legendre-Hadamard* condition in linear elasticity, which states [98] that if the elastic tensor satisfies (2.49), there exist a wave-form solution to the system given as

$$\mathbf{u}(\mathbf{x}, t) = \boldsymbol{\nu}\, f(\mathbf{x} \cdot \boldsymbol{w} \pm ct) \tag{2.50}$$

   In (2.50), $\mathbf{u}$ indicates the displacements, $\boldsymbol{w}$ is a constant, unit vector, and $\boldsymbol{\nu}$ and c are, respectively, the eigenvectors and eigenvalues of the equation of motion in linear elasticity:

$$\rho \frac{\partial^2 \mathbf{u}}{\partial t^2} = \nabla \cdot (\boldsymbol{\mathcal{C}} : \nabla \mathbf{u}) \tag{2.51}$$

2. It implies local convexity (by linearisation) of the elastic potential of hyperelastic materials [172].

3. Most importantly, strong ellipticity leads to the Baker-Ericksen inequality (2.46). In linear elasticity, this, and the fact that there are wave-form solutions guaranteed by the Legendre-Hadamard condition above, provides strong physical groundings in favour of the plausibility of the eventual solutions. Additionally, strong ellipticity is beneficial for mathematical proofs of existence and uniqueness of such solutions (see [13, 172]).

Thus, strong ellipticity is a precondition for the existence of dependable solutions only in the realm of linear elasticity, or, at most, local nonlinearity, both in statics [245] and dynamics [113].

In [13], Ball provided a proof of global existence of solutions for nonlinear elastostatics, by resorting to the notion of *polyconvexity*, which translates into a convexity condition of the elastic potential with respect to multiple independent variables, as in the following:

$$\Psi = \Psi(\mathbf{F}, \operatorname{cof}\mathbf{F}, \det\mathbf{F}) = \Psi(\mathbf{F}, \mathbf{H}, J) \tag{2.52}$$

Much less is known about global solutions in elastodynamics, as remarked in section 2.7. However, elastodynamics is embedded in elastostatics, in the

sense that each solution for the latter problem is a point in the evolution trajectory of the former.

If the elastic potential is polyconvex in the sense of (2.52), then, in general [15, 133], the variational problem leads to the existence of minimisers of such potential, corresponding to correct solutions [172, 219]. Reduction of the quasilinear equations of classical nonlinear elasticity to semilinear form (by suppressing problematic higher frequency waves) also leads to stable solutions.

Some recent results providing global existence of dynamic solutions for polyconvex energies in presence of small deformations were produced by Sideris in [230, 231].

2.9 NONLINEAR CONSTITUTIVE MODELS IN ELASTICITY

We have noted in section 2.8 that the intuitive considerations on the relation between stresses and strains were at the root of the Baker-Ericksen inequality (2.46), and an additional constraint on the elastic potential Ψ to ensure realistic solutions (or, mathematically, to ensure the existence of minimising parameters to the variational problem associated with elasticity).

In this section, our aim is to quantify this relation for elastic, that is, reversible, material behaviour in the presence of finite deformation. We will lay out the foundation for a general elastic potential $\Psi(\mathbf{F})$, and then develop it into the polyconvex version, $\Psi(\mathbf{F}, \mathbf{H}, J)$ in section 2.11.

Defining the temperature of a thermodynamic system as θ, the Helmholtz free energy potential $A = A(\mathbf{F}, \theta)$ is a function of state that can be established as [138]

$$A(\mathbf{F}, \theta) = \Psi(\mathbf{F}, \theta) - s\theta \tag{2.53}$$

In isothermal conditions, (2.53) becomes $A(\mathbf{F}) = \Psi(\mathbf{F})$, and their rates:

$$\dot{A}(\mathbf{F}) = \dot{\Psi}(\mathbf{F}) \tag{2.54}$$

Now, in case of a reversible process, the *internal dissipation rate* $\dot{\mu}$ [109] equals to zero:

$$\dot{\mu} = \mathbf{P} : \dot{\mathbf{F}} - \dot{A} = \mathbf{P} : \dot{\mathbf{F}} - \dot{\Psi} = 0 \tag{2.55}$$

By applying the chain rule as defined in tensor calculus [39, 148], it follows from (2.55) that

$$\mathbf{P} : \dot{\mathbf{F}} - \dot{\Psi} = \left(\mathbf{P} - \frac{\partial \Psi(\mathbf{F})}{\partial \mathbf{F}} \right) : \dot{\mathbf{F}} = 0 \tag{2.56}$$

Finally, from (2.56) the definition for the first Piola-Kirchhoff stress tensor can be recovered as

$$\mathbf{P} = \frac{\partial \Psi(\mathbf{F})}{\partial \mathbf{F}} \tag{2.57}$$

It is possible to identify two separate contributions from the stress $\mathbf{P}$: the *pressure* component $\mathbf{P}_{vol}$, responsible for any volumetric changes, and the remaining *deviatoric* part, $\mathbf{P}_{dev}$, tracking the shear forces. An analogous decomposition can be introduced for the elastic potential $\Psi = \Psi_{vol} + \Psi_{dev}$, and the pressure and deviatoric contributions to the first Piola-Kirchhoff stress tensor $\mathbf{P}$ can be obtained from the respective components of Ψ, and can be completely decoupled from each other:

$$\mathbf{P}_{dev} = \frac{\partial \Psi_{dev}}{\partial \mathbf{F}} \qquad \mathbf{P}_{vol} = \frac{\partial \Psi_{vol}}{\partial \mathbf{F}} = \frac{\partial \Psi_{vol}}{\partial J} \frac{\partial J}{\partial \mathbf{F}} = p \, J \mathbf{F}^{-T} \tag{2.58}$$

In (2.58), $p = {}^{\partial \Psi_{vol}}/_{\partial J}$. The first Piola-Kirchhoff stress tensor $\mathbf{P}$ can then be obtained as the additive composition of the pressure and deviatoric contributions, $\mathbf{P} = \mathbf{P}_{vol} + \mathbf{P}_{dev}$.

The decoupling operated in (2.58) is essential in the presence of nearly or totally incompressible behaviour of any material [39, 109, 196].

The pressure p can also be directly expressed in Lagrangian terms as $p = {}^1/_3 \, J^{-1} \mathbf{P} : \mathbf{F}$.

Suitable forms of the elastic potentials Ψ have been verified to well agree with realistic applications of both compressible and (nearly) incompressible finite elasticity (see [42, 67, 171, 244]). These models are applicable to motion of isotropic and homogeneous materials in an isothermal environment.

We will now introduce three types of well-established hyperelastic elastic potentials, that have been proven to be truly polyconvex [102, 219, 232] according to (2.52): the *Ogden* model, the *Mooney-Rivlin* model and the *neo-Hookean* model. These models were historically introduced for the study

of rubbers, that, in common with biological tissues, share the property of allowing a large range (stretches $\lambda > 0.5$) of reversible deformation [109, 196]. All three models are based on phenomenological considerations, i.e. they try to fit polynomial functions on the experimental set of stress-strain curves for vulcanised rubber of Treloar [261]. In [261], experimental data were collected in conditions of uniaxial, biaxial and pure shear deformations.

1. The first hyperelastic strain energy model to appear in literature, amongst those mentioned above, is the formulation developed by Mooney in [185] and later perfected by Rivlin [216]. The Mooney-Rivlin model is based on strain-invariance, that is, it expresses the strain potential as $\Psi = \Psi(I_1, I_2, I_3)$, a function of the *strain invariants* of the *right Cauchy-Green* tensor $\mathbf{C} = \mathbf{F}^T \mathbf{F}$, that can be defined as:

$$\begin{cases} I_1 = \mathrm{tr}(\mathbf{C}) = \mathbf{F} : \mathbf{F} \\ I_2 = \mathbf{C} : \mathbf{C} = \mathrm{tr}(\mathbf{C}^2) \\ I_3 = \det \mathbf{C} \end{cases} \tag{2.59}$$

The elastic potential function Ψ can be expressed as a Taylor series expansion, of the form:

$$\Psi = \sum_{i,j,k} c_{ijk} \, (I_1 - 3)^i \, (I_2 - 3)^j \, (I_3 - 3)^k \qquad i, j, k = 0, 1, \ldots \infty \tag{2.60}$$

Introducing the incompressibility constraint

$$J = \det \mathbf{F} = \sqrt{\det \mathbf{C}} = I_3 = 1 \tag{2.61}$$

equation (2.60) reduces to

$$\Psi = \sum_{i,j} c_{ij} \left(\hat{I}_1 - 3\right)^i \left(\hat{I}_2 - 3\right)^j \qquad i, j = 0, 1, \ldots \infty \tag{2.62}$$

In (2.62), $\hat{I}_1$ and $\hat{I}_2$ are the first two invariants of $\hat{\mathbf{C}}$, the *distortional part of* $\mathbf{C}$, defined as

$$\hat{\mathbf{C}} = (\det \mathbf{C})^{-1/3}\ \mathbf{C} = J^{-2/3}\,\mathbf{C} \tag{2.63}$$

$$\hat{I}_1 = J^{-2/3} I_1 \tag{2.64}$$

$$\hat{I}_2 = J^{-4/3} I_2 \tag{2.65}$$

If only linear expansions are considered, (2.62) becomes

$$\begin{aligned}\Psi\left(\hat{I}_1, \hat{I}_2\right) = c_{00} + c_{10}\left(\hat{I}_1 - 3\right) + c_{01}\left(\hat{I}_2 - 3\right) + \\ + c_{11}\left(\hat{I}_1 - 3\right)\left(\hat{I}_2 - 3\right)\end{aligned} \tag{2.66}$$

If we set

$$c_{00} = 0 \qquad c_{10} = \frac{\mu_1}{2}$$

$$c_{01} = -\frac{\mu_2}{2} \qquad c_{11} = 0$$

where μ_1 and μ_2 are constants with dimensional units same as that of shear modulus, and yield the shear modulus of the material as $\mu = \mu_1 - \mu_2$.

The *Mooney-Rivlin* elastic potential $\Psi_{MR}\left(\hat{I}_1, \hat{I}_2\right)$ is then obtained as

$$\Psi_{MR}\left(\hat{I}_1, \hat{I}_2\right) = \frac{\mu_1}{2}\left(\hat{I}_1 - 3\right) - \frac{\mu_2}{2}\left(\hat{I}_2 - 3\right) \tag{2.67}$$

For near incompressibility, a volumetric component can be added to the isochoric part of Ψ_{MR} in (2.67) [39] to yield

$$\Psi_{MR}\left(\hat{I}_1, \hat{I}_2, J\right) = \frac{\mu_1}{2}\left(\hat{I}_1 - 3\right) - \frac{\mu_2}{2}\left(\hat{I}_2 - 3\right) + \frac{\kappa}{2}(J-1)^2 \tag{2.68}$$

where κ is the material bulk modulus. In this manner, the first Piola-Kirchhoff stress tensor $\mathbf{P}_{MR}$ is given as

$$\mathbf{P}_{MR} = \mu_1 J^{-2/3} \left[\mathbf{F} - \frac{1}{3} (\mathbf{F} : \mathbf{F}) \mathbf{F}^T \right] + \mu_2 J^{-4/3} \cdot \cdot \left\{ \frac{2}{3} \mathbf{F}^{-T} [(\mathbf{C} : \mathbf{C}) - 3] - \mathbf{C} \left(\mathbf{F}^T + \mathbf{F} \right) \right\} + p J \mathbf{F}^{-T} \tag{2.69}$$

In (2.69), the pressure value p is

$$p = \kappa(J - 1) \tag{2.70}$$

In their work [244], Steinmann et al. have compared simulation results to the set of experimental tests carried out by Treloar in [261]: uniaxial tension, biaxial equivalent tension, and pure shearing. Material parameters for the simulations were obtained from each of the three experimental tests by means of fitting the data presented in [261] in two distinct manners: firstly, data are fit from one type of experiment; secondly, alternative values for the parameters were obtained by fitting the data from the other two tests (*cross-fitting* simulations). Using this procedure, the accuracy of the various hyperelastic models could be verified for different loading conditions, other than for a specific load test.

For the Mooney-Rivlin model, it was found that accuracy was good for small strains (stretch $\lambda < 1.5$), but, for larger ranges of deformations, only results for biaxial strains were acceptable. In addition, the simulations based on cross-fitting data are seen in [244] as not being reliable.

2. The next hyperelastic model of interest is the so-called *neo-Hookean* model [261]. It is derived from (2.66) by choosing

$$c_{00} = 0 \qquad c_{10} = \frac{\mu}{2}$$
$$c_{01} = 0 \qquad c_{11} = 0$$

where μ corresponds to the shear modulus of the material.

The neo-Hookean elastic potential can then be expressed in terms of the strain invariants of $\mathbf{C}$ as

$$\Psi_{nH}(I_1) = \frac{\mu}{2}(I_1 - 3) \tag{2.71}$$

If the material is considered to be nearly incompressible, a volumetric strain potential $U(J) = \kappa/2\,(J-1)^2$ can be added to (2.71), as done previously for the Mooney-Rivlin model:

$$\Psi_{nH}(\hat{I}_1, J) = \frac{\mu}{2}(\hat{I}_1 - 3) + \frac{\kappa}{2}(J-1)^2 \tag{2.72}$$

The first Piola-Kirchhoff stress tensor is then

$$\mathbf{P}_{nH} = \frac{\partial \Psi_{nH}}{\partial \mathbf{F}} = \mu J^{-2/3}\left[\mathbf{F} - \frac{1}{3}(\mathbf{F} : \mathbf{F})\,\mathbf{F}^{T}\right] + p\,J\mathbf{F}^{-T} \tag{2.73}$$

In (2.73), we made use of the definition of pressure p found in (2.70).

Clearly, the neo-Hookean model is a simplification of the linearised Mooney-Rivlin model. Its performances, as reported in [244], do not accurately fit the results of Treloar [261] beyond a stretch coefficient of $\lambda = 1.5$.

3. The last large strain hyperelastic model to be considered, by virtue of its proven polyconvexity [219], is the *Ogden* model, first formulated in [195]. The model was developed due to the necessity to increase the accuracy attained by simulations of rubber-like materials, when very large deformations are involved.

   Its formulation is based on a polynomial combination of the principal stretches λ_i, $i = 1, 2, 3$, the square roots of the eigenvalues of the right Cauchy-Green strain tensor $\mathbf{C}$ (or of the left Cauchy-Green tensor $\mathbf{b}$, as λ_i, $i = 1, 2, 3$ are identical for the two tensors, see for instance [262] or [39]).

In light of this, the Ogden hyperelastic strain potential function used to model incompressibility is expressed as:

$$\Psi_O(\lambda_1,\lambda_2,\lambda_3) = \sum_{p=1}^{N} \frac{\mu_p}{\alpha_p}\left(\lambda_1^{\alpha_p} + \lambda_2^{\alpha_p} + \lambda_3^{\alpha_p} - 3\right) \qquad p = 1,\ldots,N \tag{2.74}$$

where α_p are constants, and μ_p have the dimensional unit of shear moduli. Equation (2.74) is subjected to the constraint

$$\mu = \frac{1}{2}\sum_{p=1}^{N} \mu_p \alpha_p \qquad \text{with } \mu_p\alpha_p > 0 \tag{2.75}$$

In equation (2.75), μ is the shear modulus of the material.

The best fit to Treloar empirical data in [261] was realised for a choice of $N = 3$ in (2.74), with the material parameters assuming the following numerical values:

$$\begin{aligned} \alpha_1 &= 1.3 & \mu_1 &= 0.63\,\text{MPa} \\ \alpha_2 &= 5 & \mu_2 &= 0.0012\,\text{MPa} \\ \alpha_3 &= -2 & \mu_3 &= -0.01\,\text{MPa} \end{aligned} \tag{2.76}$$

For a nearly incompressible material, the isochoric component of the strain energy $\hat{\Psi}_O$ given by equation (2.74), is appropriately rewritten as a function of the principal strains of the distortional strain tensor $\hat{\mathbf{C}}$ defined in (2.63):

$$\hat{\Psi}_O(\hat{\lambda}_1,\hat{\lambda}_2,\hat{\lambda}_3) = \sum_{p=1}^{3} \frac{\mu_p}{\alpha_p}\left(\hat{\lambda}_1^{\alpha_p} + \hat{\lambda}_2^{\alpha_p} + \hat{\lambda}_3^{\alpha_p} - 3\right) \qquad p = 1,2,3 \tag{2.77}$$

where the $\hat{\lambda}_i$ are related to the principal strains of $\mathbf{C}$ by

$$\hat{\lambda}_i = J^{-1/3}\lambda_i \qquad i = 1,2,3 \tag{2.78}$$

An expression for the volumetric part of Ψ_O as a convex function can be found in [194] and it is reproduced below:

$$\Psi_O^{vol}(J) = \frac{\kappa}{\beta^2}\left(\beta \ln J + \frac{1}{J^\beta} - 1\right) \tag{2.79}$$

In equation (2.79), κ is the bulk modulus and β is an empirically determined constant. It was found [109] that a set value of $\beta = 9$ accounts well for volumetric changes in rubber-like materials as recorded experimentally, for instance, in [47].

Since the component $\hat{\Psi}_O$ of the strain potential energy in (2.77) is a function of the principal strains, it is convenient to obtain the second Piola-Kirchhoff stress tensor $\mathbf{S}$ first, and then use it for determining $\mathbf{P}$.

The reason for proceeding in this manner is that $\mathbf{S}$ shares the same principal material directions $\mathbf{N}_i$, as eigenvectors, with the right Cauchy-Green strain tensor $\mathbf{C}$ (but not with the left Cauchy-Green tensor $\mathbf{b}$, the eigenproblem of which yields the principal spatial directions $\mathbf{n}_i$).

The distortional part of the stress tensor $\hat{\mathbf{S}}$ can be spectrally decomposed as

$$\hat{\mathbf{S}} = \sum_{i=1}^{3} \hat{\varsigma}_i \mathbf{N}_i \otimes \mathbf{N}_i \tag{2.80}$$

To find the eigenvalues $\hat{\varsigma}_i$ in (2.80) we need to solve the eigenproblem

$$\left(\hat{\mathbf{S}} - \hat{\varsigma}_i \mathbf{I}\right)\mathbf{N}_i = \mathbf{0} \tag{2.81}$$

Now, $\hat{\mathbf{S}}$ can be found as a derivative of $\hat{\Psi}_O$ using a relation similar to (2.57):

$$\hat{\mathbf{S}} = 2\frac{\partial \hat{\Psi}_O}{\partial \mathbf{C}} \tag{2.82}$$

By using the chain rule on the RHS of (2.82) we obtain:

$$\frac{\partial \hat{\Psi}_O(\hat{\lambda}_1, \hat{\lambda}_2, \hat{\lambda}_3)}{\partial \mathbf{C}} = \sum_{i=1}^{3}\sum_{j=1}^{3} \underbrace{\frac{\partial \hat{\Psi}_O}{\partial \hat{\lambda}_j}}_{\text{ⓐ}} \underbrace{\frac{\partial \hat{\lambda}_j}{\partial \lambda_i}}_{\text{ⓑ}} \underbrace{\frac{\partial \lambda_i}{\partial \lambda_i^2}}_{\text{ⓒ}} \underbrace{\frac{\partial \lambda_i^2}{\partial \mathbf{C}}}_{\text{ⓓ}} \tag{2.83}$$

We will now separately analyse the four terms in the RHS of (2.83).

a) Standard derivation of (2.77) yields

$$\frac{\partial \hat{\Psi}_O}{\partial \hat{\lambda}_j} = \sum_{p=1}^{3} \mu_p \hat{\lambda}_j^{\alpha_p - 1} \qquad j = 1,2,3 \tag{2.84}$$

b) In consideration of (2.78), this term can be expanded to

$$\frac{\partial \hat{\lambda}_j}{\partial \lambda_i} = \frac{\partial \left(J^{-1/3} \lambda_j \right)}{\partial \lambda_i} = -\frac{1}{3} J^{-4/3} \frac{\partial J}{\partial \lambda_i} \lambda_j + J^{-1/3} \delta_{ij} \qquad i,j = 1,2,3 \tag{2.85}$$

Expansion of the derivative $\frac{\partial J}{\partial \lambda_i}$ in (2.85) can be achieved taking into account (see [39], among others) that

$$\frac{\partial J^2}{\partial \mathbf{C}} = \frac{J}{2} \mathbf{C}^{-1}$$

Being $J^2 = \det \mathbf{C} = I_3$ the third invariant of $\mathbf{C}$, as in (2.59).

Then we have

$$\begin{aligned} \frac{\partial J}{\partial \lambda_i} = \frac{\partial J}{\partial \mathbf{C}} \frac{\partial \mathbf{C}}{\partial \lambda_i} = \frac{J}{2} \mathbf{C}^{-1} \sum_{j=1}^{3} \frac{\partial \lambda_j^2}{\partial \lambda_i} \mathbf{N}_j \otimes \mathbf{N}_j = \\ = J \lambda_i \left(\sum_{k=1}^{3} \frac{1}{\lambda_k^2} \mathbf{N}_k \otimes \mathbf{N}_k \right) (\mathbf{N}_i \otimes \mathbf{N}_i) = \frac{J}{\lambda_i} \\ i = 1,2,3 \end{aligned} \tag{2.86}$$

In expanding (2.86), we made use of the property of orthonormality of the vectors of principal directions $\mathbf{N}_i$.

Equation (2.86) can be employed to further develop (2.85) into

$$\begin{aligned} \frac{\partial \hat{\lambda}_j}{\partial \lambda_i} = -\frac{1}{3} J^{-4/3} \frac{\partial J}{\partial \lambda_i} \lambda_j + J^{-1/3} \delta_{ij} = \\ = -\frac{1}{3} J^{-4/3} J \frac{\lambda_j}{\lambda_i} + J^{-1/3} \delta_{ij} = J^{-1/3} \left(\delta_{ij} - \frac{1}{3} \frac{\lambda_j}{\lambda_i} \right) \\ i,j = 1,2,3 \end{aligned} \tag{2.87}$$

Remembering (2.78), expression (2.87) can be put in terms of the principal distortional strains as

$$\frac{\partial \hat{\lambda}_j}{\partial \lambda_i} = J^{-1/3}\left(\delta_{ij} - \frac{1}{3}\frac{\hat{\lambda}_j}{\hat{\lambda}_i}\right) \qquad i,j = 1,2,3 \tag{2.88}$$

c) From basic derivation rules, and (2.78), it follows that:

$$\frac{\partial \lambda_i}{\partial\left(\lambda_i^2\right)} = \frac{1}{2\lambda_i} = \frac{J^{-1/3}}{2\hat{\lambda}_i} \qquad i = 1,2,3 \tag{2.89}$$

d) The last term on the RHS of (2.83) may be reformulated in a more suitable manner by observing that a differential increment of $\mathbf{C}$ in terms of principal strains and directions reads

$$\begin{aligned} d\mathbf{C} &= d\left(\sum_{i=1}^{3} \lambda_i^2 \mathbf{N}_i \otimes \mathbf{N}_i\right) = \\ &= \sum_{i=1}^{3} \left\{2\lambda_i d\lambda_i \mathbf{N}_i \otimes \mathbf{N}_i + \lambda_i^2 \left(d\mathbf{N}_i \otimes \mathbf{N}_i + \mathbf{N}_i \otimes d\mathbf{N}_i\right)\right\} \end{aligned} \tag{2.90}$$

Pre- and post-multiplication of (2.90) by $\mathbf{N}_i$ yields

$$\begin{aligned} \mathbf{N}_i^T d\mathbf{C}\mathbf{N}_i &= \sum_{j=1}^{3} \left\{2\lambda_i d\lambda_i \mathbf{N}_i \cdot \mathbf{N}_j \otimes \mathbf{N}_j \cdot \mathbf{N}_i + \right. \\ &\left. + \lambda_i^2 \left(\mathbf{N}_i \cdot d\mathbf{N}_j \otimes \mathbf{N}_j \cdot \mathbf{N}_i + \mathbf{N}_i \cdot \mathbf{N}_j \otimes d\mathbf{N}_j \cdot \mathbf{N}_i\right)\right\} = \\ &= 2\lambda_i d\lambda_i \qquad\qquad i = 1,2,3 \end{aligned} \tag{2.91}$$

In the RHS of (2.91), the second and third addenda are reduced to 0 because vectors $\mathbf{N}_i$ are normalised, and hence an increment $d\mathbf{N}_i$ can happen only in the direction orthogonal to $\mathbf{N}_i$, giving $\mathbf{N}_i \cdot d\mathbf{N}_i = 0$.

We can now exploit a property of the trace of tensors (see [39]) to obtain

$$\begin{aligned}\mathbf{N}_i^T d\mathbf{C}\mathbf{N}_i = d\mathbf{C} : \mathbf{N}_i \otimes \mathbf{N}_i = \\ = \frac{\partial \mathbf{C}}{\partial \lambda_i} d\lambda_i : \mathbf{N}_i \otimes \mathbf{N}_i = 2\lambda_i d\lambda_i \qquad i = 1,2,3\end{aligned} \tag{2.92}$$

And, noting that

$$\frac{\partial \mathbf{C}}{\partial \lambda_i} : \frac{\partial \lambda_i}{\partial \mathbf{C}} = 1 \qquad i = 1,2,3$$

we have:

$$\frac{\partial \lambda_i}{\partial \mathbf{C}} = \frac{1}{2\lambda_i} \mathbf{N}_i \otimes \mathbf{N}_i \qquad i = 1,2,3 \tag{2.93}$$

Finally, term ⓓ in (2.83) can be expressed as

$$\frac{\partial \lambda_i^2}{\partial \mathbf{C}} = \frac{\partial \lambda_i^2}{\partial \lambda_i} \frac{\partial \lambda_i}{\partial \mathbf{C}} = \mathbf{N}_i \otimes \mathbf{N}_i \qquad i = 1,2,3 \tag{2.94}$$

Now, with the help of equations (2.84), (2.85), (2.89) and (2.94), we are able to expand the RHS of (2.83) in order to obtain $\hat{\mathbf{S}}_O$ in (2.82):

$$\hat{\mathbf{S}}_O = 2\frac{\partial \hat{\Psi}_O}{\partial \mathbf{C}} = 2\sum_{i=1}^{3}\sum_{j=1}^{3} \underbrace{\left[\sum_{p=1}^{3} \mu_p \hat{\lambda}_j^{\alpha_p - 1}\right]}_{ⓐ} \underbrace{\left[J^{-1/3}\left(\delta_{ji} - \frac{1}{3}\frac{\hat{\lambda}_j}{\hat{\lambda}_i}\right)\right]}_{ⓑ} \underbrace{\left[\frac{J^{-1/3}}{2\hat{\lambda}_i}\right]}_{ⓒ} \underbrace{\left[\mathbf{N}_i \otimes \mathbf{N}_i\right]}_{ⓓ} \tag{2.95}$$

Algebraic manipulation of expression (2.95) leads to

$$\hat{\mathbf{S}}_O = J^{-2/3} \sum_{i=1}^{3}\sum_{p=1}^{3} \frac{\mu_p}{\hat{\lambda}_i^2} \left(\hat{\lambda}_i^{\alpha_p} - \frac{1}{3}\sum_{j=1}^{3} \hat{\lambda}_j^{\alpha_p}\right) \mathbf{N}_i \otimes \mathbf{N}_i \tag{2.96}$$

Comparing (2.96) with the spectral decomposition of the deviatoric second Piola-Kirchhoff stress tensor $\hat{\mathbf{S}}$ in (2.80), we can thus specify the eigenvalues $\hat{\varsigma}_i|_O$ of $\hat{\mathbf{S}}_O$ as

$$\hat{\varsigma}_i|_O = \frac{J^{-2/3}}{\hat{\lambda}_i^2} \sum_{p=1}^{3} \mu_p \left(\hat{\lambda}_i^{\alpha_p} - \frac{1}{3} \sum_{j=1}^{3} \hat{\lambda}_j^{\alpha_p} \right) \qquad i = 1, 2, 3 \tag{2.97}$$

Analogously to the procedure discussed above for the isochoric tensor $\hat{\mathbf{S}}_O$, the volumetric component $\mathbf{S}_O^{vol}$ can be derived from Ψ_O^{vol} in (2.79) in the following manner

$$\begin{aligned} \mathbf{S}_O^{vol} &= 2\frac{\partial \Psi_O^{vol}(J)}{\partial \mathbf{C}} = 2\frac{d\Psi_O^{vol}(J)}{dJ}\frac{\partial J}{\partial \mathbf{C}} = \\ &= 2\left[\frac{\kappa}{\beta^2}\left(\frac{\beta}{J} - \beta J^{-(\beta+1)}\right)\right]\left[\frac{J\mathbf{C}^{-1}}{2}\right] = \frac{\kappa}{\beta}\left(1 - J^{-\beta}\right)\mathbf{C}^{-1} \end{aligned} \tag{2.98}$$

Having obtained both the isochoric (equation (2.96)) and volumetric (equation (2.98)) contributions to $\mathbf{S}_O$, still the need remains to map the *current* stress distribution onto the material configuration. This task could be performed by the first Piola-Kirchhoff stress tensor $\mathbf{P}_O$ [39, 109, 262], which for the Ogden model can be obtained by the transformation below

$$\begin{aligned} \mathbf{P}_O &= \mathbf{F}\left(\mathbf{S}_O^{vol} + \hat{\mathbf{S}}_O\right) = \mathbf{F}\left[\frac{\kappa}{\beta}\left(1 - J^{-\beta}\right)\mathbf{C}^{-1}\right] + \\ &+ \mathbf{F}\left[J^{-2/3}\sum_{i=1}^{3}\sum_{p=1}^{3}\frac{\mu_p}{\hat{\lambda}_i^2}\left(\hat{\lambda}_i^{\alpha_p} - \frac{1}{3}\sum_{j=1}^{3}\hat{\lambda}_j^{\alpha_p}\right)\mathbf{N}_i \otimes \mathbf{N}_i\right] \end{aligned} \tag{2.99}$$

As a concluding note to this section, we observe that the isochoric contributions to the strain potential energies for the Mooney-Rivlin and neo-Hookean models can be readily expressed in terms of principal strains. In fact, they can be seen as special cases of the Ogden model.

To demonstrate this, let us consider the relations between invariants and principal stretches of $\mathbf{C}$ in the incompressible regime:

$$\begin{cases} I_1 = \lambda_1^2 + \lambda_2^2 + \lambda_3^2 \\ I_2 = \lambda_1^2\lambda_2^2 + \lambda_1^2\lambda_3^2 + \lambda_2^2\lambda_3^2 \\ I_3 = J^2 = \lambda_1^2\lambda_2^2\lambda_3^2 = 1 \end{cases} \tag{2.100}$$

- For the Mooney-Rivlin model, it suffices to set the parameters in (2.67) to

$$c_1 = \frac{\mu_1}{2} \qquad\qquad c_2 = -\frac{\mu_1}{2}$$

to obtain the following potential function from (2.67):

$$\Psi_{MR} = \sum_{p=1}^{2} \frac{\mu_p}{\alpha_p} \left(\lambda_1^{\alpha_p} + \lambda_2^{\alpha_p} + \lambda_3^{\alpha_p} - 3\right) \tag{2.101}$$

Equation (2.101) corresponds to (2.74) with parameters

$$N = 2 \qquad\qquad \alpha_1 = 2 \qquad\qquad \alpha_2 = -2$$

- For the neo-Hookean model, the Ogden model (2.74) is obtained in a straightforward manner by substituting in (2.71) parameters

$$N = 1 \qquad\qquad \alpha_1 = 2$$

Albeit it has been shown that it is fairly easy to transform from an invariant-based to a principal stretches-based hyperelastic model, it is not possible to operate in the opposite sense, converting from the Ogden model (2.74) to an invariant-based form of the type (2.60).

As a consequence, for an elastic finite response of the Ogden type, there will always be the additional cost of having to solve the eigenproblem associated to the current deformation state (in order to extract the principal stretches and directions of $\mathbf{C}$).

Algorithm 1 summarises in steps the whole procedure to obtain $\mathbf{P}_0$.

1. Assume Ogden model material parameters in (2.74) as

$$\begin{aligned} \beta &= 9 & N &= 3 \\ \alpha_1 &= 1.3 & \mu_1 &= 0.63\,\text{MPa} \\ \alpha_2 &= 5 & \mu_2 &= 0.0012\,\text{MPa} \\ \alpha_3 &= -2 & \mu_3 &= -0.01\,\text{MPa} \end{aligned}$$

2. Assume known the bulk modulus κ of the material
3. Assume the solving algorithm provides the deformation gradient at current time, $\mathbf{F}$
4. Evaluate the right Cauchy-Green strain tensor $\mathbf{C} = \mathbf{F}^T\mathbf{F}$, and Jacobian $J = \det \mathbf{F}$
5. Solve the eigenvalue problem $(\mathbf{C} - \mu_i \mathbf{I})\,\mathbf{N}_i = \mathbf{0}$ for $i = 1, 2, 3$ to obtain principal directions $\mathbf{N}_i$
6. Get principal strains of $\mathbf{C}$ as $\lambda_i = \sqrt{\mu_i}$ and principal stretches of $\hat{\mathbf{C}}$ as $\hat{\lambda}_i = J^{-1/3}\lambda_i$, for $i = 1, 2, 3$
7. Compute the 2nd Piola-Kirchhoff stress as $\mathbf{S}_0 = \hat{\mathbf{S}}_0 + \mathbf{S}_0^{vol}$:
   a) $\hat{\mathbf{S}}_0$ through (2.96)
   b) $\mathbf{S}_0^{vol}$ through (2.98)
8. Derive $\mathbf{P}_0 = \mathbf{F}\mathbf{S}_0$, (2.99).

ALGORITHM 1 : Ogden hyperelastic model

2.10 TREATMENT OF INELASTIC DEFORMATIONS

A complete description of nonlinear deformation should include treatment of inelastic effects, that, in the scope of this thesis, reduce to non-recoverable *plastic* strains. Plastic deformation on a body $\mathcal{B}$ takes place without inducing

changes to volume; computationally, this means that an incompressibility constraint has to be imposed during the process. There are, however, exceptions to this rule: yielding in porous metals, for instance, is compressible when studied at the macroscopic level [69]. Nevertheless, the elasto-plastic deformation process, as a whole, has to be treated as nearly-incompressible. The elastic strain is in fact generally compressible, but incompressible plastic strain makes up the larger part of the deformation, once the yielding point is reached [39].

The deformation gradient $\mathbf{F}$ keeps track of the total strain, and can be multiplicatively decomposed into two components, $\mathbf{F}_e$, elastic, and $\mathbf{F}_p$, plastic, so that

$$\mathbf{F} = \mathbf{F}_e \mathbf{F}_p \tag{2.102}$$

Even though the internal stress state depends uniquely on the $\mathbf{F}_e$ in (2.102), it is not possible to compute the two components separately by virtually unloading the structure at each step, because local neighbourhoods would not be necessarily geometrically compatible with each other, once the load is removed [236]. The Cauchy-Green right ($\mathbf{C}$) and left ($\mathbf{b}$) strain tensors are the preferred measures of representing deformations in the constitutive equations, given their symmetry, and hence their independence from rigid body rotations. In turn, $\mathbf{C}$ and $\mathbf{b}$ can also be split into an elastic and a plastic contribution, derived from the respective components of $\mathbf{F}$:

$$\begin{aligned} \mathbf{C}_e &= \mathbf{F}_e^T \mathbf{F}_e \,; & \mathbf{C}_p &= \mathbf{F}_p^T \mathbf{F}_p \,; \\ \mathbf{b}_e &= \mathbf{F}_e \mathbf{F}_e^T \,; & \mathbf{b}_p &= \mathbf{F}_p \mathbf{F}_p^T \,. \end{aligned} \tag{2.103}$$

Among the strain measures in (2.103), $\mathbf{b}_e$ and $\mathbf{C}_p$ satisfy the condition of being invariant not only with respect to global rotations, but also to local ones that were applied after elastic unloading of the local state [39]. Thus, the elastic potential energy, from which we will later derive the stress state, shall be expressed as $\Psi = \Psi(\mathbf{X}, \mathbf{b}_e)$, while $\mathbf{C}_p$ will be treated as the main indicator to detect and follow plastic deformation. $\mathbf{C}_p$ and $\mathbf{b}_e$ can be seen

as being a function of each other, as can be verified by operating on (2.102) and (2.103) in the following manner:

$$\mathbf{b}_e = \mathbf{F}_e\mathbf{F}_e^T = \mathbf{F}\mathbf{F}_p^{-1}\mathbf{F}_p^{-T}\mathbf{F}^T = \mathbf{F}\mathbf{C}_p^{-1}\mathbf{F}^T \tag{2.104}$$

Given the non-conservative nature of plastic strain $\mathbf{C}_p$, $\mathbf{b}_e$ can be exactly evaluated with (2.104) only if all previous states of deformation are known. This is obtained by integrating the rate of plastic deformation $\mathbf{l}_p$, which is the part of the velocity gradient tensor $\mathbf{l} = \nabla_0 v\,(\mathbf{F}(t),\, \mathbf{C}_p(t))$ that is associated with plastic effects [39]:

$$\mathbf{l}_p = -\frac{1}{2}\left.\frac{d\mathbf{b}_e}{dt}\right|_{\mathbf{F}=\text{const}} \mathbf{b}_e^{-1} \tag{2.105}$$

In order to derive the inelastic constitutive relation, the tensor $\mathbf{l}_p$ has to be associated with the current stress distribution over the body. Assigning a relation of the type $\mathbf{b}_e = \mathbf{b}_e(\boldsymbol{\sigma})$ establishes a *flow rule* for the material. To this end, it is useful to define the *yield criterion* as a function of $\boldsymbol{\sigma}$ that monitors when the yield limit of stress is reached, and when plastic strain occurs. Among the many yield criteria developed in the past [165], we will hereby resort to the one formulated by von Mises [175] as

$$f\left(\sigma', \bar{\epsilon}_p\right) = J\left(\boldsymbol{\sigma}_{eq} - \bar{\sigma}_y\left(\bar{\epsilon}_p\right)\right) \tag{2.106}$$

The yield condition prescribes that if

$$f\left(\sigma', \bar{\epsilon}_p\right) = 0 \tag{2.107}$$

then it follows that the structure is at the point of yield, and plastic strain $\bar{\epsilon}_p$ is needed to hold (2.107) true. This is because, as a fundamental hypothesis for the theory of plastic deformation, $f(\sigma', \bar{\epsilon}_p)$ in (2.107) has to be non-positive [175].

In (2.106), the (local) state of internal stress being tested for yield is scalarly represented as an *equivalent deviatoric stress* σ_{eq},

$$\sigma_{eq} = \sqrt{\frac{3}{2}\left(\boldsymbol{\sigma} : \boldsymbol{\sigma}\right)} \tag{2.108}$$

The *yield stress* $\bar{\sigma}_y$ in (2.106) is in general a function of the *equivalent plastic strain* $\bar{\varepsilon}_p$, and assumes the form

$$\bar{\sigma}_y = \bar{\sigma}_y^0 + h(\bar{\varepsilon}_p) \tag{2.109}$$

In (2.109), $\bar{\sigma}_y^0$ is the initial yield stress, and $h(\bar{\varepsilon}_p)$ is an *hardening* function that governs the additional quantity of stress that is required to further increase the plastic strain, once the yield point is reached.

The yield criterion (2.107) can then be expanded, using (2.106) and (2.108), as

$$f(\sigma', \bar{\varepsilon}_p) = \sqrt{\frac{3}{2}(\boldsymbol{\sigma} : \boldsymbol{\sigma})} - \bar{\sigma}_y^0 + h(\bar{\varepsilon}_p) = 0 \tag{2.110}$$

It can be noted from (2.110), that $f(\sigma', \bar{\varepsilon}_p)$, other than being independent of the pressure component of stress, is also a symmetric function, reflecting independence from the selected coordinates system.

Given that, in principal stresses $\{\sigma_1, \sigma_2, \sigma_3\}$, the von Mises equivalent stress σ_{eq} becomes

$$\sigma_{eq} = \sqrt{\frac{(\sigma_1 - \sigma_2)^2 + (\sigma_2 - \sigma_3)^2 + (\sigma_3 - \sigma_1)^2}{2}} \tag{2.111}$$

then, in light of (2.111), equation (2.110) clearly represents a cylinder in the $\{\sigma_1, \sigma_2, \sigma_3\}$ space. If a section is taken at $\sigma_3 = 0$, the *yield surface* would assume a shape similar to that illustrated in fig. 2.4.

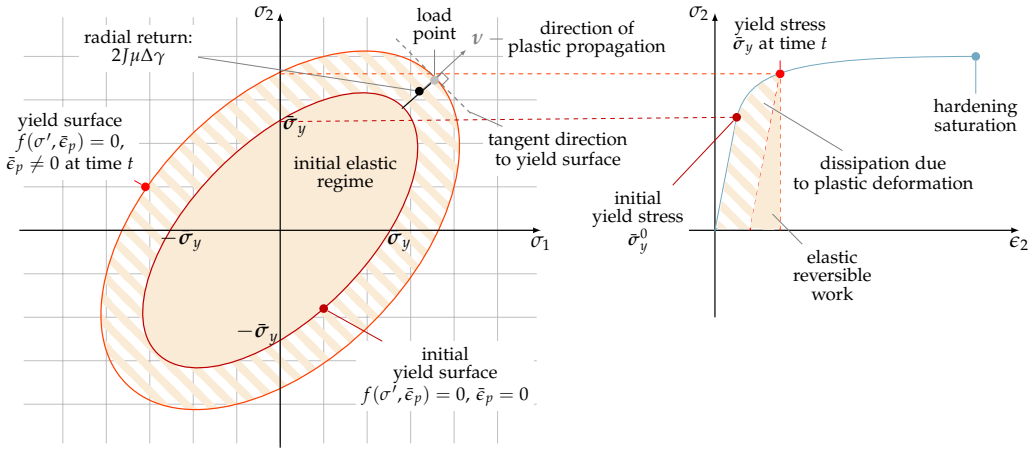

Figure 2.4: von Mises-defined yield surface in plain stress ($\sigma_3 = 0$) and in presence of isotropic hardening; radial return mapping procedure also shown.

Working in principal directions has also the advantage of facilitating the integration of the flow rule (2.105). Current *elastic* principal directions $\mathbf{n}_i$ are shared by the left Cauchy-Green strain tensor $\mathbf{b}_e$ and the Cauchy stress tensor $\boldsymbol{\sigma}$:

$$\mathbf{b}_e = \sum_{i=1}^{3} \lambda_{e,i}^2 \, \mathbf{n}_i \otimes \mathbf{n}_i \tag{2.112}$$

$$\boldsymbol{\sigma} = \sum_{i=1}^{3} \sigma_i \, \mathbf{n}_i \otimes \mathbf{n}_i \tag{2.113}$$

Principal stresses σ_i in (2.113) are derived from the adopted hyperelastic potential function Ψ:

$$\sigma_i = \frac{1}{J} \frac{\partial \Psi}{\partial \ln \lambda_{e,i}} = \frac{\lambda_{e,i}}{J} \frac{\partial \Psi}{\partial \lambda_{e,i}} \qquad i = 1, 2, 3 \tag{2.114}$$

Specifically, for the three types of hyperelastic material models considered in the previous section (Mooney-Rivlin, neo-Hookean, Ogden), (2.114) yields:

$$\begin{cases} \sigma_{MR,i} = \frac{1}{J} \left(\mu_1 \, \lambda_{e,i}^2 + \mu_2 \, \lambda_{e,i}^{-2} \right) = \mu_1 \, J^{-1/3} \, \hat{\lambda}_{e,i}^2 + \mu_2 \, J^{-5/3} \, \hat{\lambda}_{e,i}^{-2} \\ \sigma_{nH,i} = \frac{\mu \, \lambda_{e,i}^2}{J} = \mu \, J^{-1/3} \, \hat{\lambda}_{e,i}^2 \\ \sigma_{O,i} = \frac{1}{J} \left(\mu_1 \lambda_{e,i}^{\alpha_1} + \mu_2 \lambda_{e,i}^{\alpha_2} + \mu_3 \lambda_{e,i}^{\alpha_3} \right) = \\ \quad = \mu_1 \, J^{\alpha_1/3 - 1} \hat{\lambda}_{e,i}^{\alpha_1} + \mu_2 \, J^{\alpha_2/3 - 1} \, \hat{\lambda}_{e,i}^{\alpha_2} + \mu_3 \, J^{\alpha_3/3 - 1} \, \hat{\lambda}_{e,i}^{\alpha_3} \qquad i = 1, 2, 3 \end{cases} \tag{2.115}$$

where, as before, $\hat{\lambda}_{e,i}$ are the deviatoric principal stretches, related to $\lambda_{e,i}$ by (2.78).

A general formulation for a nearly incompressible hyperelastic material in principal directions $\Psi_M = \Psi_M^{vol} + \hat{\Psi}_M$, useful to simulate the behaviour of metals undergoing plasticity, can be found in [39]:

$$\begin{cases} \Psi_M^{vol}(J) = \frac{1}{2}\kappa (\ln J)^2 \\ \hat{\Psi}_M(\hat{\lambda}_{e,1}, \hat{\lambda}_{e,2}, \hat{\lambda}_{e,3}) = \mu \left[(\ln \hat{\lambda}_{e,1})^2 + (\ln \hat{\lambda}_{e,2})^2 + (\ln \hat{\lambda}_{e,3})^2 \right] = \\ \qquad\qquad = \mu \left[(\ln \lambda_{e,1})^2 + (\ln \lambda_{e,2})^2 + (\ln \lambda_{e,3})^2 \right] - \frac{1}{3}\mu (\ln J)^2 \end{cases} \tag{2.116}$$

The principal components of the deviatoric Cauchy stress tensors for the three hyper elastic formulations considered, are easily obtained by subtracting the hydrostatic pressure component, in (2.70), from (2.115):

$$\begin{cases} \sigma'_{MR,i} = \sigma_{MR,i} - p = \mu_1 J^{-1/3} \hat{\lambda}_{e,i}^2 + \mu_2 J^{-5/3} \hat{\lambda}_{e,i}^{-2} - \kappa (J-1) \\ \sigma'_{nH,i} = \mu J^{-1/3} \hat{\lambda}_{e,i}^2 - \kappa (J-1) \qquad\qquad i = 1,2,3 \\ \sigma'_{O,i} = \mu_1 J^{\alpha_1/3 - 1} \hat{\lambda}_{e,i}^{\alpha_1} + \mu_2 J^{\alpha_2/3 - 1} \hat{\lambda}_{e,i}^{\alpha_2} + \mu_3 J^{\alpha_3/3 - 1} \hat{\lambda}_{e,i}^{\alpha_3} - \kappa (J-1) \end{cases} \tag{2.117}$$

For the material in (2.116), the deviatoric Cauchy stress tensor can be expressed in its principal components as

$$\sigma'_{M,i} = 2\frac{\mu}{J} \ln \lambda_{e,i} - \frac{2}{3}\mu \frac{\ln J}{J} \qquad i = 1,2,3 \tag{2.118}$$

In deriving (2.118), it is worth recalling that the bulk modulus κ can be written in terms of Lamé constants as

$$\kappa = \lambda + \frac{2}{3}\mu \tag{2.119}$$

Integration of (2.104) expressed in principal directions with (2.112), can then provide with the flow rule (see [39]):

$$\mathbf{l}_p = \frac{\dot{\bar{\varepsilon}}_p}{J} \sum_{i=1}^{3} \frac{\partial f(\sigma_{ii}, \bar{\varepsilon}_p)}{\partial \sigma_{ii}} \mathbf{n}_i \otimes \mathbf{n}_i \tag{2.120}$$

where $\dot{\bar{\varepsilon}}_p$ is the *plastic multiplier*, which can be interpreted as a Lagrange multiplier in a maximisation problem involving the plastic dissipation rate in the functional, $J\boldsymbol{\sigma} : \mathbf{l}_p$ (see [236]). It is this very *postulate of maximum plastic*

dissipation that determines the proportionality of $\mathbf{l}_p$ to the gradient of the yield surface $f(\sigma_{ii}, \bar{\epsilon}_p)$ in (2.120).

In other words, when represented in the principal stresses spaces, the increment of plastic strain will always lie in the direction $\boldsymbol{\nu}$ normal to the tangent of the yield surface f at the load point.

Then, using this notion of plastic deformation normality in conjunction with (2.110), we obtain $\boldsymbol{\nu}$ as the derivative of the yield function in (2.120):

$$\nu_i = \frac{\partial f(\sigma_{ii}, \bar{\epsilon}_p)}{\partial \sigma_{ii}} = \frac{\sigma'_{ii}}{J\sqrt{\frac{2}{3}\,\boldsymbol{\sigma}' : \boldsymbol{\sigma}'}} \qquad i = 1, 2, 3 \tag{2.121}$$

Resorting to (2.121) we obtain the principal components of the rate of plastic deformation $\mathbf{l}_p$ as

$$l_{p,i} = \frac{\dot{\bar{\epsilon}}_p}{J}\,\nu_i \qquad i = 1, 2, 3 \tag{2.122}$$

The theory described so far will form the basis of the numerical procedure employed in the next chapter to extract the plastic strain $\bar{\epsilon}_p$, and update the material stress $\mathbf{P}$.

The overall procedure discussed in this section is presented schematically in algorithm 2, where for ease of notation the deviatoric *Kirchhoff stress tensor* $\boldsymbol{\tau}'$ is used in the computations.

2.11 CONJUGATE STRESSES AND THE HESSIAN OPERATOR

We have seen in section 2.8 that the polyconvexity condition in (2.52) requires the elastic potential function to be dependent of three strain measures, $\Psi = \Psi(\mathbf{F}, \mathbf{H}, J)$. *Work conjugate* stresses $\boldsymbol{\Sigma}_F$, $\boldsymbol{\Sigma}_H$ and Σ_J can be associated to strains $\mathbf{F}$, $\mathbf{H}$ and J, so that their generalised products return energy quantities. Taking the total differential of $\Psi(\mathbf{F}, \mathbf{H}, J)$ yields

$$D\Psi(\mathbf{F}, \mathbf{H}, J) = \frac{\partial \Psi}{\partial \mathbf{F}} : d\mathbf{F} + \frac{\partial \Psi}{\partial \mathbf{H}} : d\mathbf{H} + \frac{\partial \Psi}{\partial J}\,dJ \tag{2.123}$$

From (2.123), we can define the work conjugate stresses as [32]

$$\boldsymbol{\Sigma}_{\mathbf{F}} = \frac{\partial \Psi}{\partial \mathbf{F}}; \qquad \boldsymbol{\Sigma}_{\mathbf{H}} = \frac{\partial \Psi}{\partial \mathbf{H}}; \qquad \Sigma_{\mathrm{J}} = \frac{\partial \Psi}{\partial \mathrm{J}} \tag{2.124}$$

The main task now is to derive from the polyconvex energy $\Psi(\mathbf{F}, \mathbf{H}, \mathrm{J})$ a practical expression for the first Piola-Kirchhoff stress tensor $\mathbf{P} = \mathbf{P}(\mathbf{F}, \mathbf{H}, \mathrm{J})$ in polyconvex variables. To this end, we may want to consider the expression for $\mathrm{D}\Psi(\mathbf{F})$, and compare it with (2.123) in order to formulate a polyconvex description for $\mathrm{D}\Psi$:

$$\mathrm{D}\Psi(\mathbf{F}) = \mathbf{P} : \mathbf{F} \tag{2.125}$$

with $\mathbf{P}$ in (2.125) given by (2.57). Then, by comparison of (2.123) with (2.125), and with the help of the properties of the tensor cross product (see, for instance, appendix in [31]) we may find

$$\mathrm{D}\Psi(\mathbf{F}) = \mathbf{P} : \mathbf{F} = \mathrm{D}\Psi(\mathbf{F}, \mathbf{H}, \mathrm{J}) = \boldsymbol{\Sigma}_{\mathbf{F}} : \mathrm{d}\mathbf{F} + \boldsymbol{\Sigma}_{\mathbf{H}} : \mathrm{d}\mathbf{H} + \Sigma_{\mathrm{J}}\, \mathrm{dJ} \tag{2.126}$$

using the definitions in (2.124). With respect to an arbitrary small displacement $\delta\mathbf{u}$, the linearised deformation gradient $\mathrm{D}\mathbf{F}[\delta\mathbf{u}]$ is known [39] to be

$$\mathrm{D}\mathbf{F}[\delta\mathbf{u}] = \frac{\partial \delta\mathbf{u}(\mathbf{X})}{\partial \mathbf{X}} = \nabla_0 \delta\mathbf{u} \tag{2.127}$$

Using the last property listed in table 2.2 to express $\mathbf{H}$ as a function of $\mathbf{F}$, using the above (2.127), and the product rule of derivation, we can define $\mathrm{D}\mathbf{H}$ as

$$\mathrm{D}\mathbf{H}[\delta\mathbf{u}] = \mathrm{D}\left(\frac{1}{2}\mathbf{F} \times \mathbf{F}\right)[\delta\mathbf{u}] = \frac{1}{2}\mathbf{F} \times \mathrm{D}\mathbf{F} + \frac{1}{2}\mathrm{D}\mathbf{F} \times \mathbf{F} = \mathbf{F} \times \nabla_0 \delta\mathbf{u} \tag{2.128}$$

Similarly to (2.128), and, in addition, expressing J as a function of $\mathbf{F}$ and $\mathbf{H}$ (thanks to the 12^{th} property in table 2.2), we are also able to expand $\mathrm{D}\mathrm{J}$ as

$$\mathrm{D}\mathrm{J}[\delta\mathbf{u}] = \mathrm{D}\left(\frac{1}{3}\mathbf{H} : \mathbf{F}\right)[\delta\mathbf{u}] = \frac{1}{3}\mathrm{D}\mathbf{H}[\delta\mathbf{u}] : \mathbf{F} + \frac{1}{3}\mathbf{H} : \mathrm{D}\mathbf{F}[\delta\mathbf{u}] = \mathbf{H} : \nabla_0 \delta\mathbf{u} \tag{2.129}$$

In light of eqs. (2.127) to (2.129), we can further develop the RHS in (2.126):

$$\begin{aligned} D\Psi(\mathbf{F}, \mathbf{H}, J) &= \Sigma_{\mathbf{F}} : \nabla_0 \delta\mathbf{u} + (\Sigma_{\mathbf{H}} \times \mathbf{F}) : \nabla_0 \delta\mathbf{u} + \Sigma_J \mathbf{H} : \nabla_0 \delta\mathbf{u} = \\ &= (\Sigma_{\mathbf{F}} + \Sigma_{\mathbf{H}} \times \mathbf{F} + \Sigma_J \mathbf{H}) : \nabla_0 \delta\mathbf{u} \end{aligned} \tag{2.130}$$

Thus, from (2.130) it can be assumed that in the case a polyconvex elastic potential function, an equivalent $\mathbf{P}(\mathbf{F}, \mathbf{H}, J)$ to the first Piola-Kirchhoff stress tensor can be established by comparison with (2.125) as

$$\mathbf{P}(\mathbf{F}, \mathbf{H}, J) = \Sigma_{\mathbf{F}} + \Sigma_{\mathbf{H}} \times \mathbf{F} + \Sigma_J \mathbf{H} \tag{2.131}$$

Equation (2.131) can be readily applied to the three hyperelastic constitutive models discussed earlier:

- MOONEY-RIVLIN:

$$\begin{aligned} \Sigma_{\mathbf{F}}^{(MR)} &= \mu_1 J^{-2/3} \mathbf{F}; \qquad \Sigma_{\mathbf{H}}^{(MR)} = -\mu_2 J^{-4/3} \mathbf{H}; \\ \Sigma_J^{(MR)} &= -\frac{\mu_1}{3} J^{-5/3} (\mathbf{F} : \mathbf{F}) + \frac{2}{3} \mu_2 J^{-7/3} (\mathbf{H} : \mathbf{H}) + \kappa (J - 1) \\ \mathbf{P}^{(MR)} &= \mu_1 J^{-2/3} \mathbf{F} - \mu_2 J^{-4/3} \mathbf{H} \times \mathbf{F} - \frac{\mu_1}{3} J^{-5/3} (\mathbf{F} : \mathbf{F}) + \\ &\quad + \frac{2}{3} \mu_2 J^{-7/3} (\mathbf{H} : \mathbf{H}) + \kappa (J - 1) \mathbf{H} \end{aligned} \tag{2.132}$$

- NEO-HOOKEAN:

$$\begin{aligned} \Sigma_{\mathbf{F}}^{(nH)} &= \mu J^{-2/3} \mathbf{F}; \qquad \Sigma_{\mathbf{H}}^{(nH)} = \mathbf{0}; \\ \Sigma_J^{(nH)} &= -\frac{\mu}{3} J^{-5/3} (\mathbf{F} : \mathbf{F}) + \kappa (J - 1) \\ \mathbf{P}^{(nH)} &= \mu J^{-2/3} \mathbf{F} + \left[\kappa (J - 1) - \frac{\mu}{3} J^{-5/3} (\mathbf{F} : \mathbf{F}) \right] \mathbf{H} \end{aligned} \tag{2.133}$$

The strain energy of an Ogden material, recalling (2.74), depends on the principal stretches λ_i, and not on the invariants of $\mathbf{C}$.

1. Plastic state from previous time step (n): $\left(\mathbf{C}_p^n\right)^{-1}$, $\bar{\varepsilon}_p^n$
   Known from solver at current time step $(n+1)$: $\mathbf{F}^{n+1}$, J^{n+1}

2. Compute pressure: $p^{n+1} = \kappa \frac{\ln J^{n+1}}{J^{n+1}}$

3. Guess trial elastic left Cauchy-Green strain tensor:
   $\mathbf{b}_e^{(\text{trial})} = \mathbf{F}^{n+1} \left(\mathbf{C}_p^n\right)^{-1} \left(\mathbf{F}^{n+1}\right)^T$

4. Obtain $\lambda_{e|i}^{(\text{trial})}$, $\mathbf{n}_i^{(\text{trial})}$ from spectral decomposition of $\mathbf{b}_e^{(\text{trial})}$:
   $\mathbf{b}_e^{(\text{trial})} = \sum_{i=1}^{3} \left(\lambda_{e|i}^{(\text{trial})}\right)^2 \mathbf{n}_i^{(\text{trial})} \otimes \mathbf{n}_i^{(\text{trial})}$

5. Principal components of the trial deviatoric Kirchhoff stress tensor: $\tau_{ii}'^{(\text{trial})} = 2\mu \left(\ln \lambda_{e|i}^{(\text{trial})} - \frac{\ln J^{n+1}}{3}\right) \quad i = 1,2,3;$
   $\|\boldsymbol{\tau}'^{(\text{trial})}\| = \sqrt{\sum_{i=1}^{d} \left(\tau_{ii}'^{(\text{trial})}\right)^2} \quad d = 2,3$

6. Define yield surface function $f = f(\boldsymbol{\tau}'^{(\text{trial})}, \bar{\varepsilon}_p^n)$ and verify presence of yielding:
   IF $f(\boldsymbol{\tau}'^{(\text{trial})}, \bar{\varepsilon}_p^n) > 0$ THEN
   $\Delta\gamma = \frac{f(\boldsymbol{\tau}'^{(\text{trial})}, \bar{\varepsilon}_p^n)}{3\mu + H}; \qquad \boldsymbol{\nu}_i^{n+1} = \frac{\tau_{ii}'^{(\text{trial})}}{\sqrt{\frac{2}{3}}\|\boldsymbol{\tau}'^{(\text{trial})}\|}$
   ELSE: $\Delta\gamma = 0; \qquad \boldsymbol{\nu}_i^{n+1} = \boldsymbol{\nu}_i^n \qquad i = 1,2,3$

7. Update components of deviatoric Kirchhoff stress tensor:
   $\tau_{ii}'^{n+1} = \tau_{ii}'^{(\text{trial})} - 2\mu\,\Delta\gamma\,\boldsymbol{\nu}_i^{n+1} \qquad i = 1,2,3$

8. Update elastic stretches and directions $i = 1,2,3$:
   $\lambda_{e|i}^{n+1} = \exp\left(\ln \lambda_{e|i}^{(\text{trial})} - \Delta\gamma \boldsymbol{\nu}_i^{n+1}\right) \qquad \mathbf{n}_i^{n+1} = \mathbf{n}_i^{(\text{trial})}$

9. Update elastic left Cauchy-Green strain tensor:
   $\mathbf{b}_e^{n+1} = \sum_{i=1}^{3} \left(\lambda_{e|i}^{n+1}\right)^2 \mathbf{n}_i^{n+1} \otimes \mathbf{n}_i^{n+1}$

10. Update plastic deformation data:
    $\bar{\varepsilon}_p^{n+1} = \bar{\varepsilon}_p^n + \Delta\gamma \qquad \left(\mathbf{C}_p^{n+1}\right)^{-1} = \left(\mathbf{F}^{n+1}\right)^{-1} \mathbf{b}_e^{n+1} \left(\mathbf{F}^{n+1}\right)^{-T}$

11. Obtain Cauchy and first Piola-Kirchhoff stress tensors:
    $\sigma_{ii}^{n+1} = \frac{\tau_{ii}'^{n+1}}{J^{n+1}} + p^{n+1} \quad \Rightarrow \quad \boldsymbol{\sigma}^{n+1} = \sum_{i=1}^{3} \sigma_{ii}^{n+1} \mathbf{n}_i^{n+1} \otimes \mathbf{n}_i^{n+1}$
    $\mathbf{P}^{n+1} = J^{n+1} \boldsymbol{\sigma}^{n+1} \left(\mathbf{F}^{n+1}\right)^{-T}$

ALGORITHM 2 : extension of the material model to plastic deformation

Therefore, while determining $\mathbf{P}^{(O)}$ from (2.131) for the Ogden model, it should be noted that tensors $\mathbf{F}$ and $\mathbf{H}$ can be written in terms of their eigenvalues and eigenvectors, where, in particular, $(\lambda_1, \lambda_2, \lambda_3)$ are the eigenvalues of $\mathbf{F}$ and $(\lambda_1\lambda_2, \lambda_1\lambda_3, \lambda_2\lambda_3)$ are the eigenvalues of $\mathbf{H}$ ‡:

$$\mathbf{F} = \sum_{i=1}^{3} \lambda_i \mathbf{n}_i \otimes \mathbf{N}_i \tag{2.134a}$$

$$\mathbf{H} = \sum_{k=1}^{3} \lambda_i \lambda_j \mathbf{n}_k \otimes \mathbf{N}_k \qquad i, j, k = 1, 2, 3\,, \qquad i \neq j \neq k \tag{2.134b}$$

The polyconvex version of the hyperelastic strain function can then be written in terms of the principal stretches as

$$\Psi(\mathbf{F}, \mathbf{H}, J) = \Psi(\lambda_1, \lambda_2, \lambda_3; \lambda_1\lambda_2, \lambda_1\lambda_3, \lambda_2\lambda_3; J) \tag{2.135}$$

In addition, for the purposes of deriving the Ogden model stress tensor $\mathbf{P}^{(O)}$, it will be worth to recall the following result, valid for a tensor $\mathbf{A}$ with material $\mathbf{N}_i$ and spatial $\mathbf{n}_i$ principal directions, $i = 1, 2, 3$:

$$\frac{d\lambda_i|_{\mathbf{A}}}{d\mathbf{A}} = \mathbf{n}_i \otimes \mathbf{N}_i \quad i = 1, 2, 3 \tag{2.136}$$

‡ In fact, this can be seen by expanding $\mathbf{H}(\mathbf{F})$:

$$\mathbf{H} = \frac{1}{2}\mathbf{F} \times \mathbf{F} = \frac{1}{2}\left(\sum_{i=1}^{3} \lambda_i \mathbf{n}_i \otimes \mathbf{N}_i\right) \times \left(\sum_{j=1}^{3} \lambda_j \mathbf{n}_j \otimes \mathbf{N}_j\right) =$$

$$= \frac{1}{2}\sum_{i,j=1}^{3} \lambda_i \lambda_j (\mathbf{n}_i \times \mathbf{n}_j) \otimes (\mathbf{N}_i \times \mathbf{N}_j) = \sum_{k=1}^{3} \lambda_i \lambda_j \mathbf{n}_k \otimes \mathbf{N}_k$$

with $i \neq j \neq k$. This computation benefited from the property of the tensor product between vectors [33], below:

$$(\mathbf{a} \otimes \mathbf{b}) \times (\mathbf{u} \otimes \mathbf{v}) = (\mathbf{a} \times \mathbf{u}) \otimes (\mathbf{b} \times \mathbf{v})$$

In the case of $\mathbf{F}$, eq. (2.136) results from considering the trace of the right Cauchy-Green deformation tensor $\mathbf{C}$ expressed in terms of principal stretches:

$$\operatorname{tr}\mathbf{C} = \underbrace{\mathbf{F} : \mathbf{F}}_{ⓐ} = \underbrace{\sum_{i=1}^{3} \lambda_i^2}_{ⓑ} \tag{2.137}$$

The outcome in (2.136) is obtained by linearising separately terms ⓐ and ⓑ in (2.137) and subsequently by comparing the results:

$$\begin{aligned} \mathrm{D}\left(\mathbf{F} : \mathbf{F}\right)[\delta\mathbf{u}] &= 2\mathbf{F} : \mathrm{D}\mathbf{F}[\delta\mathbf{u}] = 2\mathbf{F} : \nabla_0\delta\mathbf{u} = \\ &= 2\left(\sum_{i=1}^{3} \lambda_i \mathbf{n}_i \otimes \mathbf{N}_i\right) : \nabla_0\delta\mathbf{u} \end{aligned} \tag{2.138a}$$

$$\mathrm{D}\left(\sum_{i=1}^{3} \lambda_i^2\right)[\delta\mathbf{u}] = 2\sum_{i=1}^{3} \lambda_i \mathrm{D}\lambda_i[\delta\mathbf{u}] = 2\left(\sum_{i=1}^{3} \lambda_i \frac{\partial\lambda_i}{\partial\mathbf{F}}\right) : \nabla_0\delta\mathbf{u} \tag{2.138b}$$

Comparing the RHS of (2.138a) and (2.138b) verifies (2.136). Moreover, the same procedure employed in (2.137) and (2.138) can be applied to $\mathbf{H} : \mathbf{H}$, so to prove that (2.136) is also valid for $\mathbf{H}$.

At this point, we may proceed with the linearisation $\mathrm{D}\Psi^{(O)}\left(\lambda_{\mathbf{F}}, \lambda_{\mathbf{H}}, J\right)$ in order to extract the stress tensor $\mathbf{P}^{(O)}$ for this particular energy functional, as already seen for other forms in (2.125) and (2.130):

$$\begin{aligned} &\mathrm{D}\Psi^{(O)}\left(\lambda_{\mathbf{F}}, \lambda_{\mathbf{H}}, J\right)[\delta\mathbf{u}] = \\ &\quad = \sum_{i=1}^{3} \frac{\partial\Psi^{(O)}}{\partial\lambda_{\mathbf{F}i}} \mathrm{D}\lambda_{\mathbf{F}i}[\delta\mathbf{u}] + \sum_{i=1}^{3} \frac{\partial\Psi^{(O)}}{\partial\lambda_{\mathbf{H}i}} \mathrm{D}\lambda_{\mathbf{H}i}[\delta\mathbf{u}] + \frac{\partial\Psi^{(O)}}{\partial J} \mathrm{D}J[\delta\mathbf{u}] \end{aligned} \tag{2.139}$$

In (2.139), $\mathrm{D}\lambda_{\mathbf{F}i}[\delta\mathbf{u}]$ and $\mathrm{D}\lambda_{\mathbf{H}i}[\delta\mathbf{u}]$ can be expressed as

$$\mathrm{D}\lambda_{\mathbf{F}i}[\delta\mathbf{u}] = \frac{\partial\lambda_{\mathbf{F}i}}{\partial\mathbf{F}} : \mathrm{D}\mathbf{F}[\delta\mathbf{u}] = (\mathbf{n}_i \otimes \mathbf{N}_i) : \nabla_0\delta\mathbf{u} \tag{2.140a}$$

$$\mathrm{D}\lambda_{\mathbf{H}i}[\delta\mathbf{u}] = \frac{\partial\lambda_{\mathbf{H}i}}{\partial\mathbf{H}} : \mathrm{D}\mathbf{H}[\delta\mathbf{u}] = [(\mathbf{n}_i \otimes \mathbf{N}_i) \times \mathbf{F}] : \nabla_0\delta\mathbf{u} \tag{2.140b}$$

$\mathrm{D}J[\delta\mathbf{u}]$ in (2.139) is found in (2.129).

Hence, considering (2.131), the stress conjugates in the case of the polyconvex Ogden material strain energy can be defined as

$$\mathbf{\Sigma}_{\mathbf{F}}^{(O)} = \sum_{i=1}^{3} \frac{\partial \Psi_O}{\partial \lambda_{Fi}} (\mathbf{n}_i \otimes \mathbf{N}_i) \tag{2.141a}$$

$$\mathbf{\Sigma}_{\mathbf{H}}^{(O)} = \sum_{i=1}^{3} \frac{\partial \Psi_O}{\partial \lambda_{Hi}} (\mathbf{n}_i \otimes \mathbf{N}_i) \tag{2.141b}$$

$$\Sigma_J^{(O)} = \frac{\partial \Psi_O}{\partial J} \tag{2.141c}$$

The Ogden strain energy (2.74) $\Psi^{(O)}(\lambda_{Fi}, J)$ that was considered in section 2.9 lacks any dependence from λ_{Hi}. This further simplifies things, and thanks to (2.135) and to (2.136), we are now in possess of all elements needed to derive the conjugate stresses (2.141) for an Ogden material:

- OGDEN:

$$\begin{aligned}
\mathbf{\Sigma}_{\mathbf{F}}^{(O)} &= \frac{\partial \Psi_O(\mathbf{F}, \mathbf{H}, J)}{\partial \mathbf{F}} = \sum_{i=1}^{3} \frac{\partial \Psi_O}{\partial \lambda_{F|i}} \frac{\partial \lambda_{F|i}}{\partial \mathbf{F}} = \\
&= J^{-\frac{2}{3}} \left[\left(\mu_1 \lambda_1^{\alpha_1 - 1} + \mu_2 \lambda_1^{\alpha_2 - 1} + \mu_3 \lambda_1^{\alpha_3 - 1} \right) (\mathbf{n}_1 \otimes \mathbf{N}_1) + \right. \\
&+ \left(\mu_1 \lambda_2^{\alpha_1 - 1} + \mu_2 \lambda_2^{\alpha_2 - 1} + \mu_3 \lambda_2^{\alpha_3 - 1} \right) (\mathbf{n}_2 \otimes \mathbf{N}_2) + \\
&+ \left. \left(\mu_1 \lambda_3^{\alpha_1 - 1} + \mu_2 \lambda_3^{\alpha_2 - 1} + \mu_3 \lambda_3^{\alpha_3 - 1} \right) (\mathbf{n}_3 \otimes \mathbf{N}_3) \right] \\
\mathbf{\Sigma}_{\mathbf{H}}^{(O)} &= \frac{\partial \Psi_O(\mathbf{F}, \mathbf{H}, J)}{\partial \mathbf{H}} = 0 \\
\Sigma_J^{(O)} &= \frac{\partial \Psi_O}{\partial J} = \\
&= -\sum_{p=1}^{3} \frac{\mu_p}{3} \left(\lambda_1^{\alpha_p} + \lambda_2^{\alpha_p} + \lambda_3^{\alpha_p} \right) J^{-\left(\frac{\alpha_p}{3} + 1\right)} + \frac{\kappa}{\beta J} \left(1 - \frac{1}{J^\beta} \right) \\
\mathbf{P}^{(O)} &= \mathbf{\Sigma}_{\mathbf{F}}^{(O)} + \mathbf{\Sigma}_{\mathbf{H}}^{(O)} \times \mathbf{F} + \Sigma_J^{(O)} \mathbf{H}
\end{aligned} \tag{2.142}$$

It is known from RA (see [148], or [3]) and, in more detail, from the topic of convex optimisation (see [43]), that a multivariate, differentiable convex

function $f(x_i)$, $i = 1, \ldots, n$ possesses a positive semi-definite *Hessian* H_f, defined as the matrix of the second derivatives of f:

$$H_f = \begin{bmatrix} f_{x_1x_1} & f_{x_1x_2} & \cdots & f_{x_1x_n} \\ f_{x_2x_1} & \ddots & & f_{x_2x_n} \\ \vdots & & \ddots & \vdots \\ f_{x_nx_1} & \cdots & f_{x_nx_{n-1}} & f_{x_nx_n} \end{bmatrix} \tag{2.143}$$

In the context of nonlinear elastostatics, the Hessian operator in (2.143) applies to the elastic strain potential Ψ as H_ψ, and it is used to evaluate the tangent elasticity operator [31, 32].

Each one of the three hyperelastic models presented so far can all be made *strictly* polyconvex, if the coefficients that appear in the expressions for the strain potentials (2.68), (2.72) and (2.77) + (2.79) are chosen so that they satisfy the convexity condition (2.47) in a strict sense. In this case, being positive definite, the Hessian H_Ψ will have all real and positive eigenvalues λ_i [148], and its determinant, as a consequence, can never be equal to 0:

$$\det H_\Psi = \prod_i \lambda_i > 0 \qquad\qquad i = 1, \ldots, n \tag{2.144}$$

By virtue of equation (2.144), the Hessian H_Ψ is evidently a non-singular and thus invertible matrix. In turn, this allows the same properties to be enjoyed by the tangent elasticity operator [39]. A Newton-Raphson numerical procedure can then be safely employed to search for an equilibrium solution.

However, as stated in section 2.7, guarantee of global existence and uniqueness of solutions for polyconvex strain energy potentials cannot be extended from elastostatics to elastodynamics problems, given that a rigorous argument supporting that claim has yet to be advanced.

On the other hand, empirical evidence of stable and realistic solutions to nonlinear elastodynamic problems by use of polyconvex hyperelastic strain energies leads to speculate, that it is useful to extend the polyconvexity prerequisite to the dynamic regime. Further examples corroborating the point just made will be advanced in the remainder of this work.

2.12 GEOMETRIC CONSERVATION LAWS FOR POLYCONVEX VARIABLES

Additional conservation laws – other than the ones, involving kinetic quantities, presented in section 2.3 to section 2.6 – can be formulated for the geometric arguments of a polyconvex potential function as defined in (2.52), namely, the deformation gradient $\mathbf{F}$, its cofactors matrix $\mathbf{H}$ and its determinant, the Jacobian J.

Conservation properties for $\mathbf{F}$, $\mathbf{H}$ and J unveil no physical insight that can be intuitively understood, as was the case for the conservation of mass, or that of energy. They mainly exploit symmetry properties of the mathematical representation of solid continua [62, 191, 198–202].

2.12.1 *Conservation of deformation gradient* $\mathbf{F}$

A *local* expression for the conservation law of the deformation gradient tensor $\mathbf{F}$ can be derived directly from the definition of $\mathbf{F}$ (2.3), that, in terms of current position $\boldsymbol{x}$ reads:

$$\mathbf{F}(\mathbf{X}, t) = \frac{\partial \boldsymbol{x}(\mathbf{X}, t)}{\partial \mathbf{X}} \tag{2.145}$$

Given the total differential of $\boldsymbol{x}$

$$d\boldsymbol{x}(\mathbf{X}, t) = \frac{\partial \boldsymbol{x}}{\partial \mathbf{X}} d\mathbf{X} + \frac{\partial \boldsymbol{x}}{\partial t} dt \tag{2.146}$$

Considering $\boldsymbol{x}(\mathbf{X}, t)$ as smoothly differentiable both in space and time, (2.146) represents a closed and exact differential form: that is, respectively, $d\boldsymbol{x} = 0$ (closure), and there exists a primitive function $\mathbf{U}$ such that $\int_{x_a}^{x_b} d\boldsymbol{x} = \mathbf{U}_b - \mathbf{U}_a$ (exactness).

Under these conditions, second derivatives of $\boldsymbol{x}$ with respect to both $\mathbf{X}$ and t do not depend from the sequential order of variables with which the derivation is made.

We can then write:

$$\frac{\partial}{\partial t}\left(\frac{\partial \mathbf{x}}{\partial \mathbf{X}}\right) = \frac{\partial \mathbf{F}}{\partial t} = \\ = \frac{\partial}{\partial \mathbf{X}}\left(\frac{\partial \mathbf{x}}{\partial t}\right) = \frac{\partial \mathbf{v}}{\partial \mathbf{X}} = \frac{1}{\rho}\nabla_0 \mathbf{p} = \nabla_0 \cdot \left(\frac{1}{\rho}\mathbf{p} \otimes \mathbf{I}\right) \tag{2.147}$$

The local, differential formula for the conservation of $\mathbf{F}$ can be extrapolated from (2.147) as

$$\frac{\partial \mathbf{F}}{\partial t} - \nabla_0 \cdot \left(\frac{1}{\rho}\mathbf{p} \otimes \mathbf{I}\right) = \mathbf{0} \tag{2.148}$$

By using the divergence theorem, we can obtain the corresponding integral expression for (2.148), as

$$\frac{\partial}{\partial t}\int_V \mathbf{F}\, dV = \int_{\partial V} \frac{1}{\rho}\mathbf{p} \otimes \mathbf{N}\, dA \tag{2.149}$$

To ensure that the deformation gradient $\mathbf{F}$ obtained through (2.149) would yield a continuous and single-valued displacement field $(\mathbf{x}(t) - \mathbf{x}(t_0))$, with time instants $t \geqslant t_0$, the following compatibility condition should be imposed [138, 165, 255] on $\mathbf{F}$:

$$\nabla_0 \times \mathbf{F} = \mathbf{0} \tag{2.150}$$

It is easy to recognise in condition (2.150) a basic property of tensor calculus, namely, that the curl of the gradient of a vector (and $\mathbf{F}$ is the gradient of $\mathbf{x}$, $\mathbf{F} = \nabla_0 \mathbf{x}$) be null [108]. In addition, (2.150) is automatically verified in the displacement-based formulation, where the deformation gradient is computed from the position $\mathbf{x}$ by definition $\mathbf{F} = \nabla_0 \mathbf{x}$. Given that we employ the hyperbolic first order mixed framework, (2.150) has to be identified with an *involution* of the hyperbolic system; once reached the discretisation stage of the analysis, there is the need to enforce it at each time step to avoid spurious deformation modes [143].

A more in-depth survey of involutions will follow, towards the end of this chapter.

2.12.2 *Conservation of the cofactors matrix* $\mathbf{H}$ *of* $\mathbf{F}$

We defined in (2.6) the matrix of cofactors, $\mathbf{H} = \mathrm{cof}(\mathbf{F})$.

We start this section by noting that an alternative expression for $\mathbf{H}$ can be easily obtained by using the last property of the tensorial cross product amongst those listed in table 2.2:

$$\mathbf{H} = \frac{\mathbf{F} \times \mathbf{F}}{2} \tag{2.151}$$

In [33] it has been proven that from (2.151) descends

$$\mathbf{H} = \frac{\nabla_0 \times (\mathbf{x} \times \mathbf{F})}{2} \tag{2.152}$$

By expressing the matrix of cofactors $\mathbf{H}$ as in (2.152), we may observe that the antisymmetry of the curl operator, combined with the symmetry of second derivatives ($\mathbf{F}$ is already $\mathbf{F} = \nabla_0 \mathbf{x}$) [33] leads to

$$\nabla_0 \cdot \mathbf{H} = \mathbf{0} \tag{2.153}$$

Equation (2.153) constitutes a second involution condition that the mixed system of conservation laws has to satisfy.

Using the commutative property of the tensorial cross product (fourth row in table 2.2), the temporal derivative of (2.151) yields:

$$\frac{\partial \mathbf{H}}{\partial t} = \frac{1}{2\rho} \left(\nabla_0 \mathbf{p} \times \mathbf{F} + \mathbf{F} \times \nabla_0 \mathbf{p} \right) = \left(\mathbf{F} \times \frac{\nabla_0 \mathbf{p}}{\rho} \right) \tag{2.154}$$

In order to obtain the global form of the conservation law, integrating (2.154) over the initial volume V and applying the divergence theorem gives

$$\begin{aligned} \frac{\partial}{\partial t} \int_V \mathbf{H} \, dV = \int_V \mathbf{F} \times \frac{\nabla_0 \mathbf{p}}{\rho} \, dV = \\ = \int_{\partial V} \mathbf{F} \times \frac{\mathbf{p}}{\rho} \otimes \mathbf{N} \, dA - \cancel{\int_V \frac{\mathbf{p}}{\rho} \times (\nabla_0 \times \mathbf{F}) \, dV} = \\ \frac{\partial}{\partial t} \int_V \mathbf{H} \, dV = \int_{\partial V} \mathbf{F} \times \frac{\mathbf{p}}{\rho} \otimes d\mathbf{A} \end{aligned} \tag{2.155}$$

In (2.155), a term has been eliminated by virtue of (2.150), and integration by parts was used.

Condition (2.150) permits an alternative formulation of the local conservation law for $\mathbf{H}$ (2.154), as [33]

$$\frac{\partial \mathbf{H}}{\partial t} - \nabla_0 \times \left(\frac{\mathbf{p}}{\rho} \times \mathbf{F} \right) = \mathbf{0} \tag{2.156}$$

2.12.3 *Conservation of the Jacobian* J *of* $\mathbf{F}$

The observation that the Jacobian, as defined in (2.4), is a measure of the volumetric dilatation, consents to derive a conservation law for J. Its integral version may be formulated by considering the Reynold's transport theorem [173, 213], useful to assess the rate of change of a test volume v in the Eulerian framework:

$$\frac{\partial}{\partial t} \int_v \mathrm{d}v = \int_{\partial v} v \cdot \mathbf{n} \, \mathrm{d}a \tag{2.157}$$

where v is the velocity of matter inside v, as this evolves. With the help of interpretations, made in (2.8) and (2.5), of $\mathbf{H}$ and J in terms of area and volume change, (2.157) can be expressed in Lagrangian frame as the global form of a conservation law for J:

$$\frac{\partial}{\partial t} \int_V J \, \mathrm{d}V = \int_{\partial V} \frac{\mathbf{p}}{\rho} \cdot \mathbf{H}\mathbf{N} \, \mathrm{d}A \tag{2.158}$$

Alternatively, using the following identity involving vectors $\mathbf{a}$, $\mathbf{b}$ and tensor $\mathbf{S}$, found in [39]:

$$\mathbf{a} \cdot \mathbf{S}\mathbf{b} = \mathbf{S} : (\mathbf{a} \otimes \mathbf{b}) \tag{2.159}$$

we may express (2.158) as

$$\frac{\partial}{\partial t} \int_V J \, \mathrm{d}V = \int_{\partial V} \mathbf{H} : \left(\frac{\mathbf{p}}{\rho} \otimes \mathbf{N} \right) \mathrm{d}A \tag{2.160}$$

A local form analogous to the integral (2.158) can be derived with the help of the divergence theorem:

$$\frac{\partial J}{\partial t} - \nabla_0 \cdot \left(\mathbf{H}^T \frac{\mathbf{p}}{\rho} \right) = 0 \tag{2.161}$$

2.13 THE COMPLETE FIRST ORDER MIXED SYSTEM OF CONSERVATION LAWS

It is customary to solve dynamic problems in nonlinear solid mechanics for displacements $\mathbf{u}$, by creating a system of equations combining the linear momentum conservation law (2.23), with a kinematic equation connecting displacements and velocities $v = p/\rho$, of the type (2.1).

The first Piola-Kirchhoff stress $\mathbf{P}$ that appears in (2.23) has to be obtained by applying the material gradient operator to the spatial vector of positions $\mathbf{x}$, $\mathbf{P} = \mathbf{P}(\nabla_0 \mathbf{x}, \mathbf{X})$. The deformation gradient $\mathbf{F}$, therefore, is obtained directly from (2.3) as per its definition.

In a Lagrangian framework, the imposition of the conservation of mass (2.17) is not strictly necessary, as the density of the material, ρ, is always implied to be the initial one, and the effects of volumetric deformation are tracked by the updating of $J = \det \mathbf{F}$. Imposition of initial and BCs complete the problem.

Proceeding this way, involutions (2.150) and (2.153) are automatically satisfied, as the relation between positions ($\mathbf{x}$) and deformations ($\mathbf{F}$) is strictly enforced in the equation of motion [262]. The same is true for the conservation of angular momentum.

However, the equation of motion that has to be solved in this manner is a second order PDE. On the numerical side, this means that there may be drawbacks in terms of accuracy and stability of the approximated solution of the discretised equation.

To bypass these numerical problems, in the course of this chapter we laid the foundation of a different representation of the dynamic problem, made through a mixed system of first order PDEs, where the unknowns are the strain measures $\mathbf{F}$, $\mathbf{H}$ and J that define a polyconvex material, and the linear momentum $\mathbf{p}$. As mentioned in section 2.7, polyconvexity ensures the existence of solutions for the nonlinear problem [62]. The mixed system of first order PDEs can be proven to be hyperbolic, and hence numerical dissipation techniques prevalent in CFD become available, ensuring stability and enhanced order of accuracy to the numerical solution. Displacements

$\mathbf{u}$ are not unknown variables of the system anymore, and thus can be computed on the side of main calculations, by integrating $\mathbf{p}$ over the length of the time step.

As a cost for the adoption of the mixed system as the governing equations of the problem, we may cite the loss of a direct kinematic relation between deformations and displacements, which was instead straightforward in the case of the displacement-based method. Consequently, the conservation of angular momentum is not being directly fulfilled, as it requires the employment of $\mathbf{x}$ as an independent variable, and has thus to be enforced through a numerical algorithm.

The first order mixed system of PDEs governing elastodynamics analyses can be assembled together from the relevant local conservation laws as defined in previous sections, (2.23), (2.148), (2.154) and (2.161):

$$\frac{\partial \mathbf{p}}{\partial t} - \nabla_0 \cdot \mathbf{P} = \rho \mathbf{b}_F \tag{2.162a}$$

$$\frac{\partial \mathbf{F}}{\partial t} - \nabla_0 \cdot \left(\frac{1}{\rho} \mathbf{p} \otimes \mathbf{I} \right) = \mathbf{0} \tag{2.162b}$$

$$\frac{\partial \mathbf{H}}{\partial t} - \nabla_0 \times \left(\frac{\mathbf{p}}{\rho} \times \mathbf{F} \right) = \mathbf{0} \tag{2.162c}$$

$$\frac{\partial J}{\partial t} - \nabla_0 \cdot \left(\mathbf{H}^T \frac{\mathbf{p}}{\rho} \right) = 0 \tag{2.162d}$$

System (2.162) is valid for isothermal (adiabatic) conditions; in the presence of heat exchange, (2.36) should be added as a fifth equation with the internal energy e as extra unknown.

We can write (2.162) more succinctly, in the general structure of a conservation law, as:

$$\frac{\partial \boldsymbol{\mathcal{U}}}{\partial t} + \nabla_0 \cdot \boldsymbol{\mathcal{F}} = \boldsymbol{\mathcal{S}} \tag{2.163}$$

In (2.163), we define $\boldsymbol{\mathcal{U}}$ as the generalised vector of unknown variables, $\boldsymbol{\mathcal{F}}_I = \boldsymbol{\mathcal{F}} \mathbf{e}_I$ as the generalised vector of *flux* terms projected in the three

directions of space, $\boldsymbol{e}_I$, for $I = 1,2,3$. and $\boldsymbol{\mathcal{S}}$ as the generalised vector of external sources. More explicitly:

$$\boldsymbol{\mathcal{U}} = \begin{pmatrix} \mathbf{p} \\ \mathbf{F} \\ \mathbf{H} \\ \mathbf{J} \end{pmatrix} \qquad \boldsymbol{\mathcal{F}}_I = \begin{bmatrix} \boldsymbol{\mathcal{F}}_I^{\mathbf{p}} \\ \boldsymbol{\mathcal{F}}_I^{\mathbf{F}} \\ \boldsymbol{\mathcal{F}}_I^{\mathbf{H}} \\ \boldsymbol{\mathcal{F}}_I^{\mathbf{J}} \end{bmatrix} = - \begin{bmatrix} \mathbf{P}\boldsymbol{e}_I \\ \mathbf{p}/\rho \otimes \boldsymbol{e}_I \\ \mathbf{F} \times (\mathbf{p}/\rho \otimes \boldsymbol{e}_I) \\ \mathbf{H} : (\mathbf{p}/\rho \otimes \boldsymbol{e}_I) \end{bmatrix} \qquad \boldsymbol{\mathcal{S}} = \begin{pmatrix} \rho \mathbf{b}_F \\ \mathbf{0} \\ \mathbf{0} \\ 0 \end{pmatrix} \tag{2.164}$$

The structure of system (2.163), for instance, can be found in the Euler equation in fluid dynamics [5], known to be a system of hyperbolic PDEs. It can be formulated in *quasi-linear form* [256] by operating a linearisation of the flux matrix, obtaining

$$\frac{\partial \boldsymbol{\mathcal{U}}}{\partial t} + \boldsymbol{\mathcal{A}}_I \frac{\partial \boldsymbol{\mathcal{U}}}{\partial X_I} = \boldsymbol{\mathcal{S}} \qquad I = 1,2,3 \tag{2.165}$$

where

$$\boldsymbol{\mathcal{A}}_I \frac{\partial \boldsymbol{\mathcal{U}}}{\partial X_I} = \boldsymbol{\mathcal{A}}_I \begin{pmatrix} \cdot \frac{\partial \mathbf{p}}{\partial X_I} \\ : \frac{\partial \mathbf{F}}{\partial X_I} \\ : \frac{\partial \mathbf{H}}{\partial X_I} \\ \frac{\partial \mathbf{J}}{\partial X_I} \end{pmatrix}$$

and

$$\boldsymbol{\mathcal{A}}_I = \frac{\partial \boldsymbol{\mathcal{F}}_I}{\partial \boldsymbol{\mathcal{U}}} = \begin{bmatrix} \boldsymbol{\mathcal{F}}_{I_\mathbf{p}}^{\mathbf{p}} & \boldsymbol{\mathcal{F}}_{I_\mathbf{F}}^{\mathbf{p}} & \boldsymbol{\mathcal{F}}_{I_\mathbf{H}}^{\mathbf{p}} & \boldsymbol{\mathcal{F}}_{I_\mathbf{J}}^{\mathbf{p}} \\ \boldsymbol{\mathcal{F}}_{I_\mathbf{p}}^{\mathbf{F}} & \boldsymbol{\mathcal{F}}_{I_\mathbf{F}}^{\mathbf{F}} & \boldsymbol{\mathcal{F}}_{I_\mathbf{H}}^{\mathbf{F}} & \boldsymbol{\mathcal{F}}_{I_\mathbf{J}}^{\mathbf{F}} \\ \boldsymbol{\mathcal{F}}_{I_\mathbf{p}}^{\mathbf{H}} & \boldsymbol{\mathcal{F}}_{I_\mathbf{F}}^{\mathbf{H}} & \boldsymbol{\mathcal{F}}_{I_\mathbf{H}}^{\mathbf{H}} & \boldsymbol{\mathcal{F}}_{I_\mathbf{J}}^{\mathbf{H}} \\ \boldsymbol{\mathcal{F}}_{I_\mathbf{p}}^{\mathbf{J}} & \boldsymbol{\mathcal{F}}_{I_\mathbf{F}}^{\mathbf{J}} & \boldsymbol{\mathcal{F}}_{I_\mathbf{H}}^{\mathbf{J}} & \boldsymbol{\mathcal{F}}_{I_\mathbf{J}}^{\mathbf{J}} \end{bmatrix} = \tag{2.166}$$

$$= - \begin{bmatrix} \mathbf{0}_{3\times3} & [\mathbf{P}_\mathbf{F}\boldsymbol{e}_I]_{3\times3\times3} & [\mathbf{P}_\mathbf{H}\boldsymbol{e}_I]_{3\times3\times3} & \mathbf{P}_\mathbf{J}\boldsymbol{e}_I \\ 1/\rho\,[\delta_{ik}\delta_{IK}]_{3\times3\times3} & \mathbf{0}_{3\times3\times3\times3} & \mathbf{0}_{3\times3\times3\times3} & \mathbf{0}_{3\times3} \\ 1/\rho\,[\boldsymbol{\mathcal{E}}_{ilk}\boldsymbol{\mathcal{E}}_{KLI}F_{lL}]_{3\times3\times3} & \mathbf{0}_{3\times3\times3\times3} & \mathbf{0}_{3\times3\times3\times3} & \mathbf{0}_{3\times3} \\ 1/\rho\,[H_{iI}]_{1\times3} & \mathbf{0}_{3\times3} & \mathbf{0}_{3\times3} & 0 \end{bmatrix}$$

The generalised matrix $\mathcal{A}_I$ defined in (2.166) uses derivatives of the first Piola-Kirchhoff stress tensor (2.131), depending on the hyperelastic potential Ψ chosen:

$$\mathbf{P}_F = \frac{\partial^2 \Psi}{\partial \mathbf{F} \partial \mathbf{F}} = \Psi_{FF} + \Psi_{HF} \times \mathbf{F} + \Psi_{JF} \otimes \mathbf{H} \tag{2.167a}$$

$$\mathbf{P}_H = \frac{\partial^2 \Psi}{\partial \mathbf{F} \partial \mathbf{H}} = \Psi_{FH} + \Psi_{HH} \times \mathbf{F} + \Psi_{JH} \otimes \mathbf{H} \tag{2.167b}$$

$$\mathbf{P}_J = \frac{\partial^2 \Psi}{\partial \mathbf{F} \partial J} = \Psi_{FJ} + \Psi_{HJ} \times \mathbf{F} + \Psi_{JJ} \mathbf{H} \tag{2.167c}$$

2.14 BOUNDARY AND INITIAL CONDITIONS; INVOLUTIONS

In order to close the system of governing equations (2.162) for a solid dynamics problem, BCs and ICs need to be defined.

Assignment of mechanical BCs depends on the linear momentum $\mathbf{p}$ and the stress tensor $\mathbf{P}$ [2]. Equation (2.162a) involves $\mathbf{p}$ as unknown variable and $\mathbf{P}$ as part of the flux term; $\mathbf{p}$ appears in the flux terms of the other equations in (2.162). Thus $\mathbf{p}$ can be imposed directly as a Dirichlet boundary condition (BC) for (2.162a) and weakly, as a Neumann BC for the other governing equations. $\mathbf{P}$ on the other hand can act as Neumann condition for (2.162a).

Types of possible BCs that can be imposed are listed in table 2.4.

Table 2.4: sets of mechanical BCs that can be assigned to the first order form system of PDEs. Below, $\mathbf{n}$ is the current normal direction to the boundary, obtained from its initial direction $\mathbf{N}$ as $\mathbf{n} = \frac{\mathbf{F}^{-\mathsf{T}}\mathbf{N}}{\|\mathbf{F}^{-\mathsf{T}}\mathbf{N}\|}$, while $\mathbf{t}_{\partial V}$ and $\mathbf{t}_{\partial V_\parallel}$ are the traction value imposed on the boundary, and its tangential component.

	clamp		free		sliding	
	Dirichlet	Neumann	Dirichlet	Neumann	Dirichlet	Neumann
$\mathbf{p}(\mathbf{X})$	0	0	not imposed	not imposed	$\mathbf{p}(\mathbf{X}) \cdot \mathbf{n} = 0$	$\mathbf{p}(\mathbf{X}) \cdot \mathbf{n} = 0$
$\mathbf{P}(\mathbf{X})$		not imposed		$\mathbf{P}_\mathbf{n}(\mathbf{X}) = \mathbf{P}(\mathbf{X})\mathbf{n} = \mathbf{t}_{\partial V}(\mathbf{X})$		$\mathbf{P}(\mathbf{X}) - \mathbf{P}_\mathbf{n}(\mathbf{X}) = \mathbf{t}_{\partial V_\parallel}(\mathbf{X}, t)$

In this work, applications will be limited to cases where only the linear momentum is imposed, meaning that the structures considered will never be pre-stressed.

ICs determine the reference configuration of the problem, and are therefore essential in total Lagrangian dynamics. A set of initial data to start the problem is required for all unknowns, $\mathbf{p}$, $\mathbf{F}$, $\mathbf{H}$ and J.

As ICs on strain measures have to be imposed, a further constrain is added by compatibility conditions, that ought to be respected for the purpose of the problem well-posedness. For a first order hyperbolic system of partial differential equations, involutions ensure the compatibility between deformations and displacements [62, 63, 172].

Involutions were already introduced in section 2.7 in a $\{\mathbf{p}, \mathbf{F}\}$ system for the $\mathbf{F}$ variable. Under those conditions, we have observed that (2.41) holds. Its equivalent is equation (2.150) in section 2.12.1, that, once pulled back to the initial configuration, reads:

$$\nabla_0 \times \mathbf{F} = \mathbf{0} \tag{2.168}$$

In section 2.12.2 we formulated the other set of involutions relevant to the full $\{\mathbf{p}, \mathbf{F}, \mathbf{H}, J\}$ system, presented in (2.153). The complete set of involutions can be summarised below for ease of recall

$$\nabla_0 \times \mathbf{F} = \mathbf{0} \tag{2.169a}$$

$$\nabla_0 \cdot \mathbf{H} = \mathbf{0} \tag{2.169b}$$

As briefly mentioned in section 2.7, conditions (2.169) need only to be satisfied at the initial configuration, in order to be fulfilled throughout the analysis. If this is true, the existence of a unique solution to the elastodynamic problem is ensured [62]. They can be viewed, for the purpose of physical interpretation, as compatibility conditions, relating the various measures of deformation with the respective kinematic variable, in (2.162).

However, fulfilment of (2.169) has to be carefully ensured when discretising (2.162) throughout the analysis, in order to avoid numerical errors.

2.15 EIGENSTRUCTURE OF THE FULL MIXED SYSTEM

Conclusive proof of hyperbolicity for system (2.162) is provided by the existence of solutions $\mathcal{U}$ of a plane, wave-form nature [13, 98, 172]. For the quasi-linear reduction of the problem (2.165), $\mathcal{U}$ would assume the form

$$\mathcal{U} = f(\mathbf{X}\cdot\mathbf{N} - c_\alpha t)\,\mathcal{U}^R_\alpha \qquad \alpha = 1,2,3,\ldots,22 \tag{2.170}$$

In (2.170) t stands for time, $\mathbf{N}$ is the normalised directional vector of wave propagation, while c_α is the eigenvalue/wave speed of mode α, and $\mathcal{U}^R_\alpha$ is the right eigenvector of that same mode α.

In order to demonstrate that (2.170) constitutes an alternative manner of representing $\mathcal{U}$ as defined in (2.164), we start by substituting the wave-like form (2.170) into the homogeneous version of our quasi-linear system (2.165):

$$-c_\alpha f'\mathcal{U}^R_\alpha + (\mathcal{A}_I\cdot\mathbf{N})\,f'\mathcal{U}^R_\alpha = 0 \tag{2.171}$$

and then

$$[\mathcal{A}_\mathbf{N} - c_\alpha\mathcal{I}]\,\mathcal{U}^R_\alpha = 0 \tag{2.172}$$

where $\mathcal{A}_\mathbf{N} = \mathcal{A}_I\cdot\mathbf{N} = {}^{\partial\mathcal{F}\cdot\mathbf{N}}/_{\partial\mathcal{U}}$, and $\mathcal{I}$ is a 22×22 identity tensor in the space of $\mathcal{U}$.

Considering now the projection in the direction $\mathbf{N}$ of the generalised flux vector $\mathcal{F}_I$ in (2.164), we obtain:

$$\mathcal{F}_N = \mathcal{F}_I\cdot\mathbf{N} = \begin{bmatrix}\mathcal{F}^p_\mathbf{N}\\ \mathcal{F}^F_\mathbf{N}\\ \mathcal{F}^H_\mathbf{N}\\ \mathcal{F}^I_\mathbf{N}\end{bmatrix} = -\begin{bmatrix}\mathbf{P}\mathbf{N}\\ p/\rho\otimes\mathbf{N}\\ -p/\rho\times\mathbf{F}\times\mathbf{N}\\ p/\rho\cdot(\mathbf{P}\mathbf{N})\end{bmatrix} \tag{2.173}$$

Consequently, projecting the whole system (2.172) on $\mathbf{N}$ yields:

$$\mathcal{A}_\mathbf{N}\mathcal{U}^R_\alpha = c_\alpha\mathcal{U}^R_\alpha \tag{2.174}$$

The expanded form of equation (2.174), reads

$$-\begin{bmatrix} 0_{3\times3} & [\mathbf{P}_F\mathbf{N}]_{3\times9} & [\mathbf{P}_H\mathbf{N}]_{3\times9} & [\mathbf{P}_J\mathbf{N}]_{3\times1} \\ 1/\rho\,\mathcal{F}^F_{\mathbf{N}_p}|_{9\times3} & 0_{9\times9} & 0_{9\times9} & 0_{9\times1} \\ 1/\rho\,\mathcal{F}^H_{\mathbf{N}_p}|_{9\times3} & 0_{9\times9} & 0_{9\times9} & 0_{9\times1} \\ 1/\rho\,[\mathbf{H}\mathbf{N}]^T|_{1\times3} & 0_{1\times9} & 0_{1\times9} & 0 \end{bmatrix} \begin{pmatrix} \mathbf{p}^R_\alpha \\ \mathbf{F}^R_\alpha \\ \mathbf{H}^R_\alpha \\ J^R_\alpha \end{pmatrix} = c_\alpha \begin{pmatrix} \mathbf{p}^R_\alpha \\ \mathbf{F}^R_\alpha \\ \mathbf{H}^R_\alpha \\ J^R_\alpha \end{pmatrix} \tag{2.175}$$

In (2.175), $\mathbf{P}_F$, $\mathbf{P}_H$ and $\mathbf{P}_J$ are those defined, for a polyconvex material energy function, in equations (2.167), while $\mathcal{F}^F_{\mathbf{N}_p}$ and $\mathcal{F}^H_{\mathbf{N}_p}$ are the tensors below:

$$\mathcal{F}^F_{\mathbf{N}_p} = \begin{bmatrix} \mathbf{N}|_{3\times1} & 0_{3\times1} & 0_{3\times1} \\ 0_{3\times1} & \mathbf{N}|_{3\times1} & 0_{3\times1} \\ 0_{3\times1} & 0_{3\times1} & \mathbf{N}|_{3\times1} \end{bmatrix} \tag{2.176}$$

$$\mathcal{F}^H_{\mathbf{N}_p} = \begin{bmatrix} 0_{3\times1} & [\mathbf{F}\times\mathbf{N}]^T_3|_{3\times1} & -[\mathbf{F}\times\mathbf{N}]^T_2|_{3\times1} \\ -[\mathbf{F}\times\mathbf{N}]^T_3|_{3\times1} & 0_{3\times1} & [\mathbf{F}\times\mathbf{N}]^T_1|_{3\times1} \\ [\mathbf{F}\times\mathbf{N}]^T_2|_{3\times1} & -[\mathbf{F}\times\mathbf{N}]^T_1|_{3\times1} & 0_{3\times1} \end{bmatrix} \tag{2.177}$$

In (2.176), $\mathbf{N}$ is the direction of wave propagation in Cartesian coordinates. In (2.177), vectors $[\mathbf{F}\times\mathbf{N}]_i$ for $i = 1,2,3$ are the rows of the tensor cross product between $\mathbf{F}$ and $\mathbf{N}$:

$$\mathbf{F}\times\mathbf{N} = \begin{bmatrix} [\mathbf{F}\times\mathbf{N}]_1|_{1\times3} \\ [\mathbf{F}\times\mathbf{N}]_2|_{1\times3} \\ [\mathbf{F}\times\mathbf{N}]_3|_{1\times3} \end{bmatrix}$$

From (2.175), it can be seen that the eigenvalues for the strain measures $\mathbf{F}^R_\alpha$, $\mathbf{H}^R_\alpha$ and J^R_α are uncoupled, and only depend on the eigenvalues of the linear momentum, $\mathbf{p}^R_\alpha$. This observation leads to the formulation of the eigenvalues $\mathbf{F}^R_\alpha$ in terms of those of $\mathbf{p}^R_\alpha$, as

$$\mathbf{F}^R_\alpha = -\frac{1}{\rho c_\alpha}\left(\mathbf{p}^R_\alpha \otimes \mathbf{N}\right) \tag{2.178}$$

Eigenvectors for the surface strain measure $\mathbf{H}$ are also readily obtained by looking at (2.175) and (2.177):

$$\mathbf{H}_\alpha^R = \frac{1}{\rho c_\alpha}\left(\mathbf{p}_\alpha^R \times \mathbf{F} \times \mathbf{N}\right) \tag{2.179}$$

Equation (2.175) yields the eigenvectors of J as

$$J_\alpha^R = -\frac{1}{\rho c_\alpha}\mathbf{p}_\alpha^R \cdot [\mathbf{H}\mathbf{N}] \tag{2.180}$$

Further, from (2.179) using the property of the tensor cross product listed as tenth in table 2.2, we get

$$\mathbf{H}_\alpha^R = -\frac{1}{\rho c_\alpha}\mathbf{F} \times \left(\mathbf{p}_\alpha^R \otimes \mathbf{N}\right) \tag{2.181}$$

Remembering the property (2.159) of double contraction for second order tensors, [39], equation (2.180) can be rearranged as

$$J_\alpha^R = -\frac{1}{\rho c_\alpha}\mathbf{H} : \left[\mathbf{p}_\alpha^R \otimes \mathbf{N}\right] \tag{2.182}$$

Lastly, the first set of equations in (2.175) yields the eigenvectors $\mathbf{p}_\alpha^R$ of the linear momentum. Expanding these equations results in

$$-\left[(\mathbf{P}_F\mathbf{N}) : \mathbf{F}_\alpha^R + (\mathbf{P}_H\mathbf{N}) : \mathbf{H}_\alpha^R + (\mathbf{P}_J\mathbf{N})\, J_\alpha^R\right] = c_\alpha \mathbf{p}_\alpha^R \tag{2.183}$$

Substituting the full expressions for polyconvex stress conjugates (2.167) to strain measures $\mathbf{F}$, $\mathbf{H}$ and J in (2.183) yields

$$\begin{aligned} -\left(\Psi_{FF} + \mathbf{F} \times \Psi_{HF} + \mathbf{H} \otimes \Psi_{JF}\right)\mathbf{N} : \left(-\frac{1}{\rho c_\alpha}\mathbf{p}_\alpha^R \otimes \mathbf{N}\right) + \\ -\left(\Psi_{FH} + \mathbf{F} \times \Psi_{HH} + \mathbf{H} \otimes \Psi_{JH}\right)\mathbf{N} : \left[-\mathbf{F} \times \left(\frac{1}{\rho c_\alpha}\mathbf{p}_\alpha^R \otimes \mathbf{N}\right)\right] + \\ -\left(\Psi_{FJ} + \mathbf{F} \times \Psi_{HJ} + \mathbf{H}\,\Psi_{JJ}\right)\mathbf{N} : \left(-\frac{1}{\rho c_\alpha}\mathbf{p}_\alpha^R \otimes \mathbf{N}\right) = c_\alpha \mathbf{p}_\alpha^R \end{aligned} \tag{2.184}$$

Now, by noticing the following property for the product between 2nd, or higher, order tensors ($\mathcal{A}$) and vectors ($\mathbf{u}$ and $\mathbf{v}$) [39]

$$(\mathcal{A}\mathbf{v})\,\mathbf{u} = \mathcal{A} : (\mathbf{u} \otimes \mathbf{v})$$

we can then pre-multiply (2.184) by $\mathbf{p}^R_\alpha$, and, arranging the terms opportunely, obtain:

$$\begin{aligned}
&\left(\mathbf{p}^R_\alpha \otimes \mathbf{N}\right) : (\Psi_{FF} + \mathbf{F} \times \Psi_{HF} + \mathbf{H} \otimes \Psi_{JF}) : \left(\mathbf{p}^R_\alpha \otimes \mathbf{N}\right) + \\
&+ \left(\mathbf{p}^R_\alpha \otimes \mathbf{N}\right) : (\Psi_{FH} + \mathbf{F} \times \Psi_{HH} + \mathbf{H} \otimes \Psi_{JH}) : \left[\mathbf{F} \times \left(\mathbf{p}^R_\alpha \otimes \mathbf{N}\right)\right] + \\
&+ \left(\mathbf{p}^R_\alpha \otimes \mathbf{N}\right) : (\Psi_{FJ} + \mathbf{F} \times \Psi_{HJ} + \mathbf{H}\,\Psi_{JJ}) : \left[\mathbf{H} : \left(\mathbf{p}^R_\alpha \otimes \mathbf{N}\right)\right] = \\
&= \rho c^2_\alpha \mathbf{p}^R_\alpha \cdot \mathbf{p}^R_\alpha
\end{aligned} \tag{2.185}$$

Use of property 8 in table 2.2 enables to arrange (2.185) in matrix form, namely

$$\begin{pmatrix} (\mathbf{p}^R_\alpha \otimes \mathbf{N}) : \\ \mathbf{F} \times (\mathbf{p}^R_\alpha \otimes \mathbf{N}) : \\ \mathbf{H} : (\mathbf{p}^R_\alpha \otimes \mathbf{N}) \end{pmatrix}^T \begin{bmatrix} \frac{\partial^2\Psi}{\partial F \partial F} & \frac{\partial^2\Psi}{\partial F \partial H} & \frac{\partial^2\Psi}{\partial F \partial J} \\ \frac{\partial^2\Psi}{\partial H \partial F} & \frac{\partial^2\Psi}{\partial H \partial H} & \frac{\partial^2\Psi}{\partial H \partial J} \\ \frac{\partial^2\Psi}{\partial J \partial F} & \frac{\partial^2\Psi}{\partial J \partial H} & \frac{\partial^2\Psi}{\partial J \partial J} \end{bmatrix} \begin{pmatrix} : (\mathbf{p}^R_\alpha \otimes \mathbf{N}) \\ : (\mathbf{p}^R_\alpha \otimes \mathbf{N}) \times \mathbf{F} \\ (\mathbf{p}^R_\alpha \otimes \mathbf{N}) : \mathbf{H} \end{pmatrix} = \\ = \rho c^2_\alpha\, \mathbf{p}^R_\alpha \cdot \mathbf{p}^R_\alpha \tag{2.186}$$

The generalised matrix of second derivatives of the polyconvex potential energy $\Psi(\mathbf{F}, \mathbf{H}, J)$ that appears in (2.186) is the Hessian of Ψ, $\mathcal{H}_\Psi$, as defined in (2.143):

$$\mathcal{H}_\Psi = \begin{bmatrix} \frac{\partial^2\Psi}{\partial F \partial F} & \frac{\partial^2\Psi}{\partial F \partial H} & \frac{\partial^2\Psi}{\partial F \partial J} \\ \frac{\partial^2\Psi}{\partial H \partial F} & \frac{\partial^2\Psi}{\partial H \partial H} & \frac{\partial^2\Psi}{\partial H \partial J} \\ \frac{\partial^2\Psi}{\partial J \partial F} & \frac{\partial^2\Psi}{\partial J \partial H} & \frac{\partial^2\Psi}{\partial J \partial J} \end{bmatrix}_{19\times 19} \tag{2.187}$$

Given the polyconvexity of Ψ, that $\mathcal{H}_\Psi$ in (2.187) be positive definite follows directly from (2.144).

This proves the existence of real and positive elastic wave speeds in a medium governed by the system of first order mixed equations (2.162). As a consequence, such a system can be classified as hyperbolic.

The positive-definiteness of Ψ could also be inferred from (2.49), as polyconvexity is a stricter condition than strong ellipticity, and inclusive of it.

In order to better appreciate this, it can constitute a useful exercise to substitute for $\Psi(\mathbf{F}, \mathbf{H}, J)$ in (2.175) – by way of $\mathbf{P}(\partial\Psi/\partial\mathbf{F}, \partial\Psi/\partial\mathbf{H}, \partial\Psi/\partial J)$ – the potential elastic energy of one of the three polyconvex hyperelastic models presented in section 2.9.

2.16 EIGENSTRUCTURE FOR THE OGDEN MATERIAL MODEL

In the following, guidelines for this derivation process are sketched for the Ogden model.

The energy expression for this type of material is the sum of its isochoric component in (2.77) and its volumetric in (2.79), as reported below:

$$\Psi_O = \sum_{p=1}^{3} \frac{\mu_p}{\alpha_p} \left[J^{-1/3} \left(\lambda_1^{\alpha_p} + \lambda_2^{\alpha_p} + \lambda_3^{\alpha_p} \right) - 3 \right] + \frac{\kappa}{\beta^2} \left(\beta \ln J + \frac{1}{J^\beta} - 1 \right) \tag{2.188}$$

See section 2.9 for the meaning of symbols in (2.188).

Observing that the Ogden potential energy Ψ_O in (2.188) does not depend on the surface strain measure $\mathbf{H}$, we can simplify its Hessian $\boldsymbol{\mathcal{H}}_{\Psi_O}$, (2.187), to

$$\boldsymbol{\mathcal{H}}_{\Psi_O} = \begin{bmatrix} \frac{\partial^2 \Psi_O}{\partial \mathbf{F} \partial \mathbf{F}} & 0 & \frac{\partial^2 \Psi_O}{\partial \mathbf{F} \partial J} \\ 0 & 0 & 0 \\ \frac{\partial^2 \Psi_O}{\partial J \partial \mathbf{F}} & 0 & \frac{\partial^2 \Psi_O}{\partial J \partial J} \end{bmatrix} \tag{2.189}$$

First derivatives of Ψ_O with respect to $\mathbf{F}$, $\mathbf{H}$, and J are pre-condition to evaluate the Hessian, and can be retrieved from (2.142):

$$\begin{aligned}\frac{\partial \Psi_O}{\partial \mathbf{F}} &= J^{-2/3}\left[\left(\mu_1\lambda_1^{\alpha_1-1}+\mu_2\lambda_1^{\alpha_2-1}+\mu_3\lambda_1^{\alpha_3-1}\right)(\mathbf{n}_1\otimes\mathbf{N}_1)+\right.\\ &+\left(\mu_1\lambda_2^{\alpha_1-1}+\mu_2\lambda_2^{\alpha_2-1}+\mu_3\lambda_2^{\alpha_3-1}\right)(\mathbf{n}_2\otimes\mathbf{N}_2)+\\ &+\left.\left(\mu_1\lambda_3^{\alpha_1-1}+\mu_2\lambda_3^{\alpha_2-1}+\mu_3\lambda_3^{\alpha_3-1}\right)(\mathbf{n}_3\otimes\mathbf{N}_3)\right] \qquad (2.190a)\\ \frac{\partial \Psi_O}{\partial \mathbf{H}} &= \mathbf{0} \qquad (2.190b)\\ \frac{\partial \Psi_O}{\partial J} &= -\sum_{p=1}^{3}\frac{\mu_p}{3}\left(\lambda_1^{\alpha_p}+\lambda_2^{\alpha_p}+\lambda_3^{\alpha_p}\right)J^{-\left(\frac{\alpha_p}{3}+1\right)}+\frac{\kappa}{\beta J}\left(1-\frac{1}{J^\beta}\right) \qquad (2.190c)\end{aligned}$$

The four non-zero terms in (2.189) have to be computed one by one.

- The term $\frac{\partial^2\Psi_O}{\partial \mathbf{F}\partial \mathbf{F}}$ should be computed as:

$$\frac{\partial^2\Psi_O}{\partial \mathbf{F}\partial \mathbf{F}} = \sum_{i=1}^{3}\overbrace{\frac{\partial\left(\frac{\partial\Psi_O}{\partial \mathbf{F}}\right)}{\partial\lambda_i}}^{(2.192a)}\overbrace{\frac{\partial\lambda_i}{\partial \mathbf{F}}}^{(2.192b)}+\overbrace{\frac{\partial\left(\frac{\partial\Psi_O}{\partial \mathbf{F}}\right)}{\partial \mathbf{n}_i}}^{(2.192c)}\overbrace{\frac{\partial \mathbf{n}_i}{\partial \mathbf{F}}}^{(2.192d)} \qquad (2.191)$$

  Noting the rendition of Ψ_O in (2.188), the four components in (2.191) can be readily expressed as following

$$\begin{aligned}\frac{\partial\left(\frac{\partial\Psi_O}{\partial \mathbf{F}}\right)}{\partial\lambda_i} &= J^{-2/3}\left[\mu_1(\alpha_1-1)\lambda_i^{\alpha_1-2}+\mu_2(\alpha_2-1)\lambda_i^{\alpha_2-2}+\right.\\ &\left.+\mu_3(\alpha_3-1)\lambda_i^{\alpha_3-2}\right](\mathbf{n}_i\otimes\mathbf{N}_i) \qquad (2.192a)\\ \frac{\partial\lambda_i}{\partial \mathbf{F}} &= \mathbf{n}_i\otimes\mathbf{N}_i \qquad (2.192b)\\ \frac{\partial\left(\frac{\partial\Psi_O}{\partial \mathbf{F}}\right)}{\partial \mathbf{n}_i} &= J^{-2/3}\left(\mu_1\lambda_i^{\alpha_1-1}+\mu_2\lambda_i^{\alpha_2-1}+\mu_3\lambda_i^{\alpha_3-1}\right)\cdot\\ &\cdot(\mathbf{e}_1\otimes\mathbf{N}_i\otimes\mathbf{e}_1+\mathbf{e}_2\otimes\mathbf{N}_i\otimes\mathbf{e}_2+\mathbf{e}_3\otimes\mathbf{N}_i\otimes\mathbf{e}_3) \qquad (2.192c)\\ \frac{\partial \mathbf{n}_i}{\partial \mathbf{F}} &= -J\frac{dA}{da}\mathbf{F}^{-T}\Delta\mathbf{F}\,\mathbf{F}^{-T}\mathbf{N}_i \qquad i=1,2,3 \qquad (2.192d)\end{aligned}$$

  In (2.192c), $\mathbf{e}_i$, $i=1,2,3$ represent the 3 axes of the Cartesian frame reference our continuum body is immersed into.

Term (2.192d) comes from considering the dependence of the current principal direction $\mathbf{n}_i$, $i = 1,2,3$ from the deformation gradient $\mathbf{F}$ through the Nanson formula [196, 242] reproduced below:

$$\mathbf{n}_i da = J\mathbf{F}^{-T}\mathbf{N}_i dA \tag{2.193}$$

In (2.192c) and (2.193), scalars dA and da respectively indicate the measures of a unit of body surface in the initial configuration, and how it has evolved in the current configuration. In (2.192c), $\Delta\mathbf{F}$ is an increment from the present $\mathbf{F}$, used to evaluate the directional derivative $D\mathbf{F}^{-T}[\mathbf{F}]$.

Substituting the four derivatives found in (2.192) into (2.191) yields the sought-after first Hessian term:

$$\begin{aligned}
&\frac{\partial^2\Psi_O}{\partial\mathbf{F}\partial\mathbf{F}} = J^{-2/3}\sum_{i=1}^{3} \\
&\left\{ \left[\mu_1(\alpha_1-1)\lambda_i^{\alpha_1-2} + \mu_2(\alpha_2-1)\lambda_i^{\alpha_2-2} + \mu_3(\alpha_3-1)\lambda_i^{\alpha_3-2}\right]\cdot \right. \\
&\quad \cdot(\mathbf{n}_i\otimes\mathbf{N}_i\otimes\mathbf{n}_i\otimes\mathbf{N}_i) + \left(\mu_1\lambda_i^{\alpha_1-1} + \mu_2\lambda_i^{\alpha_2-1} + \mu_3\lambda_i^{\alpha_3-1}\right)\cdot \\
&\quad \cdot(\boldsymbol{e}_1\otimes\mathbf{N}_i\otimes\boldsymbol{e}_1 + \boldsymbol{e}_2\otimes\mathbf{N}_i\otimes\boldsymbol{e}_2 + \boldsymbol{e}_3\otimes\mathbf{N}_i\otimes\boldsymbol{e}_3)\otimes \\
&\quad \left.\otimes\left(-J\frac{dA}{da}\mathbf{F}^{-T}\Delta\mathbf{F}\,\mathbf{F}^{-T}\mathbf{N}_i\right)\right\}
\end{aligned} \tag{2.194}$$

- The second non-zero term in the Hessian (2.189) is $\frac{\partial^2\Psi_O}{\partial\mathbf{F}\partial J}$

$$\frac{\partial^2\Psi_O}{\partial\mathbf{F}\partial J} = \frac{\partial\left[\frac{\partial\Psi_O}{\partial\mathbf{F}}(J,\mathbf{n}_i)\right]}{\partial J} + \sum_{i=1}^{3}\frac{\partial\left[\frac{\partial\Psi_O}{\partial\mathbf{F}}(J,\mathbf{n}_i)\right]}{\partial J}\frac{\partial\mathbf{n}_i}{\partial J} \tag{2.195}$$

Using (2.190a), (2.192c) and (2.193), we can expand (2.195) as

$$\begin{aligned}\frac{\partial^2\Psi_O}{\partial \mathbf{F}\partial J} = &-\frac{2}{3}J^{-5/3}\sum_{i=1}^{3} \\ &\left[\left(\mu_1\lambda_i^{\alpha_1-1}+\mu_2\lambda_i^{\alpha_2-1}+\mu_3\lambda_i^{\alpha_3-1}\right)(\mathbf{n}_i\otimes\mathbf{N}_i)\right]+ \\ &+J^{-2/3}\sum_{i=1}^{3}\left[\left(\mu_1\lambda_i^{\alpha_1-1}+\mu_2\lambda_i^{\alpha_2-1}+\mu_3\lambda_i^{\alpha_3-1}\right)(\boldsymbol{e}_1\otimes\mathbf{N}_i\otimes\boldsymbol{e}_1+\right. \\ &\left.+\boldsymbol{e}_2\otimes\mathbf{N}_i\otimes\boldsymbol{e}_2+\boldsymbol{e}_3\otimes\mathbf{N}_i\otimes\boldsymbol{e}_3)\otimes\left(\frac{dA}{da}\mathbf{F}^{-T}\mathbf{N}_i\right)\right] \end{aligned} \tag{2.196}$$

- The third non-zero component of (2.189) is

$$\frac{\partial^2\Psi_O}{\partial J\partial \mathbf{F}} = \sum_{i=1}^{3}\frac{\partial\left[\frac{\partial\Psi_O}{\partial J}(\lambda_i)\right]}{\partial\lambda_i}\frac{\partial\lambda_i}{\partial \mathbf{F}} \tag{2.197}$$

Using (2.190c) and (2.192b), we can expand (2.197) as

$$\begin{aligned}\frac{\partial^2\Psi_O}{\partial J\partial \mathbf{F}} = &-\sum_{i=1}^{3}\left\{\left[\frac{\mu_1}{3}\alpha_1 J^{-\left(\frac{\alpha_1}{3}+1\right)}\lambda_i^{\alpha_1-1}+\right.\right. \\ &\left.\left.+\frac{\mu_2}{3}\alpha_2 J^{-\left(\frac{\alpha_2}{3}+1\right)}\lambda_i^{\alpha_2-1}+\frac{\mu_3}{3}\alpha_3 J^{-\left(\frac{\alpha_3}{3}+1\right)}\lambda_i^{\alpha_3-1}\right](\mathbf{n}_i\otimes\mathbf{N}_i)\right\}\end{aligned} \tag{2.198}$$

- The last non-zero component of (2.189) can be obtained directly from (2.190c):

$$\begin{aligned}\frac{\partial^2\Psi_O}{\partial J\partial J} = &\frac{1}{3}\sum_{i=1}^{3}\left[\mu_i\left(\frac{\alpha_i}{3}+1\right)J^{-\left(\frac{\alpha_i}{3}+2\right)}\left(\lambda_1^{\alpha_i}+\lambda_2^{\alpha_i}+\lambda_3^{\alpha_i}\right)\right]+ \\ &+\frac{\kappa}{\beta J^2}\left[\frac{\beta+1}{J^\beta}-1\right]\end{aligned} \tag{2.199}$$

Substituting the Hessian for the Ogden model, (2.189), in (2.186) allows to write

$$\begin{pmatrix} (\mathbf{p}_\alpha^R \otimes \mathbf{N}) : \\ \mathbf{F} \times (\mathbf{p}_\alpha^R \otimes \mathbf{N}) : \\ \mathbf{H} : (\mathbf{p}_\alpha^R \otimes \mathbf{N}) \end{pmatrix}^T \begin{bmatrix} \frac{\partial^2 \Psi_O}{\partial \mathbf{F} \partial \mathbf{F}} & 0 & \frac{\partial^2 \Psi_O}{\partial \mathbf{F} \partial J} \\ 0 & 0 & 0 \\ \frac{\partial^2 \Psi_O}{\partial J \partial \mathbf{F}} & 0 & \frac{\partial^2 \Psi_O}{\partial J \partial J} \end{bmatrix} \begin{pmatrix} : (\mathbf{p}_\alpha^R \otimes \mathbf{N}) \\ : (\mathbf{p}_\alpha^R \otimes \mathbf{N}) \times \mathbf{F} \\ (\mathbf{p}_\alpha^R \otimes \mathbf{N}) : \mathbf{H} \end{pmatrix} = \\ = \rho c_\alpha^2 \, \mathbf{p}_\alpha^R \cdot \mathbf{p}_\alpha^R \qquad (2.200)$$

Further developing (2.200) leads to the characteristic equation, from which to extract the eigenvalues (pressure and shear wave velocities) of the mixed Ogden polyconvex system:

$$\left(\mathbf{p}_\alpha^R\right)^T \left.\frac{\partial^2 \Psi_O}{\partial \mathbf{F} \partial \mathbf{F}}\right|_{\mathbf{NN}} \mathbf{p}_\alpha^R + \left(\mathbf{p}_\alpha^R \cdot \mathbf{H}\mathbf{N}\right) \left[\left(\frac{\partial^2 \Psi_O}{\partial \mathbf{F} \partial J} \mathbf{N}\right) \cdot \mathbf{p}_\alpha^R + \left(\frac{\partial^2 \Psi_O}{\partial J \partial \mathbf{F}} \mathbf{N}\right) \cdot \mathbf{p}_\alpha^R \right] + \\ + \frac{\partial^2 \Psi_O}{\partial J \partial J} \left[\mathbf{p}_\alpha^R \cdot (\mathbf{H}\mathbf{N})\right]^2 = \rho c_\alpha^2 \, \mathbf{p}_\alpha^R \cdot \mathbf{p}_\alpha^R \qquad (2.201)$$

where $\left.\frac{\partial^2 \Psi_O}{\partial \mathbf{F} \partial \mathbf{F}}\right|_{\mathbf{NN}} = \mathbf{N}^T \left(\frac{\partial^2 \Psi_O}{\partial \mathbf{F} \partial \mathbf{F}}\right) \mathbf{N}$.

2.17 CONCLUDING REMARKS

In the course of the present chapter we have laid out the mathematical frame needed to understand the set-up of a first order, mixed system of PDEs to represent solid dynamics problems, in place of the standard, second order, displacement-based description.

Essentially, proof of hyperbolicity for the first order mixed system has to be provided in order for it to produce reliable solutions for elastodynamics simulations. This is demonstrated by analysis of the eigenvalues of the matrix of the linearised system: real and distinct eigenvalues are directly related to corresponding pressure and shear elastic wave speeds.

After defining relevant concepts, and setting up conservation laws for kinetic quantities in sections leading up to section 2.6, we go on discussing the requirements that are necessary from these conservation laws in order to build a well-posed hyperbolic system of PDEs.

Constitutive inequalities and the notion of strong ellipticity (2.49) are defined and described in sections 2.7 and 2.8. In particular, in section 2.8 we introduce polyconvexity, a more stringent condition than strong ellipticity on the constitutive material behaviour, that under certain regimes ensures the existence and uniqueness of solutions. Polyconvexity requires an extension of the dependence of the elastic potential function $\Psi(\mathbf{F})$ to include not only the deformation gradient, but also its determinant J and its matrix of cofactors $\mathbf{H}$, as shown in (2.52).

In section 2.9 we identify three well-known hyperelastic material models: the Mooney-Rivlin, neo-Hookean, and Ogden models, which we reformulate in the frame of polyconvexity. This task is further discussed in section 2.11, while in section 2.10 the developed model is expanded to include plastic deformation.

Additional conservation laws can then be established for $\mathbf{F}$, $\mathbf{H}$ and J in section 2.12, and a complete, first order mixed $\{\mathbf{p}, \mathbf{F}, \mathbf{H}, J\}$ system of PDEs is formulated in section 2.13, see (2.162). Boundary and initial conditions for system (2.162) are discussed in section 2.14, along with compatibility issues (involutions).

As mentioned in chapter 1, (2.162) clearly presents analogies with the Euler equations in fluid dynamics. This will be further explored in chapter 3, where the possibility to employ stabilisation techniques from CFD will be exploited in order to devise a new discretisation strategy for nonlinear fast solid dynamics problems.

Finally, in the last two sections, a study of the eigenstructure of system (2.162) is attempted: first its characteristic equation is derived in section 2.15 in the most general manner (eqs. (2.185) and (2.186)), without specifying any constitutive model. Afterwards, this formulation is adapted for the Ogden model in section 2.16; the derivation, yielding characteristic equation in eqs. (2.200) and (2.201), provides a framework for the study of the polyconvex version of the Ogden material in the context of a first order, mixed system of conservation laws PDEs. At present, and to the author's knowledge, detailed discussion of this formulation is not available in literature, and the contribution made in this thesis would be a good starting point for further study.

3 THE JST-SPH DISCRETISATION SCHEME

In the previous chapter, we have covered some aspects of the mathematical representation of fast dynamics solid deformations, with a focus on hyper-elastic and elasto-plastic material behaviours. We introduced the problem in the form of a set of conservation laws, seeking a solution capable of completely describing stress and strain states at a given time and on any location of the body of interest during the simulation.

In order to do this, we have proceeded in an unconventional manner, by adopting the linear momentum $\mathbf{p}$ and a set of strain measures – the deformation gradient $\mathbf{F}$, the cofactors matrix of $\mathbf{F}$, $\mathbf{H}$, and the Jacobian of the deformation J – as the main unknowns for the system of conservation laws. Displacements $\mathbf{u}$, can then be easily calculated from these quantities.

By adopting the aforementioned approach, in place of solving the classical second order equation of motion (2.37) with displacements as unknowns, there will be an additional cost incurred in handling a system of first order PDEs. However, in so doing, the mixed governing system of PDEs will be hyperbolic in nature, mirroring typical governing equations in CFD. This similarity holds the decisive advantage of enabling to borrow effective and reliable dissipation techniques from the (by now) vast CFD literature on the subject.

Benefits arising from this analogy will be made clearer during the course of the present chapter, which is structured as following: section 3.1 will provide some fundamental notions over the basic Galerkin type weak discretisation problem and its solution by the FEM. In section 3.2 we will give an overview of the various typologies of meshfree numerical methods, their main features, and how they differ from the FEM. Our focus will be on meshless techniques based on the concept of *reproducing kernel*. The SPH method, a reproducing kernel technique, will be described in more detail in sections 3.3 and 3.4, and will be used to discretise equation (2.162) in the subsequent section 3.5.

As mentioned above, the spatially semi-discretised system of ordinary differential equations (ODEs) obtained with SPH can be enhanced via a numerical dissipation term that helps in suppressing spurious oscillations, as typically done in the field of CFD, with the Euler and Navier-Stokes equations for inviscid and viscous flows, respectively. To this aim, in section 3.6 a dissipation term obtained using the JST artificial dissipation algorithm will be added to the RHS of ODEs in the semi-discretised system.

Finally, the system of ODEs will be fully discretised by the use of an explicit time integration scheme of the RK family in section 3.7. Yet, the introduction of artificial dissipation can lead to the unintended consequence of violating the global angular momentum of the discretised system. To avoid this, a correction procedure based on Lagrange multipliers is implemented in section 3.8. As a result, corrected values for the JST dissipation terms and for internal stresses are obtained.

Brief details on the computer implementation of the method are outlined in section 3.9, and some concluding remarks are finally provided in section 3.10.

3.1 INTRODUCTION: FORMULATION OF THE PROBLEM, GALERKIN DISCRETISATION, FINITE ELEMENT METHOD

Before introducing meshless methods, it is convenient to start from the classic FEM theory. Thorough description of the method can be found in texts such as [16, 115, 125, 271]; however it was felt that a swift summary of its most relevant points will help to get a better understanding of the topics more of interest to this thesis, and to better appreciate the advantages lying in the decision of modelling system (2.162) with a particle method.

3.1.1 *Strong and weak formulations of the problem*

Let the *strong form* of the problem at hand be to find an unknown function $\mathbf{u}(\mathbf{x})$, defined over a domain $\mathcal{B} \in \mathbb{R}^3$, that solves the following system:

$$\begin{aligned} \mathcal{A}(\mathbf{u}) &= \mathbf{f} \quad && \forall \mathbf{x} \in \mathcal{B} \\ \mathbf{u} &= \mathbf{u}_0 && \forall \mathbf{x} \in \Gamma_D \\ \frac{\partial \mathbf{u}}{\partial \mathbf{n}} &= \mathbf{h} && \forall \mathbf{x} \in \Gamma_N \end{aligned} \tag{3.1}$$

In (3.1), $\mathcal{A}$ is a generic differential operator containing derivatives with respect to space $\mathbf{x}$; $\mathbf{f}$ is a term that renders the equation non-homogeneous, Γ_D and Γ_N are the boundary regions of $\mathcal{B}$ with normal direction $\mathbf{n}$ where, respectively, Dirichlet boundary values $\mathbf{u}_0$ and Neumann boundary values $\mathbf{h} \cdot \mathbf{n}$ are imposed. Equations (3.1) state the so called *strong form* of the problem: that is, they formulate it locally in a differential sense.

Numerical methods that operate directly on (3.1) to extract an approximate solution include the finite differences method (FDM) [6, 115, 139], and the family of *collocation methods* [118, 151]. In particular, the latter family of methods is mainly limited to look for a solution over a finite number of points in the domain.

In spite of the availability of strong forms, the greater part of numerical approximation methods for PDEs are set up to operate on what is known as the *weak form* of problem (3.1). To properly define it, we first need to introduce a set of auxiliary *test*, or *weighting functions* $\mathbf{w}$ such that they assume the value of 0 on the boundary region Γ_D of $\mathcal{B}$, where Dirichlet (essential) boundary conditions were imposed in (3.1). The weak formulation of (3.1) can then be stated as

$$\int_{\mathcal{B}} \mathbf{w}\mathcal{A}(\mathbf{u}) \, d\mathcal{B} = \int_{\mathcal{B}} \mathbf{w}\mathbf{f} \, d\mathcal{B} + \int_{\Gamma_N} \mathbf{w}\mathbf{h} \, d\Gamma \tag{3.2}$$

The expression in (3.2) is essentially an average of the strong differential form on the domain $\mathcal{B}$, weighted by the test function $\mathbf{w}$. In other words, the residual of (3.1) $(\mathcal{A}(\mathbf{u}) - \mathbf{f})$ is required in (3.2) to cancel out in a weighted

(by $\boldsymbol{w}$) average sense everywhere on $\boldsymbol{\mathcal{B}}$, and to assume the prescribed value on Γ_N.

As a further requirement to ensure the equivalence of the weak problem (3.2) to the strong one (3.1), special attention has to be given to the way the functional spaces containing functions $\mathbf{u}$ and $\boldsymbol{w}$ are defined. We seek a solution function $\mathbf{u}$ amongst the set of those that satisfy the essential boundary conditions on Γ_D. In addition, both sets of functions $\mathbf{u}$ and $\boldsymbol{w}$ have to be endowed with a certain degree of *regularity* (i. e. continuity and differentiability) across the domain $\boldsymbol{\mathcal{B}}$. However, this regularity should be less strict than that guaranteed by continuously differentiable functional spaces (in this case of order k) $\boldsymbol{\mathcal{C}}^k$. This has to be ascribed to the nature of real world applications that these type of numerical approaches are designed to tackle, which often include discontinuities, in the solutions or in their derivatives, arising inside the domain (e. g. cracks in solid mechanics, or shocks in gas dynamics).

In order to build functions $\mathbf{u}$ and $\boldsymbol{w}$ in possess of the desired regularity, the definition of *square-integrable* functional space is given as

$$L^2(\boldsymbol{\mathcal{B}}) = \left\{ \mathbf{u} \,\middle|\, \int_{\boldsymbol{\mathcal{B}}} |\mathbf{u}|^2 \, d\boldsymbol{\mathcal{B}} < \infty \right\} \tag{3.3}$$

It then makes sense to look for solutions $\mathbf{u}$ of (3.2) with the property of being square-integrable as in (3.3), to the k^{th} maximum order of derivatives present in the differential operator $\boldsymbol{\mathcal{A}}$:

$$\begin{aligned} &H^k(\boldsymbol{\mathcal{B}}) = \\ &= \left\{ \mathbf{u}(x_1, \ldots, x_m) \,\middle|\, \mathbf{u} \in L^2(\boldsymbol{\mathcal{B}}), \, \frac{\partial^N \mathbf{u}}{\partial x_1^{N_1} \ldots \partial x_m^{N_m}} \in L^2(\boldsymbol{\mathcal{B}}), \, \forall |N| \leqslant k \right\} \\ &\text{with } N = N_1 + \cdots + N_m \end{aligned} \tag{3.4}$$

Functional spaces such as those defined in (3.4) are called *Sobolev spaces*; they ensure that the energy integral associated with (3.2) is bounded by a finite constant [44].

The FEM is the most established among the numerical procedures based on a weak formulation (3.2) of the analytical problem at hand. A schematic illustration of the FEM discretisation process is provided in fig. 3.1.

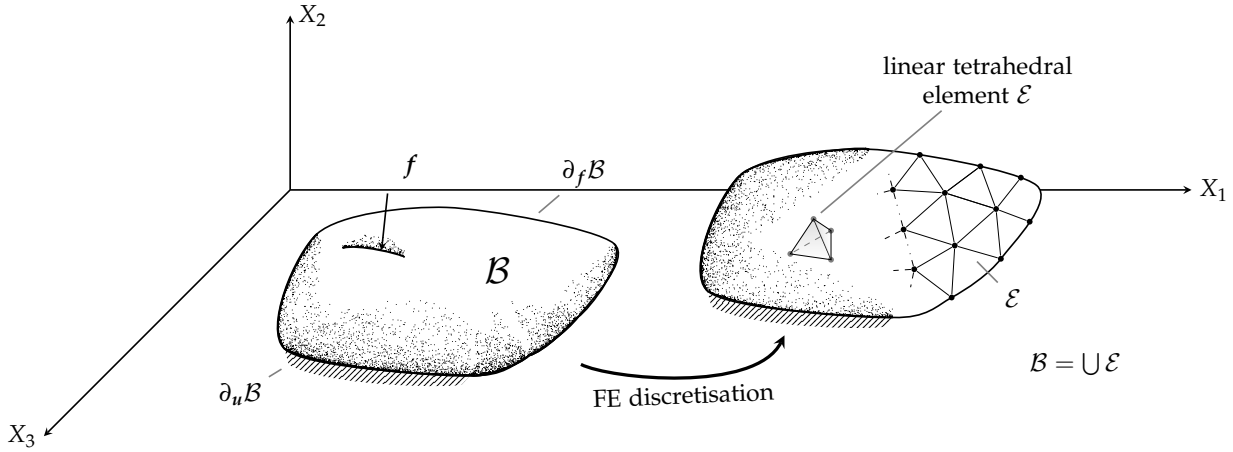

Figure 3.1: discretisation of a continuum medium $\mathcal{B}$ by the FE procedure into a set of linear tetrahedra elements $\mathcal{E}$. Also shown are a generic external force $\mathbf{f}$ and the surface regions where Dirichlet, $\partial_u\mathcal{B}$, and Neumann, $\partial_f\mathcal{B}$ boundary conditions apply.

It is useful to introduce a more compact notation for (3.2), valid in case the differential operator $\mathcal{A}$ applied on $\mathbf{u}$ leads to a bounded, symmetric *bilinear form* $a(\mathbf{u}, \mathbf{w})$:

$$a(\mathbf{u}, \mathbf{w}) \equiv \int_{\mathcal{B}} \mathbf{w}\mathcal{A}(\mathbf{u})\, d\mathcal{B} \leqslant C_1 \|\mathbf{u}\| \|\mathbf{w}\| \qquad C_1 > 0 \tag{3.5a}$$

$$(\mathbf{f}, \mathbf{w}) = \int_{\mathcal{B}} \mathbf{f}\mathbf{w}\, d\mathcal{B} \leqslant C_2 \|\mathbf{f}\| \|\mathbf{w}\| \qquad C_2 > 0 \tag{3.5b}$$

$$(\mathbf{h}, \mathbf{w})|_{\Gamma_N} = \int_{\Gamma_N} \mathbf{h}\mathbf{w}\, d\Gamma \leqslant C_3 \|\mathbf{h}\| \|\mathbf{w}\| \qquad C_3 > 0 \tag{3.5c}$$

In equations (3.5), C_i, $i = 1, 2, 3$ are positive, finite constants, and $\|\cdot\|$ are norms defined in the functional spaces.

The variational statement (3.2) can then be reformulated as

$$a(\mathbf{u}, \mathbf{w}) = (\mathbf{f}, \mathbf{w}) + (\mathbf{h}, \mathbf{w})|_{\Gamma_N} \tag{3.6}$$

Formulation (3.6) is used as a starting point to derive weak form discretisation methods.

3.1.2 *Galerkin approximation*

Now, let trial solution functions be $\mathbf{u} \in \boldsymbol{\mathcal{U}}$, and test functions be $\boldsymbol{v} \in \boldsymbol{\mathcal{V}}$, where $\boldsymbol{\mathcal{U}}$ and $\boldsymbol{\mathcal{V}}$ are two infinite dimensional functional spaces.

The approximation introduced by a *Galerkin method* of solution of (3.6) rests on the relocation of the problem from infinite dimensional functional spaces $\boldsymbol{\mathcal{U}}$ and $\boldsymbol{\mathcal{V}}$ to finite ones, $\boldsymbol{\mathcal{U}}_h \subset \boldsymbol{\mathcal{U}}$ and $\boldsymbol{\mathcal{V}}_h \subset \boldsymbol{\mathcal{V}}$, respectively built upon the finite sets of all linear combinations of *basis* or *shape* functions v_i, $i = 1, \dots, M$ and β_j, $j = 1, \dots, N$. In these bases, trial and test functions are expressed as

$$\mathbf{u}_h = \sum_{i=1}^{M} u_i v_i \tag{3.7a}$$

$$\boldsymbol{v} = \sum_{j=1}^{N} \beta_j \tag{3.7b}$$

The simplest choice of bases is made in the case of the *Bubnov-Galerkin* methods, where the same set is employed for test and trial spaces, $\boldsymbol{\mathcal{U}}_h \equiv \boldsymbol{\mathcal{V}}_h$, so that $M = N$ and $v_i = \beta_i$, $i = 1, \dots, M$.

This allows one to reformulate the variational statement (3.6) as

$$\sum_{i=1}^{M} a(u_i v_i, v_j) = (\mathbf{f}, v_j) + (\mathbf{h}, v_j)|_{\Gamma_N} \qquad j = 1, \dots, M \tag{3.8}$$

where the finite functional spaces are defined by

$$\boldsymbol{\mathcal{U}}_h = \{\mathbf{u}_h \,|\, \mathbf{u}_h \in H^k(\boldsymbol{\mathcal{B}}),\, \mathbf{u}_h|_{\Gamma_D} = \mathbf{u}_0\} \tag{3.9a}$$

$$\boldsymbol{\mathcal{V}}_h = \{\boldsymbol{v}_h \,|\, \boldsymbol{v}_h \in H^k(\boldsymbol{\mathcal{B}}),\, \boldsymbol{v}_h|_{\Gamma_N} = \mathbf{0}\} \tag{3.9b}$$

The Galerkin-approximated version of the weak problem, in equation (3.8), has to satisfy the essential BC in (3.1).

To attain this goal, the shape functions space $\mathcal{U}_h$ should be expanded to accommodate a set of $(R-M)$ additional bases v_r, $r = M, \ldots, R$ that assume value 1 on Γ_D:

$$v_r|_{\Gamma_D} = 1 \qquad r = M, \ldots, R, \quad R > M \tag{3.10}$$

Using (3.10) it is possible to express the BC u_0 in (3.1) in the following manner

$$u_{0h} = \sum_{r=M}^{R} u_0 v_r \tag{3.11}$$

This way, we have updated the set of shape functions v_i at the boundary Γ_D of our domain $\mathcal{B}$ so that

$$v_i|_{\Gamma_D} = \begin{cases} 0 & \text{if } 0 < i \leqslant M \\ 1 & \text{if } M < i \leqslant R \end{cases} \tag{3.12}$$

With the help of (3.11) and (3.12), we can reformulate (3.8) as

$$\sum_{i=1}^{M} a(u_i v_i, v_j) + \sum_{r=M}^{R} a(u_{0h} v_r, v_j) = (f, v_j) + (h, v_j)|_{\Gamma_N} \qquad j = 1, \ldots, M \tag{3.13}$$

Equation (3.13) represents a linear system of algebraic equations, that can be rearranged in a more succinct manner as

$$\sum_{i=1}^{M} K_{ij} u_i = F_j \qquad j = 1, \ldots, M \tag{3.14}$$

where

$$K_{ij} = a(v_i, v_j) \tag{3.15a}$$

$$F_j = (f, v_j) + (h, v_j)|_{\Gamma_N} - \sum_{r=M}^{R} a(u_{0h} v_r, v_j) \tag{3.15b}$$

From (3.15), a global *stiffness matrix* $\mathbf{K}$ can be assembled using submatrices K_{ij}, acting as nodal connectivities. This leads to the classic matrix form for the displacement problem

$$\mathbf{K}\hat{\mathbf{u}} = \mathbf{F} \tag{3.16}$$

In equation (3.16), $\hat{\mathbf{u}} = (u_1, \dots, u_M)^T$ is known as the solution vector, and $\mathbf{F} = (F_1, \dots, F_M)^T$ as the external force vector.

It has long been proven [115, 125] that $\mathbf{K}$ is a symmetric, positive definite – and hence, invertible – matrix. The solution to problem (3.16) can therefore be found as

$$\hat{\mathbf{u}} = \mathbf{K}^{-1}\mathbf{F} \tag{3.17}$$

3.1.3 *The finite element method*

In brief, a FE approach to problem (3.16) would consist in selecting a set of M points $\mathbf{x}_i$, $i = 1, \dots, M$ across the domain $\boldsymbol{\mathcal{B}}$ as *nodes*, determining their interconnectivity by linking them with a *mesh*, in this manner partitioning $\boldsymbol{\mathcal{B}}$ into separate, non-overlapping *elements*. The next, fundamental step would then be to select a family of shape functions v_i, $i = 1, \dots, M$ endowed with the properties listed below:

- Satisfaction of the *Kronecker delta property* at nodes: each shape function v_i is associated with a node $\mathbf{x}_i$ so that its value is exactly 1 on $\mathbf{x}_i$, and 0 at the other nodes locations: $v_i(\mathbf{x}_j) = \delta_{ij}$, $i, j = 1, \dots, M$.
- $v_i \neq 0$ only across the elements sharing $\mathbf{x}_i$ as one of their node.
- The FE solution $\hat{\mathbf{u}}$ should be exact at nodes $\mathbf{x}_i$, i. e. $\hat{u}_i = u(\mathbf{x}_i)$ where $u(\mathbf{x}_i)$ solves (3.1) at $\mathbf{x}_i$.
- Regularity: the shape functions v_i, $i = 1, \dots, M$ should be at least continuous and differentiable to the same order p of the highest derivative appearing in the PDEs: $v_i \in \mathcal{C}^p(\boldsymbol{\mathcal{B}})$. They should also have up to an order $(p-1)$ of regularity on boundaries, $v_i \in \mathcal{C}^{p-1}(\Gamma(\boldsymbol{\mathcal{B}}))$.
- Completeness of representation: the FE solution $\hat{\mathbf{u}}$ should be able to correctly reconstruct polynomials of order p at nodes positions.

Now that the general features of the FEM, and the procedure of interpolation to achieve the solution, have been briefly presented, it is worth to focus on the way stiffness matrix coefficients K_{ij} and force components F_i in (3.15) are calculated. These terms are made of the bilinear forms defined in (3.5), that require integration of the shape functions and their derivatives inside the domain of interest. The evaluation of these integrals is performed numerically, through a weighted sum of the integrand values at particular *integration points* $\mathbf{x}_{int}$ inside the finite element $\mathcal{E}$:

$$\int_{\mathcal{E}} K(\mathbf{x})\, d\mathcal{E} = \int_{\mathcal{E}} \tilde{K}(\mathbf{x})\omega(\mathbf{x})\, d\mathcal{E} \approx \sum_{i=1}^{n_{int}} \tilde{K}(\mathbf{x}_{int})\omega(\mathbf{x}_{int}) \tag{3.18}$$

Equation (3.18) shows that the function $K(\mathbf{x})$ to be integrated can be decomposed as the product of another polynomial function $\tilde{K}(\mathbf{x})$ with a non-negative weight function $\omega(\mathbf{x})$ [90]. In turn, and in addition to the interpolation error introduced by adopting finite basis functions in (3.7), further approximation error is provided in (3.18) by substituting the integral with the weighted sum at a number (n_{int}) of integration points. Many techniques of numerical integration are currently at disposal [105, 214], each differing from the other in terms of the number of integration points, their location inside the element, and the weight they are assigned in the summation. Whilst considering this issue, it is important to strike a balance between accuracy (increasing with the number of integration points considered) and practicality (the fewer the integration points, the less the cost [115]). Families of quadrature rules include the *Newton-Cotes formulas*, and the *Gaussian quadrature rules*. Newton-Cotes formulas use a grid of integration points at fixed distance from each other, and are thus easily scalable. Gaussian quadrature rules instead look to solve an optimization problem, with the aim of placing the integration points in spots where the highest possible degree of accuracy can be reached, all the while using the lowest possible number of points [246].

On the other hand, the methodology of *nodal integration*, devised to minimise computational costs by using nodes as integration points, introduces sizeable inaccuracies that can seriously undermine the robustness of any simulation scheme. This prospective issue will affect the chosen discreti-

sation method, and will be addressed more extensively in the following sections.

3.2 MESHLESS METHODS

3.2.1 *Finite Elements and Meshless Methods*

The FEM, of which a very general sketch was provided in section 3.1, is nowadays the standard method for solving engineering problems. However, as applications of interest become more and more complicated, FEM is beginning to encounter some limitation:

1. Automated quality meshes are not easy to generate, especially for studies involving large deformations. This results in a time consuming process for the analyst, as often automated mesh generators fail to create good meshes on complex geometries. As a consequence, these have to be designed and created manually. It is also essential to consider that a mesh needs to be made up of elements with a degree of smoothness high enough to capture the geometry of the underlying problem with sufficient accuracy.

2. Material discontinuities (such as crack growth and propagation) are difficult to treat if they do not follow nodal connection lines, i. e. the mesh lines, as it is more than often the case. Thus, these types of analyses require frequent remeshing, with associated loss of time and accuracy, in order to realign the mesh on crack lines. Therefore, enhanced FEM techniques have to be introduced.

3. Mesh refinement is in some cases required locally to capture stress and strain states with accuracy. However, reliable *adaptive* mesh generation procedures are very costly in terms of computational time, because they require a mapping of field variables from the old to the new mesh. In addition, remeshing is very challenging in presence of impacts, fragmentations, complex contact geometries, fluid-structure interactions. The process also carries a certain numerical error with it, causing degradation of the quality of the sequential solutions obtained each time a new mesh is generated. In particular, the source of

numerical error lies in just a few distorted elements, created by the otherwise robust adaptive algorithm in situations where, for instance, a local high gradient is present. Loss of accuracy also appears due to the consecutive mapping of state variables to the current mesh.

4. High-order interpolation fields are expensive to construct in FEM, which is at its most practical when employing linear ($\mathcal{C}^0$) shape functions. This limits the ability of the method to solve plates and shells applications, and nonlinear, high-gradient plastic behaviour.

5. For linear finite elements analyses, the stress and strain field outputs are an order of accuracy below those of velocities and displacements.

6. In the presence of complete material disintegration (for instance, in impact or explosion analyses), fragmentation patterns change with the mesh adopted, i. e. different disintegration patterns are observed for different discretisations of the same medium. Furthermore, single elements do not allow for internal breakage, requiring the generation of a more refined mesh through adaptive processes. Strain localisations are also difficult to represent due to this *mesh alignment sensitivity* issue.

7. Mesh compatibility does not enforce continuum compatibility across the physical medium, as can be seen in the case of large deformations and more in general highly nonlinear Lagrangian analyses, where excessive mesh distortion leads to poor and inaccurate solutions.

The root of the problems listed above lies in the very existence of the finite elements, that have to be organised into a mesh. Meshless methods arose with the idea of eliminating elements and meshes altogether. Conveniently, these new meshless methods can bypass most of the limitations of FE listed above, while maintaining conservation of essential parameters in the governing equations.

Compatibility of the interpolation functions across finite elements is ensured by the *mesh*, a topological map connecting them together. Meshfree methods rely on relinquishing the concept of element as the main unit of discretisation, and that of mesh as the main unit of connectivity among nodes; the idea of *domain of influence* of a particle, in the meshless domain, is in itself a way less demanding substitute for the idea of a mesh, while

elements are entirely discarded. Moreover, while in the FEM the problem domain is partitioned into *non-overlapping* finite elements, many meshless techniques allow for overlapping domains of influence.

The advantages in terms of costs and improved quality that meshless methodologies bring along can be summarised as follows:

1. reduced computational and time costs in mesh generation for the analyst, due to absence of a mesh, and due to the availability of automated algorithms for proper distribution of particles over the problem domain.

2. Higher accuracies are easy to achieve, as the implementation of adaptive refinement in meshless methods reduces to merely adding more particles where needed.

3. The ease at which shape functions of polynomial high order (> 1) can be readily built, enables high-gradient analyses.

4. Large deformations and nonlinear problems do not pose difficulties such as single elements excessive distortion in FE, as the connectivity between particles can be rearranged during the simulation.

5. Particle methods are suited, by their very nature, to solve disintegration problems such as fragmentation or explosions.

A further advantage of meshless methods over the FEM lies in the fact that shape functions are built directly on nodes in the domain, without the need of a mesh of elements.

In turn, absence of a mesh then avoids the need for *coordinate mapping* from natural coordinates – where shape functions are defined based on the nature of finite element used – to the inevitably more complex geometry of the domain to be discretised.

3.2.2 *Classes of Meshless Methods*

Meshless or particle techniques can be classified in two groups:

- those following the *direct approach*: employed directly on the strong form of PDEs;

- those following the *indirect approach*: based on the discretisation of the integral form of the governing equations (weak statement of the problem).

The first category resorts to *collocation* techniques: namely, evaluates the unknown function on a cloud of positions across the domain, and then interpolates the unknown function values over the rest of the domain from the values at those collocation points.

Direct approach (strong form) methods are easy to implement, efficient, and truly meshless. But, on the other hand, they tend to suffer from instability and lack of accuracy. Among these methods, SPH is perhaps the most popular; others include the radial basis collocation method, also known as Kansa method [128], the finite point method [203], and the generalised finite difference method [156].

SPH was initially developed as a probabilistic method by Lucy [166] and Gingold and Monaghan [88] to study astrophysics phenomena, through the use of Montecarlo estimations for the volumes to assign to each particle.

Methods based on weak statements of the problem are, on the contrary, very stable and accurate, due to the integral formulation producing a smearing effect on the computational error across the domain. The indirect approach, in fact, shifts the focus from the local to the global behaviour of the PDEs that govern the problem. It presents the relaxed requirement, with respects to the direct approach, of having to be satisfied only in an average sense over the domain of integration. The final equations for indirect formulations are obtained through procedures that look for a stationary, stable state for a functional designed to be a meaningful representation of the problem.

A good example of such functionals can for instance be the total energy of the system. The *minimum potential energy principle* then will search for the configuration that minimises the total energy, out of all the legitimate states of deformation the system can assume at the moment of calculation. Proceeding this way, only first derivatives are required to compute the global energy, while there appear second derivatives in the PDEs governing the displacement-based problem.

Another advantage is that Neumann boundary conditions are naturally satisfied in the weak form, so imposing stresses on the problem boundaries does not end up being an issue.

However, meshless weak form methods are not truly meshfree, since most of them have to resort to some sort of background mesh or set of cells, to perform the integration of system matrices. Meshes have to be created by employing triangulation techniques, using the particles as vertices; in the event refinement is needed, e. g. at areas of stress concentration, the introduction of new particles will require these background cells to be updated. For these methods, interpolation of field variables is still obtained in true meshless form, only using node positions. However, the way numerical integrations are performed make weak form methods computationally expensive, and difficult to implement.

Amongst the meshless weak form methods are the element free Galerkin method (EFGM) [23, 24] and its predecessor, the diffuse element method (DEM) [189], the radial point interpolation method (RPIM) [268], the maximum entropy (Max-Ent) method [7], the hp-cloud method [68], and the meshless local Petrov-Galerkin (MLPG) method [8].

The first two methods mentioned above use MLS approximations [137] in building the shape functions. In particular, the element free Galerkin (EFG) approach has proven itself successful over the years, in terms of range of applications and influence over later meshless techniques.

Derived as a variation from the EFG theme is the RPIM, which uses a blend of radial basis functions and polynomial functions to build an efficient and consistent interpolation [268].

In the Max-Ent method [7, 247], the role of MLS in building the shape functions is assumed by the probability distribution that maximises its associated informational entropy [123], as defined by Shannon [228]. In the context of building a Max-Ent meshless method, the shape functions are adapted to be the probability functions for a node to fall in the domain of influence of another node [247]. Max-Ent shape functions are particularly interesting because of a host of favourable properties: positivity, continuity, the stability-enhancing total variation diminishing (TVD) feature, and, above all, the fact that nodes at the boundary of the computational domain enjoy the Kronecker

delta property, facilitating the imposition of BCs. These properties make the Max-Ent shape functions more attractive than their MLS-built counterparts.

Also of interest is the hp-cloud method [68], which calculates its shape functions with a procedure directly based on the partition of unity concept.

The MLPG method [8] aims to avoid global integration by focussing on local weak statements. It is peculiar in that a *Petrov-Galerkin* procedure is used, in which trial and test functions are computed on different solution spaces, with the latter, as a result, not required to vanish at the boundaries of the domain. In contrast, the more conventional (Bubnov-)Galerkin methods employ trial and test functions belonging to the same solution space.

For each of the aforementioned meshless methods based on a weak statement of the problem, meshes of cells for integration purposes are easily created by triangulation techniques, using the particles as vertices. In the event that refinement be needed (e. g. at areas of stress concentration), new nodes are added and the background cells have to be updated by recalculating new triangulations.

3.2.3 *Properties of Meshless Methods*

The *support domain* of a point $\mathbf{x}$ is a region in the domain centred on $\mathbf{x}$ and bounded by a support radius $\mathbf{r}$. Particles that lie inside the support domain give a weighted contribution to the interpolation of some field variable $\mathbf{f}(\mathbf{x})$ in $\mathbf{x}$. The weight is determined by the particular shape function that the selected meshless method employs.

An interesting concept is also that of *domain of influence* of a particle $\mathbf{x}_a$, defined as the union of support domains that include $\mathbf{x}_a$, or, in other words, the region where the contribution of $\mathbf{x}_a$ to the determination of field variables is not zero.

The main principle underlying meshless techniques is the *partition of unity* [11], that, for a set of regular functions $W_i \in \mathcal{C}^n(\mathbb{R}^3)$, $i = 1, \ldots, n$, over a domain Ω, can be defined as follows:

$$\sum_{i=1}^{n} W_i(\mathbf{x}) = 1 \quad \forall W_i(\mathbf{x}) \mid 0 \leqslant W_i(\mathbf{x}) \leqslant 1, \quad \forall \mathbf{x} \in \Omega, \, i = 1, \ldots, n \tag{3.19}$$

Functions W_i, $i = 1, \dots, n$ in (3.19) are each defined locally over a support domain $\Omega_i \subset \Omega$ centred around a node $\mathbf{x}_i$, $i = 1, \dots, n$. Support domains Ω_i are an *overlapping covering* of Ω, in the sense that:

$$\bigcup_{i=1}^{n} \Omega_i \supset \Omega\,, \qquad i = 1, \dots, n \tag{3.20}$$

Property (3.20) is clearly a distinctive feature with respect to the strict non-overlapping definition of finite elements.

Implementation of meshless methods usually follows the ensuing sequence of steps:

1. *Geometry creation*: a set of nodes with the opportune spatial density and distribution is created in the domain of interest, trying to strike a balance between the pattern of gradients expected in the solution, and the accuracy requirements.

2. *Field function interpolation (approximation)*: build the interpolated field variable $\mathbf{u}^h$ as a linear combination of shape functions $N_b(\mathbf{x}_a)$ on neighbouring nodes $b = 1, \dots, n$ with unknown coefficients u_b at point of interest $\mathbf{x}_a$:

$$\mathbf{u}(\mathbf{x}_a) \approx \mathbf{u}^h(\mathbf{x}_a) = \sum_{b=1}^{n} N_b(\mathbf{x}_a) u_b \tag{3.21}$$

3. *Governing system discretisation*: either strong approximation of the differential form of the PDE at the field node (problems with imposing Dirichlet BCs), or weak approach through numerical integration of the weak forms of the PDEs and BCs, yielding a sort of average value over each cell. Additional costs come with the weak approach since a grid of background cells is needed, but, on the plus side, it improves the stability of the algorithm, and BCs are easier to implement.

4. *Solving the system of discretised equations*: in dynamics, time integration schemes are employed that are essentially based on a FD reduction, of either explicit or implicit nature, of the ordinary differential equation (ODE) yielded by spatial discretisation of the original PDE.

Meshless shape functions N_i, $i = 1, \ldots, n$ should satisfy (3.19), and corrective mechanisms should be put in place in case such condition cannot be guaranteed. Other than that, the way each method builds its shape functions is what more starkly distinguishes it from the next one.

Properties such as *consistency*, *stability*, *compatibility*, *Kronecker delta p.*, *compact support p.* should drive the development process of shape functions.

- CONSISTENCY: a meshless interpolation (3.21) that is able to exactly *reproduce* polynomial functions of order k, can then be called k^{th} order consistent. For instance, if we aim at 1^{st} order consistency, the approximation should satisfy the requirement:

$$\sum_{i=1}^{n} N_i(\boldsymbol{x})\boldsymbol{x}_i = \boldsymbol{x} \tag{3.22}$$

  Condition (3.22) should be valid everywhere across domain Ω.

  Consistency is a prerequisite for the convergence of the numerical scheme to the exact solution, when the distance between particles is progressively reduced, $h \to 0$. In particular, we observe that Galerkin weak forms of PDEs with order of differentiation $2k$, require an interpolation scheme up to order k of consistency, as necessary condition for convergence.

- STABILITY: the particle distribution in the domain Ω, however irregular, should be such that at any position $\boldsymbol{x} \in \Omega$ there is always a sufficient number of particles as needed in order to form a shape function support.

- COMPATIBILITY: in weak formulations, the interpolated function has to be continuous all across the overlapping support domains on Ω.

- KRONECKER DELTA PROPERTY: satisfaction of the Kronecker delta property, which is helpful to impose essential (Dirichlet) BCs:

$$N_i(\boldsymbol{x}_j) = \delta_{ij} = \begin{cases} 1, & i = j \\ 0, & i \neq j, \end{cases} \qquad i, j = 1, \ldots, n \tag{3.23}$$

An *interpolant operator* $\mathcal{I}[\cdot]$, when applied to a function $f(x)$, gives

$$\mathcal{I}[f(x)] = \sum_{i=1}^{N} W_i(x) f(x_i) \mid \mathcal{I}[f(x_i)] = f(x_i) \qquad i = 1, \dots, N \tag{3.24}$$

The interpolant as defined in (3.24) can only be built from shape functions N_i, $i = 1, \dots, N$ that satisfy the Kronecker delta property. When this is not true, an additional *approximation* error is added to the solution.

- COMPACT SUPPORT: the shape functions supports should remain reasonably small in size in order to include only the number of nodes strictly necessary for a correct local interpolation. This property is useful to obtain discretised equations that are as decoupled as possible from each other (i. e. a sparse system matrix).

3.3 SMOOTH PARTICLE HYDRODYNAMICS

3.3.1 *Generalities*

Lucy [166], Gingold and Monaghan [88] came up simultaneously (in the same year) with the concept of SPH, for the purpose simulating astrophysical phenomena such as the formation of stars and galaxies. Instead of breaking down a continuum into a discrete set of points, as it is mostly the case for numerical methods used in mechanics, SPH was used in astrophysics as a mean to blend a system made of many, discrete pieces of matter into a continuum field, that could as a consequence be governed by PDEs. In order to achieve this, they ([166] and [88]) employed an interpolating *kernel function* capable of determining the local value of the field $f(x)$ at a position x, based on the surrounding particles B at positions x_B, representing scattered matter.

The closer a particle B is to x ($\|x - x_B\| \to 0$), the greater the weight that the interpolation process assigns to B for the evaluation of $f(x)$.

Therefore, in astrophysics the kernel function characterises a position x with the *probability* of finding a particle B there, or, in other words, that

$\mathbf{x} = \mathbf{x}_B$. It is in this context that SPH can be seen as a probabilistic method based on Montecarlo estimations [177].

Soon was the potential of the method discovered for fluid dynamics [176] and continuum mechanics applications [154], but this time playing the reverse role than that in astrophysics: the role of an innovative discretisation technique for the analysis of continuum media. This was the first completely meshless method to appear in literature.

3.3.2 *In the continuum: reproducing kernel approximation*

A square integrable function $\mathbf{f}(\mathbf{x}) \in L^2(\mathbb{R})$ can always be representable using the *Dirac delta* generalised function $\delta(\mathbf{x})$ as

$$\mathbf{f}(\mathbf{x}) = \int_{-\infty}^{+\infty} \mathbf{f}(\mathbf{y})\, \delta(\mathbf{x}-\mathbf{y})\, d\mathbf{y} \tag{3.25}$$

In (3.25), $\delta(\mathbf{x}-\mathbf{y})$ denotes the Dirac delta function, commonly defined as

$$\delta(\mathbf{x}, \epsilon) = \lim_{\epsilon \to 0} \begin{cases} 0 & \text{if} \quad \|\mathbf{x}\| < -\frac{\epsilon}{2} \\ \frac{1}{\epsilon} & \text{if} \quad -\frac{\epsilon}{2} < \|\mathbf{x}\| < \frac{\epsilon}{2} \\ 0 & \text{if} \quad \|\mathbf{x}\| > \frac{\epsilon}{2} \end{cases} \tag{3.26}$$

The reproducing kernel approximation procedure employed in SPH aims to approximate the integral version of $\mathbf{f}(\mathbf{x})$ expressed in (3.25), defined over a finite domain Ω, by substituting the Dirac delta function with a weighting function over a support domain known as window [153] or *kernel* function $W(\mathbf{x}-\mathbf{x}', h)$ centred at location $\mathbf{x}$, and averaging contributions from all particles at locations $\mathbf{x}'$ found inside the (usually compact) support of $W(\mathbf{x}-\mathbf{x}', h)$, with the radius depending on the *smoothing length* h.

$$\langle \mathbf{f}(\mathbf{x}) \rangle = \int_{\Omega} \mathbf{f}(\mathbf{x}')\, W(\mathbf{x}-\mathbf{x}', h)\, d\mathbf{x}' \tag{3.27}$$

The Dirac delta function (3.26) does indeed possess some interesting properties, one akin to the partition of unity:

$$\int_{-\infty}^{+\infty} \delta(\mathbf{x})\, d\mathbf{x} = 1 \tag{3.28}$$

and another resembling the Kronecker delta property (which, in effect, constitutes its discrete analogue [3]):

$$\int_{-\infty}^{+\infty} \delta(\mathbf{y}-\mathbf{x})\, \mathbf{f}(\mathbf{y})\, d\mathbf{y} = \mathbf{f}(\mathbf{x}) \tag{3.29}$$

However, (3.25) cannot be used to interpolate the field of $\mathbf{f}(\mathbf{x})$ because of its lack of regularity, namely, continuity and differentiability.

The kernel function $W(\mathbf{x}, h)$ in (3.27) can be easily constructed to achieve a high order of regularity k,

$$W(\mathbf{x}, h) \in \mathcal{C}^k\left(\mathbb{R}^d\right) \qquad k \geqslant 1 \tag{3.30}$$

In (3.30), d is the dimensionality of the problem.

It may be speculated that the smoothness property (3.30) of the kernel functions $W(\mathbf{x}, h)$ is the reason why the "smooth particle hydrodynamics" method was called as such. Alternatively, the "smooth" denomination may be due to the averaging effect exercised by the kernel function on the field interpolation across the neighbouring particles, seen as collocation points over the local support [158].

The majority of SPH kernel functions are defined over a compact support which enhances the local character of the interpolation and is also computationally more efficient. A kernel function $W(\mathbf{x}, h)$ centred at position $\mathbf{x}_a$ is provided with a compact support $\Omega_{\mathbf{x}_a}$ if the following property is verified:

$$W(\mathbf{x}-\mathbf{x}_a, h) = 0 \qquad \forall \mathbf{x} \notin \Omega_{\mathbf{x}_a} \tag{3.31}$$

Upholding (3.31), the interpolation of a field variable at $\mathbf{x}_a$ will depend only on neighbouring particles, enhancing its local character, and thus improving its accuracy.

As the smoothing length $h \to 0$, the kernel function behaviour should be as close as possible to that of a Dirac delta function (3.28):

$$\lim_{h\to 0} W(\mathbf{x}-\mathbf{x}_a, h) = \delta(\mathbf{x}_a) \qquad \forall \mathbf{x} \in \Omega \tag{3.32}$$

As a consequence of (3.32), in case (3.28) holds then (3.27) will be equivalent to (3.25) for $h \to 0$.

Other than properties (3.28) and (3.31), SPH kernel functions $W(\mathbf{x}, h)$ should also:

- be *positive*, in order to be numerically stable [158]

$$W(\mathbf{x}-\mathbf{x}_a, h) > 0 \qquad \forall \mathbf{x} \in \Omega_{\bar{\mathbf{x}}} \tag{3.33}$$

- be *monotonically decreasing* as the particles distance $\|\mathbf{x}-\mathbf{x}_a\|$ increases

$$\frac{\partial^2 W(\mathbf{r}, h)}{\partial \mathbf{r}^2} < 0 \qquad \mathbf{r} = \|\mathbf{x}-\mathbf{x}_a\| \tag{3.34}$$

- be $\mathcal{C}^1$-*consistent*, in order to at least be able to reproduce linear fields.

  $\mathcal{C}^1$-consistency implies $\mathcal{C}^0$-consistency, or the ability to correctly replicate constants. The requirements that a SPH kernel function has to satisfy in order to meet the consistency conditions are

$$\int_{\Omega_{\mathbf{x}_a}} W(\mathbf{x}-\mathbf{x}_a, h)\, d\mathbf{x} = 1 \tag{3.35a}$$

$$\int_{\Omega_{\mathbf{x}_a}} \mathbf{x} W(\mathbf{x}-\mathbf{x}_a, h)\, d\mathbf{x} = \mathbf{x} \tag{3.35b}$$

  It is interesting to note that condition (3.35a) also imposes the normalisation of kernel function $W(\mathbf{x}, h)$, while (3.35b) is satisfied by kernels that are symmetric around the origin [158].

  Symmetric kernels are built so by construction, and thus (3.35b) is easily met inside the domain. Problems originate for particles at or

near the boundaries, where the particles support domains get cut off, and the kernel functions that rest upon them end up incomplete, thus failing to satisfy both conditions (3.35). This is shown graphically in fig. 3.2.

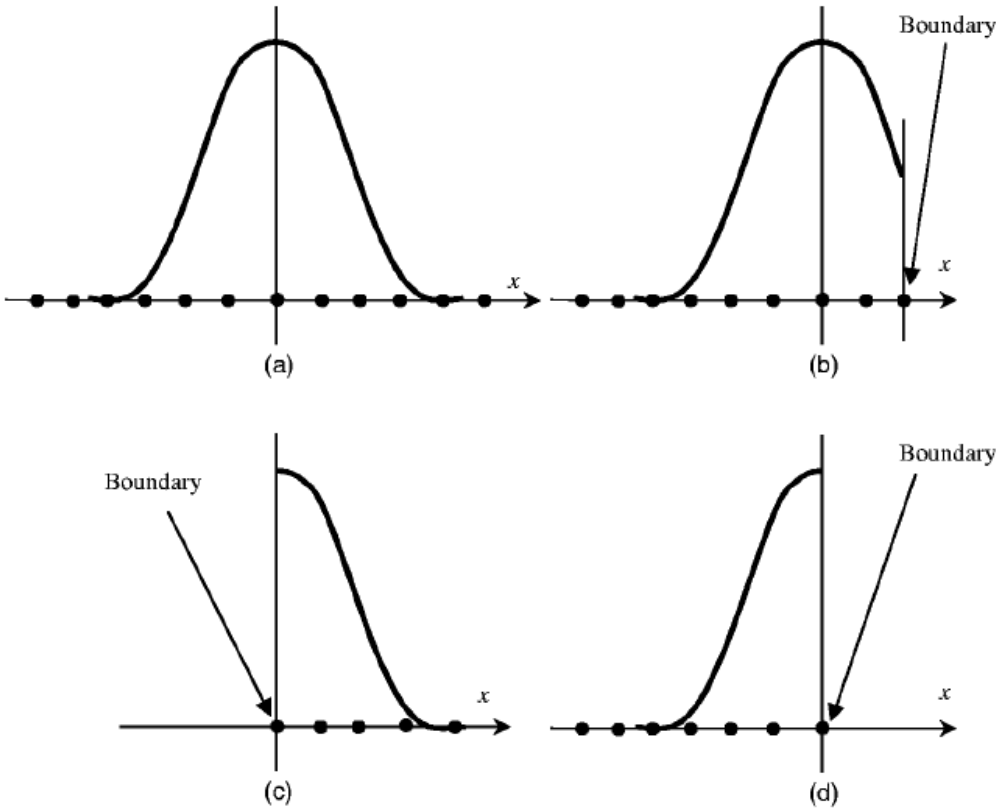

Figure 3.2: one-dimensional representation of a bell-shaped SPH kernel: the compact kernel support is complete in the interior of the domain, leading to symmetric kernel functions (a); however, the presence of the boundary truncates part of the support for target particles located in the proximity (b) or directly on the boundary (c, d), leading to incomplete supports, unsymmetrical kernel functions and inconsistent interpolations. (Source: [158])

Ad-hoc correction procedures have to be implemented for regions at or near boundaries, in order to offset the lack of symmetry of local kernels.

3.3.3 *Discrete kernel evaluation*

Kernel properties (3.33)-(3.35) refer to integral formulations of the reproducing kernel approximation. In order to implement the SPH discretisation of the governing PDEs, it is required to reduce integrals across the domain to sums over the particles contained therein. In practice, this entails transforming (3.27) into

$$\mathbf{f}_h(\mathbf{x}) = \sum_{b=1}^{n} V_b \mathbf{f}(\mathbf{x}_b)\, W(\mathbf{x}-\mathbf{x}_b, h) \tag{3.36}$$

In (3.36), n is the total number of particles discretising problem domain Ω, while V_b is the volume attributed to each particle, at position $\mathbf{x}_b$. To emphasise the dependence on the smoothing length h, the radius of influence of the chosen position x, the approximated field variable $\mathbf{f}$ is denoted by $\mathbf{f}_h$. In fact, the smoothing length h is an important parameter as it determines the number of particles that are used in the computation (3.36) at each position, that in turn governs the accuracy of the numerical scheme.

To further underline the importance of this dependence from h, Monaghan in [179] recommends to consider Gaussian kernel functions as the most faithful to the original continuous form of the PDEs. As it will be described in subsequent sections, the Gaussian kernel is not compactly supported, meaning that every particle in the domain enters (3.36) for any position, although the weight assigned to each particle drops significantly with the distance from the target point.

Using the notion of shape function as defined in (3.7a), (3.36) can be rewritten as

$$\mathbf{f}_h(\mathbf{x}) = \sum_{b=1}^{n} \mathbf{f}(\mathbf{x}_b)\, v_b(\mathbf{x}) \tag{3.37}$$

By comparing (3.37) with (3.36), SPH shape functions $v_b(\mathbf{x})$ are defined as

$$v_b(\mathbf{x}) = V_b W(\mathbf{x}-\mathbf{x}_b, h) \qquad b = 1,\dots,n \tag{3.38}$$

As SPH shape functions $v_b(\mathbf{x})$ in (3.38) depend on kernel function $W(\mathbf{x}-\mathbf{x}_b, h)$, they differ from their finite elements equivalents in that:

- SPH shape functions do not satisfy the Kronecker delta property (3.23), $\mathbf{f}_h(\mathbf{x}_a) \neq \mathbf{f}(\mathbf{x}_a)$. Therefore, they cannot be defined as interpolants, but are instead only approximants for a given function at a position $\mathbf{x}_a$.

- The discrete form of consistency conditions (3.35) has to be imposed directly on the kernels, in order to ensure the reproducibility of at least first order polynomial functions:

$$\sum_{b=1}^{n} V_b W(\mathbf{x}-\mathbf{x}_b, h) = 1 \tag{3.39a}$$

$$\sum_{b=1}^{n} (\mathbf{x}-\mathbf{x}_b) V_b W(\mathbf{x}-\mathbf{x}_b, h) = 0 \tag{3.39b}$$

3.3.4 *Numerical errors*

The SPH method introduces three types of numerical errors when it is used to solve a differential equation in discrete terms:

1. The *smoothing error* that originates from adopting an integral representation (3.27) which uses kernel functions that do not select the target position $\mathbf{x}$, filtering out values at other positions as Dirac delta functions (3.25) would do, but act by distributing the local field value $\mathbf{f}(\mathbf{x})$ over a neighbourhood of $\mathbf{x}$.

$$\begin{aligned} \epsilon_S &= \|\mathbf{f}(\mathbf{x}) - \langle \mathbf{f}(\mathbf{x}) \rangle\| = \\ &= \|\mathbf{f}(\mathbf{x}) - \int_\Omega \mathbf{f}(\mathbf{x}')\ W(\mathbf{x}-\mathbf{x}', h)\ d\mathbf{x}'\| \end{aligned} \tag{3.40}$$

Taylor series expansion of $\langle \mathbf{f}(\mathbf{x}) \rangle$ would yield

$$\begin{aligned}\langle \mathbf{f}(\mathbf{x}) \rangle = \mathbf{f}(\mathbf{x}) \int_\Omega W(\mathbf{x}-\mathbf{x}')\,d\mathbf{x}' + \\ - \frac{d\mathbf{f}(\mathbf{x})}{d\mathbf{x}} \int_\Omega (\mathbf{x}-\mathbf{x}') W(\mathbf{x}-\mathbf{x}')\,d\mathbf{x}' + \\ + \frac{1}{2}\frac{d^2\mathbf{f}(\mathbf{x})}{d\mathbf{x}^2} \int_\Omega (\mathbf{x}-\mathbf{x}')^2 W(\mathbf{x}-\mathbf{x}')\,d\mathbf{x}' + \dots \\ \dots + \frac{1}{k!}\frac{d^k\mathbf{f}(\mathbf{x})}{d\mathbf{x}^k} \int_\Omega (\mathbf{x}-\mathbf{x}')^k W(\mathbf{x}-\mathbf{x}')\,d\mathbf{x}' \end{aligned} \tag{3.41}$$

Considering consistency conditions (3.35) to be holding, substituting $\langle \mathbf{f}(\mathbf{x}) \rangle$ from (3.41) in (3.40) leads to [18]

$$\epsilon_S \propto \frac{1}{2}\frac{d^2\mathbf{f}(\mathbf{x})}{d\mathbf{x}^2} h^2 + \mathcal{O}\left(h^3\right) \tag{3.42}$$

In going from (3.40) to (3.42), distance $\mathbf{x}-\mathbf{x}'$ is assumed to be a multiple of the smoothing length h.

In case we were to impose consistency conditions similar to (3.35b), but of higher polynomial order, i. e. of the type

$$\int_\Omega (\mathbf{x}-\mathbf{x}')^j W(\mathbf{x}-\mathbf{x}', h)\, d\mathbf{x}' = 0 \qquad 0 < j \leqslant k \tag{3.43}$$

then (3.42) would become

$$\epsilon_S \propto \frac{1}{(k+1)!}\frac{d^{(k+1)}\mathbf{f}(\mathbf{x})}{d\mathbf{x}^{(k+1)}} + \mathcal{O}\left(h^{k+2}\right) \tag{3.44}$$

Other than the imposed order of consistency, smoothing error ϵ_S in (3.40) also depends on the choice of kernel function $W(\mathbf{x}, h)$ [153].

2. A *truncation error* that arises from the finite approximation (3.36) of integral form (3.27).

$$\epsilon_T = \| \langle \mathbf{f}(\mathbf{x}) \rangle - \mathbf{f}_h(\mathbf{x}) \| = \\ = \| \int_\Omega \mathbf{f}(\mathbf{x}') \; W(\mathbf{x} - \mathbf{x}', h) \; d\mathbf{x}' - \sum_{b=1}^{n} V_b \mathbf{f}(\mathbf{x}_b) \; W(\mathbf{x} - \mathbf{x}_b, h) \| \tag{3.45}$$

   The truncation error ϵ_T in (3.45) mainly depends on the number of particles used for the discrete representation [162].

3. A further source of error is the *nodal integration* scheme that is inherent to the particle approximation and to the overlapping support domain structure of SPH. Direct integration of the field variable at the nodes, on the one hand has the advantage of avoiding the deployment of an auxiliary mesh of Gauss quadrature points, rendering SPH a truly meshless method and facilitating large deformation analyses [208], but on the other hand it inevitably suffers from cost of numerical instabilities (pressure oscillations, tensile instabilities, locking scenarios) caused by rank deficiency in the stiffness matrix, see fig. 3.3 [35, 115]. In essence, the nodal integration error is conceptually very close in meaning to the truncation error discussed above, and depends on the way in which particles are distributed across the domain [65].

   There is a correlation between the stability of a numerical method, and the conservation properties of the system it is set to discretise: at each point in the domain, the relevant properties – that, for a purely mechanical system, amount to mass, linear and angular momenta, and energy – shall remain conserved [52].

   SPH, along with other strong form collocation particle methods, satisfies conservation requirements globally, as a sum on the whole domain, but not locally [53]. This statement is shown valid for the discrete angular momentum in [36], which does not get preserved in the course of a simulation, and thus special techniques have to be used to modify the kernels, with the aim of satisfying the local conservation prerequisite. These modifications, in turn, have an effect on other conserved

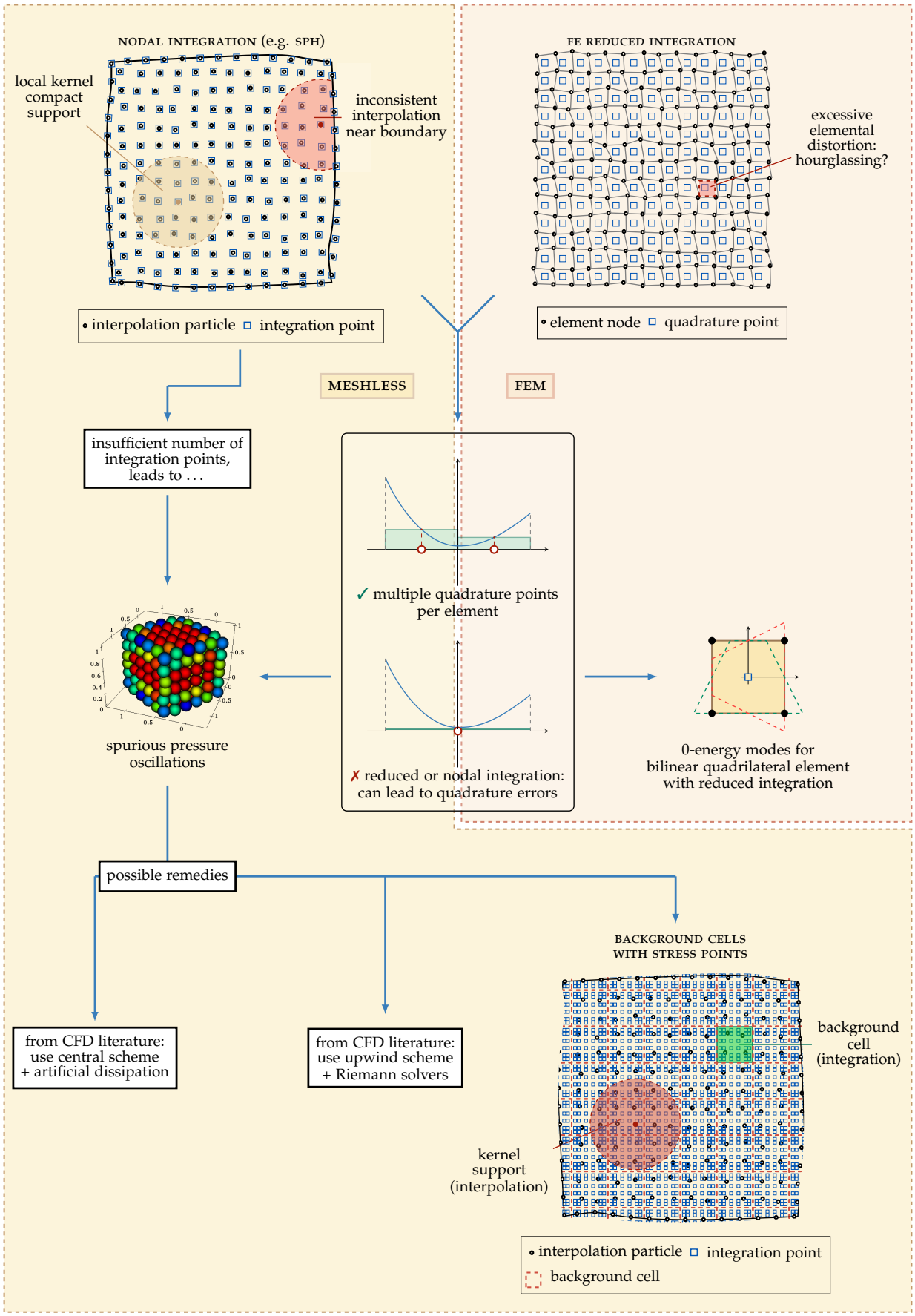

Figure 3.3: nodal integration creates rank deficiency in the system matrix, as the number of quadrature points is insufficient for a correct numerical integration. Spurious modes are generated, critically affecting the accuracy of the simulation. A similar problem faced in FEM is that of hourglassing instabilities caused by reduced integration. The figure also shows possible remedies to the problem.

properties, that as a consequence are left themselves in need to be corrected. This entire chain of modifications, and their consequences will be made clearer in subsequent sections.

3.3.5 *Artificial viscosity*

As stated above, the numerical error induced by the SPH nodal integration gives raise to spurious oscillations of pressure and velocity in the solution, depending on the type of physical problem and unknown variables [153].

Spurious oscillations could also be caused by discontinuities in the field variable (the so-called shocks in fluid dynamics [107, 139], and high-strain solid dynamics [104, 155]).

In the context of the FDM, the most expedient numerical device envisaged to alleviate these instabilities was found to be the introduction of an *artificial viscosity* term to the momentum equations, which is specifically designed to smooth out the spurious oscillations from the solution. This has been especially well-developed in the field of CFD [139], and is generally expressed in the case of the linear momentum equation (in spatial configuration) as

$$\rho\dot{v} = \nabla \cdot (\boldsymbol{\sigma} + \boldsymbol{\sigma}_v) \tag{3.46}$$

In (3.46), $\boldsymbol{\sigma}$ is the Cauchy stress tensor, and $\boldsymbol{\sigma}_v$ is the artificial viscous stress term, which in general will indirectly depend on the velocity.

SPH bears resemblance, in its basis concept, to FD, being a collocation, nodally integrated algorithm. Hence, it was found that adding an artificial viscous pressure to SPH-discretised field equations could be an effective means to get rid of unwanted oscillations.

Monaghan and Gingold [182] found that the most common models of artificial viscosity used in FDM – *von Neumann-Richtmyer viscosity*, proportional to the square of the velocity gradient [267], and *artificial bulk viscosity*, directly proportional to the velocity gradient ([170], [197]) – cannot be successfully adapted to SPH. This is mainly due to the dependence of artificial viscous terms on smoothing length h as reference length, which is too small to

account for discontinuities of particles motions that take place at a larger scale [182].

In order to address this issue, the following viscous term was proposed by Monaghan in [182]:

$$\begin{aligned}\boldsymbol{\sigma}_\nu &= \Pi_{ij}\, \boldsymbol{e}_i \otimes \boldsymbol{e}_j = \\ &= \begin{cases} -\frac{1}{\rho}\left[\alpha c_{ij} \frac{h v_{ij}\cdot \mathbf{r}_{ij}}{\mathbf{r}_{ij}^2+\eta^2} + \beta\left(\frac{h v_{ij}\cdot \mathbf{r}_{ij}}{\mathbf{r}_{ij}^2+\eta^2}\right)^2\right](\boldsymbol{e}_i \otimes \boldsymbol{e}_j) & \text{if } v_{ij}\cdot \mathbf{r}_{ij} < 0 \\ 0 & \text{if } v_{ij}\cdot \mathbf{r}_{ij} \geqslant 0 \end{cases}\end{aligned} \tag{3.47}$$

In (3.47), c_{ij} is the mean speed of sound, and $\mathbf{r}_{ij} = \|\mathbf{x}_i - \mathbf{x}_j\|$ the distance, between particles at positions $\mathbf{x}_i$ and $\mathbf{x}_j$; α, β are appropriately chosen constants coefficients that regulate the damping intensity of the viscous stress (usually β is chosen as $\beta = 2\alpha$, with $0.5 \leqslant \alpha \leqslant 1$), while η is a small valued parameter introduced to avoid invalid results when particles i and j are very close to each other. The product $v_{ij}\cdot \mathbf{r}_{ij}$ can be shown to be equivalent, in the case of a SPH discretisation using a Gaussian kernel [153, 182], to $\nabla \cdot v$, measure of volumetric compression or dilatation. This establishes a direct correlation between the artificial viscous term Π_{ij} in (3.47) and the divergence of the velocity. Density ρ is assumed to be constant for all particles.

The Monaghan artificial viscosity term Π_{ij} in (3.47) contains a term linearly dependent from the product $v_{ij}\cdot \mathbf{r}_{ij}$, as in the bulk viscosity, and a term with a quadratic dependence from the same product, as in the von Neumann-Richtmyer viscosity model. The presence of $\mathbf{r}_{ij}$ in (3.47) ensures that the viscous parameter modifies the equations at the appropriate length scale at which shocks can be simulated as discontinuous particles behaviour.

The viscous term defined in (3.47) is able to treat the discontinuities that may arise in the solution of hyperbolic systems of PDEs, as those governing CFD problems. However, there are some drawbacks associated with the adoption of this type of artificial viscosity, namely:

- artificial viscosity $\boldsymbol{\sigma}_\nu$ may inadvertently affect the solution of the original PDEs;

- inability to gauge and control the deterioration of accuracy. Such deterioration stems out of the error introduced by the addition of a non-physical term to the governing equations.

These points will be addressed in later sections, where an alternative numerical dissipation scheme, well known in the field of CFD, will be introduced for applications in the context of mixed formulation solid dynamics.

3.3.6 *Enforcement of boundary conditions*

As noted earlier, the enforcement of essential (Dirichlet) BCs is problematic for a strong form, collocation type method such as SPH. This is due to the fact that the kernel interpolant is intrinsically non-local (namely, in order to define it, information needs to be gathered not just at the target position, but also from surrounding particles) and therefore, most importantly, it does not satisfy the Kronecker delta property. Moreover, the presence of boundaries divides kernel compact supports in regions inside and outside the computational domain: as a result, the SPH interpolation functions lose their properties of unity (3.19) and consistency (3.39).

In literature, this shortcoming is addressed through a variety of approaches.

In the context of fluid dynamics, Monaghan in [179] proposed to add a layer of particles on the boundary, capable of preventing other particles located inside the domain from crossing it. This is achieved by the introduction of boundary fictitious forces (e. g. Lennard-Jones inter-particle forces) acting in the opposite direction.

Alternatively, in [59], a set of *mirror particles*, arranged in a specular manner with respect to the domain particles at or near boundaries, are placed on the other side of walls, or fixed constraints. These mirror particles do not enter calculations in any way other than exerting a velocity that is equal and opposite in direction to that of the inner particles they mirror. In this manner, the velocities of particles at the boundary are enforced to reduce to zero, as these particles are specifically conceived to have an equal number of real and mirror neighbours.

As just seen for the mirror particles method, the *ghost particle approach* [211, 251] populates the space outside the boundary of the domain with dummy particles, but improves on the former technique by eliminating the requirement that dummy particles should mirror the inner particles arrangement.

The topic of lack of consistency at and near boundaries in SPH is not exhausted by the remedies briefly mentioned above. All these methods have a common feature in that they act on the problem configuration, adding dummy particles or ad-hoc forces, but they do not amend the original form of the SPH kernel function. The issue of lack of consistency however can also be addressed by modifying the kernel interpolant, in order to ensure that the particle interpolation complies with partition of unity (3.19), and with consistency and completeness conditions (3.39). The modifications should be done in such a way as to be activated only on the boundary region, or, more specifically, in regions of the problem domain where SPH cannot even provide correct representation of rigid body motions [21, 163].

In the next section, a different type of SPH kernel correction will be introduced, with the aim of improving consistency at and near boundaries. This novel methodology has the advantage of being far less computationally expensive than RKPM, another particle method described in appendix A.1, at the expense, however, of achieving a smaller order of polynomial reproduction.

3.4 CORRECTED SMOOTH PARTICLE HYDRODYNAMICS

3.4.1 *Types of Kernel functions*

Generally speaking, the function chosen as kernel should be sufficiently smooth, and as both the smoothing length $h \to 0$ and the inter-particles distance $\Delta \mathbf{x} \to 0$, the discrete solution should converge to the analytical solution (i. e. $\mathbf{f}_h(\mathbf{x}) \to \mathbf{f}(\mathbf{x})$), no matter the choice of kernel function [81]. However, an SPH simulation will always employ a finite number of particles, so the limits $h \to 0$ and $\Delta \mathbf{x} \to 0$ will never be realised in practice, and the type of kernel function chosen will influence the smoothing error ϵ_S in (3.40).

Different classes of functions have been employed as kernels in SPH literature. An early survey of these (in one-dimensional examples) was made by Fulk et al. [81], who distinguished four main types: the *bell-shaped* kernels, that resemble statistical normal distributions around a mean; *hyperbolic*-type kernels, shaped as negative exponentials; the *parabolic*-type kernels, shaped as convex parabolas; and the *double hump* type of kernels, derived from bell-shaped curves, and modified in order to have a minimum at the centre and two maxima symmetrically placed left and right of the centre. See fig. 3.4 for a visual representation of these four main groups of SPH kernel functions.

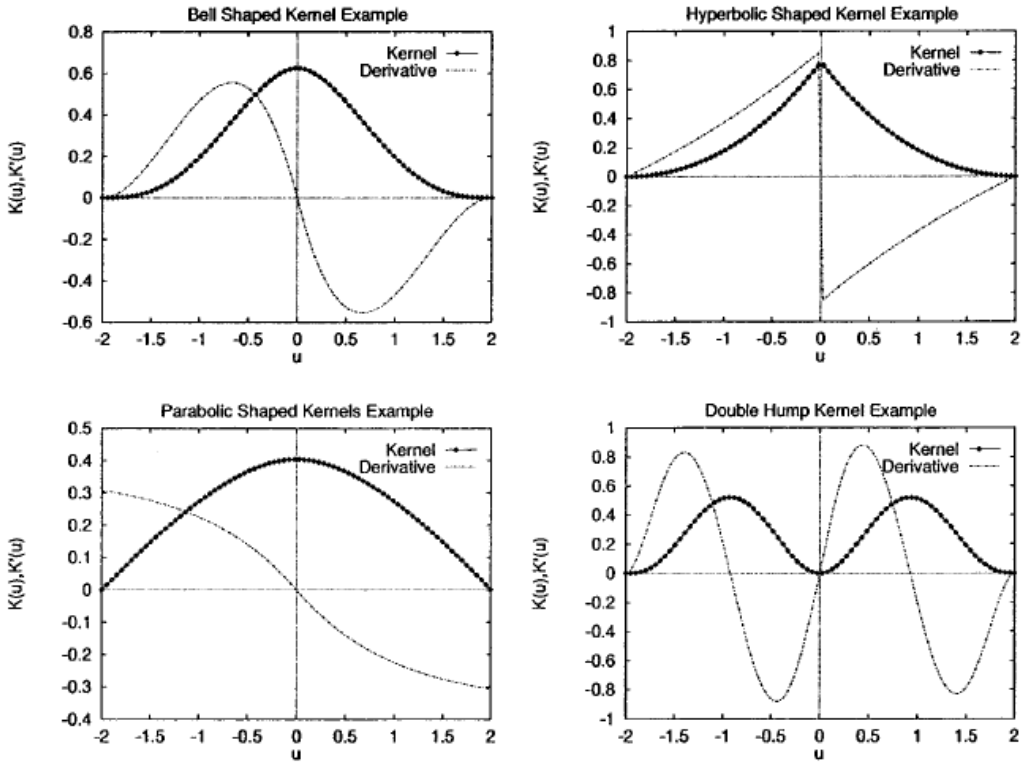

Figure 3.4: four main types of SPH kernel functions as described in [81]. K and K′ as listed in the y-axis represent the kernel function and its derivative with respect to space, respectively. The x-axis has the target particle lying at the 0 point, with u measuring the distance from it. (Source: [81])

It was concluded in [81] that, out of all the kernel types considered, the bell-shaped functions provide the best SPH approximation of a continuous function.

The bell-shaped kernel functions can, in turn, be classified into a kernel with compact or non-compact support. In the case of non-compact supports, the whole domain acts as support for each particle; however, the influence of

particles beyond the immediate neighbourhood of the target position rapidly decays. In general, any kernel function can be expressed in the following form:

$$W(\mathbf{x}, h) = \frac{\alpha}{h^d}\Phi(\mathbf{x}, h) \tag{3.48}$$

In (3.48), $\Phi(\mathbf{x}, h)$ is the mathematical expression chosen as kernel, d is the problem dimensionality and α is a constant of normalisation to ensure that (3.39a) is satisfied by $W(\mathbf{x}, h)$.

The *Gaussian* function belongs to the group of kernels with non-compact support, and is commonly defined by:

$$\Phi(\mathbf{x}, h) = \exp\left(-\frac{\|\mathbf{x} - \mathbf{x}_a\|^2}{h^2}\right) \qquad \alpha = \frac{1}{\pi^{d/2}} \tag{3.49}$$

As the Gaussian kernel (3.49) is not compactly supported, and as a consequence it is more computationally more expensive to use. However, as indicated earlier, it leads to the most accurate representation of the continuous form for field variables in the original PDEs.

The *spline polynomial* kernel functions can be ideally considered as the adaptation of the Gaussian kernel to a compact support [64, 183]. For the set of spline functions that follow, $\mathbf{x}_a$ is intended as the target position where the kernel is centred.

The *cubic* spline function [178] is expressed as

$$\Phi(\mathbf{x}, h) = \begin{cases} 1 - \frac{3}{2}\left(\frac{\|\mathbf{x}-\mathbf{x}_a\|}{h}\right)^2 + \frac{3}{4}\left(\frac{\|\mathbf{x}-\mathbf{x}_a\|}{h}\right)^3; & 0 \leqslant \frac{\|\mathbf{x}-\mathbf{x}_a\|}{h} \leqslant 1 \\ \frac{1}{4}\left(2 - \frac{\|\mathbf{x}-\mathbf{x}_a\|}{h}\right)^3; & 1 \leqslant \frac{\|\mathbf{x}-\mathbf{x}_a\|}{h} \leqslant 2 \\ 0; & \frac{\|\mathbf{x}-\mathbf{x}_a\|}{h} > 2 \end{cases} \tag{3.50}$$

To complete the definition of the cubic spline function, (3.50) should be normalised by introducing constant α determined by (3.39a). To be consistent with (3.50), ensuing definitions of other spline kernel functions also will not include normalisation factor α.

An example of *quartic* spline function is found in [64] expressed as

$$\Phi(\mathbf{x},h)=\begin{cases}\left(1-\frac{1}{2}\frac{\|\mathbf{x}-\mathbf{x}_a\|}{h}\right)^4-5\left(\frac{3}{5}-\frac{1}{2}\frac{\|\mathbf{x}-\mathbf{x}_a\|}{h}\right)^4+10\left(\frac{1}{5}-\frac{1}{2}\frac{\|\mathbf{x}-\mathbf{x}_a\|}{h}\right)^4; & \\ & 0\leqslant\frac{\|\mathbf{x}-\mathbf{x}_a\|}{h}<0.4\\ \left(1-\frac{1}{2}\frac{\|\mathbf{x}-\mathbf{x}_a\|}{h}\right)^4-5\left(\frac{3}{5}-\frac{1}{2}\frac{\|\mathbf{x}-\mathbf{x}_a\|}{h}\right)^4; & 0.4\leqslant\frac{\|\mathbf{x}-\mathbf{x}_a\|}{h}<1.2\\ \left(1-\frac{1}{2}\frac{\|\mathbf{x}-\mathbf{x}_a\|}{h}\right)^4; & 1.2\leqslant\frac{\|\mathbf{x}-\mathbf{x}_a\|}{h}<2\\ 0; & \frac{\|\mathbf{x}-\mathbf{x}_a\|}{h}\geqslant 2\end{cases} \tag{3.51}$$

The *quintic* spline function was used in [34, 35], and also appeared in [187]. Derivatives of an SPH approximation up to the 4^{th} order can be calculated, and this enables the determination of interpolated values of the Laplacian of Laplacian. The quintic kernel assumes the form:

$$\Phi(\mathbf{x},h)=\begin{cases}\left(2-\frac{\|\mathbf{x}-\mathbf{x}_a\|}{h}\right)^5-16\left(1-\frac{\|\mathbf{x}-\mathbf{x}_a\|}{h}\right)^5; & 0\leqslant\frac{\|\mathbf{x}-\mathbf{x}_a\|}{h}\leqslant 1\\ \left(2-\frac{\|\mathbf{x}-\mathbf{x}_a\|}{h}\right)^5; & 1<\frac{\|\mathbf{x}-\mathbf{x}_a\|}{h}\leqslant 2\\ 0; & \frac{\|\mathbf{x}-\mathbf{x}_a\|}{h}>2\end{cases} \tag{3.52}$$

It has been shown in [64] that a non-negative Fourier transform of the kernel function [152] is a necessary condition for stability in analyses with a large number of particles.

The Gaussian kernel function (3.49) would satisfy this condition, yet its open support renders it computationally unattractive when there are too many particles. An alternative class of functions, defined over a compact support, is the family of *Wendland* functions [269]. Wendland-type kernels are computationally inexpensive, as they are based on low order polynomials:

$$\Phi(\mathbf{x},h)=\begin{cases}\max\left(0,1-\frac{\|\mathbf{x}-\mathbf{x}_a\|}{h}\right)^3\cdot\left(1+3\frac{\|\mathbf{x}-\mathbf{x}_a\|}{h}\right) & \text{in 1-D}\\ \max\left(0,1-\frac{\|\mathbf{x}-\mathbf{x}_a\|}{h}\right)^4\cdot\left(1+4\frac{\|\mathbf{x}-\mathbf{x}_a\|}{h}\right) & \text{in 2-D and 3-D}\end{cases} \tag{3.53}$$

with normalising factors being

$$\alpha = \begin{cases} \frac{5}{4} & \text{in 1-D} \\ \frac{7}{\pi} & \text{in 2-D} \\ \frac{21}{2\pi} & \text{in 3-D} \end{cases} \tag{3.54}$$

Wendland kernels $W(\mathbf{x}, h) = \alpha\Phi(\mathbf{x}, h)$ defined by (3.53) and (3.54) are those of 2^{nd} order differentiability. Additional examples of Wendland kernels that reach $\mathcal{C}^4$ and $\mathcal{C}^6$ orders can also be found in [64].

All kernel functions reported above are y-symmetrical about their centre; this leads to

$$\Phi(\Delta\mathbf{x}_{ij}, h) = f\left(\frac{\Delta\mathbf{x}_{ij}}{h}\right) = \Phi_{ij} = \Phi_{ji} = f\left(\frac{\Delta\mathbf{x}_{ji}}{h}\right) \tag{3.55}$$

with

$$\Delta\mathbf{x}_{ij} = \|\mathbf{x}_i - \mathbf{x}_j\| = \|\mathbf{x}_j - \mathbf{x}_i\| = \Delta\mathbf{x}_{ji}.$$

From (3.55) a useful property of symmetry can be derived also for the gradients of $W(\mathbf{x}, h)$ as:

$$\begin{aligned} \nabla_i W\left(\Delta\mathbf{x}_{ij}, h\right) &= \frac{\partial W\left(\Delta\mathbf{x}_{ij}, h\right)}{\partial x_i}\boldsymbol{e}_i = \frac{\Delta\mathbf{x}_{ij}}{\|\Delta\mathbf{x}_{ij}\|}\frac{\partial W\left(\Delta\mathbf{x}_{ij}, h\right)}{\partial\Delta\mathbf{x}_{ij}} = \\ &= -\frac{\Delta\mathbf{x}_{ji}}{\|\Delta\mathbf{x}_{ji}\|}\frac{\partial W\left(\Delta\mathbf{x}_{ji}, h\right)}{\partial\Delta\mathbf{x}_{ji}} = -\nabla_j W\left(\Delta\mathbf{x}_{ji}, h\right) \end{aligned} \tag{3.56}$$

In (3.56), $\nabla_i W\left(\Delta\mathbf{x}_{ij}, h\right)$ is the gradient of the kernel function at particle at position $\mathbf{x}_i$.

The five types of bell-shaped kernel functions just described are graphically represented in fig. 3.5.

3.4.2 *Kernel correction*

In order to at least ensure that, using SPH, linear fields get correctly interpolated – or, in other words, in order to cure the adverse effects caused by the truncation of particle support domains at or near the boundaries –

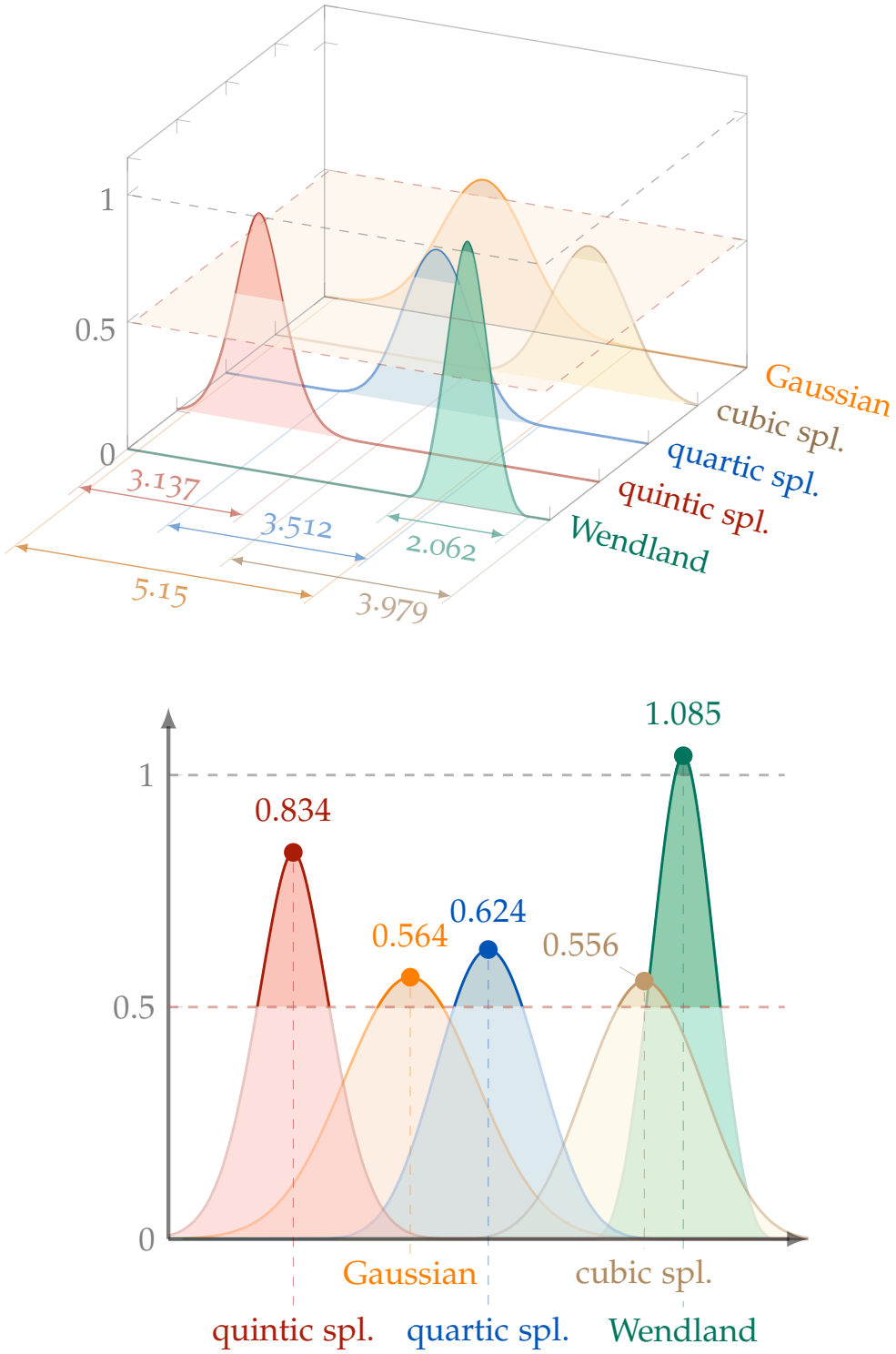

Figure 3.5: superimposition, for purpose of visual comparison, of different types of one-dimensional SPH bell-shaped kernel functions: Gaussian (orange), cubic spline (brown), quartic spline (blue), quintic spline (red) and Wendland-type (green). This is also the order at which diameters of compact supports grow progressively thinner (see illustration at the top), and the kernels more biased towards the center (see bottom illustration). Kernel diameters in the upper figure are computed as the distance between the two tail points where the bell-shaped kernel function is reduced to 1% of its peak value. Chosen smoothing length of $h = 1.2$.

corrections have to be introduced in the formulation of the kernel functions, so that consistency conditions (3.39) are satisfied.

RKPM, as briefly described in appendix A.1, can be one way to obtain this result. A simple correction procedure was proposed in [36], taking inspiration from what done in [152, 164] in the context of RKPM modified in a MLS sense.

In [36], the corrected kernel* $\widetilde{W}(\mathbf{x})$ is defined as the product of the original SPH kernel $W(\mathbf{x})$ function and a corrective polynomial $\Psi(\mathbf{x})$:

$$\widetilde{W}(\mathbf{x}) = \Psi(\mathbf{x}) W(\mathbf{x}); \qquad \Psi(\mathbf{x}) = \alpha(\mathbf{x}) \left[1 + \boldsymbol{\beta}(\mathbf{x}) \cdot (\mathbf{x} - \mathbf{x}_b)\right] \tag{3.57}$$

In (3.57), $\alpha(\mathbf{x})$ and $\boldsymbol{\beta}(\mathbf{x})$ are parameters that locally estimate the correction. They are determined by imposing conditions (3.39) on the corrected kernel $\widetilde{W}(\mathbf{x})$ in (3.57), namely:

$$\sum_{b=1}^{n} V_b \widetilde{W}(\mathbf{x} - \mathbf{x}_b) = 1 \tag{3.58a}$$

$$\sum_{b=1}^{n} (\mathbf{x} - \mathbf{x}_b) V_b \widetilde{W}(\mathbf{x} - \mathbf{x}_b) = \mathbf{0} \tag{3.58b}$$

Substitution of (3.57) in (3.58b) first allows to identify $\boldsymbol{\beta}(\mathbf{x})$; afterwards, substituting in (3.58a) yields $\alpha(\mathbf{x})$, as:

$$\alpha(\mathbf{x}) = \frac{1}{\sum_{b=1}^{n} V_b \left[1 + \boldsymbol{\beta}(\mathbf{x}) \cdot (\mathbf{x} - \mathbf{x}_b)\right] W(\mathbf{x} - \mathbf{x}_b)} \tag{3.59a}$$

$$\boldsymbol{\beta}(\mathbf{x}) = \left[\sum_{b=1}^{n} V_b (\mathbf{x} - \mathbf{x}_b) \otimes (\mathbf{x} - \mathbf{x}_b) W(\mathbf{x} - \mathbf{x}_b)\right]^{-1} \sum_{b=1}^{N} V_b (\mathbf{x}_b - \mathbf{x}) \cdot \cdot W(\mathbf{x} - \mathbf{x}_b) \tag{3.59b}$$

It can be noted that $\alpha(\mathbf{x})$ in (3.59a) depends on $\boldsymbol{\beta}(\mathbf{x})$.

* For conciseness, dependence of W from the smoothing length h will be omitted from notation from this point onward.

Corrections (3.59) allow the SPH interpolation to reproduce exactly linear functions of the type $\mathbf{f}(\mathbf{x}) = \mathbf{a}\mathbf{x} + \mathbf{b}$. This follows from first considering the SPH approximation $\mathbf{f}_h(\mathbf{x})$ of the linear function $\mathbf{f}(\mathbf{x})$:

$$\begin{aligned}\mathbf{f}_h(\mathbf{x}) &= \sum_{b=1}^{n} V_b \left(\mathbf{a}\mathbf{x}_b + \mathbf{b}\right) \widetilde{W}\left(\mathbf{x} - \mathbf{x}_b\right) = \\ &= \mathbf{a} \sum_{b=1}^{n} V_b \mathbf{x}_b \widetilde{W}\left(\mathbf{x} - \mathbf{x}_b\right) + \mathbf{b} \underbrace{\sum_{b=1}^{n} V_b \widetilde{W}\left(\mathbf{x} - \mathbf{x}_b\right)}_{=1 \text{ from } (3.58a)}\end{aligned} \tag{3.60}$$

Given that conditions (3.58) hold true, then (3.60) leads to

$$\mathbf{f}_h(\mathbf{x}) = \mathbf{a} \overbrace{\sum_{b=1}^{n} V_b \mathbf{x}_b \widetilde{W}\left(\mathbf{x} - \mathbf{x}_b\right)}^{\text{see } (3.58b)} + \mathbf{b} = \mathbf{a}\mathbf{x} + \mathbf{b} = \mathbf{f}(\mathbf{x}) \tag{3.61}$$

Superimposed plots of an uncorrected and a corrected version of a one-dimensional kernel in the proximity of a boundary are drawn in fig. 3.6a. Values of coefficients $\alpha(\mathbf{x})$ and $\boldsymbol{\beta}(\mathbf{x})$ for the corrected kernel in fig. 3.6a, as calculated in (3.59), are presented in fig. 3.6b.

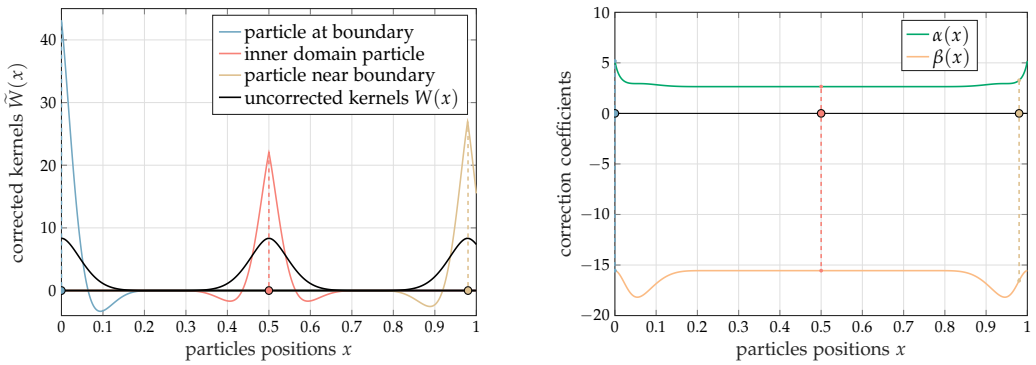

(a) (b)

Figure 3.6: on the left, plot of one-dimensional corrected kernel functions $\widetilde{W}(x)$ on a line of unit length, for particles: at the boundary ($x = 0$, blue), inside the domain ($x = 0.5$, red), near the boundary ($x = 0.98$, brown). Corresponding uncorrected kernels $W(x)$ are plotted in black. Quintic kernel (3.52), 1001 particles, particles distance $h = 0.001$, smoothing length coefficient in (3.48) $\alpha = 120$. On the right, coefficients $\alpha(x)$ and $\boldsymbol{\beta}(x)$ for the corrected kernels in fig. 3.6a, as calculated in (3.59) along the domain; positions of the three particles in fig. 3.6a are highlighted.

3.4.3 *Correction for the gradient of kernel*

Conditions (3.39) should also apply to the gradient of kernel $\nabla W(\mathbf{x})$, as the governing system (2.162) is made of first order PDEs in all the unknowns of the problem. At the least, we want to be able to correctly reproduce linear fields, because the artificial dissipation term to be included in the numerical scheme will require the evaluation of the Laplacians of field variables (see section 3.6 further on).

In order to fulfil first order completeness, that is, for the SPH representation to be able to exactly fit a linear field, from (3.39b) it follows that the corrected gradient $\widetilde{\nabla} W(\mathbf{x})$ of the kernel should satisfy, for all particles $\mathbf{x}_a$ in which the domain is discretised:

$$\sum_{b=1}^{n} V_b \left(\mathbf{x}_b - \mathbf{x}_a\right) \otimes \widetilde{\nabla} W(\mathbf{x}_b - \mathbf{x}_a) = \mathbf{I} \qquad a = 1, \ldots, n \tag{3.62}$$

In [36], the corrected gradient $\widetilde{\nabla} W(\mathbf{x})$ was implemented to comply with constraint (3.62), as

$$\widetilde{\nabla} W\left(\mathbf{x}_b - \mathbf{x}_a\right) = \mathbf{L}_a \nabla W(\mathbf{x}_b - \mathbf{x}_a) \tag{3.63}$$

with *correction matrix* $\mathbf{L}_a$ in (3.63) being defined as

$$\mathbf{L}_a = \left[\sum_{b=1}^{n} V_b \nabla W(\mathbf{x}_b - \mathbf{x}_a) \otimes (\mathbf{x}_b - \mathbf{x}_a)\right]^{-1} \tag{3.64}$$

Substituting $\widetilde{\nabla} W(\mathbf{x}_a)$ as defined in (3.63) into $\nabla W(\mathbf{x}_a)$ in (3.62), the correction matrix $\mathbf{L}_a$ in (3.64) ensures first order consistency for each target particle at $\mathbf{x}_a$.

Having guaranteed the satisfaction of (3.39b), there remain to be verified that $\widetilde{\nabla} W(\mathbf{x})$ is in compliance with 0^{th} degree consistency condition (3.39a), that is, the gradients of constant functions should vanish across the domain.

As already shown in early SPH papers [177, 178], this goal can be easily achieved by subtracting from the SPH summation the value of the function $\mathbf{f}(\mathbf{x}_a)$ at target point $\mathbf{x}_a$.

Normalisation of the corrected kernel, as in (3.58a), should in general be enough to ensure correct reproduction of constant functions by the SPH method.

Ultimately, the corrected SPH interpolation of the gradient of a function $\mathbf{f}(\mathbf{x})$ can then be expressed as

$$\nabla \mathbf{f}(\mathbf{x}_a) = \sum_{b=1}^{n} V_b \left[\mathbf{f}(\mathbf{x}_b) - \mathbf{f}(\mathbf{x}_a)\right] \otimes \widetilde{\nabla} W(\mathbf{x}_b - \mathbf{x}_a) \tag{3.65}$$

3.4.4 *Correction for the Laplacian of kernel*

In sections 3.4.2 and 3.4.3 we introduced the kernel modifications necessary to correctly implement a consistent discretisation of mixed system (2.162).

In any event, the artificial dissipation that will be employed to stabilise the SPH-discretised governing system will rely on the undivided [82] discrete harmonic (Laplacian) and biharmonic (Laplacian of Laplacian) operators.

In analogy with (3.58) and (3.62), consistency of the discretised kernel Laplacian $\widetilde{\nabla}^2 W(\mathbf{x})$ is obtained by enforcing the following requirements

$$\sum_{b=1}^{n} V_b \widetilde{\nabla}^2 W(\mathbf{x} - \mathbf{x}_b) = 0 \tag{3.66a}$$

$$\sum_{b=1}^{n} (\mathbf{x} - \mathbf{x}_b) V_b \widetilde{\nabla}^2 W(\mathbf{x} - \mathbf{x}_b) = 0 \tag{3.66b}$$

$$\sum_{b=1}^{n} (\mathbf{x} - \mathbf{x}_b)^2 V_b \widetilde{\nabla}^2 W(\mathbf{x} - \mathbf{x}_b) = 2d \tag{3.66c}$$

In (3.66c), $d(= 2, 3)$ indicates the dimensionality of the problem.

As already noted for the corrected kernel gradient in section 3.4.3, 0^{th} order consistency (3.66a) will be ensured by subtracting the field variable at the target position, $\mathbf{f}(\mathbf{x}_a)$, from the SPH summation. Therefore, the Laplacian of a function $\nabla^2 \mathbf{f}(\mathbf{x})$, will assume the form

$$\nabla^2 \mathbf{f}(\mathbf{x}_a) = \sum_{b=1}^{n} V_b \left[\mathbf{f}(\mathbf{x}_b) - \mathbf{f}(\mathbf{x}_a)\right] \widetilde{\nabla}^2 W(\mathbf{x}_b - \mathbf{x}_a) \tag{3.67}$$

A formulation of the term $\widetilde{\nabla}^2 W(\mathbf{x})$ above, capable of satisfying the remaining conditions (3.66b) and (3.66c), is obtained by using the method of Lagrange multipliers (see for instance [43]). The general form of the corrected Laplacian $\widetilde{\nabla}^2 W(\mathbf{x}_a)$ for a particle at $\mathbf{x}_a$ is defined up to the quadratic order as below:

$$\widetilde{\nabla}^2 W(\mathbf{x}_a) = \nabla^2 W(\mathbf{x}_a) + \boldsymbol{\alpha}_a \cdot (\mathbf{x}_a - \mathbf{x}_b) + \beta_a (\mathbf{x}_a - \mathbf{x}_b)^2 \tag{3.68}$$

Considered (3.68), equation (3.67) transforms into

$$\widetilde{\nabla}^2 \mathbf{f}(\mathbf{x}_a) = \sum_{b=1}^{n} V_b \left[\mathbf{f}(\mathbf{x}_b) - \mathbf{f}(\mathbf{x}_a)\right] \widetilde{\nabla}^2 W(\mathbf{x}_b - \mathbf{x}_a) \tag{3.69}$$

The approach described above has been adopted in [145]; a similar procedure was implemented in [34], except for the fact that, in that paper, all three conditions (3.66) are employed as constraints to the target function.

In (3.68), $\boldsymbol{\alpha}_a$ and β_a are correction parameters that are found by solving a system of equations generated by the substitution of (3.68) into (3.66b) and (3.66c), namely:

$$\begin{bmatrix} \sum_{b\in\Omega_a} V_b \|\mathbf{x}_a - \mathbf{x}_b\| \otimes \|\mathbf{x}_a - \mathbf{x}_b\| & \sum_{b\in\Omega_a} V_b \|\mathbf{x}_a - \mathbf{x}_b\|^2 \|\mathbf{x}_a - \mathbf{x}_b\| \\ \left(\sum_{b\in\Omega_a} V_b \|\mathbf{x}_a - \mathbf{x}_b\|^2 \|\mathbf{x}_a - \mathbf{x}_b\|\right)^T & \sum_{b\in\Omega_a} V_b \|\mathbf{x}_a - \mathbf{x}_b\|^4 \end{bmatrix} \cdot \begin{pmatrix} \boldsymbol{\alpha}_a \\ \beta_a \end{pmatrix} = \\ = \begin{pmatrix} -\sum_{b\in\Omega_a} V_b \|\mathbf{x}_a - \mathbf{x}_b\| \nabla^2 W(\mathbf{x}_a - \mathbf{x}_b) \\ 2d - \sum_{b\in\Omega_a} V_b \|\mathbf{x}_a - \mathbf{x}_b\|^2 \nabla^2 W(\mathbf{x}_a - \mathbf{x}_b) \end{pmatrix} \tag{3.70}$$

Given that system (3.70) has to be solved for each particle $a = 1, \ldots, n$, the computational cost of the correction procedure can increase significantly with the number of particles present in the simulation.

3.4.5 *Tensile Instability*

Tensile instability is a numerical difficulty mainly associated with SPH, encountered when simulating solid mechanics applications.

This phenomenon occurs in SPH simulations of bodies under a tensile state of stress, once in a transient regime, because a previous equilibrium state has been broken. It happens locally, and consists in a rapid and sustained growth of velocity in some particles, that afterwards stabilises into an oscillatory pattern as the particles become very close and begin clumping together in clusters. This behaviour is particularly difficult to detect in cases when particles are expected to behave that way, for instance when simulating fragmentation processes.

A significant amount of research has been undertaken in order to understand the root of this problem, and to overcome it.

Dyka et al [70, 71], for instance, developed a modified SPH scheme where particles were divided in two groups, one that evaluated velocities, and the other stresses. This approach produced encouraging results; however, it adds a certain layer of complexity to SPH procedures.

Morris [186] investigated the issue in depth, and suggested the adoption of higher order spline-type kernel functions in order to cure the instabilities.

Dilts, on the other hand, used an MLS approximation in order to alleviate the problem, in [65].

Swegle and coworkers in [248] were the first to diagnose tensile instability as an issue intrinsic to the SPH method, and to point out its possible remedies. In that work, a von Neumann stability analysis, as pioneered in [192], was performed on a linearised, one-dimensional solid mechanics problem based on the conservation of mass and linear momentum. In brief, their procedure consisted, firstly, in linearising the equations of motion subjected to a small perturbation; then, in applying the Fourier transform to the result, and finally, in studying the eigenstructure of the matrix of the resulting system of equations. In case there be eigenvalues > 1, the amplitude of some wave number would then consistently grow with time, eventually developing instabilities in the simulation.

It is possible to perform a linearised analysis to determine the potential onset of tensile instability, as this turns out to be completely time-independent.*

* This is confirmed by the fact that velocities cease to grow indefinitely after particles have moved very close to one another, in clusters.

The von Neumann analysis shows that, in an idealised interaction between two particles, tensile instability appears in case the following condition is met:

$$W''(x)\,T > 0 \tag{3.71}$$

From (3.71), it can be seen that presence or absence of instability depends on the sign of the second derivative of the kernel, $W''(x)$, and on whether the state of stress T is compressive or tensile.

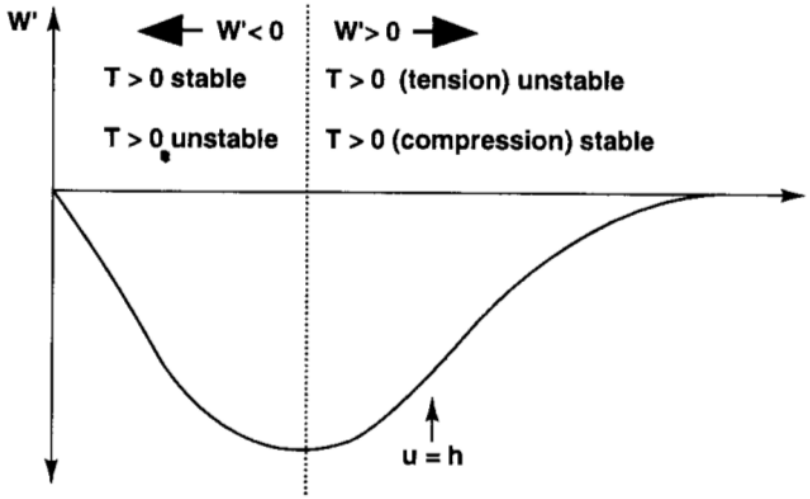

Figure 3.7: shape of first derivative of a bell-shaped kernel function. The dotted vertical line locates the saddle point at a shorter distance from the origin than the smoothing length h. In this case, neighbouring particles will fall in the region of tensile instability and compressive stability, where $W' > 0$. (Source: [248])

Figure 3.7 helps to better understand condition (3.71): given the symmetry about the target particle position (the origin of the diagram) of derivatives of bell-shaped kernel functions $W'(x)$, instability *in tension*, ($T > 0$), will happen in regions beyond the position (saddle point) where the second derivative changes sign and becomes negative, $W'' < 0$.

In compression, instead, $T < 0$ so the unstable region is the one between the origin and the saddle point, where $W'' > 0$.

As the smoothing length h is usually set to be equal to the initial distance between two neighbouring particles, Δx, and also, given that the saddle point of bell-shaped kernels (where $W''(x)$ changes sign) is located at a distance from the origin $x_s < h$, this issue mainly happens in tension, and hence it is known as "tensile instability".

When the study in [248] is extended to include multiple neighbours for a target particle, while still being in one-dimension, the condition allowing the onset of tensile instability is revealed to be very similar to (3.71):

$$\left[W''(x_a - x_{i+1}) + W''(x_a - x_{i+3}) + W''(x_a - x_{i+5}) + \dots\right] T > 0 \qquad (3.72)$$

In (3.72), x_a is the position of the target particle, assumed as origin in fig. 3.8.

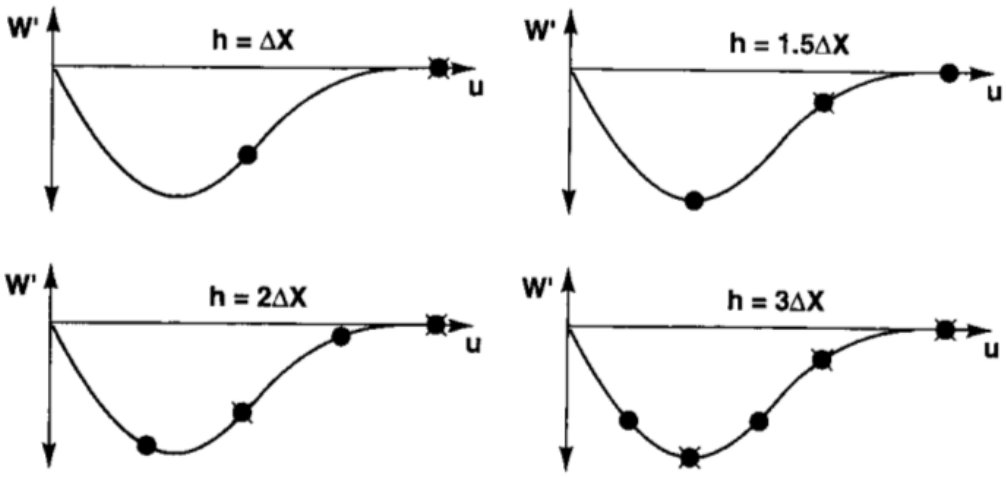

Figure 3.8: influence of neighbours position over onset of tensile instability, drawn on the first derivative of a bell-shaped kernel function. A black dot represents an odd-positioned particle, while a crossed dot represents an even-positioned one. Even-positioned neighbours do not influence the tension instability criterion (3.72). (Source: [248])

Therefore, it is seen from (3.72) that tensile instability was found to be highly dependent from particles positions, and from the shape of the kernel, which determines the saddle point position for W''.

Monaghan et al. [95, 180] proposed the addition of an artificial stress component to the equation of motion, based on the signs of stresses $\mathbf{P}$.

Later, both papers of Bonet and Kulasegaram [35], and Belytschko and co-authors [20], building on its dependency from neighbours positions, suggest that the problem of tensile instability can be eliminated altogether through the adoption of a total Lagrangian perspective. Encouraging results of SPH in an updated Lagrangian framework, devoid of tension instability, can be found in [112, 264].

In [35], analysis of tensile instability was extended to include the effects of nonlinear mechanics. It was concluded that stability at initial positions depends on the well-posedness of the constitutive model, which is ensured by any reliable material model. However, once the simulation starts and equilibrium is lost, movement of particles, as they drop in and out each other compact supports, can eventually activate condition (3.72) at some position in the domain, leading to local developments of tensile instabilities.

The danger could be entirely avoided in case a *total Lagrangian* framework is adopted. In fact, in total Lagrangian analyses, neighbours of each particle, along with their respective kernel weight, are assigned just at the initial step of the simulation, for the reference configuration, and are then left unchanged until the end of the analysis.

Proceeding this way, not only the onset of tensile instability is prevented from ever happening, but there are also conspicuous savings in computational time, stemming from having to search for neighbours and to apply corrections to the kernel and its derivatives, only once over the course of the entire simulation.

For these reasons, the total Lagrangian description will be adopted as the framework for the SPH discretisation of the equations of motion.

3.5 SPH SPATIAL DISCRETISATION OF THE MIXED SYSTEM

In order to discretise the nonlinear elastodynamics system of PDEs in space with the SPH model described in this chapter, it is essential to revisit the mixed $\{\mathbf{p}, \mathbf{F}, \mathbf{H}, J\}$ system (2.162) as developed in section 2.13. That system

can be rewritten in terms of a vector of *residuals* $\boldsymbol{\mathcal{R}} = (\boldsymbol{\mathcal{R}}_p, \boldsymbol{\mathcal{R}}_F, \boldsymbol{\mathcal{R}}_H, \boldsymbol{\mathcal{R}}_J)$ defined as†

$$\boldsymbol{\mathcal{R}}_p = \frac{\partial \mathbf{p}}{\partial t} - \nabla_0 \cdot \mathbf{P} - \rho \mathbf{b} \tag{3.73a}$$

$$\boldsymbol{\mathcal{R}}_F = \frac{\partial \mathbf{F}}{\partial t} - \nabla_0 \left(\frac{\mathbf{p}}{\rho} \right) \tag{3.73b}$$

$$\boldsymbol{\mathcal{R}}_H = \frac{\partial \mathbf{H}}{\partial t} - \mathbf{F} \times \nabla_0 \left(\frac{\mathbf{p}}{\rho} \right) \tag{3.73c}$$

$$\boldsymbol{\mathcal{R}}_J = \frac{\partial J}{\partial t} - \mathbf{H} : \nabla_0 \left(\frac{\mathbf{p}}{\rho} \right) \tag{3.73d}$$

Then, it is possible to specify a generalised expression for the rate of virtual work by employing (3.73) in conjunction with arbitrary general virtual stresses $\delta\boldsymbol{\mathcal{V}} = (\delta v, \delta\boldsymbol{\Sigma}_F, \delta\boldsymbol{\Sigma}_H, \delta\Sigma_J)$, conjugate to $\boldsymbol{\mathcal{R}}$, to yield:

$$\begin{aligned} \int_\Omega \delta\boldsymbol{\mathcal{V}}^T \boldsymbol{\mathcal{R}} \, d\Omega = \int_\Omega \left(\delta v \cdot \boldsymbol{\mathcal{R}}_p + \delta\boldsymbol{\Sigma}_F : \boldsymbol{\mathcal{R}}_F + \delta\boldsymbol{\Sigma}_H : \boldsymbol{\mathcal{R}}_H + \delta\Sigma_J \boldsymbol{\mathcal{R}}_J \right) d\Omega = \\ = 0 \end{aligned} \tag{3.74}$$

In (3.74), δv represent an arbitrary velocity field, while $\delta\boldsymbol{\Sigma}_F$, $\delta\boldsymbol{\Sigma}_H$ and $\delta\Sigma_J$ are virtual conjugate stresses to the strain measures $\mathbf{F}$, $\mathbf{H}$ and J, as defined in (2.124), and originally found in [32].

By separately setting each of the terms in (3.74) equal to 0, we obtain a system of equations in a form apt to be discretised:

$$\int_\Omega \delta v \cdot \frac{\partial \mathbf{p}}{\partial t} \, d\Omega = \int_\Omega \delta v \cdot (\nabla_0 \cdot \mathbf{P} + \rho \mathbf{b}) \, d\Omega \tag{3.75a}$$

$$\int_\Omega \delta\boldsymbol{\Sigma}_F : \frac{\partial \mathbf{F}}{\partial t} \, d\Omega = \int_\Omega \delta\boldsymbol{\Sigma}_F : \nabla_0 \left(\frac{\mathbf{p}}{\rho} \right) d\Omega \tag{3.75b}$$

$$\int_\Omega \delta\boldsymbol{\Sigma}_H : \frac{\partial \mathbf{H}}{\partial t} \, d\Omega = \int_\Omega \delta\boldsymbol{\Sigma}_H : \left[\mathbf{F} \times \nabla_0 \left(\frac{\mathbf{p}}{\rho} \right) \right] d\Omega \tag{3.75c}$$

$$\int_\Omega \delta\Sigma_J \frac{\partial J}{\partial t} \, d\Omega = \int_\Omega \delta\Sigma_J : \left[\mathbf{H} : \nabla_0 \left(\frac{\mathbf{p}}{\rho} \right) \right] d\Omega \tag{3.75d}$$

† As already specified in section 2.1, physical quantities and mathematical operators pointing to the reference configuration will be designated with a subscript $(\cdot)_0$; e. g., the gradient operator with respect to the reference configuration will be identified with ∇_0.

Equation (3.75a) can be further rearranged by using integration by parts and the divergence theorem, as

$$\int_\Omega \delta \boldsymbol{v} \cdot \frac{\partial \mathbf{p}}{\partial t}\, d\Omega = \int_\Omega \left[\nabla_0 \cdot (\delta \boldsymbol{v} \cdot \mathbf{P}) - \mathbf{P} : \nabla_0 \delta \boldsymbol{v}\right]\, d\Omega + \int_\Omega \rho \delta \boldsymbol{v} \cdot \mathbf{b}\, d\Omega = \\ = \int_{\partial\Omega} (\delta \boldsymbol{v} \cdot \mathbf{P})\, \mathbf{N}\, d\Gamma - \int_\Omega \mathbf{P} : \nabla_0 \delta \boldsymbol{v}\, d\Omega + \int_\Omega \rho \delta \boldsymbol{v} \cdot \mathbf{b}\, d\Omega \quad (3.76)$$

where $\mathbf{N}$ is the normal vector to the surface Γ acting as boundary of Ω, in the reference configuration. Remembering the relation between traction force $\mathbf{t}$ and the first Piola-Kirchhoff stress tensor $\mathbf{P}$ expressed in (2.19), (3.76) can be further simplified into

$$\int_\Omega \delta \boldsymbol{v} \cdot \frac{\partial \mathbf{p}}{\partial t}\, d\Omega = \left(\int_{\partial\Omega} \delta \boldsymbol{v} \cdot \mathbf{t}\, d\Gamma + \int_\Omega \rho \delta \boldsymbol{v} \cdot \mathbf{b}\, d\Omega\right) + \\ + \left(-\int_\Omega \mathbf{P} : \nabla_0 \delta \boldsymbol{v}\, d\Omega\right) = \delta \mathcal{W}_{\text{ext}} + \delta \mathcal{W}_{\text{int}} \quad (3.77)$$

In (3.77), $\delta \mathcal{W}_{\text{int}}$ stands for the internal virtual work generated by stresses inside the body reacting to externally applied conditions. These conditions are exemplified by the external virtual work $\delta \mathcal{W}_{\text{ext}}$ term, defined as

$$\delta \mathcal{W}_{\text{ext}} = \int_{\partial\Omega} \delta \boldsymbol{v} \cdot \mathbf{t}\, d\Gamma + \int_\Omega \rho \delta \boldsymbol{v} \cdot \mathbf{b}\, d\Omega \quad (3.78)$$

It is useful to note that traction forces $\mathbf{t}$ in (3.78) are natural boundary conditions that can be imposed along with external body forces $\mathbf{b}$.

As a first step towards meshless discretisation of equations (3.77), (3.75b)-(3.75d), the collocation method is used to approximate the integrals over domain Ω as sums over a cloud of particles scattered across Ω.

$$\sum_{a\in\Omega} V_a \delta \boldsymbol{v}_a \cdot \frac{\partial \mathbf{p}_a}{\partial t} = \sum_{a\in\Omega} V_a \delta \boldsymbol{v}_a \cdot \left(\frac{A_a}{V_a} \mathbf{t} + \rho \mathbf{b}_a \right) + - \sum_{a\in\Omega} V_a \mathbf{P}_a : \nabla_0 \delta \boldsymbol{v}_a \tag{3.79a}$$

$$\sum_{a\in\Omega} V_a \delta \boldsymbol{\Sigma}_{\mathbf{F}|a} : \frac{\partial \mathbf{F}_a}{\partial t} = \sum_{a\in\Omega} V_a \delta \boldsymbol{\Sigma}_{\mathbf{F}|a} : \nabla_0 \left(\frac{\mathbf{p}_a}{\rho} \right) \tag{3.79b}$$

$$\sum_{a\in\Omega} V_a \delta \boldsymbol{\Sigma}_{\mathbf{H}|a} : \frac{\partial \mathbf{H}_a}{\partial t} = \sum_{a\in\Omega} V_a \delta \boldsymbol{\Sigma}_{\mathbf{H}|a} : \left[\mathbf{F}_a \times \nabla_0 \left(\frac{\mathbf{p}_a}{\rho} \right) \right] \tag{3.79c}$$

$$\sum_{a\in\Omega} V_a \delta \Sigma_{J|a} \frac{\partial J_a}{\partial t} = \sum_{a\in\Omega} V_a \delta \Sigma_{J|a} : \left[\mathbf{H}_a : \nabla_0 \left(\frac{\mathbf{p}_a}{\rho} \right) \right] \tag{3.79d}$$

In each of the equations (3.79), V_a is the subvolume assigned to each particle at position $\mathbf{X}_a$; more in general, physical quantities present subscript $(\cdot)_a$ refer to their value in $\mathbf{X}_a$. Density ρ is assumed uniform over the domain.

A_a in (3.79a) stands for the part of boundary surface Γ assigned to a particle in $\mathbf{X}_a$ that is itself located on the boundary, so that:

$$\begin{cases} A_a = 0 & \text{if } \mathbf{X}_a \in \Gamma \\ A_a \neq 0 & \text{if } \mathbf{X}_a \notin \Gamma \end{cases} \tag{3.80}$$

We now observe that the RHS of equations in system (3.79) present gradients of quantities (virtual velocities $\delta \boldsymbol{v}_a$ and linear momenta $\mathbf{p}_a$) that can be approximated by SPH summation, following (3.65).

The RHS of (3.79a) contains the internal virtual work $\delta\mathcal{W}_{\text{int}}$, that depends on $\nabla_0\delta v_a$ which, with the help of property (2.159) for the double contraction between second order tensors, can be simplified into

$$\begin{aligned}
\delta\mathcal{W}_{\text{int}} &= -\sum_{a\in\Omega} V_a \mathbf{P}_a : \nabla_0\delta v_a = \\
&= -\sum_{a\in\Omega} V_a \mathbf{P}_a : \left[\sum_{b\in\Omega_a} V_b \left(\delta v_a - \delta v_b\right) \otimes \widetilde{\nabla}_0 W_a\left(\mathbf{X}_b\right) \delta v_a\right] = \\
&= -\sum_{a\in\Omega} V_a \delta v_a \cdot \left[\sum_{b\in\Omega_a} V_b \left(\mathbf{P}_b \widetilde{\nabla}_0 W_a\left(\mathbf{X}_b\right) - \mathbf{P}_a \widetilde{\nabla}_0 W_b\left(\mathbf{X}_a\right)\right)\right]
\end{aligned} \tag{3.81}$$

Considering (3.81), the SPH approximation of $\nabla_0 \mathbf{p}_a$ terms on the RHS of (3.79) leads to the spatial semidiscretisation of the $\{\mathbf{p}, \mathbf{F}, \mathbf{H}, J\}$ mixed system (2.162), namely:

$$\frac{\partial \mathbf{p}_a}{\partial t} = \left(\frac{A_a}{V_a}\mathbf{t}_a + \rho \mathbf{b}_a\right) - \sum_{b\in\Omega_a} V_b \left[\mathbf{P}_b \widetilde{\nabla}_0 W_a\left(\mathbf{X}_b\right) - \mathbf{P}_a \widetilde{\nabla}_0 W_b\left(\mathbf{X}_a\right)\right] \tag{3.82a}$$

$$\frac{\partial \mathbf{F}_a}{\partial t} = \frac{1}{\rho}\sum_{b\in\Omega_a} V_b \left(\mathbf{p}_b - \mathbf{p}_a\right) \otimes \widetilde{\nabla}_0 W_b\left(\mathbf{X}_a\right) \tag{3.82b}$$

$$\frac{\partial \mathbf{H}_a}{\partial t} = \mathbf{F}_a \times \frac{1}{\rho}\sum_{b\in\Omega_a} V_b \left(\mathbf{p}_b - \mathbf{p}_a\right) \otimes \widetilde{\nabla}_0 W_b\left(\mathbf{X}_a\right) \tag{3.82c}$$

$$\frac{\partial J_a}{\partial t} = \mathbf{H}_a : \frac{1}{\rho}\sum_{b\in\Omega_a} V_b \left(\mathbf{p}_b - \mathbf{p}_a\right) \otimes \widetilde{\nabla}_0 W_b\left(\mathbf{X}_a\right) \tag{3.82d}$$

3.6 JST ARTIFICIAL DISSIPATION

The semi-discretised system (3.82), combined with any time-marching scheme, may still suffer from pressure chequerboard instabilities, due to the nodal integration nature of SPH discretisation, as already highlighted in section 3.3. Moreover, the presence of discontinuities in the solution field, system (3.82) cannot produce meaningful results.

Both these shortcomings can be addressed by the addition of an *artificial dissipation* term in the governing equations, as widely practised both in CFD and computational solid mechanics (CSM). In CSM, artificial dissipation

makes use of techniques ranging from gradient-based stabilisation [157, 207, 208] to strain smoothing [40, 52, 106]. These techniques, however, do not fully solve the issue of pressure oscillations for analyses involving incompressible and nearly-incompressible materials [72].

On the other hand, in section 3.3 we introduced (3.47) from [182] as an effective way to add artificial dissipation to a SPH problem, capable of smearing shocks and attenuate instabilities. This, however, affects the accuracy in the continuous regions of the solution [243].

As a rule, the order of accuracy of a scheme should not be altered by the introduction of an artificial dissipation term, that therefore should be associated with a lower truncation error than the one of the scheme. A straightforward way to achieve this, is to build the dissipative term out of derivatives of a higher order than the ones appearing in the equations governing the chosen problem. As an additional constraint, by their very nature, dissipative terms in hyperbolic differential equations should be made of derivatives of *even* order [107].

The JST scheme was first introduced in [122], in the context of FV schemes for the solution of the Euler equations of fluid dynamics. It is designed to provide background stabilisation in regions where the solution is spuriously oscillating, together with the ability to capture shocks in the solution by thickening the width of discontinuities with artificial viscosity.

The JST algorithm introduces artificial viscosity in a set of conservation laws, and is composed of two terms: one acts on conserved variables $\boldsymbol{\mathcal{U}}_a$ through a harmonic (Laplacian) differential operator, the other through a biharmonic (4^{th} order derivatives) operator:

$$\boldsymbol{\mathcal{D}}_{\text{JST}}(\boldsymbol{\mathcal{U}}_a) = \boldsymbol{\mathcal{D}}_2(\boldsymbol{\mathcal{U}}_a) + \boldsymbol{\mathcal{D}}_4(\boldsymbol{\mathcal{U}}_a) \tag{3.83}$$

In (3.83), the second order term $\boldsymbol{\mathcal{D}}_2(\boldsymbol{\mathcal{U}}_a)$ performs the shock-capturing role, while the fourth order term $\boldsymbol{\mathcal{D}}_4(\boldsymbol{\mathcal{U}}_a)$ smears out possible instabilities that may appear where the solution is continuous.

The two terms are activated where necessary by discontinuity switches $\varepsilon^{(2)}(\mathbf{x})$ / $\varepsilon^{(4)}(\mathbf{x})$, previously defined for FE solvers in the context of fluid dynamics in [121], and later recast in [1] for FV in mixed form conservation

laws solid dynamics. Both papers present switches $\varepsilon^{(2)}/\varepsilon^{(4)}(\mathbf{x})$ as dependent from a second order difference of pressure between adjacent nodes:

$$\varepsilon_{ab}^{(2)} = \kappa^{(2)} \max\left(\Upsilon_a, \Upsilon_b\right) \tag{3.84a}$$

$$\varepsilon_{ab}^{(4)} = \max\left(0, \kappa^{(4)} - \varepsilon_{ab}^{(2)}\right) \tag{3.84b}$$

In (3.84), $\kappa^{(2)}$ and $\kappa^{(4)}$ are appropriate coefficients (< 1), while Υ_a are normalised second order difference for pressure variable p at nodes $\mathbf{x}_a$ with respect to adjacent nodes $\mathbf{x}_b \in \Lambda_a$, defined as [1] for FV:

$$\Upsilon_{a|FV} = \frac{|\sum_{b\in\Lambda_a} \theta_{ab}\,(p_b - p_a)\,|}{\sum_{b\in\Lambda_a}(p_b + p_a)} = \frac{|\boldsymbol{\mathcal{L}}_{FV}\,[p(\mathbf{x}_a)]\,|}{\sum_{b\in\Lambda_a}(p_b + p_a)} \tag{3.85}$$

In (3.85), Λ_a represents the connectivity region of node at $\mathbf{x}_a$, and θ_{ab} are a set of weighting coefficients assigned to each node $\mathbf{x}_b \in \Lambda_a$ in order to define an undivided Laplacian [1, 80, 121] operator $\boldsymbol{\mathcal{L}}_{FV}(\cdot)$:

$$\boldsymbol{\mathcal{L}}_{FV}\,[\mathbf{f}(\mathbf{x}_a)] = \sum_{b\in\Lambda_a} \theta_{ab}\,[\mathbf{f}(\mathbf{x}_b) - \mathbf{f}(\mathbf{x}_a)] \tag{3.86}$$

Geometric weights θ_{ab} in (3.86) are obtained through a Lagrange multiplier minimisation procedure, aimed at making $\boldsymbol{\mathcal{L}}_{FV}\,[\mathbf{f}(\mathbf{x})] = 0$ from a linear function $\mathbf{f}(\mathbf{x})$. This procedure is illustrated in detail in [80].

Adaptation, to a SPH context, of the approach described above for obtaining the JST switches, would only require the substitution in (3.85) of the Laplacians of neighbouring particles at $\mathbf{x}_b \in \Omega_a$, obtained through equation (3.69):

$$\Upsilon_{a|SPH} = \frac{|\sum_{b\in\Omega_a} \boldsymbol{\mathcal{L}}\,[p\,(\mathbf{X}_b)] - \boldsymbol{\mathcal{L}}\,[p\,(\mathbf{X}_a)]\,|}{\sum_{b\in\Omega_a}(p_b + p_a)} \tag{3.87}$$

where $\boldsymbol{\mathcal{L}}\,[p\,(\mathbf{X})] = \widetilde{\nabla}^2_0 p\,(\mathbf{X})$ from (3.69) with $\mathbf{f}(\mathbf{x}) = p(\mathbf{X})$.

In (3.87), neighbours included in the computation of Υ_a for target particle at $\mathbf{X}_a$ will always be the same set of material particles determined at the reference configuration at $\mathbf{X}_b$, with each carrying the same value

of $\widetilde{\nabla}^2 W_b(\mathbf{X}_a)$ throughout the simulations, since it is computed in a total Lagrangian framework.

Having obtained the switches in (3.84), JST dissipation terms $\mathcal{D}_2(\mathcal{U}_a)$ and $\mathcal{D}_4(\mathcal{U}_a)$ are defined for SPH as

$$\mathcal{D}_2\left[\mathcal{U}\left(\mathbf{X}_a\right)\right] = \varepsilon^{(2)} c_p \Delta x_{min} \widetilde{\nabla}_0^2 \mathcal{U}\left(\mathbf{X}_a\right) \tag{3.88a}$$

$$\mathcal{D}_4\left[\mathcal{U}\left(\mathbf{X}_a\right)\right] = -\varepsilon^{(4)} c_p \Delta x_{min}^3 \cdot \cdot \sum_{b \in \Omega_a} V_b \left(\widetilde{\nabla}_0^2 \mathcal{U}\left(\mathbf{X}_b\right) - \widetilde{\nabla}_0^2 \mathcal{U}\left(\mathbf{X}_a\right)\right) \widetilde{\nabla}_0^2 W_a\left(\mathbf{X}_b\right) \tag{3.88b}$$

In (3.88), $\mathcal{U}\left(\mathbf{X}_a\right)$ can be assumed to be any of the conserved variables in (2.164) from section 2.13, evaluated at the target particle material position $\mathbf{X}_a$; c_p is the pressure elastic wave speed; Δx_{min} is the characteristic length of the problem, assumed to be equal to the smallest distance between any two particles in the simulation; $\widetilde{\nabla}_0^2 W\left(\mathbf{X}\right)$ and $\widetilde{\nabla}_0^2 \mathcal{U}\left(\mathbf{X}_a\right)$ are obtained from (3.68) and (3.69) respectively.

Switches $\varepsilon^{(2)}/\varepsilon^{(4)}(\mathbf{x})$ are now defined in terms of SPH for each particle at $\mathbf{X}_a$ as

$$\varepsilon_a^{(2)} = \kappa^{(2)} \max_{b \in \Omega_a} \left(\Upsilon_b\right) \tag{3.89a}$$

$$\varepsilon_a^{(4)} = \max\left(0,\, \kappa^{(4)} - \varepsilon_a^{(2)}\right) \tag{3.89b}$$

In (3.89), second order sensors Υ_b are taken from (3.87), and are evaluated for each neighbour $b \in \Omega_a$.

To note, the reiterated application of the Laplacian operator in (3.88b) defines the SPH *Laplacian of Laplacian* of $\mathcal{U}\left(\mathbf{X}\right)$.

An undivided Laplacian of the type (3.87) is effective in detecting discontinuities and high gradients in the solution fields, as its presence will make the Laplacian assume high values; at the same time, in regions where the solution is continuous and smooth, it will instead assume small values. The switch $\varepsilon_a^{(2)}$ in (3.89a) will therefore tend to zero, in case the solution field is sufficiently regular. In turn, this will deactivate the dissipation term $\mathcal{D}_2\left[\mathcal{U}\left(\mathbf{X}_a\right)\right]$ in (3.88a).

On the other hand, the Laplacian of Laplacian characterising the $\mathcal{D}_4\left[\mathcal{U}\left(\mathbf{X}_a\right)\right]$ term in (3.88b) adds artificial dissipation, in order to cancel oscillations in continuous regions of the solution field, where strong gradients are absent.

Switch (3.89b), however, forces $\mathcal{D}_4\left[\mathcal{U}\left(\mathbf{X}_a\right)\right] \to 0$ in presence of high gradients and discontinuities: in fact, it was reported in [121] that the fourth order term could be the source of numerical noise when activated close to large discontinuities in value of solutions.

Spurious oscillations mainly target the pressure field, and hence artificial dissipation terms (3.88) will be added to the conservation law for linear momentum, (3.82a); they will also be useful if introduced in (3.82d), the conservation law for the Jacobian, or volumetric strain, because stabilisation is needed there when considering materials near, or at, the incompressibility limit $\nu = 0.5$ [86]. The semidiscretised $\{\mathbf{p}, \mathbf{F}, \mathbf{H}, J\}$ governing mixed system then becomes:

$$\begin{aligned}
\frac{\partial \mathbf{p}_a}{\partial t} &= \left(\frac{A_a}{V_a}\mathbf{t}_a + \rho \mathbf{b}_a\right) + \\
&\quad - \sum_{b \in \Omega_a} V_b \left[\mathbf{P}_b \widetilde{\nabla}_0 W_a\left(\mathbf{X}_b\right) - \mathbf{P}_a \widetilde{\nabla}_0 W_b\left(\mathbf{X}_a\right)\right] + \\
&\quad + \mathcal{D}_2\left[\mathbf{p}\left(\mathbf{X}_a\right)\right] + \mathcal{D}_4\left[\mathbf{p}\left(\mathbf{X}_a\right)\right] && \text{(3.90a)} \\
\frac{\partial \mathbf{F}_a}{\partial t} &= \frac{1}{\rho} \sum_{b \in \Omega_a} V_b \left(\mathbf{p}_b - \mathbf{p}_a\right) \otimes \widetilde{\nabla}_0 W_b\left(\mathbf{X}_a\right) && \text{(3.90b)} \\
\frac{\partial \mathbf{H}_a}{\partial t} &= \mathbf{F}_a \times \frac{1}{\rho} \sum_{b \in \Omega_a} V_b \left(\mathbf{p}_b - \mathbf{p}_a\right) \otimes \widetilde{\nabla}_0 W_b\left(\mathbf{X}_a\right) && \text{(3.90c)} \\
\frac{\partial J_a}{\partial t} &= \mathbf{H}_a : \frac{1}{\rho} \sum_{b \in \Omega_a} V_b \left(\mathbf{p}_b - \mathbf{p}_a\right) \otimes \widetilde{\nabla}_0 W_b\left(\mathbf{X}_a\right) + \\
&\quad + \mathcal{D}_2\left[J\left(\mathbf{X}_a\right)\right] + \mathcal{D}_4\left[J\left(\mathbf{X}_a\right)\right] && \text{(3.90d)}
\end{aligned}$$

The introduction of the JST terms in (3.90a) and (3.90d) may affect their global momentum conservation properties [36]. This is due to the asymmetry introduced by corrections (3.68) in the Laplacian of kernel $\widetilde{\nabla}_0 W\left(\mathbf{X}\right)$ [145]. This will require a specific procedure to recover conservation of linear and angular momenta properties for (3.90a) and (3.90d), that will be based on minimisation through Lagrange multipliers, and will be described in one of the next sections.

On the other hand, (3.90b) and (3.90c) do not need to be altered and thus respect involution conditions (2.169) in a discrete sense, thereby ensuring the geometric compatibility and frame objectivity qualities of $\mathbf{F}$ and $\mathbf{H}$.

3.7 TIME INTEGRATION

The system of ODEs with respect to time (3.90) forms a semi-discretised representation, since the time variations are still expressed in differential form.

In the case of fast elastodynamics problems, the part of solution carrying the more significant information is the transient, unsteady initial period. Theoretically, in case simulations were instead to be run with the aim of obtaining an asymptotic, steady state solution, then time dependence in (3.90) could be either entirely discarded, or alternatively, the system could be adapted into a discrete form in only one step, by a combined space-time discretisation of the Lax-Wendroff type [141, 167], opportunely adjusted to SPH.

On the other hand, the alternative approach of separating space and time discretisations of (2.162) as two distinct and consecutive steps, is known as the *method of lines* [139, 147], and is the most widely followed procedure in CFD for analyses where the unsteady part of solution is of interest [107].

To achieve this, we had first to get to (3.90); only then it is possible to integrate the RHS of the system equations, regarded as balance of fluxes, or local residual $\boldsymbol{\mathcal{R}}(\boldsymbol{\mathcal{U}}_a)$ in the region of domain assigned to a particle in $\mathbf{X}_a$, as:

$$\frac{d\boldsymbol{\mathcal{U}}_a}{dt} = \boldsymbol{\mathcal{R}}(\boldsymbol{\mathcal{U}}_a) \tag{3.91}$$

A value of $\boldsymbol{\mathcal{R}}(\boldsymbol{\mathcal{U}}_a) = \mathbf{0}$ in (3.91) would yield the steady state solution. Finite differences can be used to discretise the left hand side (LHS) in (3.91), so that the solution will be known at discrete time instants $t^0, t^1, \ldots, t^{n-1}, t^n, t^{n+1}, \ldots, T$ where T is the final instant in the simulation. The *time step size* at instant t^n will be $\Delta t^n = t^{n+1} - t^n$.

The general form of the discretised system with the method of lines will then assume the form

$$\frac{\mathcal{U}_a^{n+1} - \mathcal{U}_a^n}{\Delta t^n} = \sum_{i=1}^{m} c_i \mathcal{R}\left(\mathcal{U}_{a|i}\right) \tag{3.92}$$

Both the acceptable limits of stability for the time step size Δt^n and the quantity m of weighting coefficients c_i on the RHS of (3.92) are to be determined based on the type of time integration scheme selected.

The choice of time integration method has to be exerted between *explicit* and *implicit* methods. The nature of the case study at hand should drive the selection, as there are advantages and drawbacks for each of the two approaches. Essentially, we want to minimise both the computational cost per time step, and the overall number of time steps.

Implicit methods have the advantage of numerical stability, allowing a larger time interval length Δt [19]. This reduces the number of time steps needed to run the simulation. On the other hand, though, these methods include unknown time position data $\mathcal{U}^{n+1}$ as part of the computations, relying on the solution of a system of equations. This requires the inversion of the system matrix, which is a computer-intensive operation, and also requires additional memory storage.

Conversely, explicit methods are designed to solve (3.92) for $\mathcal{U}_a^{n+1}$, based only on known information gathered at past instants t^i, $i \leqslant n$. This implies that no matrix has to be inverted, resulting in simpler and cheaper solution progress at single time steps, with respect to implicit procedures.

However, explicit time integration techniques carry the drawback of being unstable, in case the time step size is larger than an allowable maximum Δt determined by the so-called Courant Friedrichs Lewy (CFL) condition [56]. The CFL condition depends on the refinement level of the spatial discretisation, and on elastic properties of the material:

$$\Delta t_{max} = \sigma_{CFL} \frac{\Delta \mathbf{X}}{c_p^n} \tag{3.93}$$

In (3.93), $\Delta \mathbf{X}$ is the characteristic length of the discretisation, assumed to be the average distance between two particles, c_p^n is the pressure wave speed

of the material at time t^n, and σ_{CFL} is the CFL number ($0 \leqslant \sigma_{CFL} \leqslant 1$ has to hold), a constant parameter that can be adjusted depending on the nature of the simulation.

The stability limit imposed on explicit time integration by the CFL condition (3.93) leads to short time step lengths, and explicit analyses will require a larger number of time steps than implicit ones to be completed [107, 139].

As this work is mainly concerned with fast dynamics problems of short duration in time, the larger number of time steps required by explicit integration is not much of a hindrance; for the sake of accuracy, smaller time steps would have still to be required nevertheless. For our purposes, explicit time integration is therefore preferable to implicit schemes.

The existing literature [6, 117, 136] identifies two broad categories of well established explicit time integration algorithms: *predictor-corrector schemes* and RK *multistage methods*.

Predictor-corrector numerical schemes are based on iterative approach, where an initial guess (the predictor step) of the solution at instant t^{n+1} is firstly obtained using fast but generally less accurate approach, and then is improved to match the nominal accuracy of the scheme (corrector step).

On the other hand, RK methods were originally devised to reach high orders of accuracy by relying on multiple stages within one step, as opposed to enlarging the number of time steps involved to achieve the same effect, as seen in implicit methods [19, 84]. All schemes of the RK family, in fact, evaluate $\boldsymbol{\mathcal{R}}(\boldsymbol{\mathcal{U}})$ in (3.92) many times as the solution $\boldsymbol{\mathcal{U}}$ is advanced in multiple stages from instant t^n to t^{n+1}. All temporary solutions at intermediate stages are then averaged together, and in this way they all concur to the high order of accuracy achievable.

The RK general expression for temporary solution $\boldsymbol{\mathcal{U}}^{(i)}$ at the i^{th} stage is then derived as following:

$$\begin{aligned}
\boldsymbol{\mathcal{U}}^{(1)} &= \boldsymbol{\mathcal{U}}^n \\
\boldsymbol{\mathcal{U}}^{(2)} &= \boldsymbol{\mathcal{U}}^n + \Delta t\, c_{12} \boldsymbol{\mathcal{R}}\left(\boldsymbol{\mathcal{U}}^{(1)}\right) \\
&\vdots \\
\boldsymbol{\mathcal{U}}^{(i)} &= \boldsymbol{\mathcal{U}}^n + \Delta t \sum_{j=1}^{i-1} c_{ji} \boldsymbol{\mathcal{R}}\left(\boldsymbol{\mathcal{U}}^{(j)}\right)
\end{aligned} \tag{3.94}$$

The final solution at instant $t^{n+1} = t^n + \Delta t$ is obtained from (3.94) as

$$\mathcal{U}^{n+1} = \mathcal{U}^n + \Delta t \sum_{j=1}^{i} k_j \mathcal{R}\left(\mathcal{U}^{(j)}\right) \tag{3.95}$$

In (3.95), the index i stands for the same index in (3.94), that indicates the total number of intermediate stages. In (3.94) and (3.95), c and k are sets of weighting coefficients, and their particular combinations determine the order of accuracy of the time integration [84].

However, using values of $\mathcal{U}$ at all previous stages in order to determine the current stage value, would imply having to store in memory a considerable quantity of data. This would amount to all solution variables in $\mathcal{U}$, at all particles positions, times the number of stages required.

This practical complication imposes a restriction on the number of intermediate stages considered; it also makes convenient the adoption of a simplified RK multistage scheme, where only the stage previous to the current needs to be stored [263]:

$$\begin{aligned}
\mathcal{U}^{(1)} &= \mathcal{U}^n \\
\mathcal{U}^{(2)} &= \mathcal{U}^n + \Delta t\, c_1 \mathcal{R}\left(\mathcal{U}^{(1)}\right) \\
&\vdots \\
\mathcal{U}^{(i)} &= \mathcal{U}^n + \Delta t\, c_{i-1} \mathcal{R}\left(\mathcal{U}^{(i-1)}\right)
\end{aligned} \tag{3.96}$$

At instant t^{n+1}, the solution obtained will be a combination of those yielded at intermediate stages in (3.96), similar to what done for (3.95):

$$\mathcal{U}^{n+1} = \mathcal{U}^n + \Delta t \sum_{j=1}^{i} k_j \mathcal{R}\left(\mathcal{U}^{(j)}\right) \tag{3.97}$$

The maximum order of accuracy achievable by a RK scheme is equal to its number of stages, so for instance (3.96) will be of i^{th} order of accuracy [107]. The particular choice of weighting coefficients c and k will determine whether the maximum order of accuracy is reached or not; optimisation procedures are adopted for achieving this through error minimisation processes, as shown in [111, 210].

Alternatively, if accuracy is not the most pressing issue, one can decide to select c and k coefficients with the aim of enhancing the stability of the RK scheme, enabling to expand the time step size for the simulation [249, 250].

This latter design choice has proven popular in CFD, where fourth order RK methods are in the most widespread usage for discretisation of systems of hyperbolic equations of Euler or Navier-Stokes type. The elimination of high frequency oscillations in the solution is a very important issue for these problems: in this regard, the addition of a high-gradient artificial dissipation term – such as the JST technique presented in section 3.6 – to the discretised system has proven to be an effective remedy.

Jameson and co-workers, in particular, have demonstrated [119, 120, 122] that multistage (4^{th} order) RK time integration of the type (3.96)-(3.97), coupled with the JST technique presented in section 3.6, leads to a numerical scheme for solving systems of conservation laws that has both enhanced stability properties and high-order accuracy.

In addition, further research by Shu et al [54, 229] proved that it is possible to bring the number of stages of the RK temporal scheme down to two, while retaining a sufficiently high (2^{nd}) order of accuracy, in case the numerical discretisation satisfies the criterion of TVD, first formulated by Harten in [100, 101].

The TVD requirement essentially enforces the *monotonicity* of the scheme – that is, the solution cannot assume new maxima or minima during its time evolution, but is only allowed to retain the ones already present in the initial condition field – through bounded total variation [139]. This way, spurious oscillations cannot appear in the solution field.

Further, in the present case the 2^{nd} order of the temporal scheme would match that of the SPH spatial discretisation; higher orders of temporal accuracy should then be regarded as an unnecessary complication.

A 2-stage RK scheme reaches 2^{nd} order accuracy when the weighting coefficients c_i in (3.96) assume the values [107]:

$$c_i = \frac{1}{2}, \quad i = 1, 2 \tag{3.98}$$

The 2-stages, total variation diminishing, Runge Kutta (TVD-RK) integration scheme selected to march in time the solution vector $\mathcal{U}$ of system (3.90) will then assume the form:

$$\mathcal{U}_a^* = \mathcal{U}_a^n + \Delta t \mathcal{R}_a (\mathcal{U}_a^n, t^n) \tag{3.99a}$$

$$\mathcal{U}_a^{**} = \mathcal{U}_a^* + \Delta t \mathcal{R}_a (\mathcal{U}_a^*, t^n) \tag{3.99b}$$

$$\mathcal{U}_a^{n+1} = \frac{1}{2} (\mathcal{U}_a^n + \mathcal{U}_a^{**}) \tag{3.99c}$$

We have already mentioned that particles positions $\mathbf{x}$ do not play any role in the $\{\mathbf{p}, \mathbf{F}, \mathbf{H}, J\}$ mixed formulation system, as $\mathbf{x}$ is not part of solution vector $\mathcal{U}$.

However, the moment conservation algorithm that will be introduced in the next section will require the particles position vectors $\mathbf{x}$ to be updated at each step of a simulation. Moreover, capability to track the deformation history of an object will always be essential for visualisation purposes. Updates of $\mathbf{x}$ for each particle in the model will be performed using the TVD-RK algorithm (3.99), making JST-SPH a *monolithic solver*. Thus, for n particles, their positions $\mathbf{x}_a$, $a = 1, \ldots, n$ are to be obtained from the corresponding linear momenta $\mathbf{p}_a$ as

$$\mathbf{x}_a^* = \mathbf{x}_a^n + \frac{\Delta t}{\rho} \mathbf{p}_a^n \tag{3.100a}$$

$$\mathbf{x}_a^{**} = \mathbf{x}_a^* + \frac{\Delta t}{\rho} \mathbf{p}_a^* = \mathbf{x}_a^n + \frac{\Delta t}{\rho} (\mathbf{p}_a^n + \mathbf{p}_a^*) \tag{3.100b}$$

$$\mathbf{x}_a^{n+1} = \frac{1}{2} (\mathbf{x}_a^n + \mathbf{x}_a^{**}) = \mathbf{x}_a^n + \frac{\Delta t}{2\rho} (\mathbf{p}_a^n + \mathbf{p}_a^*) \tag{3.100c}$$

3.8 DISCRETE MOMENTUM PRESERVING ALGORITHM

Without considering external torques acting on the system, a property of physical system that numerical models should be capable to reproduce is the conservation of its angular momentum in time, which in its discrete version,

for a system with n particles (and without externally acting torques), reads as

$$\sum_{i=1}^{n} \mathbf{x}_i^{n+1} \times \mathbf{p}_i^{n+1} - \sum_{i=1}^{n} \mathbf{x}_i^{n} \times \mathbf{p}_i^{n} = \mathbf{0} \tag{3.101}$$

where the n and $n+1$ superscripts respectively stand for the current instant, and for the next one to come, in the simulation time history.

In [36], Bonet and co-workers have shown that a SPH discrete system preserves its total angular momentum if it also respects the consistency condition (3.62) imposed on the gradient of the kernel. As the JST-SPH method directly enforces (3.62) on ∇W in order to obtain a modified $\widetilde{\nabla} W$, and achieve completeness for regions at and near the boundaries, it might be thought that this algorithm is free from issues arising when principle (3.101) does not hold true. Namely, a non-physical loss of energy with time, that makes final results unreliable.

Instead, the loss of angular momentum may occur not due to a flaw of the spatial discretisation, but as a consequence of the adopted mixed system with strain variables $\mathbf{F}$, $\mathbf{H}$ and J amongst the unknowns.

As these variables do not formally depend any more from the geometry†, they cannot be relied upon in order to satisfy (3.101).

Lack of geometric compatibility for the strain unknowns in the mixed $\{\mathbf{p}, \mathbf{F}, \mathbf{H}, J\}$ system, however, is not the only cause for the missed validity of (3.101): both JST dissipation terms (3.88), in fact, are partly made of corrected Laplacians that, as a result of corrections (3.68), are left asymmetric. Asymmetries in the system, in effect, prevent it to remain invariant with respect to rigid body translations, and hence not only the angular, but even the linear momentum are not preserved when progressing from one time step to the next [36].

In a series of papers, Simo and co-workers [237, 239] were first to present a novel class of implicit time stepping algorithms of the Newmark type able to preserve the global angular momenta, as well as the energy of discretised nonlinear Hamiltonian systems, without significant additional computational costs. The same authors successfully tested the method in applications spanning from rigid body dynamics, nonlinear rods and shells

† That is, in general, here $\mathbf{F} = \nabla_0 \mathbf{x}$, $\mathbf{H} = \det(\nabla_0 \mathbf{x})\, \nabla_0 \mathbf{x}^{-\mathsf{T}}$ and $J = \det \nabla_0 \mathbf{x}$ do not generally hold.

[238], to plasticity effects in high-strain dynamics [234]. They also later improved the accuracy of their momentum-preserving formulation taking it from the 2^{nd} to the 4^{th} order [252].

Investigation of global energy and momentum preservation properties was conducted by Gonzalel and Simo in [94] on the discretisation of a simple, nonlinear solid dynamics system, with implicit time-marching algorithms. The lack of need of any additional parameters or equations makes this method attractive, and a subsequent paper by the first author appeared years later, where it was applied to treat compressible and incompressible hyperelasticity problems employing Ogden-type material models, with encouraging results [93].

A survey of the conditions that a system of PDEs must satisfy in order to preserve its overall angular momentum was conducted, from a mathematical perspective, in [46], with the aim of establishing guidelines for conception and design of momentum and energy preserving time stepping algorithms.

Komatitsch et al. [134] studied the momentum preservation properties and the temporal stability of an explicit/implicit, predictor-corrector scheme, and applied it in a geological simulation in the linear elastodynamics regime.

Betsch and co-workers employed one-step, implicit time-marching schemes in [28, 96] to build a momentum-preserving discretisation method based on borrowing strain modification quadrature rules for lower order FE in space, for the purpose of time integration.

A series of papers by Lew and co-workers [149, 150] assesses the opportunity of bypassing the issue of preservation of momentum altogether. This opportunity would be offered by the derivation and adoption of a family of *variational* time stepping algorithms, of the kind initially proposed in [127] by Kane et al. Variational time schemes would preserve symmetry properties of the elastodynamics system of PDEs, and hence guarantee the conservation of global angular momentum, without having to enforce this prerequisite by resorting to *ad hoc* modifications to the code.

Recently, global angular momentum preservation mechanisms were adopted [1, 143] in the context of a simplified, non-polyconvex $\{\mathbf{p}, \mathbf{F}\}$ mixed formulation, that were subsequently extended to the full $\{\mathbf{p}, \mathbf{F}, \mathbf{H}, J\}$ mixed formulation in the context of upwind, cell-centred FV [99]; analogous work

was done in the context of a spatial discretisation obtained with SPH for the two cases of upwind Petrov-Galerkin SPH [146] and JST-SPH [145].

The description of the global angular momentum preserving algorithm, undertaken in the remaining part of this section, will largely draw upon [145] and [99].

Substituting $\mathbf{x}^{n+1}$ from (3.100c) in (3.101) yields

$$\begin{aligned}
&\sum_{i=1}^{n}\left[\mathbf{x}_i^n+\frac{\Delta t}{2\rho}\left(\mathbf{p}_i^n+\mathbf{p}_i^*\right)\right]\times\mathbf{p}_i^{n+1}-\sum_{i=1}^{n}\mathbf{x}_i^n\times\mathbf{p}_i^n=0 \xrightarrow[\left(\mathbf{x}_i^{n+1/2}=\mathbf{x}_i^n+\frac{\Delta t}{2\rho}\mathbf{p}_i^n\right)]{}\\
&\sum_{i=1}^{n}\mathbf{x}_i^{n+1/2}\times\mathbf{p}_i^{n+1}+\frac{\Delta t}{2\rho}\sum_{i=1}^{n}\mathbf{p}_i^*\times\mathbf{p}_i^{n+1}-\sum_{i=1}^{n}\mathbf{x}_i^n\times\mathbf{p}_i^n=0 \xrightarrow[\left(\mathbf{p}_i^n\times\mathbf{p}_i^n=0\right)]{}\\
&\qquad\sum_{i=1}^{n}\mathbf{x}_i^{n+1/2}\times\left(\mathbf{p}_i^{n+1}-\mathbf{p}_i^n\right)+\frac{\Delta t}{2\rho}\sum_{i=1}^{n}\mathbf{p}_i^*\times\mathbf{p}_i^{n+1}=0
\end{aligned}\tag{3.102}$$

Positions $\mathbf{x}_i^{n+1/2}$, $i=1,\dots,n$ in (3.102) can be understood as intermediate stages in the advancement of the solution from instant t^n to t^{n+1}, in case time integration were to be performed with the trapezoidal rule [115]. In that case, $\mathbf{x}^{n+1}$ would have to be computed as:

$$\mathbf{x}_i^{n+1}=\mathbf{x}_i^n+\frac{\Delta t}{2\rho}\left(\mathbf{p}_i^n+\mathbf{p}_i^{n+1}\right)\qquad i=1,\dots,n\tag{3.103}$$

Incidentally, it is useful to bear in mind that the sequence of algebraic manipulations that equation (3.101) is being subjected to, aims to reformulate it by excluding any term at instant t^{n+1} from its final expression.

Proceeding in this manner, we will end up obtaining an expression suitable for explicit time integration.

With this purpose, (3.102) further evolves into:

$$\begin{aligned}
&\sum_{i=1}^{n}\left(\mathbf{x}_i^{n+1/2}+\frac{\Delta t}{2\rho}\mathbf{p}_i^*\right)\times\left(\mathbf{p}_i^{n+1}-\mathbf{p}_i^n\right)+\frac{\Delta t}{2\rho}\sum_{i=1}^{n}\mathbf{p}_i^*\times\mathbf{p}_i^n=0 \xrightarrow[\left(\mathbf{p}_i^*\times\mathbf{p}_i^*=0\right)]{}\\
&\qquad\sum_{i=1}^{n}\left(\mathbf{x}_i^{n+1/2}+\frac{\Delta t}{2\rho}\mathbf{p}_i^*\right)\times\left(\mathbf{p}_i^{n+1}-\mathbf{p}_i^n\right)+\frac{\Delta t}{2\rho}\sum_{i=1}^{n}\mathbf{p}_i^*\times\left(\mathbf{p}_i^n-\mathbf{p}_i^*\right)=0
\end{aligned}\tag{3.104}$$

Noting that, applying the RK scheme (3.99) for the update in time from $\mathbf{p}^n$ to $\mathbf{p}^{n+1}$ generates the following sequence of stages:

$$\mathbf{p}_i^* = \mathbf{p}_i^n + \Delta t \dot{\mathbf{p}}_i^n \tag{3.105a}$$

$$\mathbf{p}_i^{**} = \mathbf{p}_i^n + \Delta t \left(\dot{\mathbf{p}}_i^n + \dot{\mathbf{p}}_i^*\right) \tag{3.105b}$$

$$\mathbf{p}_i^{n+1} = \mathbf{p}_i^n + \frac{\Delta t}{2} \left(\dot{\mathbf{p}}_i^n + \dot{\mathbf{p}}_i^*\right) \tag{3.105c}$$

we can then introduce (3.105a) and (3.105c) into (3.104) in order to obtain

$$\begin{aligned}
&\frac{\Delta t}{2}\left[\sum_{i=1}^{n}\left(\mathbf{x}_i^{n+1/2} + \frac{\Delta t}{2\rho}\mathbf{p}_i^*\right) \times \left(\dot{\mathbf{p}}_i^n + \dot{\mathbf{p}}_i^*\right) - \frac{\Delta t}{\rho}\sum_{i=1}^{n}\mathbf{p}_i^* \times \dot{\mathbf{p}}_i^n\right] = 0 \longrightarrow \\
&\sum_{i=1}^{n}\left(\mathbf{x}_i^{n+1/2} + \frac{\Delta t}{2\rho}\mathbf{p}_i^*\right) \times \dot{\mathbf{p}}_i^* + \sum_{i=1}^{n}\mathbf{x}_i^n \times \dot{\mathbf{p}}_i^n + \\
&\qquad + \frac{\Delta t}{2\rho}\sum_{i=1}^{n}\mathbf{p}_i^n \times \dot{\mathbf{p}}_i^n - \frac{\Delta t}{2\rho}\sum_{i=1}^{n}\mathbf{p}_i^* \times \dot{\mathbf{p}}_i^n = 0 \xrightarrow[\text{see (3.105a)}]{} \\
&\sum_{i=1}^{n}\left(\mathbf{x}_i^{n+1/2} + \frac{\Delta t}{2\rho}\mathbf{p}_i^*\right) \times \dot{\mathbf{p}}_i^* + \sum_{i=1}^{n}\mathbf{x}_i^n \times \dot{\mathbf{p}}_i^n + \\
&\qquad + \frac{\Delta t}{2\rho}\sum_{i=1}^{n}\left[\cancel{(\mathbf{p}_i^n \times \dot{\mathbf{p}}_i^n)} - \cancel{(\mathbf{p}_i^n \times \dot{\mathbf{p}}_i^n)} - \Delta t\cancel{(\dot{\mathbf{p}}_i^n \times \dot{\mathbf{p}}_i^n)}\right] = 0
\end{aligned} \tag{3.106}$$

Equation (3.106) achieves the objective of rearranging (3.101) without any dependence on t^{n+1}, presenting it only in terms of quantities at the starting time instant t^n, or at first stage of the RK procedure, t^*. To highlight this aspect, (3.106) can be rewritten as

$$\sum_{i=1}^{n}\mathbf{x}_i^n \times \dot{\mathbf{p}}_i^n + \sum_{i=1}^{n}\left[\mathbf{x}_i^n + \frac{\Delta t}{2\rho}\left(\mathbf{p}_i^n + \mathbf{p}_i^*\right)\right] \times \dot{\mathbf{p}}_i^* = 0 \tag{3.107}$$

Compliance with (3.107) can be imposed by setting both summation terms that compose (3.107) to 0:

$$\sum_{i=1}^{n}\mathbf{x}_i^n \times \dot{\mathbf{p}}_i^n = 0 \tag{3.108a}$$

$$\sum_{i=1}^{n}\left[\mathbf{x}_i^n + \frac{\Delta t}{2\rho}\left(\mathbf{p}_i^n + \mathbf{p}_i^*\right)\right] \times \dot{\mathbf{p}}_i^* = 0 \tag{3.108b}$$

In essence, (3.108) imposes condition (3.108a) at the first stage of the RK algorithm, and condition (3.108b) at the second.

From the conservation law of the linear momentum, (3.90a), and ignoring external forces, it follows that $\dot{\mathbf{p}}^\eta$, for $\eta = \{n, *\}$ in (3.107) is equal to

$$\begin{aligned}\dot{\mathbf{p}}_a^\eta &= -\sum_{b\in\Omega_a} V_b \left[\mathbf{P}_b^\eta \widetilde{\nabla}_0 W_a(\mathbf{X}_b) - \mathbf{P}_a^\eta \widetilde{\nabla}_0 W_b(\mathbf{X}_a)\right] + \boldsymbol{\mathcal{D}}_{a|\mathrm{JST}}^\eta = \\ &= \mathbf{T}_a^\eta + \boldsymbol{\mathcal{D}}_{a|\mathrm{JST}}^\eta \qquad a = 1,\dots,n, \quad \eta = \{n, *\} \end{aligned} \tag{3.109}$$

In (3.109), the internal forces vector $\mathbf{T}_a^\eta$, $a = 1,\dots,n$, $\eta = \{n, *\}$, is defined as

$$\begin{aligned}\mathbf{T}_a^\eta = -\sum_{b\in\Omega_a} V_b \left[\mathbf{P}_b^\eta \widetilde{\nabla}_0 W_a(\mathbf{X}_b) - \mathbf{P}_a^\eta \widetilde{\nabla}_0 W_b(\mathbf{X}_a)\right] \\ a = 1,\dots,n; \quad \eta = \{n, *\}\end{aligned} \tag{3.110}$$

while the JST dissipation term $\boldsymbol{\mathcal{D}}_{a|\mathrm{JST}}^\eta$, $a = 1,\dots,n$, $\eta = \{n, *\}$ was first defined in (3.83).

As already mentioned in section 3.6, the inclusion of the JST artificial dissipation term introduces an asymmetry in the mixed system of conservation laws (3.82a). As a consequence of this asymmetry, the total quantity of linear momentum $\mathbf{p}$ cannot be preserved from one instant t^n to the next t^{n+1}. Additionally, satisfaction of conditions (3.108) would modify the values $\mathbf{T}^\eta$ as computed by the solver, and thus conservation of linear momentum would need to be verified anew.

Hence, it is convenient to simultaneously enforce the conservation of both linear and angular momentum in time, leading to the establishment of four

conditions for $\mathbf{T}^\eta$ and $\mathcal{D}^\eta_{JST}$ to be verified at each stage of the RK numerical time integration:

$$\sum_{a=1}^{n} V_a \mathbf{T}^\eta_a = 0 \tag{3.111a}$$

$$\sum_{a=1}^{n} V_a \mathcal{D}^\eta_{a|JST} = 0 \tag{3.111b}$$

$$\sum_{a=1}^{n} V_a \Gamma^\eta_a \times \mathbf{T}^\eta_a = 0 \qquad \eta = \{n, *\} \tag{3.111c}$$

$$\sum_{a=1}^{n} V_a \Gamma^\eta_a \times \mathcal{D}^\eta_{a|JST} = 0 \tag{3.111d}$$

In (3.111), Γ^η_a for $a = 1, \dots, n$ assumes values as following (see (3.108)):

$$\Gamma^\eta_a = \begin{cases} \mathbf{x}^n_a & \eta = n \\ \mathbf{x}^n_a + \frac{\Delta t}{2\rho}\left(\mathbf{p}^n_a + \mathbf{p}^*_a\right) & \eta = * \end{cases} \qquad a = 1, \dots, n \tag{3.112}$$

Modified internal forces $\widehat{\mathbf{T}}_a$ and JST dissipation terms $\widehat{\mathcal{D}}_a$ able to satisfy (3.111) for each particle at $\mathbf{X}_a$ can be obtained through the method of Lagrange multipliers [43], which requires the minimisation of functionals built as in below:

$$\begin{aligned} \Pi_{\mathbf{T}}\left(\widehat{\mathbf{T}}_a, \boldsymbol{\lambda}_{lin}, \boldsymbol{\lambda}_{ang}\right) = \frac{1}{2}\sum_{a=1}^{n} V_a \left(\widehat{\mathbf{T}}_a - \mathbf{T}_a\right)\cdot\left(\widehat{\mathbf{T}}_a - \mathbf{T}_a\right) + \\ - \boldsymbol{\lambda}_{lin}\sum_{a=1}^{n} V_a \widehat{\mathbf{T}}_a - \boldsymbol{\lambda}_{ang}\sum_{a=1}^{n} V_a \Gamma_a \times \widehat{\mathbf{T}}_a \end{aligned} \tag{3.113a}$$

$$\begin{aligned} \Pi_{\mathcal{D}}\left(\widehat{\mathcal{D}}_a, \gamma_{lin},\ \gamma_{ang}\right) = \frac{1}{2}\sum_{a=1}^{n} V_a \left(\widehat{\mathcal{D}}_a - \mathcal{D}_a\right)\cdot\left(\widehat{\mathcal{D}}_a - \mathcal{D}_a\right) + \\ - \gamma_{lin}\sum_{a=1}^{n} V_a \widehat{\mathcal{D}}_a - \gamma_{ang}\sum_{a=1}^{n} V_a \Gamma_a \times \widehat{\mathcal{D}}_a \end{aligned} \tag{3.113b}$$

In (3.113), $\boldsymbol{\lambda}_{lin}$, $\boldsymbol{\lambda}_{ang}$, γ_{lin} and γ_{ang} are vectorial Lagrange multipliers to be found at the end of the procedure. They will contribute to the formulation of momentum-preserving $\widehat{\mathbf{T}}$ and $\widehat{\mathcal{D}}$.

Minimisation of $\Pi_{\mathbf{T}}$ and $\Pi_{\boldsymbol{\mathcal{D}}}$ in (3.113) is accomplished by imposing the following conditions on their derivatives:

$$\frac{\partial \Pi_{\mathbf{T}}}{\partial \widehat{\mathbf{T}}} = 0\,, \qquad \frac{\partial \Pi_{\boldsymbol{\mathcal{D}}}}{\partial \widehat{\boldsymbol{\mathcal{D}}}} = 0 \tag{3.114a}$$

$$\frac{\partial \Pi_{\mathbf{T}}}{\partial \boldsymbol{\lambda}_{\mathrm{lin}}} = 0\,, \qquad \frac{\partial \Pi_{\boldsymbol{\mathcal{D}}}}{\partial \boldsymbol{\gamma}_{\mathrm{lin}}} = 0$$

$$\frac{\partial \Pi_{\mathbf{T}}}{\partial \boldsymbol{\lambda}_{\mathrm{ang}}} = 0\,, \qquad \frac{\partial \Pi_{\boldsymbol{\mathcal{D}}}}{\partial \boldsymbol{\gamma}_{\mathrm{ang}}} = 0 \tag{3.114b}$$

Conditions (3.114a) lead to the following expressions for $\widehat{\mathbf{T}}$ and $\widehat{\boldsymbol{\mathcal{D}}}$:

$$\widehat{\mathbf{T}}_a = \mathbf{T}_a + \boldsymbol{\lambda}_{\mathrm{lin}} + \boldsymbol{\lambda}_{\mathrm{ang}} \times \Gamma_a \tag{3.115a}$$

$$\widehat{\boldsymbol{\mathcal{D}}}_a = \boldsymbol{\mathcal{D}}_a + \boldsymbol{\gamma}_{\mathrm{lin}} + \boldsymbol{\gamma}_{\mathrm{ang}} \times \Gamma_a \tag{3.115b}$$

Substituting expressions (3.115) in equations (3.114b), and making use of the permutation tensor $\boldsymbol{\mathcal{E}}_{ijk}\,(\mathbf{a})_j = [\mathbf{A}]_{ik}$ ‡, and of properties of the cross product such as (2.25), we obtain two system of equations that can be solved for $\boldsymbol{\lambda}_{\mathrm{lin}}$, $\boldsymbol{\lambda}_{\mathrm{ang}}$ and for $\boldsymbol{\gamma}_{\mathrm{lin}}$, $\boldsymbol{\gamma}_{\mathrm{ang}}$:

$$\begin{bmatrix} \sum_{a=1}^{n} V_a \boldsymbol{\mathcal{E}}_{ijk}\,(\Gamma_a)_j & -\sum_{a=1}^{n} V_a \\ \sum_{a=1}^{n} V_a \left[(\Gamma_a \cdot \Gamma_a)\,\mathbf{I} - \Gamma_a \otimes \Gamma_a\right] & \sum_{a=1}^{n} V_a \boldsymbol{\mathcal{E}}_{ijk}\,(\Gamma_a)_j \end{bmatrix} \begin{pmatrix} \boldsymbol{\lambda}_{\mathrm{lin}} \\ \boldsymbol{\lambda}_{\mathrm{ang}} \end{pmatrix} = \\ = \begin{pmatrix} \sum_{a=1}^{n} V_a \mathbf{T}_a \\ -\sum_{a=1}^{n} V_a \Gamma_a \times \mathbf{T}_a \end{pmatrix} \tag{3.116a}$$

$$\begin{bmatrix} \sum_{a=1}^{n} V_a \boldsymbol{\mathcal{E}}_{ijk}\,(\Gamma_a)_j & -\sum_{a=1}^{n} V_a \\ \sum_{a=1}^{n} V_a \left[(\Gamma_a \cdot \Gamma_a)\,\mathbf{I} - \Gamma_a \otimes \Gamma_a\right] & \sum_{a=1}^{n} V_a \boldsymbol{\mathcal{E}}_{ijk}\,(\Gamma_a)_j \end{bmatrix} \begin{pmatrix} \boldsymbol{\gamma}_{\mathrm{lin}} \\ \boldsymbol{\gamma}_{\mathrm{ang}} \end{pmatrix} = \\ = \begin{pmatrix} \sum_{a=1}^{n} V_a \boldsymbol{\mathcal{D}}_a \\ -\sum_{a=1}^{n} V_a \Gamma_a \times \boldsymbol{\mathcal{D}}_a \end{pmatrix} \tag{3.116b}$$

At this point, solving systems (3.116) yields the pairs of Lagrange multipliers $\boldsymbol{\lambda}_{\mathrm{lin}}$, $\boldsymbol{\lambda}_{\mathrm{ang}}$ and $\boldsymbol{\gamma}_{\mathrm{lin}}$, $\boldsymbol{\gamma}_{\mathrm{ang}}$, that can be substituted, respectively, in (3.115a) and (3.115b) in order to finally obtain $\widehat{\mathbf{T}}$ and $\widehat{\boldsymbol{\mathcal{D}}}$ that conserve global linear and angular momenta.

‡ Here $\mathbf{a}$ is an arbitrary vector; the application of the permutation tensor on it will result in a second order tensor $\mathbf{A}$.

3.8.1 *Discrete Jacobian Preserving Algorithm*

Since non-symmetrical JST dissipation terms were added not only to the linear momentum conservation law (3.82a), but also to the Jacobian of the deformation conservation statement (3.82d), there exist now the need to develop an algorithm for preserving the Jacobian J (that as we recall tracks the volumetric deformation) at every instant of the simulation.

This algorithm can be designed along the same lines as the one described in section 3.8, with a potential to minimise $\Pi_{\mathcal{D}_{J|a}}$ depending from a scalar Lagrange multiplier $\gamma_{\mathcal{D}_J}$ as parameter:

$$\Pi_{\mathcal{D}_{J|a}}\left(\widehat{\mathcal{D}}_{J|a}, \gamma_{\mathcal{D}_J}\right) = \frac{1}{2}\sum_{a=1}^{n} V_a\left(\widehat{\mathcal{D}}_{J|a} - \mathcal{D}_{J|a}\right)^2 - \gamma_{\mathcal{D}_J}\sum_{a=1}^{n} V_a\widehat{\mathcal{D}}_{J|a} \tag{3.117}$$

where, for each particle $a = 1, \dots, n$:

$$\mathcal{D}_{J|a} = \mathcal{D}_2\left[J(\mathbf{X}_a)\right] + \mathcal{D}_4\left[J(\mathbf{X}_a)\right] .$$

Similarly to what done in the previous section, setting

$$\frac{\partial \Pi_{\mathcal{D}_{J|a}}}{\partial \widehat{\mathcal{D}}_{J|a}} = 0\,; \qquad\qquad \frac{\partial \Pi_{\mathcal{D}_{J|a}}}{\partial \gamma_{\mathcal{D}_J}} = 0 \tag{3.118}$$

will yield a set of preserved $\widehat{\mathcal{D}}_J$, modified as

$$\widehat{\mathcal{D}}_{J|a} = \mathcal{D}_{J|a} + \gamma_{\mathcal{D}_J} \qquad\qquad a = 1, \dots, n \tag{3.119}$$

The second condition in (3.118) will then give out $\gamma_{\mathcal{D}_J}$ as

$$\gamma_{\mathcal{D}_J} = -\frac{\sum_{a=1}^{n} V_a \mathcal{D}_{J|a}}{\sum_{a=1}^{n} V_a} \tag{3.120}$$

Substituting $\gamma_{\mathcal{D}_J}$ from (3.120) in (3.119) will result in a JST modified term $\widehat{\mathcal{D}}_{J|a}$ capable to preserve globally the Jacobian J of the deformation.

3.9 COMPUTER IMPLEMENTATION

Computer code implementation of the JST-SPH methodology is written in modern Fortran (using features up to version 95); for the conservation algorithms presented in this section 3.8, it makes extensive use of the LAPACK library [4] for solving linear systems of equations (3.116). More precisely, the program accomplishes that task by employing the LAPACK subroutine DGESV, which provides a solution to systems of real, linear equations of the type $\mathbf{AX} = \mathbf{B}$ with the help of a LU decomposition with partial pivoting and row interchanges [105], so that system matrix $\mathbf{A}$ is reduced to a factored form, and the system of equations can be quickly solved for $\mathbf{X}$ [4].

A scheme of the whole algorithm, illustrating the code flow, is presented in algorithm 3.

INITIALISATION

1. Initiate all variables (set of particles geometry, material properties, numerical parameters, $\mathbf{p}_a$, $\mathbf{F}_a$, $\mathbf{P}_a$, $\mathbf{x}_a$ for each particle a).
2. Compute SPH kernel smoothing length $h = \alpha(V_{tot}/N)^{1/3}$
3. Locate neighbours b for each target particle a, using the alternating digital tree (ADT) search algorithm [38].
4. Compute corrected kernel $\widetilde{W}$, its gradient $\widetilde{\boldsymbol{\nabla}}W$ and its Laplacian $\widetilde{\boldsymbol{\nabla}}^2 W$.

TIME-STEPPING THE SOLUTION

FOR $t < t_f$

1. Compute wave speeds $c_{p|a} = \frac{\sqrt{\lambda+2\mu}}{\rho_0} / \max_{\alpha} \lambda_{\mathbf{C}|\alpha}$.
2. Compute time step Δt (3.93).
3. RK time stepping (3.99):
   FOR RK $= 1, 2$
   a) Advance $\mathbf{p}$ (3.82a).
   b) Compute JST term (3.88).
   c) Apply conservation of angular momentum on $\mathbf{T}_a$ and JST term $\mathcal{D}_a$ (3.116).
   d) Advance the other variables $\mathbf{F}$, $\mathbf{H}$ and J (3.82).
   e) Impose BCs
   f) Compute first Piola-Kirchhoff stress tensor $\mathbf{P}_a$ following sections 2.9 and 2.10 and algorithm 2.
4. Obtain conserved variables values and particles positions at time $n+1$ through averaging RK steps (3.99).

ALGORITHM 3 : algorithmic flow for the JST-SPH method

3.10 CONCLUDING REMARKS

This chapter described in its main components a novel numerical methodology, named JST-SPH, intended to constitute an effective alternative to the currently widespread FEM in solving nonlinear fast solid dynamics problems. A brief description of FEM, followed by an overview of meshless numerical schemes are located respectively in section 3.1 and in section 3.2.

JST-SPH provides SPH discretisation to the mixed $\{\mathbf{p}, \mathbf{F}, \mathbf{H}, J\}$ system of conservation laws developed in chapter 2. The main features of SPH are the subject of section 3.3.

By performing a number of corrections to the original SPH scheme, of the manner detailed in section 3.4, the kernel and its derivatives do not suffer from lack of consistency at or near the domain boundaries. Also, the tensile instability issue encountered in solid dynamics simulations run with SPH is addressed by switching the framework to a total Lagrangian point of view; see section 3.4.5.

A provisional version of the spatial semi-discretisation of the mixed system performed with the aforementioned corrected SPH scheme is shown in section 3.5; however, the discretised system may still suffer from spurious oscillatory behaviour, caused by SPH nodal integration. These problems are experienced by the pressure term in the equation of motion, (3.82a), and by the Jacobian of the deformation, also a measure of volumetric dilatation and an unknown in equation eq. (3.82d). Given that non-physical oscillatory patterns are also observed in analogous hyperbolic systems of PDEs in CFD, section 3.6 introduces an artificial JST dissipation term borrowed from the CFD literature, that makes use of biharmonic $\nabla(\nabla\cdot)$ operators in order to stabilise the wiggling solution terms.

Various types of time stepping schemes for the JST-SPH spatially semi-discretised system were considered in section 3.7, before an explicit, two stages TVD-RK method is selected for its simplicity, its explicit nature advantageous for the kind of problems at hand, and its TVD quality on energy conservation.

A drawback to the introduction of the JST dissipation term is the loss of preservation of the total angular momentum of the system. A procedure that realigns the total angular momentum to its initial values at each time

step of the simulation, is presented in section 3.8; a similar readjustment is done for the Jacobian of the deformation in section 3.8.1, as also its conservation law makes use of a JST term. This novel angular momentum preserving algorithm, based on Lagrange multipliers minimisation, modifies the internal stresses term; as a consequence, the preserving algorithm has to be expanded into a system, in order to accommodate for a similar procedure targeting the linear momentum.

The next chapter will focus on the stability properties of the proposed JST-SPH scheme. Rigorous stability analyses have been established for discretisations of linear systems of PDEs, the most renown being the von Neumann stability analysis.

Hence, the JST-SPH discretisation will be investigated for stability on simple, linear PDEs; these equations are similar to the linearised version of nonlinear PDEs, and can provide with a good account on local behaviours of nonlinear problems.

4 ACCURACY AND STABILITY ANALYSIS

As previously indicated in section 3.10, the present chapter will be devoted to the study of the consistency and stability of the JST-SPH scheme.

The order of accuracy of a numerical scheme is determined from the higher order terms (h.o.t.) in its truncation error. Stability analysis, on the other hand, is performed with the tools of the *von Neumann analysis*, using spectral decomposition to yield a graphical representation of the margins of stability for a scheme. Moreover, *dissipation and dispersion errors* give out more information about the stability behaviour of a scheme.

The main limitation of the von Neumann analysis is that it applies only to linear schemes. However, the stability characteristics for discretised nonlinear systems of PDEs can only be checked at the local level, through linearisation.

A simple example of a one-dimensional linear advection equation (LAE), presenting derivatives in space and time of the unknown variable u, will constitute the object of our JST-SPH stability analysis. Its SPH discretisation is introduced in section 4.1.

In section 4.2, the truncation error and the eigenvalues decomposition of the SPH-discretised LAE are examined under the varying parameters of:

1. number of neighbouring particles per side (p.p.s.) of the target position;
2. presence (or absence) of the JST term.

For those same cases, dissipation and dispersion errors are shown in section 4.3. Some conclusive remarks are finally drawn in section 4.4.

4.1 DISCRETISATION PROCESS

The one-dimensional LAE governs the propagation of a signal having wave speed c and amplitude given by the unknown u:

$$\frac{\partial u}{\partial t} + c\frac{\partial u}{\partial x} = 0 \tag{4.1}$$

Equation (4.1) is a hyperbolic PDE. As such, it can be solved with the method of lines: first, it is reduced to an ODE in time, which then can be solved by any method able to numerically evaluate initial value problems, such as the TVD-RK algorithm described in section 3.7.

In any event, the semi-discretisation in space must be implemented first; in the present case, we will resort to SPH. The derivation of discretised equations from the weak formulation can be arranged in two steps:

1. *nodal integration* of the virtual work expression over a finite set of particles Ω discretising the domain $\mathcal{B}$;
2. *interpolation* by a *reproducing kernel* of the dependent variable at each target particle a from its values in the neighbouring particles b.

The weak formulation of (4.1) over a one-dimensional domain $\mathcal{B}$ is obtained by introducing a virtual variable δF, work conjugate to the unknown u, to yield, in the reference configuration:

$$\int_{\mathcal{B}} \delta F \frac{\partial u}{\partial t} dx = -c \int_{\mathcal{B}} \delta F \frac{\partial u}{\partial x} dx \tag{4.2}$$

Integrating by parts the RHS in (4.2), and using the divergence theorem:

$$\begin{aligned} \int_{\mathcal{B}} \delta F \frac{\partial u}{\partial t} dx &= -c \left(\int_{\mathcal{B}} \frac{\partial (\delta F u)}{\partial x} dx - \int_{\mathcal{B}} u \frac{\partial \delta F}{\partial x} dx \right) = \\ &= -c \cancel{\int_{\partial \mathcal{B}} \delta F u \, dx} + c \int_{\mathcal{B}} u \frac{\partial \delta F}{\partial x} dx \end{aligned} \tag{4.3}$$

The first term on the RHS in (4.3) can be neglected, in case BCs at the two edges of domain $\mathcal{B}$ are chosen appropriately.

1. As a first step, the domain $\mathcal{B}$ is discretised as a set of particles, Ω. Values of integrated variables are obtained by summation of their assumed values at the particles (nodal integration). It follows that (4.3) is discretised as

$$\sum_{a \in \Omega} \delta F_a \frac{\partial u_a}{\partial t} V_a = \sum_{a \in \Omega} c u_a \frac{\partial \delta F_a}{\partial x} V_a \tag{4.4}$$

where the set of particles $a \in \Omega$ represents the continuum domain $\mathcal{B}$, and V_a is the volume fraction of $\mathcal{B}$ assigned to a particle a. In a one-dimensional setting, V_a has the dimension of a length.

2. The gradient of δF_a in (4.4) can be interpolated using a reproducing kernel function $W(x - x_a, h)$, with compact support centred on target particle a and of radius h. Equation (4.4) then becomes:

$$\sum_{a\in\Omega} \delta F_a \frac{\partial u_a}{\partial t} V_a = c \sum_{a\in\Omega} V_a u_a \left(\sum_{b\in\Lambda_a} V_b \delta F_b \frac{\partial W_b(x_a)}{\partial x} \right) = \\ = c \sum_{a\in\Omega} \sum_{b\in\Lambda_a} V_a u_a \left(V_b \delta F_b \frac{\partial W_b(x_a)}{\partial x} \right) \tag{4.5}$$

In (4.5), Λ_a represents the set of particles b falling in the compact support radius of the kernel centred around target particle a. Since the sum in (4.5) is made over the whole set of particles Ω, their indices a and b can be swapped to obtain:

$$\sum_{b\in\Omega} \cancel{V_b \delta F_b} \frac{\partial u_b}{\partial t} = c \sum_{b\in\Omega} \cancel{V_b \delta F_b} \left(\sum_{a\in\Lambda_b} V_a u_a \frac{\partial W_a(x_b)}{\partial x} \right) \rightarrow \\ \rightarrow \frac{\partial u_b}{\partial t} = c \sum_{a\in\Lambda_b} V_a u_a \left(-\frac{\partial W_b(x_a)}{\partial x} \right) \tag{4.6}$$

Note that $W(x - x_a, h)$ was chosen as an even function around x_a, so that $W(x - x_a, h) = W(x_a - x, h)$. Therefore, its first derivative in space $\nabla W(x - x_a, h)$ will be an odd function, justifying the change in sign at the RHS of (4.6). The semi-discretisation in space of (4.1) using SPH will thus end up to be

$$\frac{\partial u_a}{\partial t} = -c \sum_{b\in\Lambda_a} V_b u_b \frac{\partial W_b(x_a)}{\partial x} \tag{4.7}$$

In the following, particles volume will be assumed to be constant:

$$V_i = V \approx \Delta x$$

4.1.1 *Kernel function in 1D*

The kernel function $W(x - x_a, h)$ is selected to be a polynomial function, with compact support (meaning W will vanish for $\|x - x_a\| \geqslant 2h$).

An example of such a polynomial function is the quintic spline defined in equation (3.52), which is then inserted in the general expression of the kernel function (3.48) using as normalisation parameter $\alpha = 1/8$. This particular α was chosen in order to satisfy consistency condition (3.39a).

Visualisation of $W(x - x_a, h)$, as defined in (3.52), and of its space derivatives up to the fourth order, is offered in fig. 4.1.

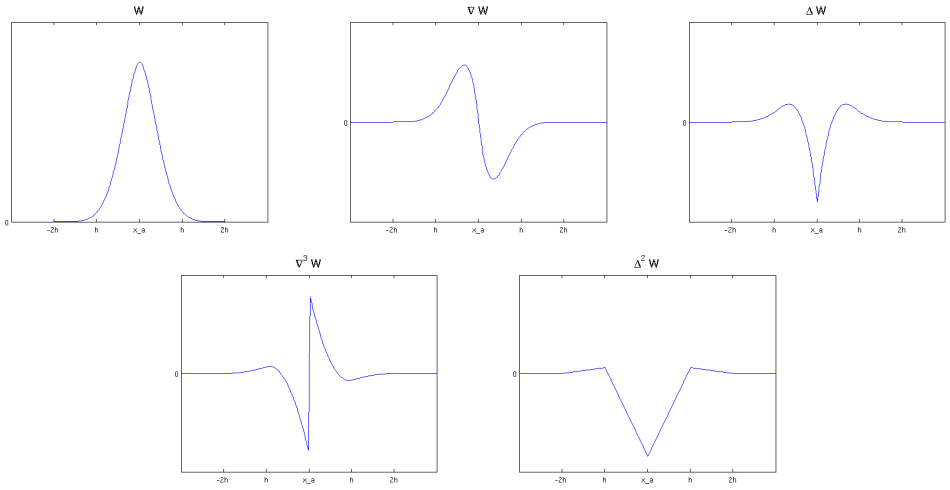

Figure 4.1: quintic spline kernel $W(x - x_a, h)$ and its derivatives up to 4^{th} order.

In the discrete domain, corrections have to be implemented to uphold the validity of consistency conditions (3.39).

Accordingly, for the corrected gradient of the kernel, $\widetilde{\nabla} W(x)$, it must hold that

$$\sum_{b \in \Lambda_a} V_b \widetilde{\nabla} W_b(x_a) = 0\,; \qquad \sum_{b \in \Lambda_a} V_b \left[x_b - x_a\right] \widetilde{\nabla} W_b(x_a) = 1 \tag{4.8}$$

Following on the same pattern of (4.8), corrections to the kernel Laplacian $\widetilde{\nabla}^2 W(x)$ will assume the form:

$$\sum_{b\in\Lambda_a} V_b \widetilde{\nabla}^2 W_b(x_a) = 0 \tag{4.9}$$

$$\sum_{b\in\Lambda_a} V_b \left[x_b - x_a\right] \widetilde{\nabla}^2 W_b(x_a) = 0 \tag{4.10}$$

$$\frac{1}{2}\sum_{b\in\Lambda_a} V_b \|x_b - x_a\|^2 \widetilde{\nabla}^2 W_b(x_a) = 1 \tag{4.11}$$

$\widetilde{\nabla}^2 W(x)$ can then be obtained as:

$$\widetilde{\nabla}^2 W_b(x_a) = \alpha_a \left[1 + \gamma_a \delta_{ab} + \beta_a (x_a - x_b)\right] \nabla^2 W_b(x_a) \tag{4.12}$$

In (4.12), α_a, β_a and γ_a are parameters chosen so that (4.9) holds true.

4.1.2 *Time integration*

The spatial discretisation discussed above yields a system of ODEs of the form:

$$\frac{du_a}{dt} = \boldsymbol{\mathcal{R}}_a(u_a, t), \tag{4.13}$$

where $\boldsymbol{\mathcal{R}}_a(u_a, t)$ represents the residual of the SPH spatial discretisation associated with particle a. The explicit, two-stage TVD-RK time integrator from section 3.7 is used to advance (4.13) in time from t^n to t^{n+1}:

$$u_a^* = u_a^n + \Delta t\, \boldsymbol{\mathcal{R}}_a(u_a^n, t^n); \qquad u_a^{**} = u_a^* + \Delta t\, \boldsymbol{\mathcal{R}}_a(u_a^*, t^{n+1});$$
$$u_a^{n+1} = \mathtt{N}_{RK}\left(u_i^n\right) = \frac{1}{2}(u_a^n + u_a^{**}). \tag{4.14}$$

As in (3.93), the time step $\Delta t = t^{n+1} - t^n$ depends on Δx by means of $\Delta t = \sigma_{CFL}\left(\Delta x / c\right)$, where σ_{CFL} is the CFL number.

4.2 ACCURACY ANALYSIS

In this section, a survey of the consistency and stability properties of the SPH discretisation for LAE (4.7)+(4.14) will be carried out.

The quintic spline function (3.52) will be used as interpolating kernel, and stencils with 2 and 3 neighbouring p.p.s. will be examined. To check a numerical scheme for consistency amounts in finding the truncation error associated with it, and evaluating its order of magnitude with respect to increments in time and space. The larger this order of magnitude, the more accurate the numerical scheme.

In the case of a discretised hyperbolic PDE, increments in time are dependent from increments in space. The magnitudes of errors in space and time can thereby be seen as exerting the same effect on accuracy; the lower value of the combined two should be regarded as the main indicator to gauge the consistency of the numerical scheme, against the original differential problem. A step by step procedure to find the truncation error in a SPH (space) combined with a two stages TVD-RK (time) scheme is drafted in algorithm 4.

1. Find the exact values for $\widetilde{W}$ and its derivatives of interest at the particles points. Then correct them, to obtain the discretised formulation of the problem, according to the numerical scheme;
2. Compute Taylor series expansion for u_i, $u_{i\pm1}$, $u_{i\pm2}$, and $u_{i\pm3}$ as needed by the 2 or 3 p.p.s. stencil under scrutiny;
3. Compute u_i^* in (4.14) as combination of quantities found in point 2;
4. Obtain $\left.\frac{\partial^k u}{\partial x^k}\right|_i^*$ by differentiating k-times the value of u_i^* found in point 3;
5. Calculate u_i^{**} in (4.14);
6. Compute the end-step value for TVD-RK, $N_{RK}\left(u_i^n\right) = \frac{1}{2}\left(u_i^{**} + u_i^*\right)$;
7. Find $u|_i^{n+1}$ as a Taylor expansion in time around $u|_i^n$;
8. Obtain the truncation error ϵ_T^n as $\epsilon_T^n = \frac{1}{\Delta t}\left(N_{RK}\left(u_i^n\right) - u|_i^{n+1}\right)$, and check the combined order of increments Δt and Δx.

ALGORITHM 4 : evaluation of truncation error

4.2.1 *2 particles per side: consistency*

The truncation error ϵ_T^n for the 2 p.p.s. stencil will be obtained by following the steps outlined in algorithm 4.

1. The exact values of the kernel function coefficients, and its derivatives for the 2 p.p.s. stencil are listed in table 4.1.

   Applying corrections to values up to the second derivative in table 4.1 leads to table 4.2.

   It is useful to point out that the value of $\widetilde{\nabla}^2 W$ in table 4.2 has not been divided by the increment Δx with each derivation, for reasons that will be explained later.

Table 4.1: uncorrected Kernel, 2 p.p.s.

	relative particles position					
	$a-2$	$a-1$	a	$a+1$	$a+2$	
W	0	$1/8$	2	$1/8$	0	$\cdot 1/\Delta x$
∇W	0	$-5/8$	0	$-5/8$	0	$\cdot 1/\Delta x^2$
$\nabla^2 W$	0	$5/2$	-20	$5/2$	0	$\cdot 1/\Delta x^3$
$\nabla^3 W$	0	$-15/2$	90	$-15/2$	0	$\cdot 1/\Delta x^4$
$\nabla^4 W$	0	15	-210	15	0	$\cdot 1/\Delta x^5$

Table 4.2: corrected Kernel, 2 p.p.s.

	relative particles position					
	$a-2$	$a-1$	a	$a+1$	$a+2$	
$\widetilde{W}$	0	$1/18$	$8/9$	$1/18$	0	$\cdot 1/\Delta x$
$\widetilde{\nabla} W$	0	$-1/2$	0	$1/2$	0	$\cdot 1/\Delta x$
$\widetilde{\nabla}^2 W$	0	1	-2	1	0	$\cdot 1/\Delta x$

Through table 4.2, the semi-discretised equation for (4.1) can be expressed as in (4.15):

$$\left.\frac{\partial u}{\partial t}\right|_a = -\frac{c}{2\Delta x}\left(u^n_{a+1} - u^n_{a-1}\right) \tag{4.15}$$

2. Compute the Taylor expansion of terms $u_{a\pm i}$ in (4.15):

$$\begin{aligned} u^n_{a+1} &= u^n_a + \left.\frac{\partial u}{\partial x}\right|^n_a \Delta x + \frac{1}{2}\left.\frac{\partial^2 u}{\partial x^2}\right|^n_a \Delta x^2 + \frac{1}{6}\left.\frac{\partial^3 u}{\partial x^3}\right|^n_a \Delta x^3 + O\left(\Delta x^4\right) \\ u^n_{a-1} &= u^n_a - \left.\frac{\partial u}{\partial x}\right|^n_a \Delta x + \frac{1}{2}\left.\frac{\partial^2 u}{\partial x^2}\right|^n_a \Delta x^2 - \frac{1}{6}\left.\frac{\partial^3 u}{\partial x^3}\right|^n_a \Delta x^3 + O\left(\Delta x^4\right) \end{aligned} \tag{4.16}$$

3. Obtain u^*_a in (4.14) by use of (4.16):

$$\begin{aligned} u^*_a &= u^n_a - c\,\Delta t \frac{u^n_{a+1} - u^n_{a-1}}{2\Delta x} = \\ &= u^n_a - c\,\Delta t\left(\left.\frac{\partial u}{\partial x}\right|^n_a + \frac{1}{6}\left.\frac{\partial^3 u}{\partial x^3}\right|^n_a \Delta x^2\right) + O(\Delta x^4) \end{aligned} \tag{4.17}$$

4. Derivatives in space of u_a^*:

$$\begin{aligned}
\left.\frac{\partial u}{\partial x}\right|_a^* &= \left.\frac{\partial u}{\partial x}\right|_a^n - c\left.\frac{\partial^2 u}{\partial x^2}\right|_a^n \Delta t - c\left.\frac{\partial^4 u}{\partial x^4}\right|_a^n \Delta t \Delta x^2 + O(\Delta x^4) \\
\left.\frac{\partial^2 u}{\partial x^2}\right|_a^* &= \left.\frac{\partial^2 u}{\partial x^2}\right|_a^n - c\left.\frac{\partial^3 u}{\partial x^3}\right|_a^n \Delta t - c\left.\frac{\partial^5 u}{\partial x^5}\right|_a^n \Delta t \Delta x^2 + O(\Delta x^4) \\
\left.\frac{\partial^3 u}{\partial x^3}\right|_a^* &= \left.\frac{\partial^3 u}{\partial x^3}\right|_a^n - c\left.\frac{\partial^4 u}{\partial x^4}\right|_a^n \Delta t - c\left.\frac{\partial^6 u}{\partial x^6}\right|_a^n \Delta t \Delta x^2 + O(\Delta x^4)
\end{aligned} \tag{4.18}$$

5. Compute u_a^{**} from (4.14), (4.17), (4.18):

$$\begin{aligned}
u_a^{**} &= u_a^* - \frac{c\,\Delta t}{\Delta x}\left(u_{a+1}^* - u_{a-1}^*\right) = \\
&= u_a^n - 2c\left.\frac{\partial u}{\partial x}\right|_a^n \Delta t + c^2\left.\frac{\partial^2 u}{\partial x^2}\right|_a^n \Delta t^2 - \frac{c}{3}\left.\frac{\partial^3 u}{\partial x^3}\right|_a^n \Delta t \Delta x^2 + O(\Delta x^4)
\end{aligned} \tag{4.19}$$

6. Runge-Kutta estimation for next step in time, $N_{RK}(u_a^n)$:

$$\begin{aligned}
N_{RK}(u_a^n) &= \frac{1}{2}(u_a^n + u_a^{**}) = \\
&= u_a^n - c\left.\frac{\partial u}{\partial x}\right|_a^n \Delta t + \frac{c^2}{2}\left.\frac{\partial^2 u}{\partial x^2}\right|_a^n \Delta t^2 - \frac{c}{6}\left.\frac{\partial^3 u}{\partial x^3}\right|_a^n \Delta t \Delta x^2 + O(\Delta x^4)
\end{aligned} \tag{4.20}$$

7. Taylor expansion of u_a^{n+1} in time around u_a^n:

$$u_a^{n+1} = u_a^n + \left.\frac{\partial u}{\partial t}\right|_a^n \Delta t + \frac{1}{2}\left.\frac{\partial^2 u}{\partial t^2}\right|_a^n \Delta t^2 + \frac{1}{6}\left.\frac{\partial^3 u}{\partial t^3}\right|_a^n \Delta t^3 + O\left(\Delta t^4\right) \tag{4.21}$$

8. Obtain the truncation error ϵ_T^n for the scheme from (4.20) and (4.21) as

$$\begin{aligned}
\epsilon_T^n =& \frac{1}{\Delta t}\left(N_{RK}(u_a^n) - u_a^{n+1}\right) = \\
=& u_a^n - c\left.\frac{\partial u}{\partial x}\right|_a^n + \frac{c^2}{2}\left.\frac{\partial^2 u}{\partial x^2}\right|_a^n \Delta t - \frac{c}{6}\left.\frac{\partial^3 u}{\partial x^3}\right|_a^n \Delta x^2 + \\
&- \left.\frac{\partial u}{\partial t}\right|_a^n - \frac{1}{2}\left.\frac{\partial^2 u}{\partial t^2}\right|_a^n \Delta t - \frac{1}{6}\left.\frac{\partial^3 u}{\partial t^3}\right|_a^n \Delta t^2 + O(\Delta x^3, \Delta t^3)
\end{aligned} \tag{4.22}$$

The previous equation (4.22) can be simplified by observing that

$$\left.\frac{\partial u}{\partial t}\right|_a^n + c \left.\frac{\partial u}{\partial x}\right|_a^n = 0 \tag{4.23}$$

is none other than (4.1), involving its exact solution u_a^n in x_a at time t^n.

Also, consider the commutative property of second derivatives:

$$\left.\frac{\partial}{\partial x}\frac{\partial u}{\partial t}\right|_a^n - \left.\frac{\partial}{\partial t}\frac{\partial u}{\partial x}\right|_a^n = 0 \tag{4.24}$$

The cross derivatives in x and t for (4.23) are

$$\begin{aligned}\frac{\partial}{\partial x}\left(\left.\frac{\partial u}{\partial t}\right|_a^n\right) &= -c \left.\frac{\partial^2 u}{\partial x^2}\right|_a^n \\ \frac{\partial}{\partial t}\left(c \left.\frac{\partial u}{\partial x}\right|_a^n\right) &= -c \left.\frac{\partial^2 u}{\partial t^2}\right|_a^n\end{aligned}$$

Applying (4.24):

$$c^2 \left.\frac{\partial^2 u}{\partial x^2}\right|_a^n - \left.\frac{\partial^2 u}{\partial t^2}\right|_a^n = 0 \tag{4.25}$$

Equation (4.25) makes it possible to further simplify ϵ_T^n in (4.22). The final expression for ϵ_T^n is then

$$\epsilon_T^n = -\frac{c}{6}\left.\frac{\partial^3 u}{\partial x^3}\right|_a^n \Delta x^2 - \frac{1}{6}\left.\frac{\partial^3 u}{\partial t^3}\right|_a^n \Delta t^2 + O(\Delta x^3, \Delta t^3) \tag{4.26}$$

Equation (4.26) proves that a stencil with two neighbours at each side of the target particle is of second order accuracy in space and time.

4.2.2 *2 particles per side: stability*

The von Neumann method is widely used for analysing the stability of a numerical scheme associated with a linear PDE. Denoting the spatial discretised nodal SPH operator as $\mathbf{D}$, (4.7) can be written in matrix form as

$$\frac{\partial \mathbf{u}}{\partial t} = \mathbf{D}\mathbf{u} \tag{4.27}$$

where, more specifically, $\mathbf{D}$ is a square matrix of dimension N equal to the number of particles in the discretisation, and $\mathbf{u}$ denotes the vector of nodal values for u.

A spectral decomposition of $\mathbf{D}$ yields the eigenvalues λ_i and eigenvectors $\mathbf{R}_i$ for each degree of freedom (d.o.f.) in the discretised system (4.27):

$$\begin{cases} \mathbf{D}\mathbf{R}_i = \lambda_i \mathbf{R}_i \\ \det\left(\mathbf{D} - \lambda_i \mathbf{I}\right) = 0 \quad \text{for} \;\; i = 1, \dots, N \end{cases} \tag{4.28}$$

System (4.28) allows to obtain the modal decomposition of the solution of the semi-discretised problem (4.7), in terms of separate contributions in space and time.

In order for (4.7) to preserve its stability, solution $\mathbf{u}$ has to remain bounded. It can be proven that this condition is met if

$$\Re(\lambda_i) \leqslant 0, \qquad \forall i = 1, \dots, n \tag{4.29}$$

Eigenvectors $\mathbf{R}_i$ can be represented via Fourier series, that is

$$\mathbf{R}_i = \sum_j e^{iI\Phi_j} \tag{4.30}$$

where $I = \sqrt{-1}$, and the phase angle $\Phi_j \in [-\pi, \pi]$. In (4.30), index i refers to the particle, and the sum is done over all frequencies j in the Fourier decomposition.

The wave number k_j associated to each j^{th}-Fourier harmonic is

$$k_j = \frac{2\pi}{\lambda_{wl|j}} = j\frac{\pi}{N\Delta x} \tag{4.31}$$

In (4.31), $\lambda_{wl|j}$ is the wavelength of the j^{th} harmonic.

Having introduced the wave number k, the phase angle can be alternatively expressed in terms of it, as $\Phi_j = k_j \Delta x$.

Substituting (4.30) in the first of (4.28) yields, in indicial notation, and for the j^{th}-harmonic of $\mathbf{R}_i$:

$$\mathbf{D}_{\alpha i}\, e^{Ii\Phi_j} = \lambda_\alpha\, e^{I\alpha\Phi_j} \qquad \text{for} \quad i = \alpha - p, \ldots, \alpha, \ldots, \alpha + p \tag{4.32}$$

where p is the number of neighbouring particles at each side of target particle α that fall inside of the kernel smoothing circle centred in x_α and of radius $2\Delta x$.

In the case of 2 p.p.s., (4.32) becomes

$$\lambda_\alpha = \mathbf{D}_{\alpha i}\, e^{I(i-\alpha)\Phi_\alpha} = -\frac{c}{2\Delta x}\left[e^{I\Phi_\alpha} - e^{-I\Phi_\alpha}\right] \tag{4.33}$$

Taking into account the following relations:

$$\begin{aligned} e^{I\Phi_\alpha} &= \cos\Phi_\alpha + I\sin\Phi_\alpha & e^{-I\Phi_\alpha} &= \cos\Phi_\alpha - I\sin\Phi_\alpha \\ e^{2I\Phi_\alpha} &= \cos 2\Phi_\alpha + I\sin 2\Phi_\alpha & e^{-2I\Phi_\alpha} &= \cos 2\Phi_\alpha - I\sin 2\Phi_\alpha \\ e^{3I\Phi_\alpha} &= \cos 3\Phi_\alpha + I\sin 3\Phi_\alpha & e^{-3I\Phi_\alpha} &= \cos 3\Phi_\alpha - I\sin 3\Phi_\alpha, \end{aligned} \tag{4.34}$$

the real and imaginary parts of λ_α, from (4.33), are:

$$\begin{aligned} \Re(\lambda_\alpha) &= 0 \\ \Im(\lambda_\alpha) &= -\frac{c}{\Delta x}\sin(\Phi_\alpha) \end{aligned} \tag{4.35}$$

The result obtained in (4.35) proves that for this particular stencil the SPH spatial discretisation of (4.1) is stable, as (4.29) is satisfied.

However, the numerical system may still harbour instabilities in time. In order to check against this, a constraint must be imposed on the *numerical amplification factor* of the time integrator z_p, to ensure that the temporal component of the modal decomposition obtained through (4.28) remains bounded during the simulation. This pre-condition can be stated as

$$|z_p(\lambda_\alpha \Delta t)| \leqslant 1 \tag{4.36}$$

Knowing the z_p for a 2-stages explicit TVD-RK time integrator, (4.36) translates in

$$|1 + \lambda_a \Delta t + \frac{1}{2}(\lambda_a \Delta t)^2| \leqslant 1 \tag{4.37}$$

A plot of (4.37) on the complex plane of $\lambda_a \Delta t$ enables to directly visualise the stability limits for the temporal scheme under study. On the same plane it is also convenient to plot the eigenvalues of the spatial discretisation, in (4.33), for the whole range of $\Phi_a \in [-\pi, \pi]$.

All of this is done in fig. 4.2. Observing fig. 4.2, it can be stated that a SPH discretisation with 2 p.p.s. is unstable, if paired with a 2 stages TVD-RK temporal integrator. This is because the eigenvalues of the spatial semi-discretisation fall outside of the time scheme stability region.

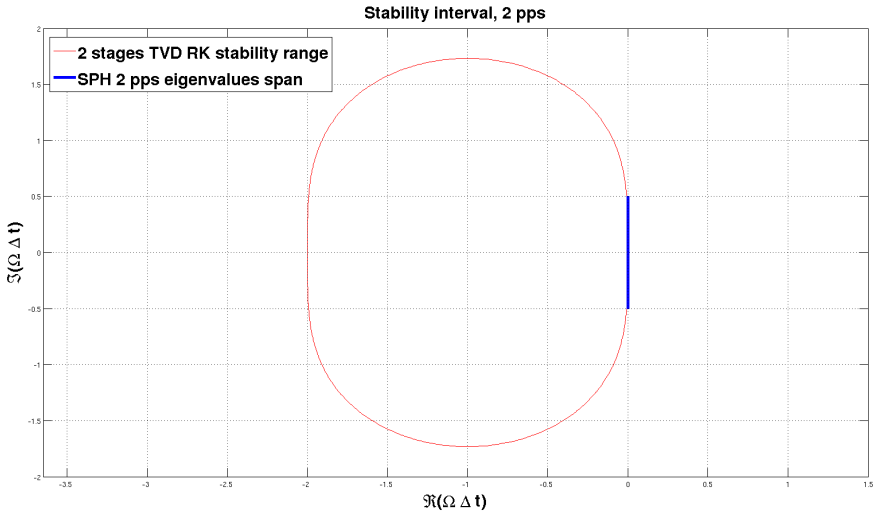

Figure 4.2: graphic representation of the stability analysis for the SPH 2 p.p.s. in space, and 2 stages TVD-RK in time, numerical scheme.

4.2.3 *2 particles per side + JST dissipation: consistency*

Results obtained in the previous section with the SPH 2 p.p.s. scheme, show there is the need to introduce numerical dissipation in the SPH semi-discretisation, in order to generate a stable numerical scheme.

To this purpose, a JST type dissipation term may be added to (4.1) as:

$$\frac{\partial u}{\partial t} + c\frac{\partial u}{\partial x} = -\frac{c k^{(4)}}{\Delta x}\frac{\partial^4 u}{\partial x^4} \tag{4.38}$$

An undivided Laplacian of Laplacian is employed in the dissipation term in (4.38). It can be seen from table 4.2 that having an undivided $\widetilde{\nabla}^4 W = \nabla^2(\widetilde{\nabla}^2 W)$ will bring down all the increment terms on the RHS of (4.38) to the same order. This will prove to be essential in order to prove the consistency of the scheme.

In the rest of this section, the discretised and corrected version of $\nabla^4 W$ is obtained in two stages:

1. firstly, the application of correction (4.12) to the SPH Laplacian of kernel, $\widetilde{\nabla}^2_{\text{SPH}} W$,
2. then, the use of a central difference operator to obtain the second Laplacian, $\Delta_{\text{CD}}\left(\widetilde{\nabla}^2_{\text{SPH}} W\right) = \widetilde{\nabla}^4 W$.

The semi-discretisation in space of (4.38) is

$$\frac{\partial u}{\partial t} = -c \sum_{b \in \Lambda_a} \Delta x \, u_b \widetilde{\nabla} W_b(x_a) - \frac{c k^{(4)}}{\Delta x} \sum_{b \in \Lambda_a} \Delta x \, u_b \widetilde{\nabla}^4 W_b(x_a) \tag{4.39}$$

The study of the consistency properties of (4.39) will be carried out following the procedure outlined in algorithm 4.

1. In the first Laplacian SPH discretisation, values in table 4.2 will be used for the corrected kernel $\widetilde{W}$ and its derivatives. Once $\widetilde{\nabla}^4 W$ is obtained, the Laplacian of Laplacian in the dissipative term can be expressed in terms of central differences as

$$\begin{aligned}
\nabla^4 u =& \Delta_{\text{CD}}\left(\widetilde{\nabla}^2_{\text{SPH}} u\right) = \Delta_{\text{CD}}\left(\sum_{b \in \Lambda_a} \Delta x \, u_b \, \widetilde{\nabla}^2 W_b\left(x_a\right)\right) = \\
&= \sum_{b \in \Lambda_{a-1}} \Delta x \, u_b \, \widetilde{\nabla}^2 W_b\left(x_{a-1}\right) - 2 \sum_{b \in \Lambda_a} \Delta x \, u_b \, \widetilde{\nabla}^2 W_b\left(x_a\right) + \\
&+ \sum_{b \in \Lambda_{a+1}} \Delta x \, u_b \, \widetilde{\nabla}^2 W_b\left(x_{a+1}\right) \\
&= u_{a+2} - 4u_{a+1} + 6u_a - 4u_{a-1} + u_{a-2}
\end{aligned} \tag{4.40}$$

In light of (4.40), (4.39) becomes:

$$\frac{\partial u}{\partial t} = -\frac{c}{2\Delta x}\left(u_{a+1}^n - u_{a-1}^n\right) + \\ -\frac{ck^{(4)}}{\Delta x}\left(u_{a+2} - 4u_{a+1} + 6u_a - 4u_{a-1} + u_{a-2}\right) \tag{4.41}$$

2. With respect to (4.16), fourth order terms will be added to the Taylor series expansions of $u_{a\pm i}$ in (4.41):

$$\begin{aligned}
u_{a+2}^n = \; & u_a^n + 2\left.\frac{\partial u}{\partial x}\right|_a^n \Delta x + 2\left.\frac{\partial^2 u}{\partial x^2}\right|_a^n \Delta x^2 + \frac{4}{3}\left.\frac{\partial^3 u}{\partial x^3}\right|_a^n \Delta x^3 + \frac{2}{3}\left.\frac{\partial^4 u}{\partial x^4}\right|_a^n \Delta x^4 + \dots \\
u_{a+1}^n = \; & u_a^n + \left.\frac{\partial u}{\partial x}\right|_a^n \Delta x + \frac{1}{2}\left.\frac{\partial^2 u}{\partial x^2}\right|_a^n \Delta x^2 + \frac{1}{6}\left.\frac{\partial^3 u}{\partial x^3}\right|_a^n \Delta x^3 + \frac{1}{24}\left.\frac{\partial^4 u}{\partial x^4}\right|_a^n \Delta x^4 + \dots \\
u_{a-1}^n = \; & u_a^n - \left.\frac{\partial u}{\partial x}\right|_a^n \Delta x + \frac{1}{2}\left.\frac{\partial^2 u}{\partial x^2}\right|_a^n \Delta x^2 - \frac{1}{6}\left.\frac{\partial^3 u}{\partial x^3}\right|_a^n \Delta x^3 + \frac{1}{24}\left.\frac{\partial^4 u}{\partial x^4}\right|_a^n \Delta x^4 + \dots \\
u_{a-2}^n = \; & u_a^n - 2\left.\frac{\partial u}{\partial x}\right|_a^n \Delta x + 2\left.\frac{\partial^2 u}{\partial x^2}\right|_a^n \Delta x^2 - \frac{4}{3}\left.\frac{\partial^3 u}{\partial x^3}\right|_a^n \Delta x^3 + \frac{2}{3}\left.\frac{\partial^4 u}{\partial x^4}\right|_a^n \Delta x^4 + \dots \\
& + O\left(\Delta x^5\right)
\end{aligned} \tag{4.42}$$

3. u_a^* is then

$$\begin{aligned}
u_a^* &= u_a^n - \frac{c\Delta t}{2\Delta x}\left(u_{a+1}^n - u_{a-1}^n\right) + \\
&- \frac{ck^{(4)}\Delta t}{\Delta x}\left(u_{a+2} - 4u_{a+1} + 6u_a - 4u_{a-1} + u_{a-2}\right) = \\
&= u_a^n - c\left.\frac{\partial u}{\partial x}\right|_a^n \Delta t - \frac{c}{6}\left.\frac{\partial^3 u}{\partial x^3}\right|_a^n \Delta x^2 \Delta t - ck^{(4)}\left.\frac{\partial^4 u}{\partial x^4}\right|_a^n \Delta x^3 \Delta t + O\left(\Delta x^4\right)
\end{aligned} \tag{4.43}$$

4. Derivatives in space of u_a^*:

$$\begin{aligned}
\left.\frac{\partial u}{\partial x}\right|_a^* &= \left.\frac{\partial u}{\partial x}\right|_a^n - c\left.\frac{\partial^2 u}{\partial x^2}\right|_a^n \Delta t - \frac{c}{6}\left.\frac{\partial^4 u}{\partial x^4}\right|_a^n \Delta x^2 \Delta t - ck^{(4)}\left.\frac{\partial^5 u}{\partial x^5}\right|_a^n \Delta x^3 \Delta t + \dots \\
\left.\frac{\partial^3 u}{\partial x^3}\right|_a^* &= \left.\frac{\partial^3 u}{\partial x^3}\right|_a^n - c\left.\frac{\partial^4 u}{\partial x^4}\right|_a^n \Delta t - \frac{c}{6}\left.\frac{\partial^6 u}{\partial x^6}\right|_a^n \Delta x^2 \Delta t - ck^{(4)}\left.\frac{\partial^7 u}{\partial x^7}\right|_a^n \Delta x^3 \Delta t + \dots \\
\left.\frac{\partial^4 u}{\partial x^4}\right|_a^* &= \left.\frac{\partial^4 u}{\partial x^4}\right|_a^n - c\left.\frac{\partial^5 u}{\partial x^5}\right|_a^n \Delta t - \frac{c}{6}\left.\frac{\partial^7 u}{\partial x^7}\right|_a^n \Delta x^2 \Delta t - ck^{(4)}\left.\frac{\partial^8 u}{\partial x^8}\right|_a^n \Delta x^3 \Delta t + \dots \\
& + O(\Delta x^4)
\end{aligned} \tag{4.44}$$

5. u_a^{**}, from (4.14), (4.43), (4.44):

$$
\begin{aligned}
u_a^{**} &= u_a^{*} - c\left.\frac{\partial u}{\partial x}\right|_a^{*}\Delta t - \frac{c}{6}\left.\frac{\partial^3 u}{\partial x^3}\right|_a^{*}\Delta x^2\Delta t - ck^{(4)}\left.\frac{\partial^4 u}{\partial x^4}\right|_a^{*}\Delta x^3\Delta t = \\
&= u_a^n - 2c\left.\frac{\partial u}{\partial x}\right|_a^n\Delta t + c^2\left.\frac{\partial^2 u}{\partial x^2}\right|_a^n\Delta t^2 - \frac{c}{3}\left.\frac{\partial^3 u}{\partial x^3}\right|_a^n\Delta x^2\Delta t + \\
&+ \frac{c^2}{3}\left.\frac{\partial^4 u}{\partial x^4}\right|_a^n\Delta x^2\Delta t^2 - 2ck^{(4)}\left.\frac{\partial^4 u}{\partial x^4}\right|_a^n\Delta x^3\Delta t - 2ck^{(4)}\left.\frac{\partial^5 u}{\partial x^5}\right|_a^n\Delta x^3\Delta t^2 + \\
&\frac{c^2}{36}\left.\frac{\partial^6 u}{\partial x^6}\right|_a^n\Delta x^4\Delta t^2 - \frac{c^2k^{(4)}}{3}\left.\frac{\partial^7 u}{\partial x^7}\right|_a^n\Delta x^5\Delta t^2 - \left(ck^{(4)}\right)^2\left.\frac{\partial^8 u}{\partial x^8}\right|_a^n\Delta x^6\Delta t^2 \\
&\qquad + O(\Delta x^7, \Delta t^3)
\end{aligned}
\tag{4.45}
$$

6. Runge-Kutta estimation for next step in time, $N_{RK}(u_a^n)$:

$$
\begin{aligned}
N_{RK}(u_a^n) &= \frac{1}{2}(u_a^n + u_a^{**}) = \\
&= u_a^n - c\left.\frac{\partial u}{\partial x}\right|_a^n\Delta t + \frac{c^2}{2}\left.\frac{\partial^2 u}{\partial x^2}\right|_a^n\Delta t^2 - \frac{c}{6}\left.\frac{\partial^3 u}{\partial x^3}\right|_a^n\Delta t\Delta x^2 + \\
&+ \frac{c^2}{6}\left.\frac{\partial^4 u}{\partial x^4}\right|_a^n\Delta x^2\Delta t^2 - ck^{(4)}\left.\frac{\partial^4 u}{\partial x^4}\right|_a^n\Delta x^3\Delta t - c^2k^{(4)}\left.\frac{\partial^5 u}{\partial x^5}\right|_a^n\Delta x^3\Delta t^2 + \\
&+ \frac{c^2}{72}\left.\frac{\partial^6 u}{\partial x^6}\right|_a^n\Delta x^4\Delta t^2 - \frac{c^2k^{(4)}}{6}\left.\frac{\partial^7 u}{\partial x^7}\right|_a^n\Delta x^5\Delta t^2 - \frac{\left(ck^{(4)}\right)^2}{2}\left.\frac{\partial^8 u}{\partial x^8}\right|_a^n\Delta x^6\Delta t^2 \\
&\qquad + O(\Delta x^7, \Delta t^3)
\end{aligned}
\tag{4.46}
$$

7. Taylor expansion of u_a^{n+1} in time around u_a^n, see (4.21).

8. Obtain the truncation error ϵ_T^n for the scheme from (4.46) and (4.21) as

$$\begin{aligned}
\epsilon_T^n &= \frac{1}{\Delta t}\left(N_{RK}(u_a^n) - u_a^{n+1}\right) = \\
&= \cancel{\frac{u_a^n}{\Delta t}} - c\left.\frac{\partial u}{\partial x}\right|_a^n + \frac{c^2}{2}\left.\frac{\partial^2 u}{\partial x^2}\right|_a^n \Delta t - \frac{c}{6}\left.\frac{\partial^3 u}{\partial x^3}\right|_a^n \Delta x^2 + \\
&+ \cancel{\frac{c^2}{6}\left.\frac{\partial^4 u}{\partial x^4}\right|_a^n \Delta x^2 \Delta t}^{\text{h.o.t.}} - \cancel{ck^{(4)}\left.\frac{\partial^4 u}{\partial x^4}\right|_a^n \Delta x^3}^{\text{h.o.t.}} + \\
&- \cancel{c^2 k^{(4)}\left.\frac{\partial^5 u}{\partial x^5}\right|_a^n \Delta x^3 \Delta t}^{\text{h.o.t.}} + \cancel{\frac{c^2}{72}\left.\frac{\partial^6 u}{\partial x^6}\right|_a^n \Delta x^4 \Delta t}^{\text{h.o.t.}} + \\
&- \cancel{\frac{c^2 k^{(4)}}{6}\left.\frac{\partial^7 u}{\partial x^7}\right|_a^n \Delta x^5 \Delta t}^{\text{h.o.t.}} - \cancel{\frac{\left(ck^{(4)}\right)^2}{2}\left.\frac{\partial^8 u}{\partial x^8}\right|_a^n \Delta x^6 \Delta t}^{\text{h.o.t.}} + \\
&- \cancel{\frac{u_a^n}{\Delta t}} - \left.\frac{\partial u}{\partial t}\right|_a^n - \frac{1}{2}\left.\frac{\partial^2 u}{\partial t^2}\right|_a^n \Delta t - \frac{1}{6}\left.\frac{\partial^3 u}{\partial t^3}\right|_a^n \Delta t^2 + O\left(\cancel{\Delta x^3}, \Delta t^3\right)
\end{aligned} \tag{4.47}$$

Applying (4.23) and (4.25), ϵ_T^n in (4.47) can be reduced to

$$\epsilon_T^n = -\frac{c}{6}\left.\frac{\partial^3 u}{\partial x^3}\right|_a^n \Delta x^2 - \frac{1}{6}\left.\frac{\partial^3 u}{\partial t^3}\right|_a^n \Delta t^2 + O(\Delta x^3, \Delta t^3) \tag{4.48}$$

4.2.4 *2 particles per side + JST dissipation: stability*

The stability analysis for the 2 p.p.s. SPH scheme with JST dissipation contribution will be conducted in the same way to what already done in section 4.2.2 for the 2 p.p.s. space semi-discretisation.

Proceeding in that manner, the specific row $\mathbf{D}_a$ of the spatial discretisation matrix $\mathbf{D}$ in (4.27) corresponding to a generic particle a, may be written as:

$$\begin{aligned}
\mathbf{D}_a = \Bigg[0 \ldots \quad & -\frac{ck^{(4)}}{\Delta x} \quad \Bigg| \quad -\frac{c}{\Delta x}\left(\frac{1}{2} - 4k^{(4)}\right) \quad \Bigg| \quad -\frac{6ck^{(4)}}{\Delta x} \quad \Bigg| \\
& \frac{c}{\Delta x}\left(\frac{1}{2} + 4k^{(4)}\right) \quad \Bigg| \quad -\frac{ck^{(4)}}{\Delta x} \quad \ldots 0 \Bigg]
\end{aligned} \tag{4.49}$$

and, using (4.32), an eigenvalue λ_a of $\mathbf{D}$ can be obtained as

$$\begin{aligned}\lambda_a = &-\frac{ck^{(4)}}{\Delta x}e^{2I\Phi_a} - \frac{c}{\Delta x}\left(\frac{1}{2} - 4k^{(4)}\right)e^{I\Phi_a} - 6\frac{ck^{(4)}}{\Delta x} + \\ &+ \frac{c}{\Delta x}\left(\frac{1}{2} + 4k^{(4)}\right)e^{-I\Phi_a} - \frac{ck^{(4)}}{\Delta x}e^{-2I\Phi_a}\end{aligned} \tag{4.50}$$

λ_a in (4.50), decomposed in its real and imaginary parts, becomes

$$\begin{aligned}\Re(\lambda_a) &= -2\frac{ck^{(4)}}{\Delta x}\cos(2\Phi_a) + 8\frac{ck^{(4)}}{\Delta x}\cos\Phi_a - 6\frac{ck^{(4)}}{\Delta x} = \\ &= -4\frac{ck^{(4)}}{\Delta x}(\cos\Phi_a - 1)^2 \\ \Im(\lambda_a) &= -\frac{c}{\Delta x}\sin\Phi_a\end{aligned} \tag{4.51}$$

The condition for stability stated in (4.29) is satisfied by $\Re(\lambda_a)$ in (4.51), $\forall\Phi_a \in [-\pi, \pi]$.

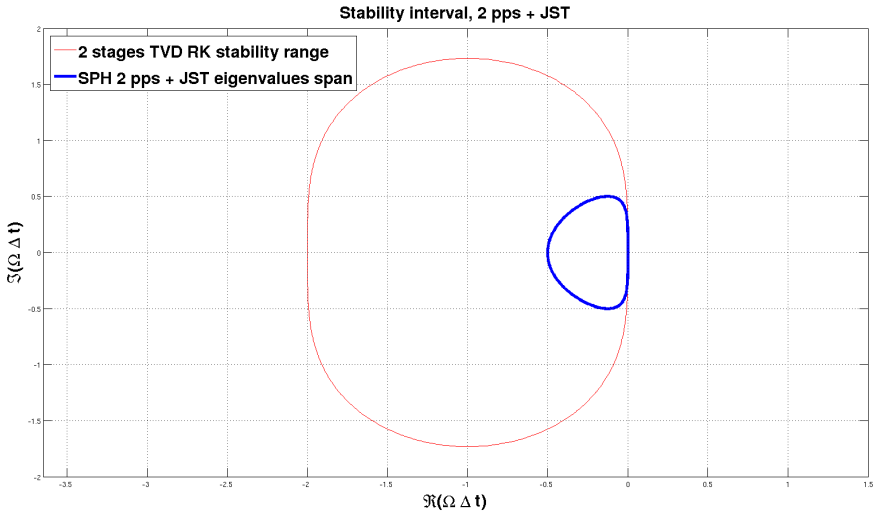

Figure 4.3: stability of the SPH 2 p.p.s. - JST dissipation (space) + 2 stages TVD-RK (time) scheme, $\alpha = 1/2$ and $k^{(4)} = 1/16$.

Figure 4.3 shows the stability of the discretising scheme with added dissipation in space and time, for values of $\alpha = c\Delta t/\Delta x = 1/2$ and $k^{(4)} = 1/16$.

To the contrary of what happened for the previous SPH scheme without artificial dissipation, this time the eigenvalues $\lambda_a \Delta t$ fall entirely inside the allowed stability domain of the time discretisation.

However, in case different combinations of values for α and $k^{(4)}$ are chosen, the range of $\lambda_a \Delta t \in [-\pi, \pi]$ can also become large enough to grow beyond the stability limits set by the amplification factor of the time scheme.

4.2.5 *3 particles per side: consistency*

Investigation of the accuracy properties for the case of a 3 p.p.s. SPH discretisation will be carried out in the same manner it was done for the 2 p.p.s. scheme in section 4.2.1.

To study the consistency of the scheme, the highest degree of the truncation error ϵ_T^n has to be determined with respect ot increments in space Δx and in time Δt. To achieve this, the procedure described in algorithm 4 will be followed.

1. The exact values of the kernel function coefficients and its derivatives for the 3 p.p.s. stencil are presented in table 4.3.

Table 4.3: uncorrected kernel, 3 p.p.s.

	stencil particles position							
	$a-3$	$a-2$	$a-1$	a	$a+1$	$a+2$	$a+3$	
W	0	$8/729$	$28/81$	$4/3$	$28/81$	$8/729$	0	$.1/\Delta x$
∇W	0	$40/729$	$200/243$	0	$-200/243$	$-40/729$	0	$.1/\Delta x^2$
$\nabla^2 W$	0	$160/729$	$320/243$	$-160/27$	$320/243$	$160/729$	0	$.1/\Delta x^3$
$\nabla^3 W$	0	$160/243$	0	$160/9$	0	$-160/243$	0	$.1/\Delta x^4$
$\nabla^4 W$	0	$320/243$	$-640/81$	$-2240/81$	$-640/81$	$320/243$	0	$.1/\Delta x^5$

Applying corrections up to the second derivative in table 4.3 yields the coefficients in table 4.4.

Table 4.4: corrected kernel, 3 p.p.s.

	stencil particles position							
	$a-3$	$a-2$	$a-1$	a	$a+1$	$a+2$	$a+3$	
$\widetilde{W}$	0	$2/373$	$63/373$	$243/373$	$63/373$	$2/373$	0	$.1/\Delta x$
$\widetilde{\nabla} W$	0	$-1/34$	$-15/34$	0	$15/34$	$1/34$	0	$.1/\Delta x$
$\widetilde{\Delta} W$	0	$1/10$	$3/5$	$-7/5$	$3/5$	$1/10$	0	$.1/\Delta x$

As was the case in section 4.2.1, values of $\widetilde{\nabla} W$ and $\widetilde{\nabla}^2 W$ in table 4.4 are undivided, i. e. they have not been divided by the increment Δx with each derivation. The semi-discretised equation for (4.1) can then be expressed as

$$\left.\frac{\partial u}{\partial t}\right|_a = -\frac{c}{34\Delta x}\left(u^n_{a+2} + 15u^n_{a+1} - 15u^n_{a-1} - u^n_{a-2}\right) \tag{4.52}$$

2. The stencil in (4.52) is the same used in the 2 p.p.s. with added JST dissipation seen in section 4.2.3 (eq. (4.41)), as it goes from the particle at x^n_{a-2} to the one in x^n_{a+2}.

   However, with respect to (4.42), in this case Taylor expansions of terms $u_{a\pm i}$ are used just up to the third order:

$$\begin{aligned}
u^n_{a+2} = &\quad u^n_a + 2\left.\frac{\partial u}{\partial x}\right|^n_a \Delta x + 2\left.\frac{\partial^2 u}{\partial x^2}\right|^n_a \Delta x^2 + \frac{4}{3}\left.\frac{\partial^3 u}{\partial x^3}\right|^n_a \Delta x^3 + O\left(\Delta x^4\right)\\
u^n_{a+1} = &\quad u^n_a + \left.\frac{\partial u}{\partial x}\right|^n_a \Delta x + \frac{1}{2}\left.\frac{\partial^2 u}{\partial x^2}\right|^n_a \Delta x^2 + \frac{1}{6}\left.\frac{\partial^3 u}{\partial x^3}\right|^n_a \Delta x^3 + O\left(\Delta x^4\right)\\
u^n_{a-1} = &\quad u^n_a - \left.\frac{\partial u}{\partial x}\right|^n_a \Delta x + \frac{1}{2}\left.\frac{\partial^2 u}{\partial x^2}\right|^n_a \Delta x^2 - \frac{1}{6}\left.\frac{\partial^3 u}{\partial x^3}\right|^n_a \Delta x^3 + O\left(\Delta x^4\right)\\
u^n_{a-2} = &\quad u^n_a - 2\left.\frac{\partial u}{\partial x}\right|^n_a \Delta x + 2\left.\frac{\partial^2 u}{\partial x^2}\right|^n_a \Delta x^2 - \frac{4}{3}\left.\frac{\partial^3 u}{\partial x^3}\right|^n_a \Delta x^3 + O\left(\Delta x^4\right)
\end{aligned} \tag{4.53}$$

3. Obtain u^*_a in (4.14) from (4.53):

$$\begin{aligned}
u^*_a &= u^n_a - \frac{c\Delta t}{34\Delta x}\left(u^n_{a+2} + 15u^n_{a+1} - 15u^n_{a-1} - u^n_{a-2}\right) =\\
&= u^n_a - c\left.\frac{\partial u}{\partial x}\right|^n_a \Delta t - \frac{23}{102}\left.\frac{\partial^3 u}{\partial x^3}\right|^n_a \Delta x^2 \Delta t
\end{aligned} \tag{4.54}$$

4. Derivatives in space of u_a^*:

$$\begin{aligned}
\left.\frac{\partial u}{\partial x}\right|_a^* &= \left.\frac{\partial u}{\partial x}\right|_a^n - c\left.\frac{\partial^2 u}{\partial x^2}\right|_a^n \Delta t - \frac{23}{102}c\left.\frac{\partial^4 u}{\partial x^4}\right|_a^n \Delta x^2\Delta t + O(\Delta x^4)\\
\left.\frac{\partial^2 u}{\partial x^2}\right|_a^* &= \left.\frac{\partial^2 u}{\partial x^2}\right|_a^n - c\left.\frac{\partial^3 u}{\partial x^3}\right|_a^n \Delta t - \frac{23}{102}c\left.\frac{\partial^5 u}{\partial x^5}\right|_a^n \Delta x^2\Delta t + O(\Delta x^4)\\
\left.\frac{\partial^3 u}{\partial x^3}\right|_a^* &= \left.\frac{\partial^3 u}{\partial x^3}\right|_a^n - c\left.\frac{\partial^4 u}{\partial x^4}\right|_a^n \Delta t - \frac{23}{102}c\left.\frac{\partial^6 u}{\partial x^6}\right|_a^n \Delta x^2\Delta t + O(\Delta x^4)
\end{aligned} \tag{4.55}$$

5. Compute u_a^{**} from (4.14), (4.54), (4.55):

$$\begin{aligned}
u_a^{**} &= u_a^* - c\left.\frac{\partial u}{\partial x}\right|_a^* \Delta t - \frac{23}{102}\left.\frac{\partial^3 u}{\partial x^3}\right|_a^* \Delta x^2\Delta t =\\
&= u_a^n - 2c\left.\frac{\partial u}{\partial x}\right|_a^n \Delta t + c^2\left.\frac{\partial^2 u}{\partial x^2}\right|_a^n \Delta t^2 - \frac{23}{51}c\left.\frac{\partial^3 u}{\partial x^3}\right|_a^n \Delta x^2\Delta t + O\left(\Delta x^3\right)
\end{aligned} \tag{4.56}$$

6. Runge-Kutta estimation for next step in time, $N_{RK}(u_a^n)$:

$$\begin{aligned}
N_{RK}(u_a^n) &= \frac{1}{2}(u_a^n + u_a^{**}) =\\
&= u_a^n - c\left.\frac{\partial u}{\partial x}\right|_a^n \Delta t + \frac{c^2}{2}\left.\frac{\partial^2 u}{\partial x^2}\right|_a^n \Delta t^2 - \frac{23}{102}c\left.\frac{\partial^3 u}{\partial x^3}\right|_a^n \Delta x^2\Delta t + O\left(\Delta x^3\right)
\end{aligned} \tag{4.57}$$

7. Taylor expansion of u_a^{n+1} in time around u_a^n, found in (4.21).

8. Obtain the truncation error ϵ_T^n for the scheme from (4.57) and (4.21) as

$$\begin{aligned}
\epsilon_T^n &= \frac{1}{\Delta t}\left(N_{RK}(u_a^n) - u_a^{n+1}\right) =\\
&= -\frac{23}{102}c\left.\frac{\partial^3 u}{\partial x^3}\right|_a^n \Delta x^2 - \frac{1}{6}\left.\frac{\partial^3 u}{\partial t^3}\right|_a^n \Delta t^2 + O\left(\Delta x^3, \Delta t^3\right)
\end{aligned} \tag{4.58}$$

To get to the final expression for ϵ_T^n in (4.58), use was made of (4.23) and (4.25). Equation (4.58) shows that the 3 p.p.s. scheme is of third order accuracy in space and time.

4.2.6 *3 particles per side: stability*

In order to study the stability of the 3 p.p.s. stencil, modifications have to be implemented into the 2 p.p.s. equation (4.27), so that it fits the 3 p.p.s. scheme. Then, for a generic particle located at x_a:

$$\frac{\partial u_a}{\partial t} = \sum_{i=-2}^{2} \mathbf{D}_{ai}\, u_{a+i} = \\ -\frac{c}{34\Delta x}\left(u^n_{a+2} + 15u^n_{a+1} - 15u^n_{a-1} - u^n_{a-2}\right) \tag{4.59}$$

A row $\mathbf{D}_a$ of matrix $\mathbf{D}$ now reads

$$\mathbf{D}_a = \left[0 \quad \dots \quad -\frac{c}{34\Delta x} \;\middle|\; -\frac{15c}{34\Delta x} \;\middle|\; 0 \;\middle|\; \frac{15c}{34\Delta x} \;\middle|\; \frac{c}{34\Delta x} \quad \dots \quad 0\right] \tag{4.60}$$

The eigenproblem for (4.59), after the eigenvectors have been decomposed in the Fourier domain, reads

$$\mathbf{D}_{ai} e^{Ii\Phi_j} = \lambda_a e^{Ia\Phi_j} \qquad i = a-2, \dots, a+2 \tag{4.61}$$

Substituting (4.60) in (4.61) allows to express λ_a as

$$\lambda_a = -\frac{c}{34\Delta x} e^{2I\Phi_j} - \frac{15c}{34\Delta x} e^{I\Phi_j} + \frac{15c}{34\Delta x} e^{-I\Phi_j} + \frac{c}{34\Delta x} e^{-2I\Phi_j} \tag{4.62}$$

By means of (4.34), (4.62) transforms into:

$$\lambda_a = I\left(-\frac{c}{17\Delta x}\sin 2\Phi_j - \frac{15c}{17\Delta x}\sin \Phi_j\right) \tag{4.63}$$

Since $\Re(\lambda_j) = 0$, the SPH spatial semi-discretisation with 3 p.p.s. fulfils the stability condition (4.29).

Despite this, fig. 4.4 shows that the time stepping of (4.59) with a 2 stages TVD-RK approach should lead to instability.

4.2.7 *3 particles per side + JST dissipation: consistency*

Section 4.2.6 showed that the 3 p.p.s. SPH spatial semi-discretisation needs artificial dissipation in order to achieve stability in time.

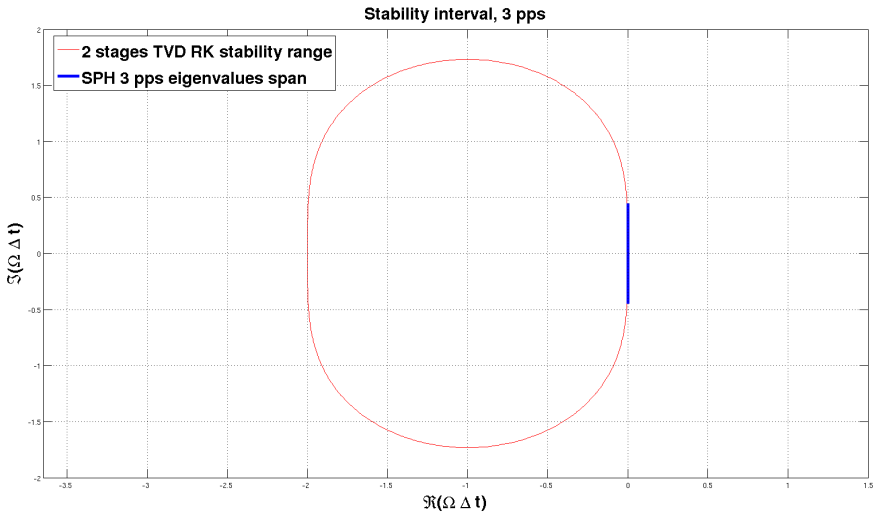

Figure 4.4: stability of the SPH 3 p.p.s. (space) + 2 stages TVD-RK (time) scheme, $\alpha = 1/2$.

For this purpose, and similarly to what was done in section 4.2.3 for the 2 p.p.s. case, a JST-type of dissipative term is added to the SPH-discretised LAE in order to obtain (4.39). As in the 2 p.p.s. case, the dissipation term employs an undivided Laplacian of Laplacian. The discretised version of $\nabla^4 W$ is obtained in the same way of section 4.2.3, by first applying a corrected SPH Laplacian, and then a central difference Laplacian operator to W in (4.39).

Algorithm 4 will be followed to derive the truncation error ϵ_T^n for the scheme.

1. Values in table 4.4 will be used for the corrected kernel $\widetilde{W}$ and its derivatives, in order to compute $\widetilde{\nabla}^2_{SPH} W$. The Laplacian of Laplacian in the dissipative term, expressed in terms of central differences, is

$$\begin{aligned}
&\nabla^4 u = \Delta_{CD}\left(\widetilde{\nabla}^2_{SPH} u\right) = \\
&\sum_{b\in\Lambda_{a-1}} \Delta x\, u_b\, \widetilde{\nabla}^2 W_b\,(x_{a-1}) - 2\sum_{b\in\Lambda_a} \Delta x\, u_b\, \widetilde{\nabla}^2 W_b\,(x_a) + \\
&+ \sum_{b\in\Lambda_{a+1}} \Delta x\, u_b\, \widetilde{\nabla}^2 W_b\,(x_{a+1}) = \\
&= \frac{1}{10}u_{a+3} + \frac{2}{5}u_{a+2} - \frac{5}{2}u_{a+1} + 4u_a - \frac{5}{2}u_{a-1} + \frac{2}{5}u_{a-2} + \frac{1}{10}u_{a-3}
\end{aligned} \tag{4.64}$$

In light of (4.64), the complete SPH 3 p.p.s. semi-discretisation in space can be put as:

$$\frac{\partial u}{\partial t} = -\frac{c}{34\Delta x}\left(u^n_{a+2} + 15u^n_{a+1} - 15u^n_{a-1} - u^n_{a-2}\right) + \\ -\frac{ck^{(4)}}{\Delta x}\left(\frac{1}{10}u_{a+3} + \frac{2}{5}u_{a+2} - \frac{5}{2}u_{a+1} + 4u_a - \frac{5}{2}u_{a-1} + \frac{2}{5}u_{a-2} + \frac{1}{10}u_{a-3}\right) \tag{4.65}$$

2. With respect to (4.53), fourth order terms have to be added to the Taylor series expansions of terms $u_{a\pm i}$ that are in (4.65). In addition, expansions for the $u_{a\pm 3}$ contributions need to be computed:

$$\begin{aligned}
u^n_{a+3} &= u^n_a + 3\left.\frac{\partial u}{\partial x}\right|^n_a \Delta x + \frac{9}{2}\left.\frac{\partial^2 u}{\partial x^2}\right|^n_a \Delta x^2 + \frac{9}{2}\left.\frac{\partial^3 u}{\partial x^3}\right|^n_a \Delta x^3 + \frac{27}{8}\left.\frac{\partial^4 u}{\partial x^4}\right|^n_a \Delta x^4 + \dots \\
u^n_{a+2} &= u^n_a + 2\left.\frac{\partial u}{\partial x}\right|^n_a \Delta x + 2\left.\frac{\partial^2 u}{\partial x^2}\right|^n_a \Delta x^2 + \frac{4}{3}\left.\frac{\partial^3 u}{\partial x^3}\right|^n_a \Delta x^3 + \frac{2}{3}\left.\frac{\partial^4 u}{\partial x^4}\right|^n_a \Delta x^4 + \dots \\
u^n_{a+1} &= u^n_a + \left.\frac{\partial u}{\partial x}\right|^n_a \Delta x + \frac{1}{2}\left.\frac{\partial^2 u}{\partial x^2}\right|^n_a \Delta x^2 + \frac{1}{6}\left.\frac{\partial^3 u}{\partial x^3}\right|^n_a \Delta x^3 + \frac{1}{24}\left.\frac{\partial^4 u}{\partial x^4}\right|^n_a \Delta x^4 + \dots \\
u^n_{a-1} &= u^n_a - \left.\frac{\partial u}{\partial x}\right|^n_a \Delta x + \frac{1}{2}\left.\frac{\partial^2 u}{\partial x^2}\right|^n_a \Delta x^2 - \frac{1}{6}\left.\frac{\partial^3 u}{\partial x^3}\right|^n_a \Delta x^3 + \frac{1}{24}\left.\frac{\partial^4 u}{\partial x^4}\right|^n_a \Delta x^4 + \dots \\
u^n_{a-2} &= u^n_a - 2\left.\frac{\partial u}{\partial x}\right|^n_a \Delta x + 2\left.\frac{\partial^2 u}{\partial x^2}\right|^n_a \Delta x^2 - \frac{4}{3}\left.\frac{\partial^3 u}{\partial x^3}\right|^n_a \Delta x^3 + \frac{2}{3}\left.\frac{\partial^4 u}{\partial x^4}\right|^n_a \Delta x^4 + \dots \\
u^n_{a-3} &= u^n_a - 3\left.\frac{\partial u}{\partial x}\right|^n_a \Delta x + \frac{9}{2}\left.\frac{\partial^2 u}{\partial x^2}\right|^n_a \Delta x^2 - \frac{9}{2}\left.\frac{\partial^3 u}{\partial x^3}\right|^n_a \Delta x^3 + \frac{27}{8}\left.\frac{\partial^4 u}{\partial x^4}\right|^n_a \Delta x^4 + \dots \\
&\qquad + O\left(\Delta x^5\right)
\end{aligned} \tag{4.66}$$

3. Obtain u^*_a in (4.14), with the help of (4.66):

$$\begin{aligned}
u^*_a &= u^n_a - \frac{c\Delta t}{34\Delta x}\left(u^n_{a+2} + 15u^n_{a+1} - 15u^n_{a-1} - u^n_{a-2}\right) + \\
&-\frac{ck^{(4)}\Delta t}{\Delta x}\left(\frac{1}{10}u_{a+3} + \frac{2}{5}u_{a+2} - \frac{5}{2}u_{a+1} + 4u_a - \frac{5}{2}u_{a-1} + \frac{2}{5}u_{a-2} + \frac{1}{10}u_{a-3}\right) = \\
&= u^n_a - c\left.\frac{\partial u}{\partial x}\right|^n_a \Delta t - \frac{23}{102}\left.\frac{\partial^3 u}{\partial x^3}\right|^n_a \Delta x^2 \Delta t - ck^{(4)}\left.\frac{\partial^4 u}{\partial x^4}\right|^n_a \Delta x^3 \Delta t + O\left(\Delta x^4\right)
\end{aligned} \tag{4.67}$$

4. Derivatives in space of u_a^*:

$$\begin{aligned}
\left.\frac{\partial u}{\partial x}\right|_a^* &= \left.\frac{\partial u}{\partial x}\right|_a^n - c\left.\frac{\partial^2 u}{\partial x^2}\right|_a^n \Delta t - \frac{23}{102}c\left.\frac{\partial^4 u}{\partial x^4}\right|_a^n \Delta x^2\Delta t - ck^{(4)}\left.\frac{\partial^5 u}{\partial x^5}\right|_a^n \Delta x^3\Delta t + \dots \\
\left.\frac{\partial^2 u}{\partial x^2}\right|_a^* &= \left.\frac{\partial^2 u}{\partial x^2}\right|_a^n - c\left.\frac{\partial^3 u}{\partial x^3}\right|_a^n \Delta t - \frac{23}{102}c\left.\frac{\partial^5 u}{\partial x^5}\right|_a^n \Delta x^2\Delta t - ck^{(4)}\left.\frac{\partial^6 u}{\partial x^6}\right|_a^n \Delta x^3\Delta t + \dots \\
\left.\frac{\partial^3 u}{\partial x^3}\right|_a^* &= \left.\frac{\partial^3 u}{\partial x^3}\right|_a^n - c\left.\frac{\partial^4 u}{\partial x^4}\right|_a^n \Delta t - \frac{23}{102}c\left.\frac{\partial^6 u}{\partial x^6}\right|_a^n \Delta x^2\Delta t - ck^{(4)}\left.\frac{\partial^7 u}{\partial x^7}\right|_a^n \Delta x^3\Delta t + \dots \\
\left.\frac{\partial^4 u}{\partial x^4}\right|_a^* &= \left.\frac{\partial^4 u}{\partial x^4}\right|_a^n - c\left.\frac{\partial^5 u}{\partial x^5}\right|_a^n \Delta t - \frac{23}{102}c\left.\frac{\partial^7 u}{\partial x^7}\right|_a^n \Delta x^2\Delta t - ck^{(4)}\left.\frac{\partial^8 u}{\partial x^8}\right|_a^n \Delta x^3\Delta t + \dots \\
&\qquad + O(\Delta x^4)
\end{aligned} \tag{4.68}$$

5. Compute u_a^{**} from (4.14), (4.67), (4.68):

$$\begin{aligned}
u_a^{**} &= u_a^* - c\left.\frac{\partial u}{\partial x}\right|_a^* \Delta t - \frac{23}{102}\left.\frac{\partial^3 u}{\partial x^3}\right|_a^* \Delta x^2\Delta t - ck^{(4)}\left.\frac{\partial^4 u}{\partial x^4}\right|_a^* \Delta x^3\Delta t = \\
&= u_a^n - 2c\left.\frac{\partial u}{\partial x}\right|_a^n \Delta t + c^2\left.\frac{\partial^2 u}{\partial x^2}\right|_a^n \Delta t^2 - \frac{23}{51}c\left.\frac{\partial^3 u}{\partial x^3}\right|_a^n \Delta x^2\Delta t + \\
&+ \cancel{\left(\frac{23}{51}c^2\Delta x^2\Delta t^2 - 2ck^{(4)}\Delta x^3\Delta t\right)\left.\frac{\partial^4 u}{\partial x^4}\right|_a^n}^{\text{h.o.t.}} + \\
&- \cancel{2c^2k^{(4)}\left.\frac{\partial^5 u}{\partial x^5}\right|_a^n \Delta x^3\Delta t^2}^{\text{h.o.t.}} + \cancel{\frac{529}{10404}c^2\left.\frac{\partial^6 u}{\partial x^6}\right|_a^n \Delta x^4\Delta t^2}^{\text{h.o.t.}} + \\
&- \cancel{\frac{23}{51}c^2k^{(4)}\left.\frac{\partial^7 u}{\partial x^7}\right|_a^n \Delta x^5\Delta t^2}^{\text{h.o.t.}} + \cancel{\left(c^2k^{(4)}\right)^2\left.\frac{\partial^8 u}{\partial x^8}\right|_a^n \Delta x^6\Delta t^2}^{\text{h.o.t.}} + \\
&+ O\left(\cancel{\Delta x^7}^{3}, \Delta t^3\right)
\end{aligned} \tag{4.69}$$

6. Runge-Kutta estimation for next step in time, $N_{RK}(u_a^n)$:

$$\begin{aligned}
N_{RK}(u_a^n) &= \frac{1}{2}(u_a^n + u_a^{**}) = \\
&= u_a^n - c\left.\frac{\partial u}{\partial x}\right|_a^n \Delta t + \frac{c^2}{2}\left.\frac{\partial^2 u}{\partial x^2}\right|_a^n \Delta t^2 - \frac{23}{102}c\left.\frac{\partial^3 u}{\partial x^3}\right|_a^n \Delta x^2\Delta t + O\left(\Delta x^3\right)
\end{aligned} \tag{4.70}$$

To note, (4.70) is the same result achieved in (4.57), meaning that the consistency of the schemes, one with and the other without dissipation, will be the same.

7. Taylor expansion of u_a^{n+1} in time around u_a^n, found in (4.21).

8. Obtain the truncation error ϵ_T^n for the scheme from (4.70) and (4.21) as

$$\begin{aligned}\epsilon_T^n =& \frac{1}{\Delta t}\left(N_{RK}(u_a^n) - u_a^{n+1}\right) = \\ =& -\frac{23}{102}c\left.\frac{\partial^3 u}{\partial x^3}\right|_a^n \Delta x^2 - \frac{1}{6}\left.\frac{\partial^3 u}{\partial t^3}\right|_a^n \Delta t^2 + O\left(\Delta x^3, \Delta t^3\right)\end{aligned} \tag{4.71}$$

The final expression for ϵ_T^n in (4.71), obtained by drawing upon (4.23) and (4.25), proves that the accuracy of the 3 p.p.s. scheme with added JST dissipation attains the same third order accuracy in space and time achieved by the 3 p.p.s. scheme in (4.58).

4.2.8 *3 particles per side + JST dissipation: stability*

As a first step, the stability of the 3 p.p.s. + JST dissipation stencil is investigated by adapting (4.27) to the current stencil. This yields, for the generic particle a:

$$\begin{aligned}&\frac{\partial u_a}{\partial t} = \sum_{i=-3}^{3} \mathbf{D}_{ai}\, u_{a+i} = -\frac{c}{34\Delta x}\left(u_{a+2}^n + 15u_{a+1}^n - 15u_{a-1}^n - u_{a-2}^n\right) + \\ &-\frac{ck^{(4)}}{\Delta x}\left(\frac{1}{10}u_{a+3}^n + \frac{2}{5}u_{a+2}^n - \frac{5}{2}u_{a+1}^n + 4u_a^n - \frac{5}{2}u_{a-1}^n + \frac{2}{5}u_{a-2}^n + \frac{1}{10}u_{a-3}^n\right)\end{aligned} \tag{4.72}$$

so that row $\mathbf{D}_a$ of matrix $\mathbf{D}$ reads

$$\begin{aligned}\mathbf{D}_a = \Bigg[0 \quad \dots \quad -\frac{ck^{(4)}}{10\Delta x} \;\Bigg|\; -\frac{c}{\Delta x}\left(\frac{1}{34} + \frac{2}{5}k^{(4)}\right) \;\Bigg|\; \frac{c}{\Delta x}\left(-\frac{15}{34} + \frac{5}{2}k^{(4)}\right) \;\Bigg|\; \\ -4\frac{ck^{(4)}}{\Delta x} \;\Bigg|\; \frac{c}{\Delta x}\left(\frac{15}{34} + \frac{5}{2}k^{(4)}\right) \;\Bigg|\; \frac{c}{\Delta x}\left(\frac{1}{34} - \frac{2}{5}k^{(4)}\right) \;\Bigg|\; -\frac{ck^{(4)}}{10\Delta x} \quad \dots \quad 0\Bigg]\end{aligned} \tag{4.73}$$

Substituting (4.73) in (4.61) allows to express λ_a as

$$\lambda_a = -\frac{ck^{(4)}}{10\Delta x}e^{3I\Phi_j} - \frac{c}{\Delta x}\left(\frac{1}{34}+\frac{2}{5}k^{(4)}\right)e^{2I\Phi_j} + \frac{c}{\Delta x}\left(-\frac{15}{34}+\frac{5}{2}k^{(4)}\right)e^{I\Phi_j} + \\ -4\frac{ck^{(4)}}{\Delta x} + \frac{c}{\Delta x}\left(\frac{15}{34}+\frac{5}{2}k^{(4)}\right)e^{-I\Phi_j} + \frac{c}{\Delta x}\left(\frac{1}{34}-\frac{2}{5}k^{(4)}\right)e^{-2I\Phi_j} - \frac{ck^{(4)}}{10\Delta x}e^{-3I\Phi_j} \tag{4.74}$$

By means of (4.34), λ_a in (4.62) can be separated into its real and imaginary parts:

$$\Re(\lambda_a) = -\frac{ck^{(4)}}{5\Delta x}\cos 3\Phi_j - \frac{4ck^{(4)}}{5\Delta x}\cos 2\Phi_j + \frac{5ck^{(4)}}{\Delta x}\cos\Phi_j - \frac{4ck^{(4)}}{\Delta x} \leqslant 0\,, \\ \forall\Phi_j \in [-\pi,\pi] \tag{4.75a}$$

$$\Im(\lambda_a) = -\frac{c}{17\Delta x}\sin 2\Phi_j - \frac{15c}{17\Delta x}\sin\Phi_j \tag{4.75b}$$

Since condition (4.29) is satisfied by (4.75a), the 3 p.p.s. SPH spatial semi-discretisation with JST artificial dissipation is proven stable.

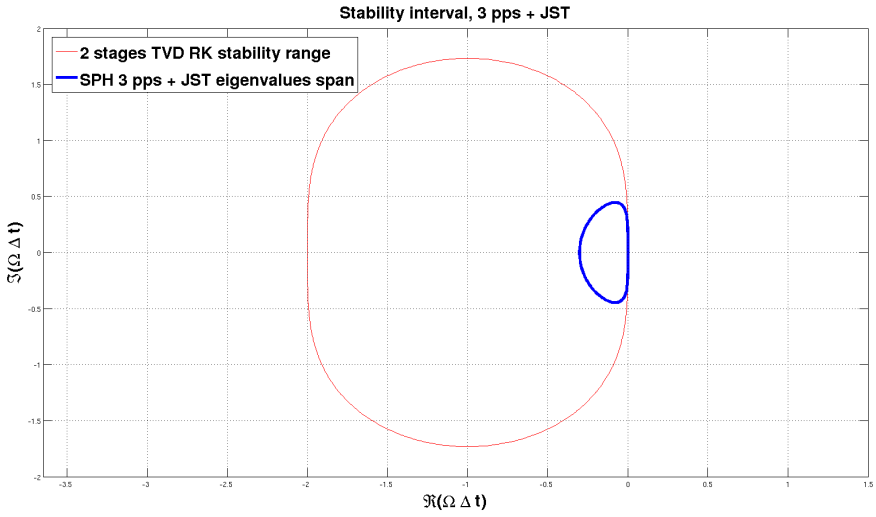

Figure 4.5: stability of the SPH 3 p.p.s. - JST artificial dissipation (space) + 2 stages TVD-RK (time) scheme, $\alpha = 1/2$ and $k^{(4)} = 1/16$.

Figure 4.5 shows the stability in space and time of the discretising scheme with added dissipation, for values of $\alpha = c\Delta t/\Delta x = 1/2$ and $k^{(4)} = 1/16$.

As opposite to the SPH 3 p.p.s. scheme without artificial dissipation seen in section 4.2.6, in fig. 4.5 the eigenvalues $\lambda_a\Delta t$ fall entirely inside the allowed

stability domain of the time discretisation. However, in case particular combinations of values for α and $k^{(4)}$ are chosen, the range of $\lambda_a \Delta t \in [-\pi, \pi]$ can possibly overrun the stability limits set up by the time scheme amplification factor z_P.

Alternatively, stability plots could be drawn on the amplification factor z_P complex plane, as shown in figs. 4.6 and 4.7.

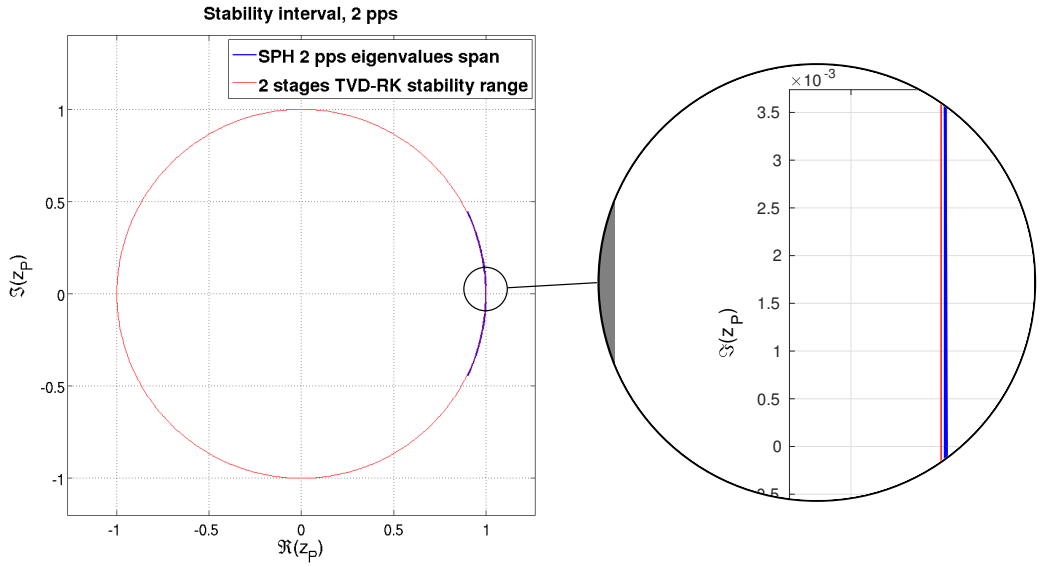

Figure 4.6: stability limits for the non stabilised SPH scheme, plotted on the amplification factor z_P complex plane. Zoomed section shows instability of the scheme, as the SPH eigenvalues lie outside the stability range.

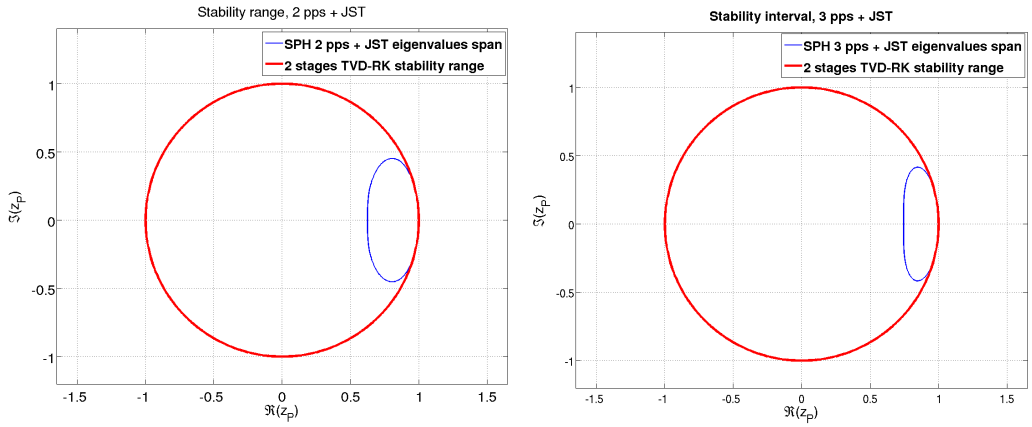

(a) JST-SPH 2 p.p.s. scheme (b) JST-SPH 3 p.p.s. scheme

Figure 4.7: stability limits for the JST-SPH scheme, plotted on the amplification factor z_P complex plane. The scheme lies inside the stability range, for both the 2 and 3 p.p.s. cases.

4.3 SPECTRAL ANALYSIS OF THE AMPLIFICATION FACTOR

The amplification factor z_P, defined in (4.37), provides more insight on the nature and behaviour of the numerical error. Since z_P is peculiar to each scheme, it allows the analyst to predict performances and pick the most appropriate scheme for the problem at hand.

The solution of (4.7) can be split into separate time- and space-dependent components:

$$u(t,x) = \sum_{j=1}^{N} l_j(t)\, R_j(x) \tag{4.76}$$

In (4.76) the space-dependent component is the eigenvector R_j, which has been already presented as a Fourier series expansion in (4.30). An expression for the time-dependent l_j is found by substituting (4.76) in (4.27), and then by using the first of (4.28) to obtain

$$\frac{dl_j}{dt} = \lambda_j l_j \qquad \forall j \in [1,N] \tag{4.77}$$

The solution for the $j^{\text{-th}}$ single equation in (4.77) is

$$l_j^n = l_j(t) = l_j(0)e^{\lambda_j t} = l_j^0 e^{\lambda_j n\Delta t} \tag{4.78}$$

where l_j^n is considered at n equispaced time instants Δt, that is $t = n\Delta t$.

In (4.78), l_j^0 is the initial solution of (4.1). It can be further expanded into Fourier series as

$$l_j(0) = \frac{1}{2L}\int_{-L}^{L} f(x)e^{-Ikx_j}\,dx \tag{4.79}$$

where L is the length of the unidimensional domain, k is the wave number defined in (4.31), here taken in its continuous form, and $x_j = j\Delta x$. The numerical amplification factor z_P has already been employed in the study of stability from section 4.2.2 onward. It is time to give a proper definition of z_P as

$$z_P = \frac{l_j^{n+1}}{l_j^n} \tag{4.80}$$

From (4.80), it follows that

$$\frac{l_j^n}{l_j^0} = (z_P)^n \tag{4.81}$$

Further, using (4.78), z_P can be written as

$$z_P = e^{\lambda_j \Delta t} \tag{4.82}$$

In general, the eigenvalue λ_j will be a complex number, and, as a consequence of (4.82), so will also be z_P. It is thus possible to separate it in an amplitude, or absolute value, $|z_P|$, and a phase angle, ϕ:

$$z_P = |z_P| e^{-I\phi} \tag{4.83}$$

The amplification factor of the numerical solution z_P can be compared with the $\widetilde{z}_P$ of the exact solution, to obtain:

- the error in amplitude, or *dissipation error* ε_D

$$\varepsilon_D = \frac{|z_P|}{|\widetilde{z}_P|} \tag{4.84}$$

  In order to achieve stability, it is necessary that $\varepsilon_D < 1$, or else the amplitude of the solution will grow along with the time steps, leading the solution to eventual divergence;

- the error in phase angle, or *dispersion error* ε_ϕ, which for convection dominated problems takes the form

$$\varepsilon_\phi = \frac{\phi}{\widetilde{\phi}} \tag{4.85}$$

  ε_ϕ could also be expressed as $\varepsilon_\phi = \phi - \widetilde{\phi}$, in case of a diffusion dominated problem. In case $\phi > \widetilde{\phi}$, ε_ϕ is said to be a *leading error*; on the contrary, if $\phi < \widetilde{\phi}$, ε_ϕ is said to be a *lagging error*.

Given the fact that in hyperbolic PDEs, such as (4.1), no physical damping is present, it holds that

$$\begin{aligned} \varepsilon_D &= |z_P| = \sqrt{[\Re(z_P)]^2 + [\Im(z_P)]^2} \\ \varepsilon_\phi &= \frac{\phi}{\alpha\Phi} = -\frac{1}{\alpha\Phi}\frac{\Im(z_P)}{\Re(z_P)} \end{aligned} \tag{4.86}$$

with Φ being the phase angle of the Fourier decomposition of eigenvectors $\mathbf{R}_i$ as defined in (4.30) of section 4.2.2. Errors as defined in (4.86) can be applied to a scheme discretised in time with TVD-RK, by substituting (4.37) in (4.86).

It is possible then to plot both errors as functions of the phase angle ϕ used in the Fourier series expansion of u_j^n, in order to gather insightful information on the solution stability and behaviour.

Values of Φ near 0 represent the contribution of low-frequency harmonics of the solution, while high-frequency contributions are located near $\Phi = \pi$.

- *Diffusion error for SPH schemes without artificial dissipation*

  The diffusion error ε_D for the 2 p.p.s. and 3 p.p.s. SPH stencils is plotted in fig. 4.8.

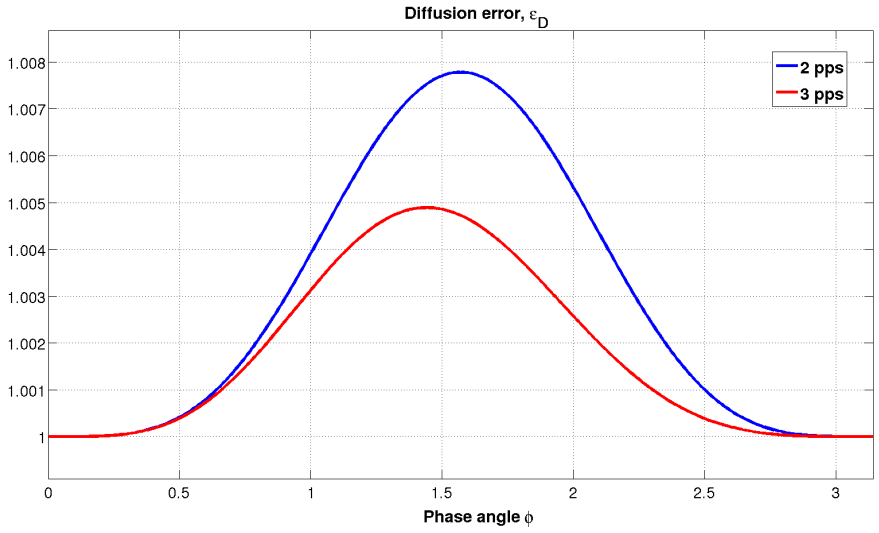

Figure 4.8: diffusion error ε_D for the 2 p.p.s. and 3 p.p.s. SPH schemes.

Both schemes in fig. 4.8 display $\varepsilon_D \geqslant 1$ for the whole spectrum $[0, \pi]$ of Φ. This proves they are unstable, confirming what had been already determined in sections 4.2.2 and 4.2.6.

- *Diffusion error for SPH schemes with JST artificial dissipation*

  The diffusion error ε_D for the 2 p.p.s. and 3 p.p.s. SPH stencils with added JST numerical dissipation is plotted in fig. 4.9.

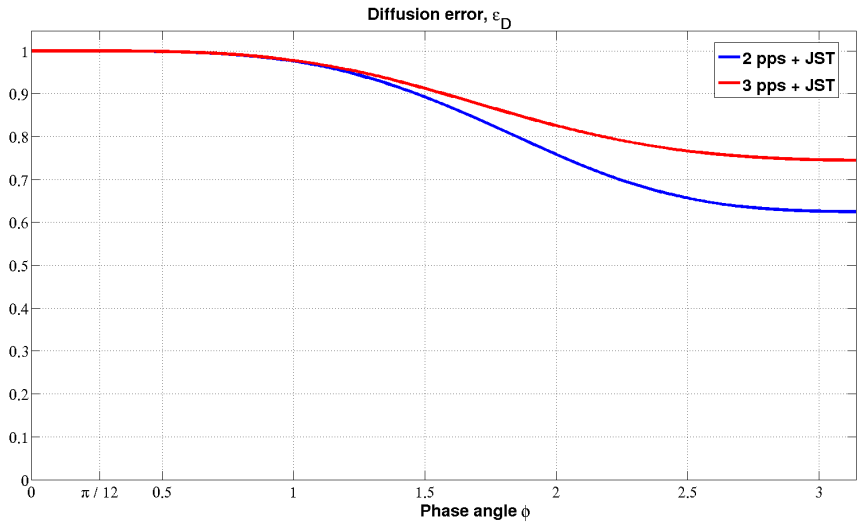

Figure 4.9: diffusion error ε_D for the 2 p.p.s. and 3 p.p.s. SPH schemes + JST.

With the addition of artificial dissipation, the schemes in fig. 4.9 now show $\varepsilon_D \leqslant 1$ for the whole spectrum $[0, \pi]$ of Φ, reaffirming conclusions drawn in sections sections 4.2.2 and 4.2.6 about their stability.

It can also be observed how ε_D stays in the neighbourhood of 1 for an ample stretch in the low-frequency harmonics range. This has a positive effect on accuracy, as that interval is much wider than the $\Phi_{lim} = \pi/12$ ($\approx$ 25 points per wavelength) needed to capture high-frequency signals.

Moreover, the smaller values ε_D assumes in the high-frequencies end up yielding a positive influence, as they help to dampen the numerical oscillations that inevitably appear when using second order schemes to approximate solutions with discontinuities.

- *Dispersion error for SPH schemes without artificial dissipation*

  The dispersion error ε_ϕ for the 2 p.p.s. and 3 p.p.s. SPH stencils is presented in fig. 4.10.

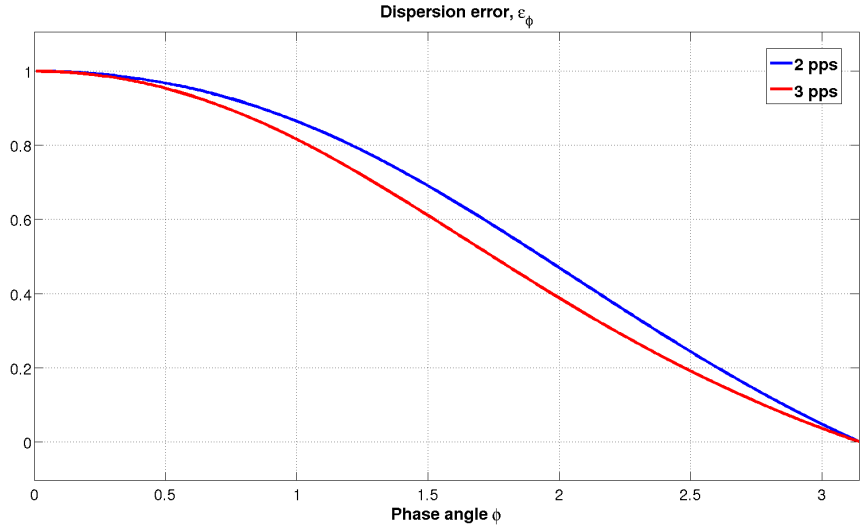

Figure 4.10: dispersion error ε_Φ for the 2 p.p.s. and 3 p.p.s. SPH schemes.

Both schemes in fig. 4.10 show $\varepsilon_\Phi \leqslant 1$ for the whole spectrum $[0, \pi]$ of ϕ, a lagging phase error. The velocity at which the numerical solution propagates will be therefore slower than velocity c in the continuum. However, this will be more true for the high-frequency wavelets, as ε_ϕ is at its smallest there, than for low-frequency harmonics. As the spectral content of numerical errors is mostly located at high frequencies, it is expected that oscillations will appear upstream of eventual discontinuities of the solution, or its derivatives. Low frequencies, on the contrary, are expected to constitute the bulk of the exact solution; therefore, the lagging effect on the numerical solution is predicted to be negligible.

- *Dispersion error for SPH schemes with JST artificial dissipation*

  The dispersion error ε_ϕ for the 2 p.p.s. and 3 p.p.s. SPH stencils, is presented in fig. 4.11.

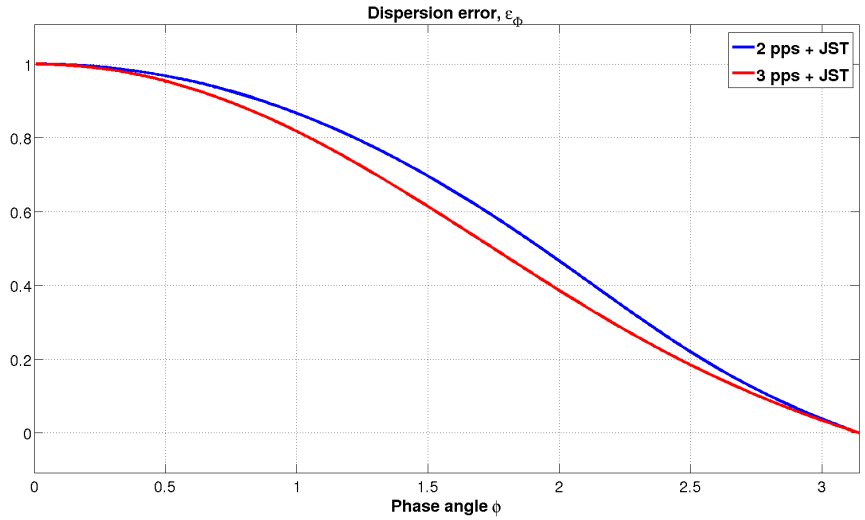

Figure 4.11: dispersion error ε_Φ for the 2 p.p.s. and 3 p.p.s. SPH schemes + JST.

Figure 4.11 does not differ much from previous fig. 4.10. As could be expected, the added numerical dissipation predominantly affects the dissipation error ε_D.

4.4 CONCLUDING REMARKS

In terms of stability, the JST-SPH discretisation of the one-dimensional LAE equation, as conducted in section 4.1, has been shown in section 4.2 to be an improvement with respect to the case without the JST dissipative term.

Data gathered on the dissipation error in section 4.3 confirm that JST is effective in damping high-frequency oscillations, such as the pressure chequerboard instabilities that are a consequence of SPH nodal integration. Appearance and development of these instabilities will be shown in the applications presented in the next chapter.

5 NUMERICAL APPLICATIONS

Numerical simulations, performed with the JST-SPH methodology described so far, constitute the subject of the present chapter. The order of presentation will be arranged according to the material constitutional law used, amongst those listed in chapter 2.

Thus, in section 5.1 the applications will consider nearly incompressible hyperelasticity; while in section 5.2 the focus will be expanded to include material deformation scenarios with permanent plastic deformations. Section 5.3 will repeat some of these tests to simulate and investigate initial configuration with unstructured (i. e. irregular) particle distribution. Section 5.4, finally, will present closing remarks.

5.1 HYPERELASTICITY

5.1.1 *Swinging cube*

A cube of side length 1 m, as illustrated in fig. 5.1, is assigned symmetric BCs (roller supports) on the faces aligned with the $X = 0$, $Y = 0$ and $Z = 0$ planes, while on faces lying on the $X = 1$, $Y = 1$ and $Z = 1$ planes its movement is restricted to the tangential direction by skew-symmetric BCs.

This example is set up to investigate the convergence of the JST-SPH scheme, as in the small strain regime a closed form solution is known to be of the form [135, 145]:

$$\mathbf{u}(\mathbf{X}, t) = U_0 \cos\left(\frac{\sqrt{3}}{2}\pi c\, t\right) \begin{bmatrix} \sin\left(\frac{\pi X_1}{2}\right)\cos\left(\frac{\pi X_2}{2}\right)\cos\left(\frac{\pi X_3}{2}\right) \\ \cos\left(\frac{\pi X_1}{2}\right)\sin\left(\frac{\pi X_2}{2}\right)\cos\left(\frac{\pi X_3}{2}\right) \\ \cos\left(\frac{\pi X_1}{2}\right)\cos\left(\frac{\pi X_2}{2}\right)\sin\left(\frac{\pi X_3}{2}\right) \end{bmatrix} \tag{5.1}$$

In (5.1), the solution is provided for the displacements $\mathbf{u}$ using material elastic speed defined as $c = \sqrt{(\lambda + 2\mu)/\rho}$. User-defined parameter U_0 governs

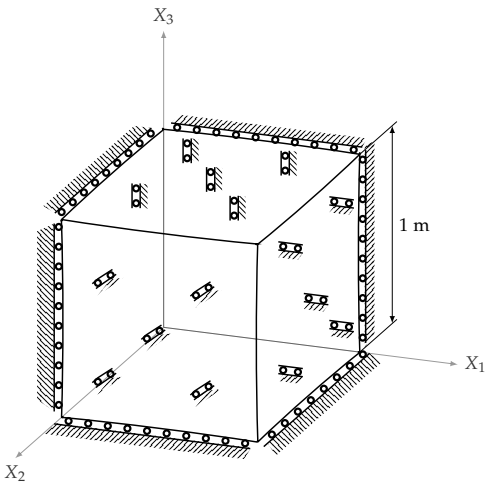

Figure 5.1: swinging cube initial configuration.

the amplitude of the solution oscillations. In case $U_0 < 10^{-3}$ is selected, $\mathbf{u}$ will be sufficiently small to assume a Saint-Venant type of material behaviour. The motion of the cube is triggered by imposing the following initial deformation field:

$$\begin{aligned} \mathbf{F}(\mathbf{X}, t = 0) &= \mathbf{I} + \boldsymbol{\nabla}_0 \mathbf{u}(\mathbf{X}, t = 0) \\ \mathbf{H}(\mathbf{X}, t = 0) &= \frac{1}{2} \mathbf{F}(\mathbf{X}, t = 0) \times \mathbf{F}(\mathbf{X}, t = 0) \\ J(\mathbf{X}, t = 0) &= \frac{1}{6} [\mathbf{F}(\mathbf{X}, t = 0) \times \mathbf{F}(\mathbf{X}, t = 0)] : \mathbf{F}(\mathbf{X}, t = 0) \end{aligned} \tag{5.2}$$

The amplitude parameter is selected as $U_0 = 0.0005$, while the material is modelled as linearly elastic, with Young modulus $E = 17\,\text{MPa}$, Poisson's ratio $\nu = 0.3$ and density $\rho = 1100\,\text{kg/m}^3$.

Assigning a JST constant $k_{JST}^{(4)} = 1/8$, a CFL number $\sigma_{CFL} = 0.3$, a SPH kernel support radius of 2.2 times the smoothing length h, and choosing a discretised mesh of $8 \times 8 \times 8 = 512$ particles, graphical representations of the cube motion are presented in fig. 5.2 at various instants of the simulation time. In fig. 5.2, deformations have been significantly enlarged for visualisation purposes.

A convergence analysis was performed in the case of the mixed $\{\mathbf{p}, \mathbf{F}\}$ JST-SPH scheme, calculating the global error norms for velocities $L^1(v)$ and $L^2(v)$, and pressures $L^1(p)$ and $L^2(p)$. Data are extracted at simulation instant

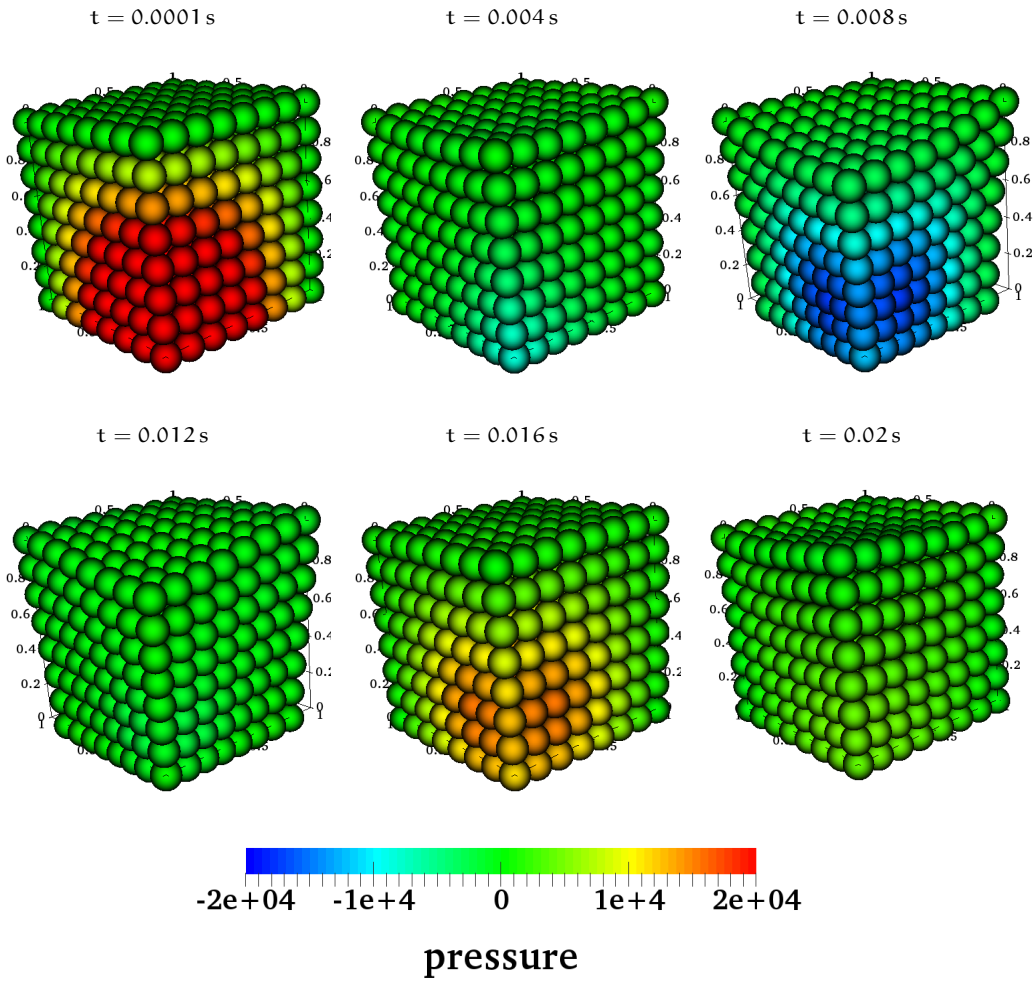

Figure 5.2: swinging cube simulation, pressure contour plot at various instants in time. Results obtained with the $\{\mathbf{p}, \mathbf{F}\}$ JST-SPH scheme. Simulation parameters: 512 particles, $k_{JST}^{(4)} = 1/8$, Saint Venant elastic material with density $\rho = 1100\,kg/m^3$, Young's modulus $E = 17\,MPa$, Poisson's ratio $\nu = 0.3$. Initial conditions are as defined in (5.2) and (5.1), with $U_0 = 0.0005$. Deformations in the images above are magnified 200 times. $\sigma_{CFL} = 0.3$ assumed.

$t = 0.004\,s$, for different discretisations of 512 (8 p.p.s.), 1728 (12 p.p.s.), 4096 (16 p.p.s.), 8000 (20 p.p.s.) and 13824 (24 p.p.s.) particles.

The norms are defined as:

$$L^1(v) = \sum_{i=1}^{N} V_i \left| v_i^{exact} - v_i \right|; \qquad L^2(v) = \sqrt{\sum_{i=1}^{N} V_i \left(v_i^{exact} - v_i \right)^2} \tag{5.3a}$$

$$L^1(p) = \sum_{i=1}^{N} V_i \left| p_i^{exact} - p_i \right|; \qquad L^2(p) = \sqrt{\sum_{i=1}^{N} V_i \left(p_i^{exact} - p_i \right)^2} \tag{5.3b}$$

In (5.3), N is the total number of particles, V_i is the portion of domain volume assigned to each particle i, v_i^{exact} is the analytical velocity obtained by differentiating (5.1) with respect to time t; while exact values of pressure p_i^{exact} are computed as the trace of the stress tensor in linear elasticity:

$$p^{exact} = \mathrm{tr}\left(2\mu\mathbf{E} + \lambda\,\mathrm{tr}\left(\mathbf{E}\right)\mathbf{I}\right) \tag{5.4}$$

In (5.4), μ and λ are the Lamé constants, and the Green strain tensor is defined as $\mathbf{E} = 0.5\left(\mathbf{F}^T\mathbf{F} - \mathbf{I}\right)$. The simulation is conducted with the same material properties reported in fig. 5.2.

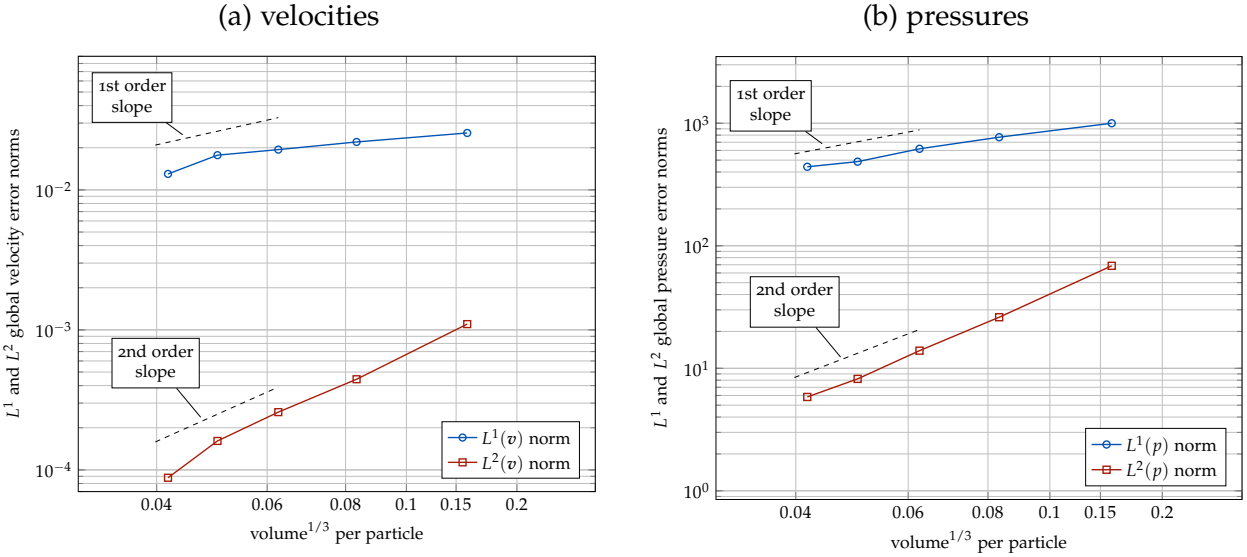

Figure 5.3: swinging cube, convergence analysis for (5.3a) velocity v and (5.3b) pressure p at $t = 0.0004\,s$. $L^1(v, p)$ and $L^2(v, p)$ error norms considered. Saint Venant material with density $\rho = 1100\,kg/m^3$, Young's modulus $E = 17\,MPa$, Poisson's ratio $\nu = 0.3$. $U_0 = 0.0005$, JST constant $k_{JST}^{(4)} = 1/8$ and $\sigma_{CFL} = 0.3$.

The study of results depicted in fig. 5.3 suggests that the JST-SPH scheme achieves and even surpasses (in fact, a logarithmic slope of 3.32 is observed when considering the most refined meshes) a 2^{nd} order of convergence with respect to the $L^2(v)$ norm.

This does not happen for the $L^1(v)$ norm, that reaches only 1^{st} order of convergence. Same behaviour is observed for the convergence of L^1 and L^2 norms for pressures p. Sensitivity of the L^1 norm to outliers may explain this discrepancy in performance. In fact, as it can be deduced from (5.3), the

L^1 norm lacks the smoothing effect achieved while using squared values of the error components, which on the other hand benefits the L^2 norm.

Results of the other mixed $\{\mathbf{p}, \mathbf{F}, J\}$ and $\{\mathbf{p}, \mathbf{F}, \mathbf{H}, J\}$ JST-SPH schemes show an almost identical path to convergence to that in fig. 5.3. Table 5.1 highlights this, by listing error norms for all three mixed schemes.

Table 5.1: swinging cube simulation, error norms for the mixed $\{\mathbf{p}, \mathbf{F}\}$, $\{\mathbf{p}, \mathbf{F}, J\}$ and $\{\mathbf{p}, \mathbf{F}, \mathbf{H}, J\}$ JST-SPH schemes. Material and simulation properties are those used in fig. 5.3. As differences between schemes are minimal, values for the $\{\mathbf{p}, \mathbf{F}, J\}$ and for the $\{\mathbf{p}, \mathbf{F}, \mathbf{H}, J\}$ mixed methods are expressed as variation percentages from $\{\mathbf{p}, \mathbf{F}\}$ results.

mixed form	particles per cube edge	total particles	$L^1(v)$	$L^2(v)$	$L^1(p)$	$L^2(p)$
$\{\mathbf{p}, \mathbf{F}\}$	8	512	0.0255	0.0011	999.938	68.625
$\{\mathbf{p}, \mathbf{F}, J\}$	8	512	±0	±0	−0.03%	−0.05%
$\{\mathbf{p}, \mathbf{F}, \mathbf{H}, J\}$	8	512	±0	±0	−0.03%	−0.05%
$\{\mathbf{p}, \mathbf{F}\}$	12	1728	0.022	$4.442 \cdot 10^{-4}$	769.522	26.112
$\{\mathbf{p}, \mathbf{F}, J\}$	12	1728	±0	±0	+0.032%	+0.015%
$\{\mathbf{p}, \mathbf{F}, \mathbf{H}, J\}$	12	1728	±0	±0	+0.032%	+0.015%
$\{\mathbf{p}, \mathbf{F}\}$	16	4096	0.019	$2.586 \cdot 10^{-4}$	618.635	13.928
$\{\mathbf{p}, \mathbf{F}, J\}$	16	4096	±0	±0	+0.017%	±0
$\{\mathbf{p}, \mathbf{F}, \mathbf{H}, J\}$	16	4096	±0	±0	+0.017%	±0
$\{\mathbf{p}, \mathbf{F}\}$	20	8000	0.018	$1.61 \cdot 10^{-4}$	485.893	8.197
$\{\mathbf{p}, \mathbf{F}, J\}$	20	8000	±0	±0	+0.027%	±0
$\{\mathbf{p}, \mathbf{F}, \mathbf{H}, J\}$	20	8000	±0	±0	+0.027%	±0
$\{\mathbf{p}, \mathbf{F}\}$	24	13824	0.013	$8.789 \cdot 10^{-5}$	441.25	5.837
$\{\mathbf{p}, \mathbf{F}, J\}$	24	13824	±0	−0.12%	+0.014%	±0
$\{\mathbf{p}, \mathbf{F}, \mathbf{H}, J\}$	24	13824	±0	−0.12%	+0.014%	±0

A series of parametric studies were carried out in order to analyse the influence of the following two parameters on convergence:

1. the smoothing length $h = \alpha_h |x_a - x_b|$, where numerical constant α_h multiplies the particles horizontal inter-distance $|x_a - x_b|$. α_h will be set to $\alpha_h = 1.2$, and to $\alpha_h = 3.2$. Previously, for the analysis in fig. 5.3, it was selected to be $\alpha_h = 2.2$;

2. the JST constant $\kappa^{(4)}$. Initially set to $\kappa^{(4)} = 1/4$ in fig. 5.3, it has been decreased to $\kappa^{(4)} = 1/64$ and to $\kappa^{(4)} = 0$ to evaluate the importance of JST dissipation on the convergence of the scheme.

Convergence plots for these two sets of parametric analyses are presented in figs. 5.4 and 5.5. The simulations were run using the mixed $\{\mathbf{p}, \mathbf{F}\}$ scheme, and, with the exception of the parameter object of study (α_h or $\kappa^{(4)}_{JST}$), with the same set of properties used for the simulations shown in fig. 5.3.

(a) velocities, varying parameter $= \alpha_h$

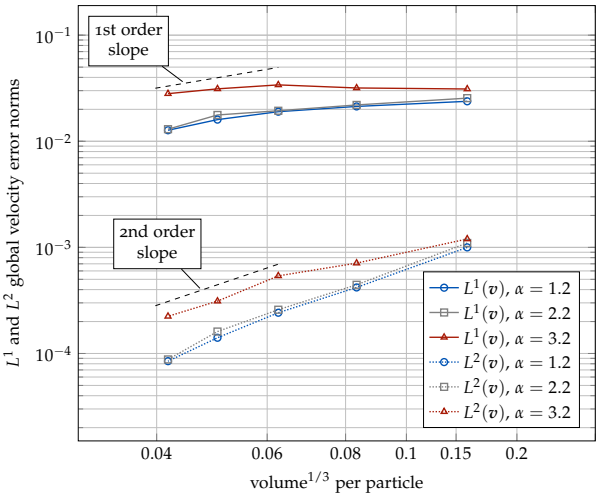

(b) pressures, varying parameter $= \alpha_h$

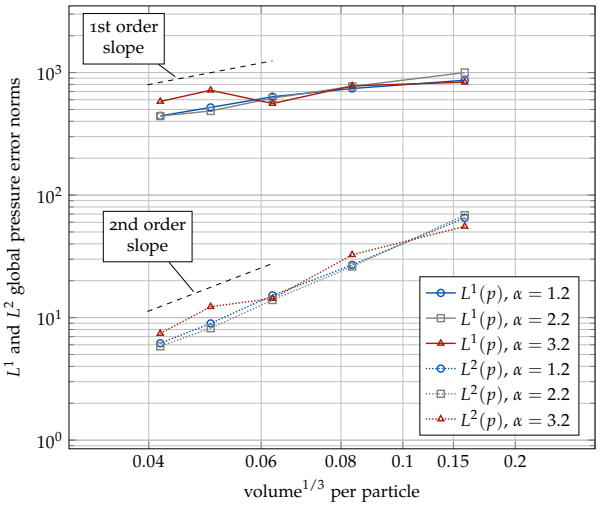

Figure 5.4: swinging cube, $\{\mathbf{p}, \mathbf{F}\}$ formulation, convergence analysis for (5.4a) velocity v and (5.4b) pressure p at t = 0.0004 s. Parameter α_h, which governs the number of neighbours for each particle, is set equal to 1.2 (red lines), 2.2 (grey lines, same value adopted in fig. 5.3) and 3.2 (blue lines). $L^1(v, p)$ and $L^2(v, p)$ global error norms considered. Other material and simulation data are the same as those used for fig. 5.3.

It is clear from fig. 5.4 that increasing α_h, the number of neighbours per particle, leads to a slower, and more irregular path to convergence. This is seen for the red lines, i. e. those with $\alpha_h = 3.2$. As in fig. 5.3, this phenomenon is more accentuated for L^1 plots. Another drawback is that computational costs also increase with α_h, as the rising number of neighbours per particle implies that more calculations have to be performed.

In order to gain a better understanding of the aforementioned computational costs, fig. 5.6 plots times to completion for simulations used in fig. 5.4 run with $\alpha_h = 1.2$ (limited number of neighbours per particle) and with $\alpha_h = 3.2$ (large number of neighbours per particle).

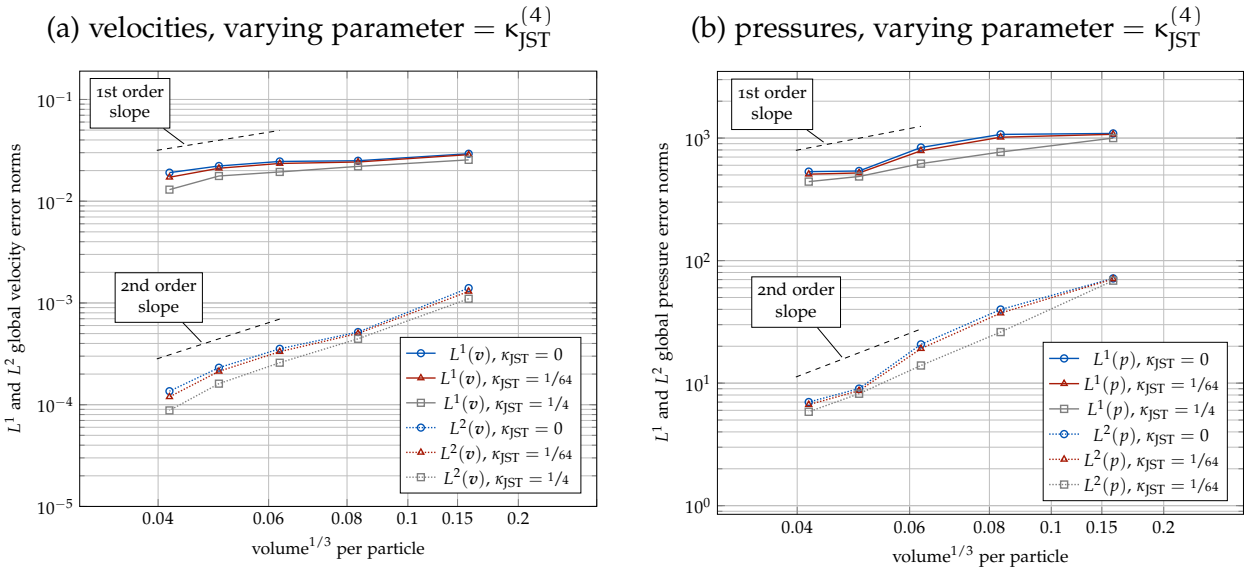

Figure 5.5: swinging cube, $\{\mathbf{p}, \mathbf{F}\}$ formulation, convergence analysis for (5.5a) velocity v and (5.5b) pressure p at $t = 0.0004$ s. JST constant $\kappa^{(4)}$ is set equal to 0 (red lines), $1/64$ (blue lines) and $1/4$ (grey lines, same value adopted in fig. 5.3). $L^1(v, p)$ and $L^2(v, p)$ global error norms considered. Other material and simulation properties are the same as in fig. 5.3.

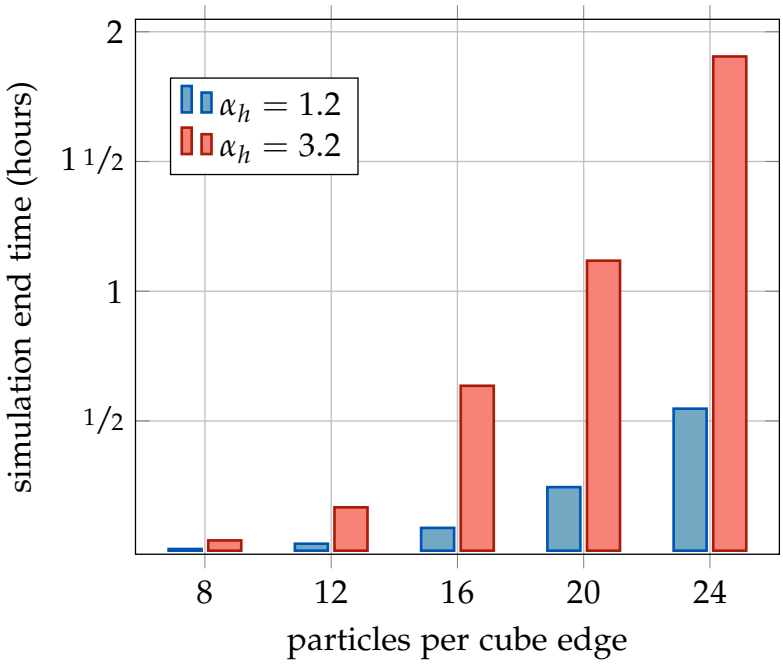

Figure 5.6: swinging cube, times to completion for analyses in fig. 5.4 with $\alpha_h = 1.2$ (blue bars) and $\alpha_h = 3.2$ (red bars), and lasting 0.005 s in simulation time.

In case the amount of JST dissipation is assumed as parameter, patterns of velocity errors in fig. 5.5a are shown to be comparable. Limiting the amount of JST dissipation leads a more irregular path to convergence for stresses, as can be observed from fig. 5.5b.

5.1.2 *Spinning cube*

The test described here will demonstrate the effectiveness of the momentum-preserving procedure introduced in section 3.8. A cube is discretised as an assemblage of $6 \times 6 \times 6$ particles in space. The cube is set to spin by an initial, impulsive angular velocity $\omega_{0z} = 105$ rad/s imposed on the axis passing through its centroid, and directed parallel to one of the coordinate axes (see fig. 5.7).

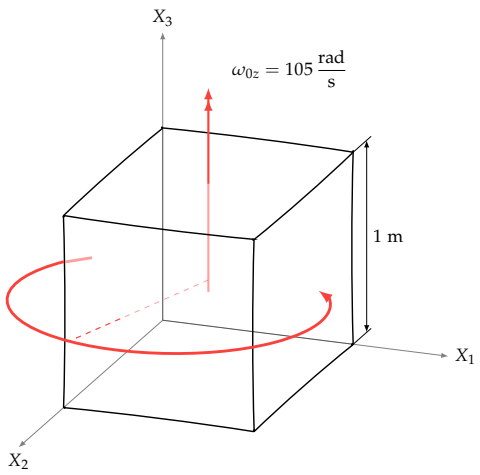

Figure 5.7: spinning cube initial configuration.

No restraint on movement is imposed. The cube is modelled with a hyperelastic, neo-Hookean material of the type described in section 2.9, with density $\rho = 1100\,\text{kg/m}^3$, Young's modulus $E = 17\,\text{MPa}$ and Poisson's ratio $\nu = 0.3$. The CFL stability coefficient is taken as $\sigma_{\text{CFL}} = 0.3$.

Graphics representing the evolution in time for this test are presented in fig. 5.8. Comparison between first and second rows in fig. 5.8 shows that JST stabilisation is essential to avoid simulation failure due to the rise of pressure instabilities. Last row in fig. 5.8 proves that differences between

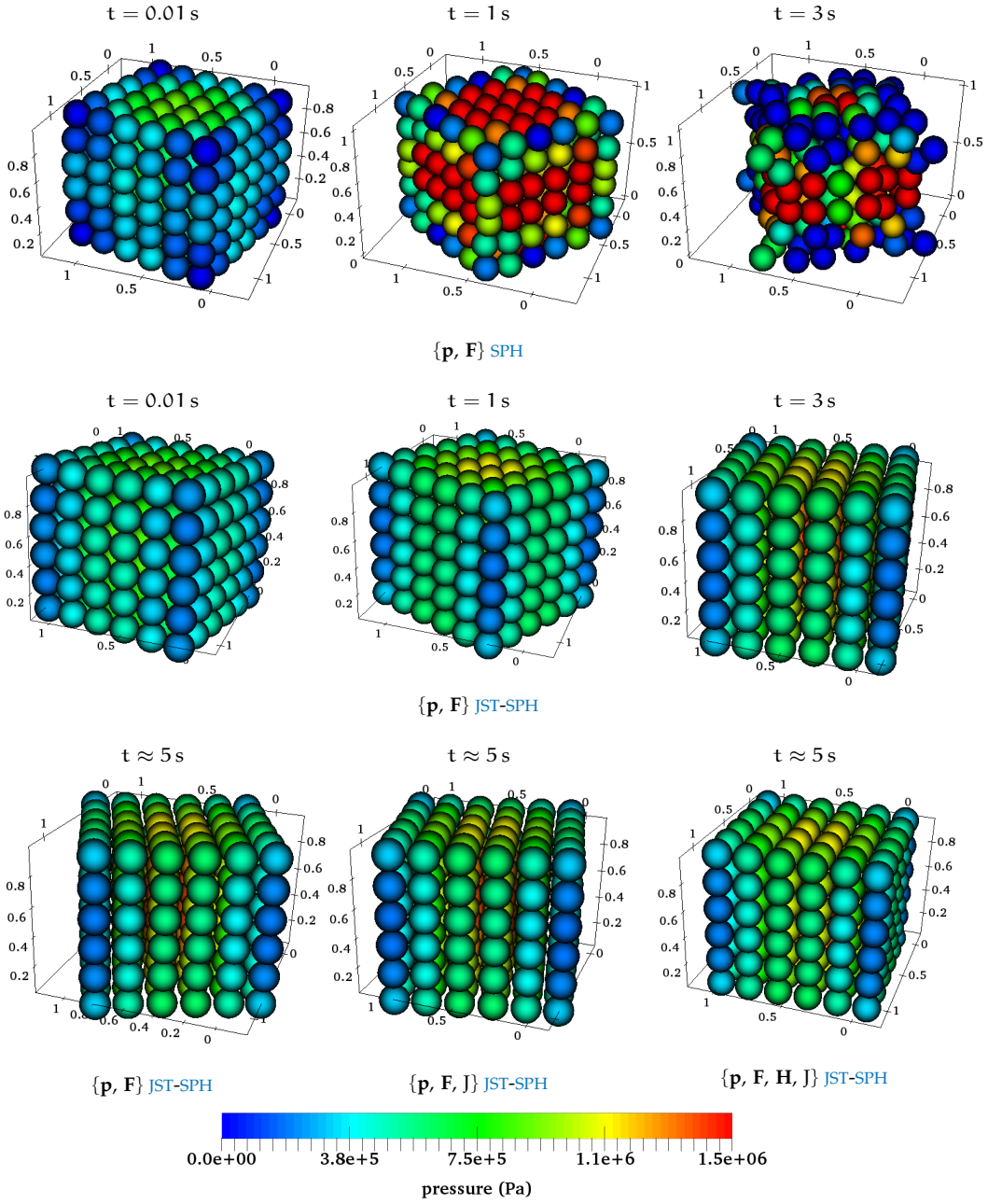

Figure 5.8: spinning cube simulation, pressure contour plot at various instants in time. Results obtained with the {**p**, **F**} SPH without JST stabilisation are presented in the first row; results obtained with {**p**, **F**} JST-SPH in the second. In the third row, results around instant $t = 5\,s$ are shown, coming from all three JST-SPH mixed formulations. Simulation parameters: $1 \times 1 \times 1\,m^3$, discretised with 216 particles, $k_{JST}^{(4)} = 1/8$, neo-Hookean hyperelastic material with density $\rho = 1100\,kg/m^3$, Young's modulus $E = 17\,MPa$, Poisson's ratio $\nu = 0.3$. Angular velocity $\omega_{0z} = 105\,rad/s$ imposed on the cube centroid only in the first time step. $\sigma_{CFL} = 0.3$ assumed.

the three mixed formulations employed, {**p**, **F**}, {**p**, **F**, J} and {**p**, **F**, **H**, J}, are minimal.

Energy considerations can be drawn from fig. 5.9.

The non-stabilised {**p**, **F**} SPH method is used to produce results in fig. 5.9a. In it, artificial increases in both kinetic and internal total energy lead to the unstable behaviour already noticed in the first row of fig. 5.8. In fig. 5.9b, it is shown that these effects are largely eliminated by the introduction of a small amount of JST dissipation.

Following, fig. 5.10 presents plots of the components of the total linear and angular momenta, obtained by summing values of these quantities over all particles a composing the cube.

The algorithm for the conservation of momentum described in section 3.8 helps in achieving the expected values in fig. 5.10. Further on this point, fig. 5.11 compares the z-components of the total angular momentum from {**p**, **F**} JST-SPH simulations, with and without the conservation of momentum algorithm.

5.1.3 *Tensile cube*

In the test that follows, the unit cube of the previous paragraphs has now its bottom side fixed to the ground.

The cube is subject to an initial vertical velocity field $v_{0z} = 800 \cdot X_3$ m/s. Figure 5.12 illustrates this configuration. The cube material will be modelled as nearly-incompressible neo-Hookean, with Young's modulus $E = 21$ GPa, Poisson's ratio $\nu = 0.3$ and density $\rho = 7000$ kg/m^3. The SPH discretisation will consist of a set of 512 particles, 8 per side, with $\sigma_{CFL} = 0.3$.

The purpose of this example is to prove that the {**p**, **F**} JST-SPH method presents no adverse effects when subjected to a tensile dynamic load of some significance.

In order to appreciate that, the first row of fig. 5.13 displays results obtained from running the test with displacement-based corrected SPH [34]. Being set in a total Lagrangian framework, this method avoids [35] the tension instability problems that are so common in SPH [211, 248]. It is clear from the first row of fig. 5.13 that the succession of tensile and compressive phases of deformation leads to pressure instabilities that make

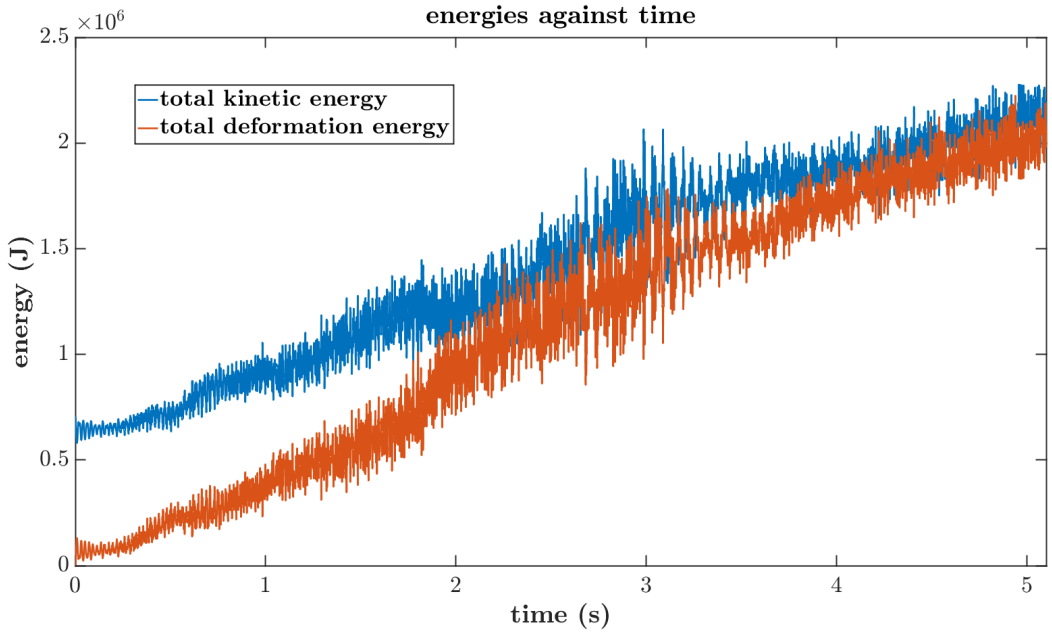

(a) {**p**, **F**} SPH

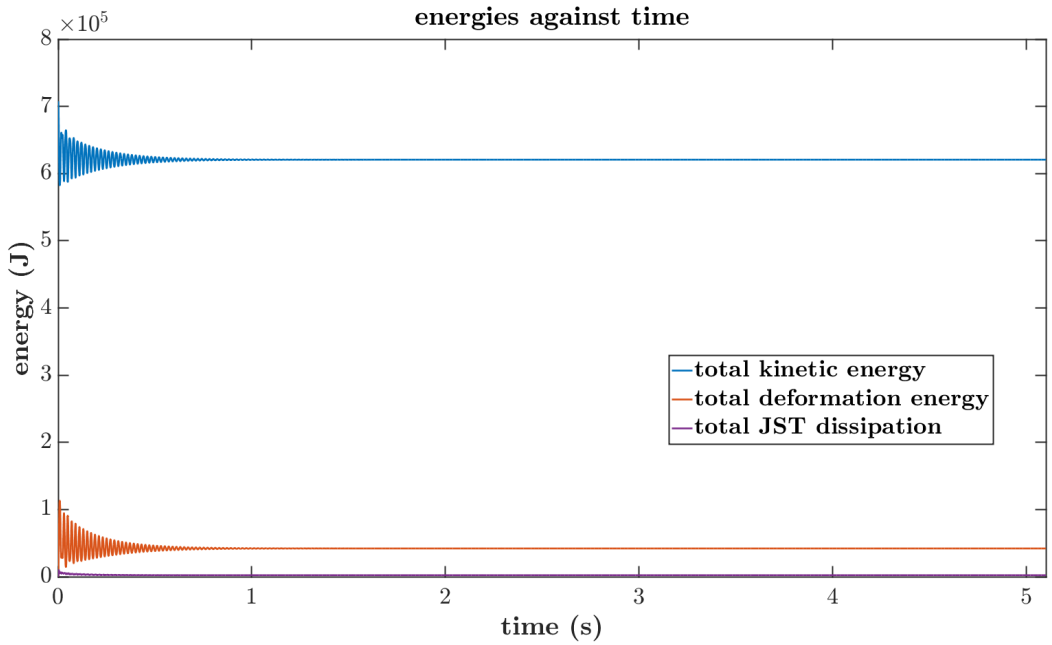

(b) {**p**, **F**} JST-SPH

Figure 5.9: spinning cube simulation, plots of total energies in time, run in (a) the {**p**, **F**} SPH formulation, and in (b) the {**p**, **F**} JST-SPH formulation. Total kinetic energy is expressed as $E_{kTOT} = \sum_a (1/2)\,\|\mathbf{p}_a\|^2/\rho$, while total deformation energy is $U_{TOT} = \sum_a (\Delta t/\rho)\,\|\mathbf{p}_a\|\,\|\mathbf{T}_a\|$ and total JST dissipation is $D^{JST}_{TOT} = \sum_a (\Delta t/\rho)\,\|\boldsymbol{\mathcal{D}}^{JST}_a\|\,\|\mathbf{p}_a\|$.

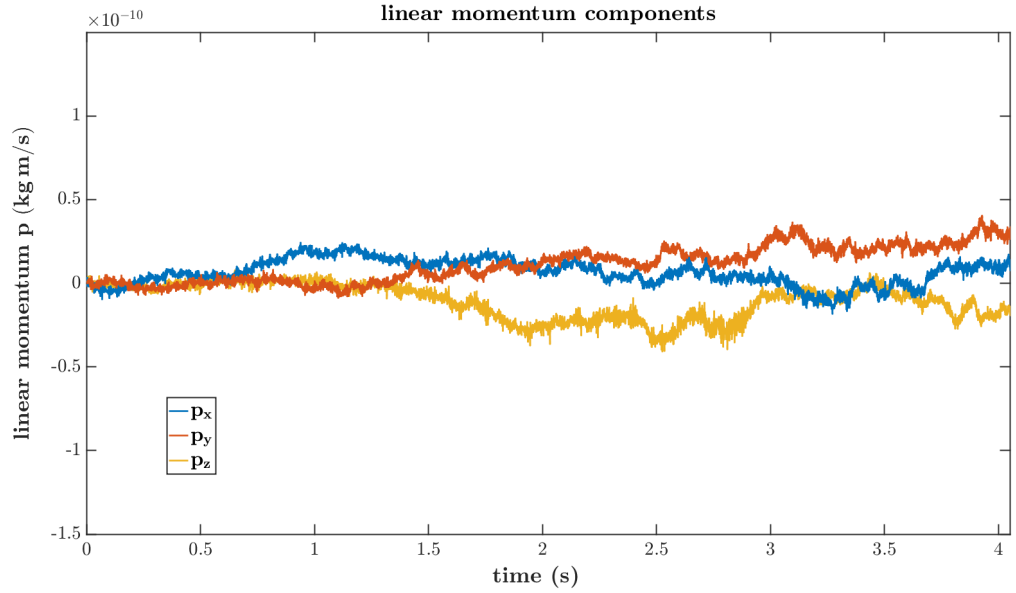

(a) {**p**, **F**} SPH

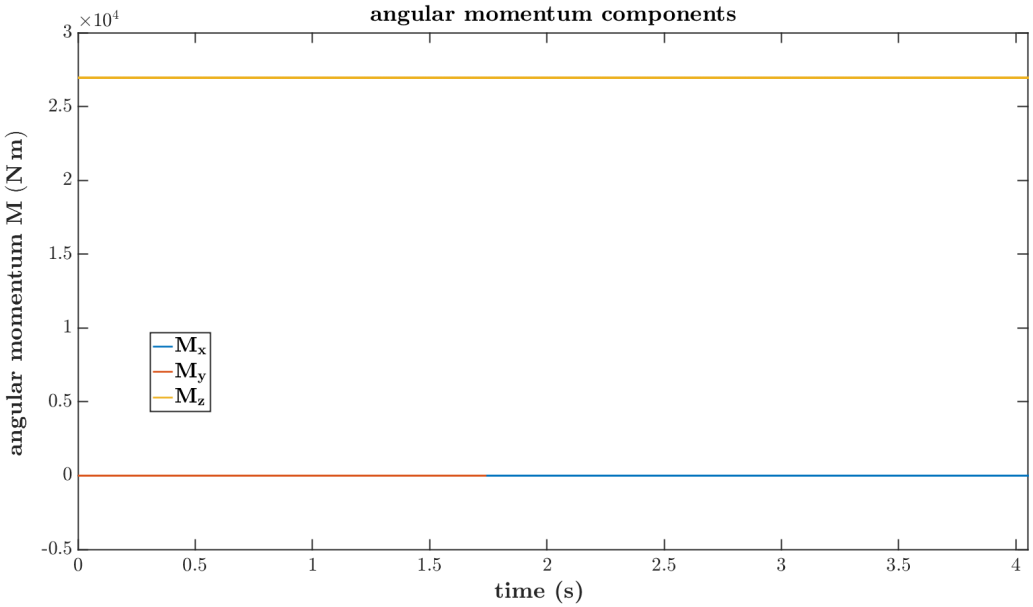

(b) {**p**, **F**} JST-SPH

Figure 5.10: spinning cube simulation, plots of total linear and angular momentum in time, run with the {**p**, **F**} JST-SPH formulation. The total linear momentum is expressed as $\mathbf{p}_{TOT} = \sum_a \mathbf{p}_a$, while total angular momentum is $\mathbf{M}_{TOT} = \sum_a \mathbf{x}_a \times \mathbf{p}_a$. The cube is made of 216 particles, with JST $k^{(4)}_{JST} = 1/8$; neo-Hookean hyperelastic material: $\rho = 1100\,kg/m^3$, $E = 17\,MPa$ and $\nu = 0.3$. Angular velocity $\omega_{0z} = 105\,rad/s$ imposed on the cube centroid only in the first time step. $\sigma_{CFL} = 0.3$ assumed.

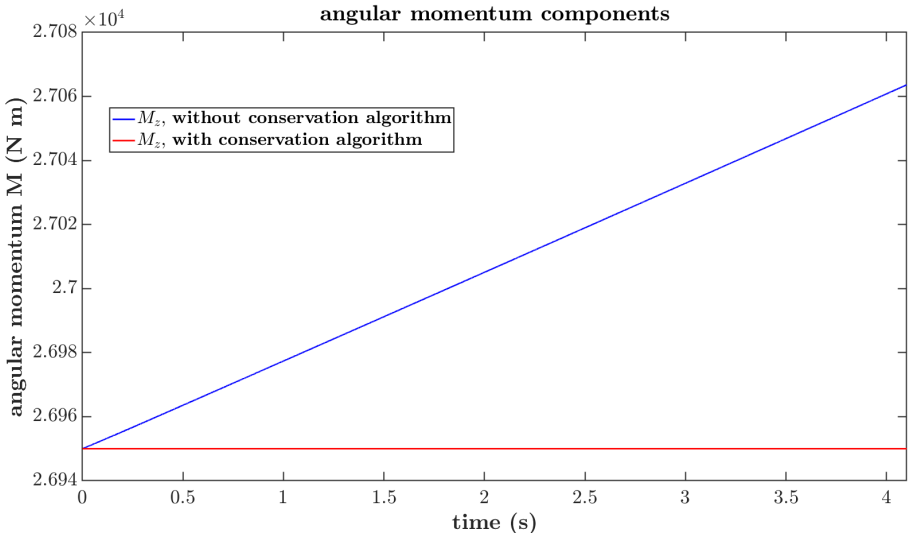

Figure 5.11: spinning cube simulation, time comparison between z-components of total angular momentum with and without application of the conservation of momentum algorithm of section 3.8. {**p**, **F**} JST-SPH formulation.

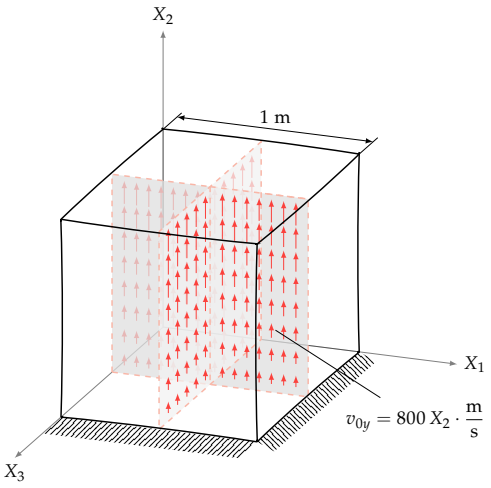

Figure 5.12: tensile cube initial configuration.

the simulation unstable. The outcome of the test run with {**p**, **F**} JST-SPH, with JST dissipation factor $k^{(4)}_{JST} = 1/8$, but $k^{(4)}_{JST|_J} = 0$, is shown in the second row of fig. 5.13. The third row of fig. 5.13 presents identical results taken from different analyses, employing the three mixed forms of JST-SPH at same instant. Given these results, it can be argued that no practical advantage is gained by adding unknowns J and **H** to the system.

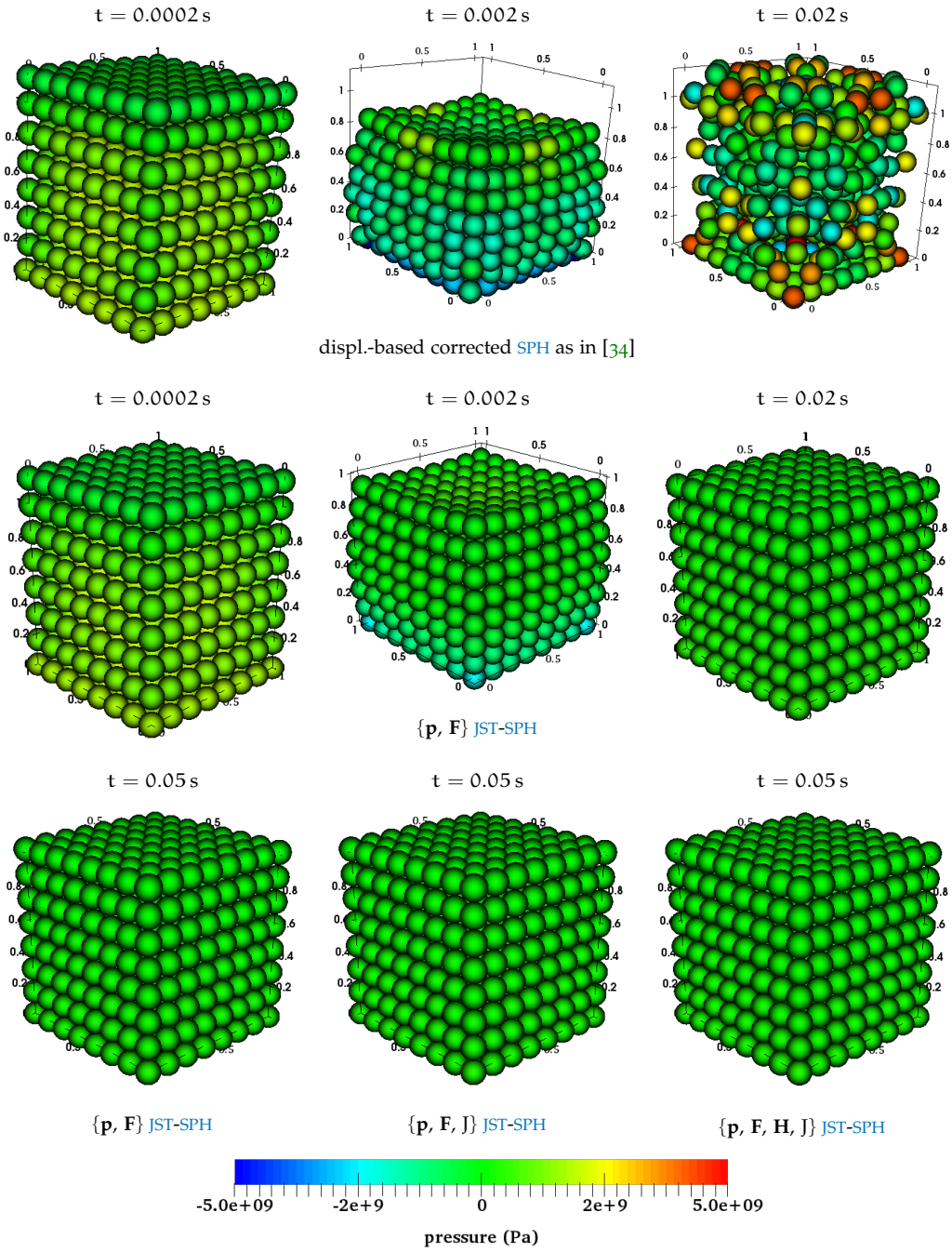

Figure 5.13: tensile cube simulation, pressure contour plot at various instants in time. Results obtained with displacement-based corrected SPH without JST stabilisation are presented in the first row; results obtained with {**p**, **F**} JST-SPH in the second. In the third row, results at time $t = 0.05\,s$ coming from all three JST-SPH mixed formulations. Simulation parameters: $1 \times 1 \times 1\,m^3$, discretised with 512 particles, smoothing length factor $\alpha_h = 2.2$, $k^{(4)}_{JST} = 1/8$; neo-Hookean hyperelastic material with density $\rho = 7000\,kg/m^3$, Young's modulus $E = 21\,GPa$, Poisson's ratio $\nu = 0.3$. Initial velocity field of $v_{0z} = 800 \cdot X_3\,m/s$ imposed only in the first time step. $\sigma_{CFL} = 0.3$ assumed.

5.1.4 *Punch test*

A rectangular region of 3 cm $\times$ 1 cm, constrained by rollers in the normal direction on its left and bottom sides, is compressed by a vertical velocity of intensity $v_y = -10\,\mathrm{m/s}$ on the leftmost third of its top side. The test lasts until this zone is compressed to 50% of its initial height. The billet is made of neo-Hookean nearly incompressible hyperelastic material, with parameters $E = 1\,\mathrm{MPa}$, $\nu = 0.495$, $\rho = 1000\,\mathrm{kg/m^3}$. The particle discretisation consists of 225 uniformly distributed particles; the selected CFL constant is $\sigma_{\mathrm{CFL}} = 0.3$. The overall setup is shown in fig. 5.14.

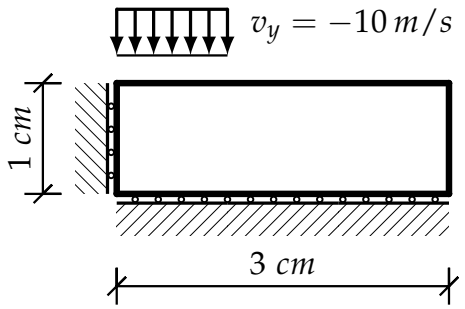

Figure 5.14: punch test configuration.

This problem was proposed, among others, by [264], where it was found that the displacement-based, corrected SPH method needed to switch from a total to an updated Lagrangian framework to be able to deal with the large distortions. As shown in fig. 5.15, the mixed-based JST-SPH methodology is able to correctly handle these same distortions. The first row of fig. 5.15 also clearly highlights the importance of the JST dissipation: without it, the bar is subjected to heavy pressure fluctuations.

Further evidence in this direction is provided in fig. 5.17, where the difference in pressure for particles left and right of the discontinuity in velocity boundary condition, $\|\Delta p\| = \|p_{\mathrm{right}} - p_{\mathrm{left}}\|$ (see fig. 5.16 for visual reference), is plotted in time.

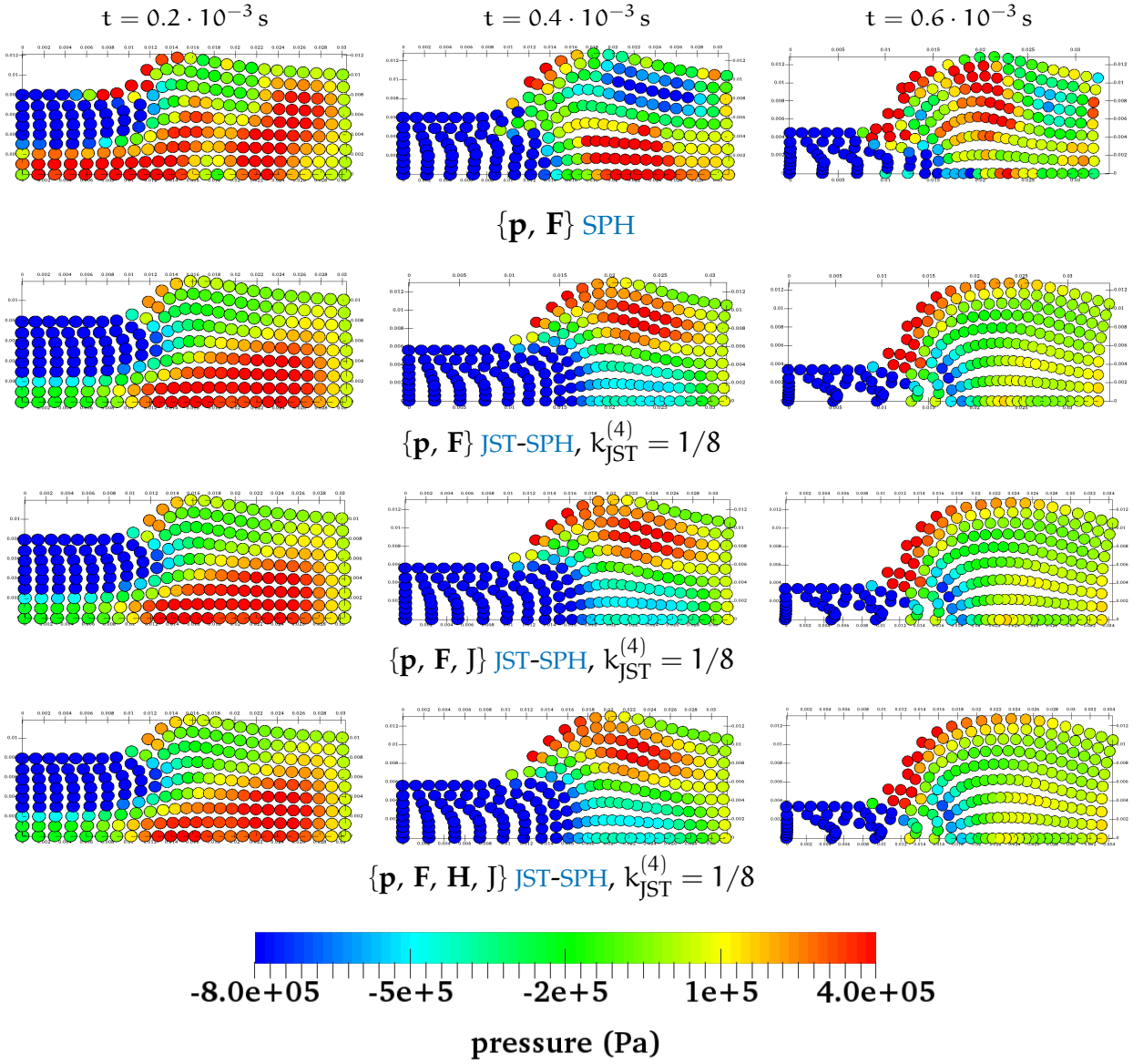

Figure 5.15: punch test simulations, pressure contour plot at various instants in time. Each row hosts results coming from a different simulation, top to bottom: {**p**, **F**} SPH with no artificial dissipation; {**p**, **F**} JST-SPH with $k^{(4)}_{JST} = 1/8$; {**p**, **F**, J} JST-SPH with $k^{(4)}_{JST} = 1/8$ and {**p**, **F**, **H**, J} JST-SPH with $k^{(4)}_{JST} = 1/8$. The simulation is carried in plane strain conditions, on a 3 cm $\times$ 1 cm bar made of hyperelastic, nearly incompressible material (density $\rho = 1000\,kg/m^3$, Young's modulus $E = 1$ MPa, Poisson coefficient $\nu = 0.495$) and discretised with 225 particles. A vertical velocity $v_y = -10\,m/s$ acts as external load throughout the simulation. $\sigma_{CFL} = 0.3$ assumed.

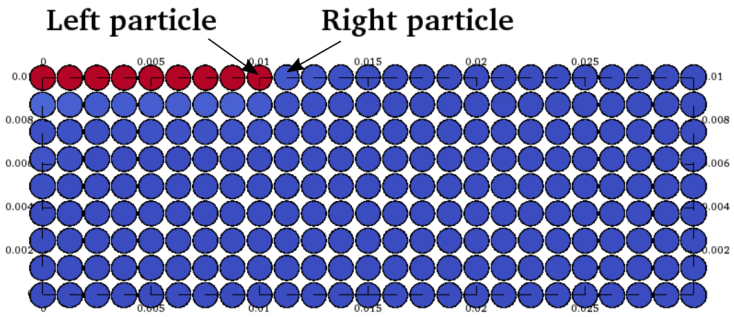

Figure 5.16: punch test, external velocity $v_y = -10\,\mathrm{m/s}$ is imposed on the red region. Highlighted are the positions of the two test particles in fig. 5.17.

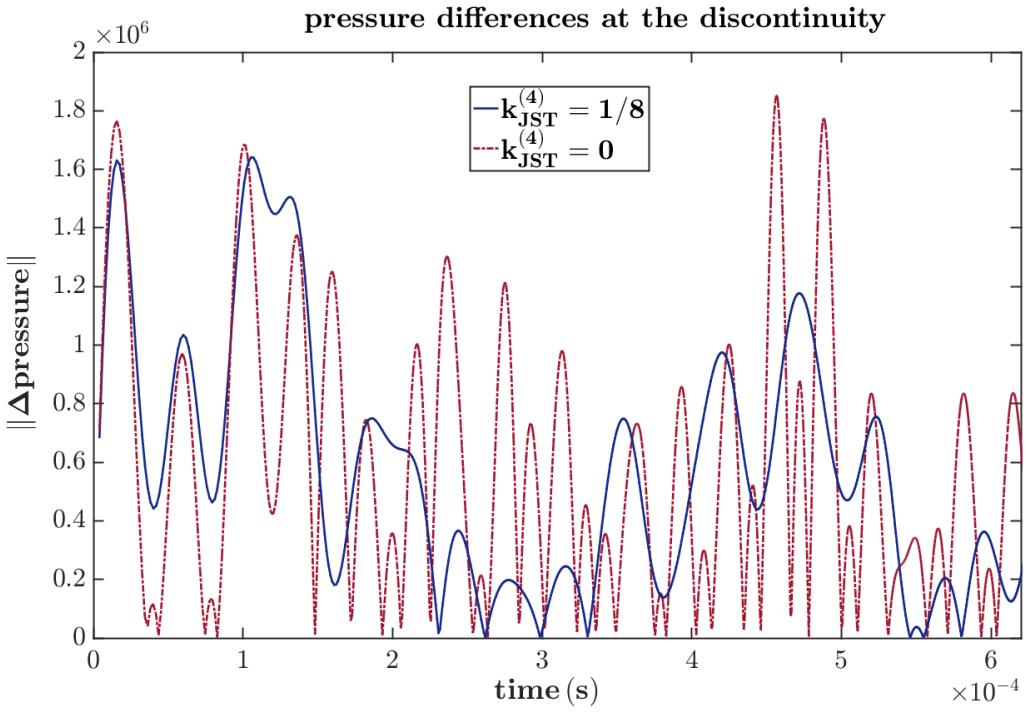

Figure 5.17: punch test, evolution in time of the pressure difference $\|\Delta p\| = \|p_{right} - p_{left}\|$ between top layer particles that belong (left) and that do not belong (right) to the region of imposed velocity (refer to fig. 5.16). Blue line for $\{\mathbf{p}, \mathbf{F}\}$ JST-SPH with $k^{(4)}_{JST} = 1/8$, red line for $\{\mathbf{p}, \mathbf{F}\}$ SPH with no artificial dissipation.

5.1.5 *Bending column*

In this simulation, a square-based column of width and depth $l = 1$ m and height $h = 6$ m is set in motion by the application of an initial velocity of value $v_{0y} = 10 \cdot \frac{X_3}{h}$ m/s, with direction orthogonal to the column axis. The column is then left oscillating in time, as shown in fig. 5.18.

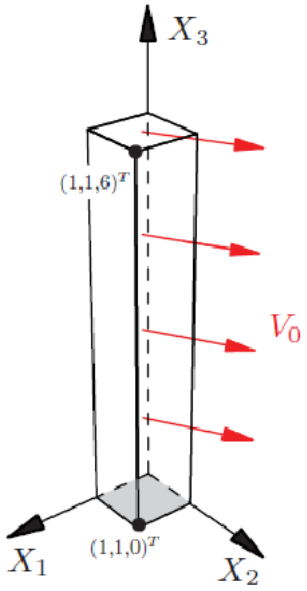

Figure 5.18: bending column, initial configuration.

A hyperelastic, nearly incompressible neo-Hookean material is chosen, with properties: density $\rho = 1100$ kg/m^3, Young's modulus $E = 17$ MPa and Poisson's ratio $\nu = 0.45$.

Reduced order FEM bending simulations of nearly incompressible rubbers are known to be affected by volumetric locking [115]. If this defect is not properly addressed with available techniques, it leads to an overly stiff response by the structure. It has already been observed in chapter 3 that SPH discretisations, by their very nature, are immune from locking phenomena. This fact notwithstanding, running the present test for a sufficiently prolonged simulation time leads to interesting results.

Figure 5.19 shows the evolution of the column captured at various instants until time $t = 1.5$ s, and with different, decreasing number of particles employed in the discretisation. In the first row, a discretisation of $12 \times 12 \times 72 = 9648$ particles is used; in the second row, the number of particles

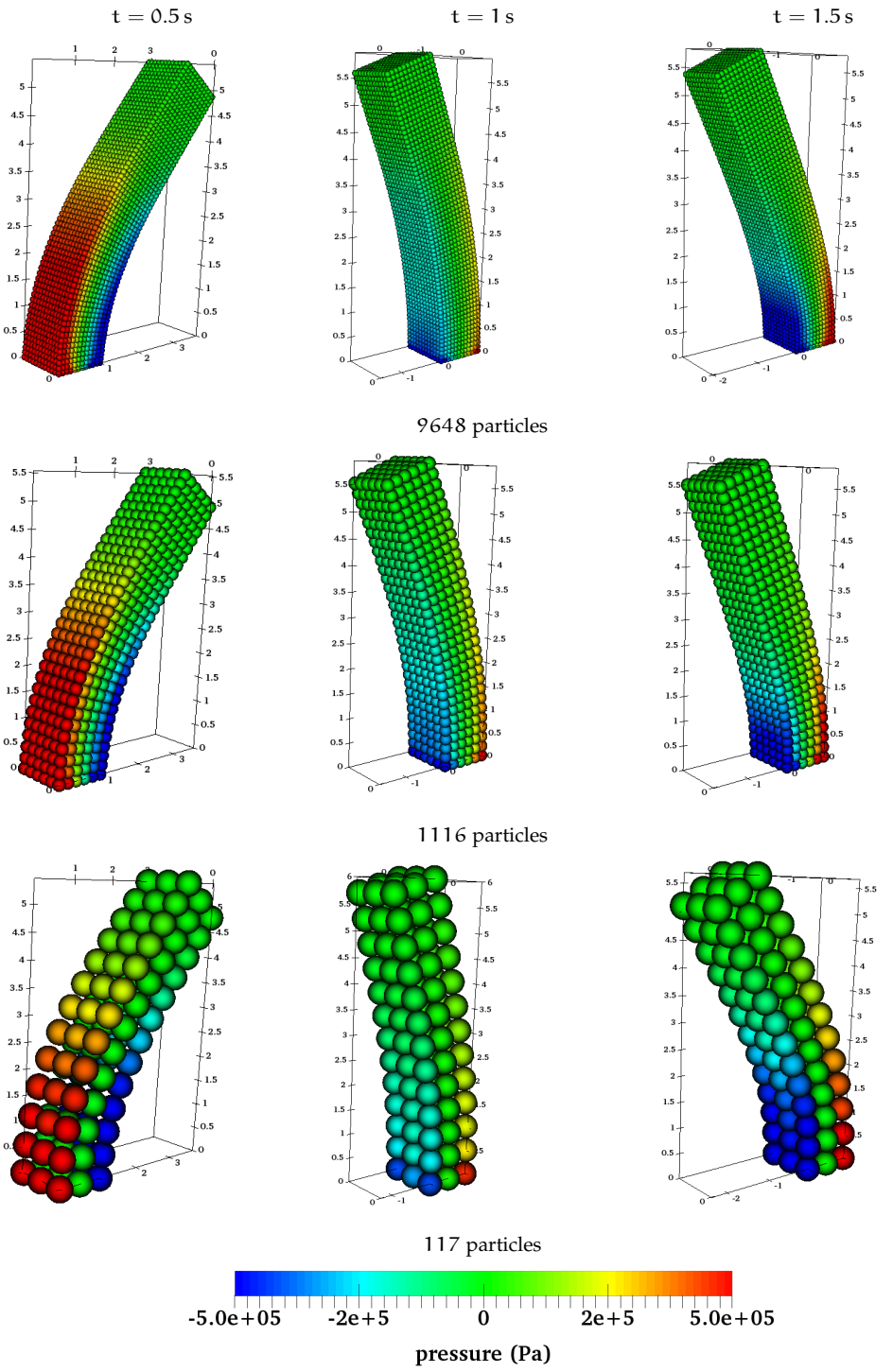

Figure 5.19: bending column simulation, pressure contour plot at instants 0.5, 1 and 1,5 s. All results obtained with the {**p**, **F**} JST-SPH methodology, smoothing length factor $\alpha_h = 2.2$, $k^{(4)}_{JST} = 1/8$. Results with 9648 particles are presented in the first row; with 1116 particles in the second, 117 particles in the third. A nearly incompressible, neo-Hookean hyperelastic material is employed, with density $\rho = 1100\,kg/m^3$, Young's modulus $E = 17\,MPa$, Poisson's ratio $\nu = 0.45$. The column has measures: short edge $l = 1\,m$, height $h = 6\,m$; the initial velocity field is $v_{0y} = 10\,X_3/h\,m/s$, imposed only in the first time step. $\sigma_{CFL} = 0.3$ assumed.

per short side is halved to $6 \times 6 \times 31 = 1116$; and again halved down to $3 \times 3 \times 13 = 117$ in the third row. All simulations are run in $\{\mathbf{p}, \mathbf{F}\}$ JST-SPH, with $k^{(4)}_{JST} = 1/8$ and $\sigma_{CFL} = 0.3$.

From fig. 5.19 it can be noted that the scheme is capable to perform appropriately even on prolonged time periods and with the bare minimum number of particles per short side (three), required to represent the bending load. Oscillations restrict themselves to the same X_2X_3 plane on which the initial velocity is assigned.

Figure 5.20 presents, plotted against time and for the discretisations considered in fig. 5.19, the X_2 displacements for a particle positioned at one of the angles on the top surface of the column. Figure 5.20 can help to appreciate the progress to convergence as the number of particles is increased.

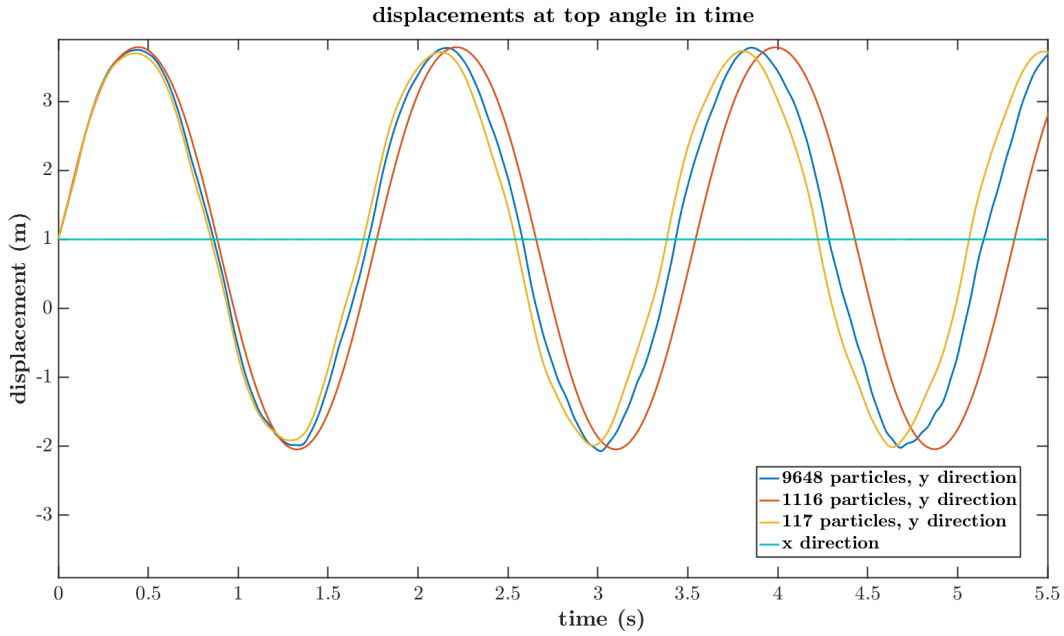

Figure 5.20: bending column simulation, time plot of displacements of particle at one of the top angles of the column, obtained with the $\{\mathbf{p}, \mathbf{F}\}$ JST-SPH formulation. X_2 (y in the legend) displacements are from analyses made with 9648, 1116 and 117 particles. X_1 (x in the legend) displacement plot is also presented, and it is the same at all resolutions, showing that symmetry of movement is preserved in all cases. JST dissipation is set to $k^{(4)}_{JST} = 1/8$. Neo-Hookean hyperelastic material, $\rho = 1100\ kg/m^3$, $E = 17$ MPa and $\nu = 0.45$. Initial velocity field of $v_{0y} = 10 \cdot X_3/h$ m/s imposed only in the first time step. $\sigma_{CFL} = 0.3$ assumed.

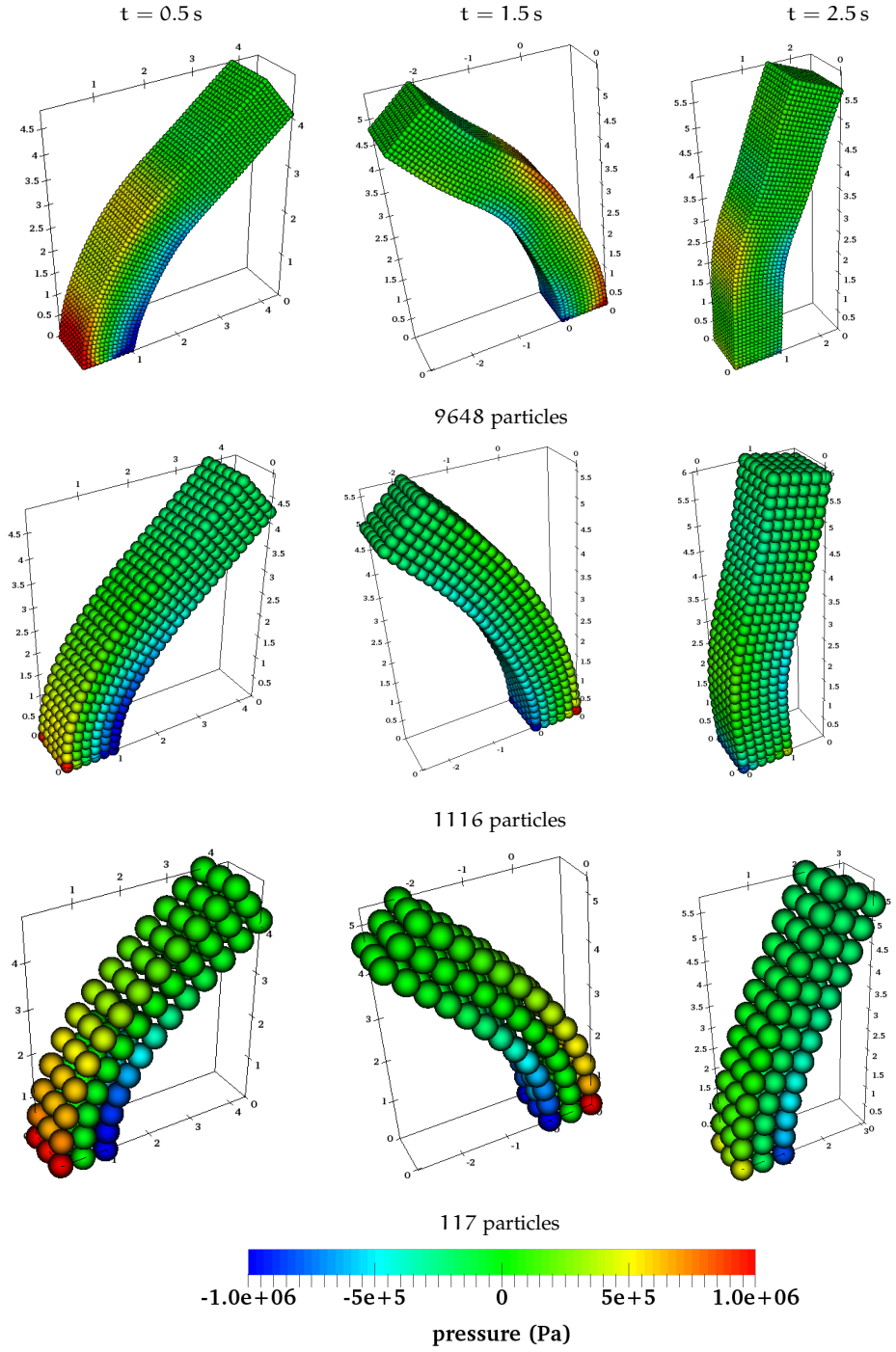

Figure 5.21: bending column simulation, pressure contour plot at instants 1.5, 2.5 and 3.5 s. The setup is the same of fig. 5.20, with the exception that now the external velocity field (imposed only in the first step) is $v_{0y} = 10$ m/s. Results with 9648 particles are presented in the first row; with 1116 particles in the second, and with 117 particles in the third.

A more challenging version of this example is presented in fig. 5.21, where the initial velocity is now $v_{0y} = 10$ m/s, uniform over the column vertical axis. The JST dissipation helps to avoid the appearance of pressure instabilities. Furthermore, although in the third row of fig. 5.21 the use of fewer particles implies that less degrees of freedom are available to represent as many deformation modes as visible in the other simulations, in no instance does the column sway out of its initial plane of movement.

5.1.6 *Twisting column*

For this test, the column of the previous example will now be subjected to an initial angular velocity $\omega_{0z} = 105 \cdot \sin \frac{\pi X_3}{2h}$ rad/s, as shown in fig. 5.22.

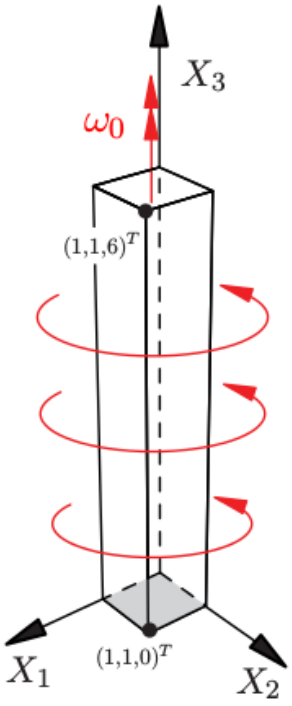

Figure 5.22: twisting column, initial configuration.

The material is characterised as nearly incompressible neo-Hookean, of density $\rho = 1100\,\mathrm{kg/m^3}$, Young's modulus $E = 17$ MPa. The SPH discretisation is carried out by a set of $6 \times 6 \times 31$ particles, with $k^{(4)}_{JST} = 1/8$ and $\sigma_{CFL} = 0.3$.

A series of three analyses is performed, each using a different value of Poisson's ratio: $\nu_1 = 0.45$, $\nu_2 = 0.495$, and $\nu_3 = 0.4995$. Other than testing the robustness of the JST-SPH algorithm in a highly nonlinear setting, the parametric study performed on ν will help assessing the potentialities of the different mixed formulations to accurately reproduce incompressibility.

Results for the $\{\mathbf{p}, \mathbf{F}\}$ JST-SPH scheme are reported in fig. 5.23.

Figure 5.23 clearly exposes the need to add further conservation laws to the solving system when the material is nearing towards incompressibility ($\nu = \kappa/\mu \to 0.5$).

Figure 5.24 displays the analyses run in the $\{\mathbf{p}, \mathbf{F}, J\}$ JST-SPH formulation, and fig. 5.25 those carried out in $\{\mathbf{p}, \mathbf{F}, \mathbf{H}, J\}$ JST-SPH. For case study $\nu_3 = 0.4995$, it is seen that the hourglass problems that were noticed in fig. 5.23 for the $\{\mathbf{p}, \mathbf{F}\}$ scheme have been fixed by setting J as an independent variable. At last, it is observed that no appreciable difference can be detected between results from the $\{\mathbf{p}, \mathbf{F}, J\}$ and from the $\{\mathbf{p}, \mathbf{F}, \mathbf{H}, J\}$ JST-SPH formulations.

In fig. 5.26, a displacement-based SPH formulation is adopted in order to perform the same test presented in fig. 5.23. The improvement in performance brought about by the adoption of a mixed formulation is substantial, as both meshes presented in fig. 5.26 fail to preserve the shape of the column during the twisting motion.

Completion times for the various analyses performed in figs. 5.23 to 5.25 are presented in table 5.2.

The degree of near-incompressibility negatively influences the time step length by increasing the pressure wave speed of the material. Table 5.2 shows that this is a far more significant factor in creating a performance bottleneck, rather than the addition of one or two more conservation laws to the governing mixed system of equations.

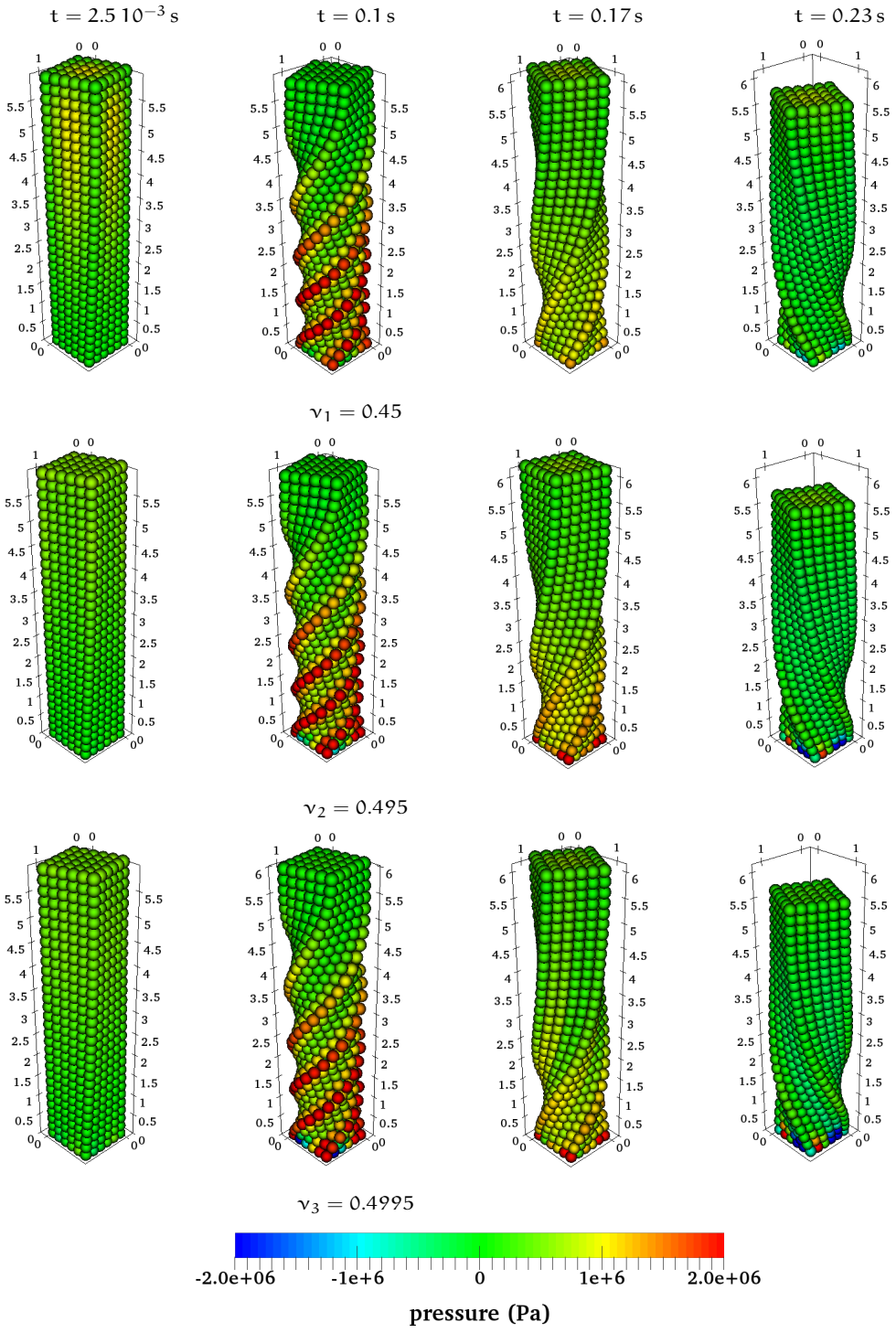

Figure 5.23: twisting column simulation, pressure contour plot at instants $2.5 \cdot 10^{-3}$, 0.1, 0.17 and 0.23 s. All results obtained with the $\{\mathbf{p}, \mathbf{F}\}$ JST-SPH methodology, with smoothing length factor $\alpha_h = 2.2$, $k^{(4)}_{JST} = 1/8$. The column is simulated with a set of $6 \times 6 \times 31 = 1116$ particles. A nearly incompressible, neo-Hookean hyperelastic material is employed, with density $\rho = 1100$ kg/m^3, Young's modulus $E = 17$ MPa. Each row of pictures is assigned a different Poisson ratio: $\nu_1 = 0.45$ for the first row, $\nu_2 = 0.495$ for the second, $\nu_3 = 0.4995$ for the third. The column has measures: short edge $\ell = 1$ m, height $h = 6$ m; the initial angular velocity field is $\omega_{0z} = 105 \cdot \sin(\pi x_3/2h)$ rad/s, imposed only in the first time step. $\sigma_{CFL} = 0.3$ assumed.

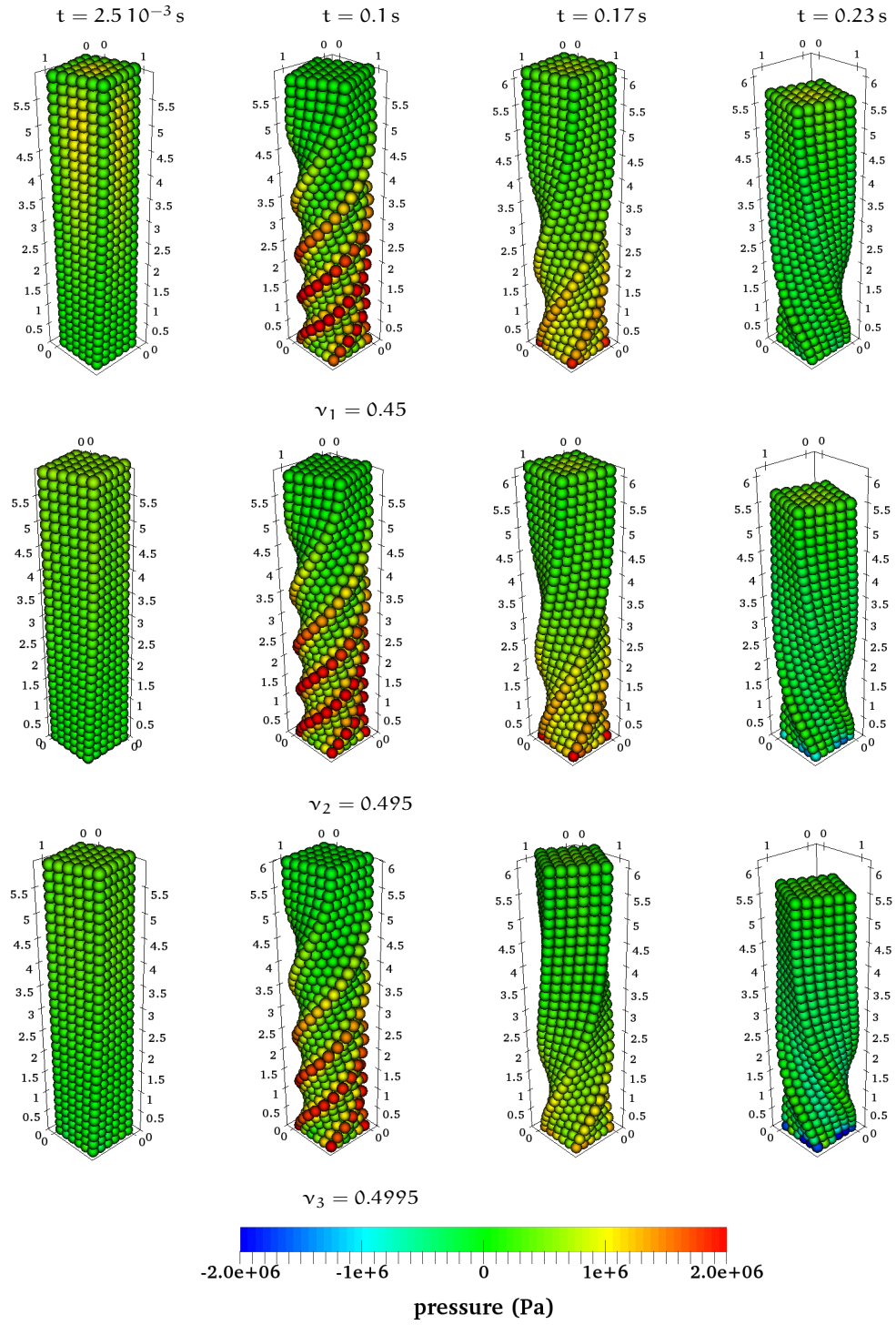

Figure 5.24: twisting column simulation, pressure contour plot at instants $2.5 \cdot 10^{-3}$, 0.1, 0.17 and 0.23 s. All results obtained with the $\{\mathbf{p}, \mathbf{F}, J\}$ JST-SPH methodology, with smoothing length factor $\alpha_h = 2.2$, $k^{(4)}_{JST} = 1/8$. The column is simulated with a set of $6 \times 6 \times 31 = 1116$ particles. A nearly incompressible, neo-Hookean hyperelastic material is employed, with density $\rho = 1100$ kg/m^3, Young's modulus $E = 17$ MPa. Each row of pictures is assigned a different Poisson ratio: $\nu_1 = 0.45$ for the first row, $\nu_2 = 0.495$ for the second, $\nu_3 = 0.4995$ for the third. The column has measures: short edge $\ell = 1$ m, height $h = 6$ m; the initial angular velocity field is $\omega_{0z} = 105 \cdot \sin(\pi x_3/2h)$ rad/s, imposed only in the first time step. $\sigma_{CFL} = 0.3$ assumed.

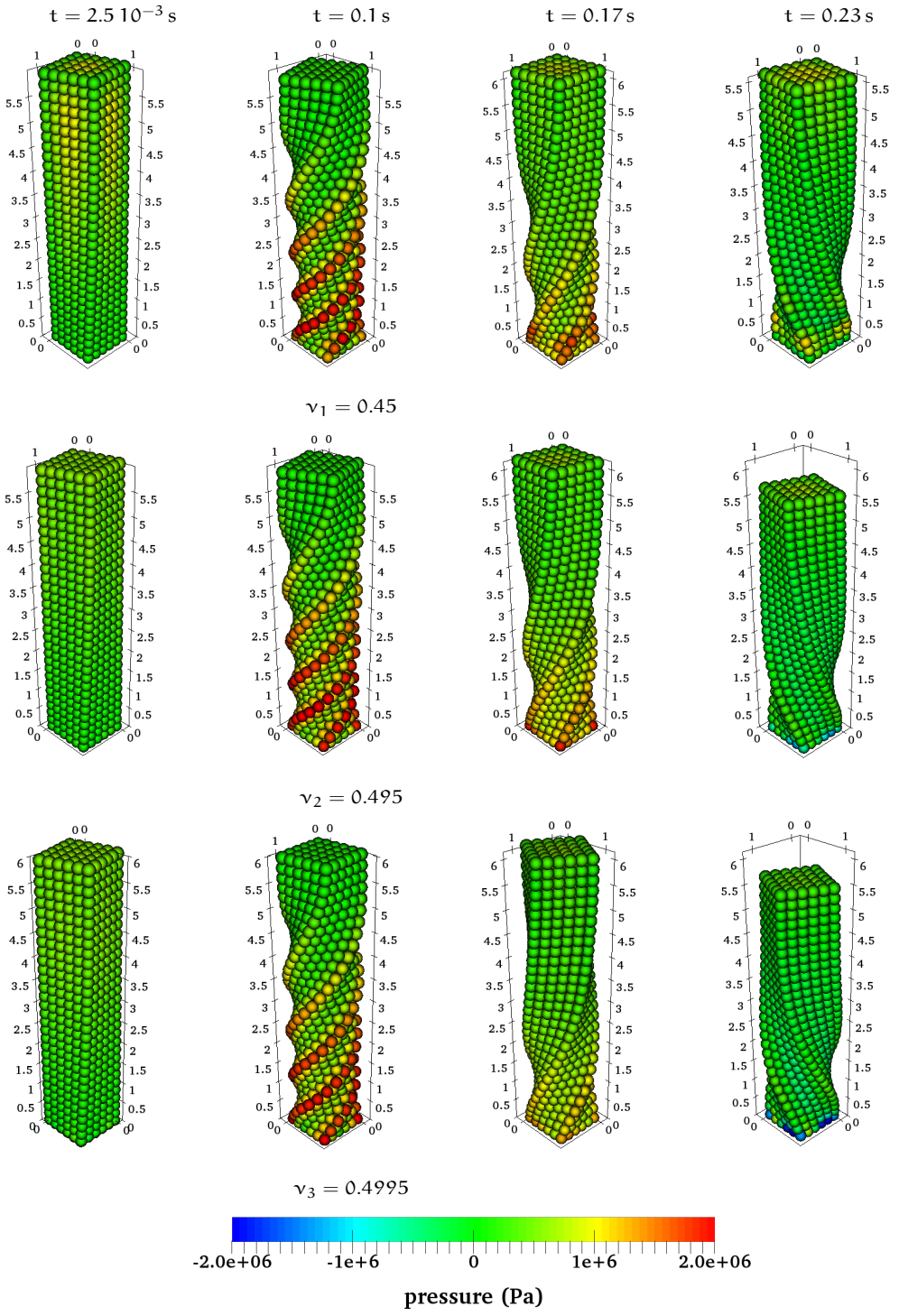

Figure 5.25: twisting column simulation, pressure contour plot at instants $2.5 \cdot 10^{-3}$, 0.1, 0.17 and 0.23 s. All results obtained with the {**p**, **F**, **H**, J} JST-SPH methodology, with smoothing length factor $\alpha_h = 2.2$, $k^{(4)}_{JST} = 1/8$. The column is simulated with a set of $6 \times 6 \times 31 = 1116$ particles. A nearly incompressible, neo-Hookean hyperelastic material is employed, with density $\rho = 1100$ kg/m^3, Young's modulus $E = 17$ MPa. Each row of pictures is assigned a different Poisson ratio: $\nu_1 = 0.45$ for the first row, $\nu_2 = 0.495$ for the second, $\nu_3 = 0.4995$ for the third. The column has measures: short edge $\ell = 1$ m, height $h = 6$ m; the initial angular velocity field is $\omega_{0z} = 105 \cdot \sin(\pi x_3/2h)$ rad/s, imposed only in the first time step. $\sigma_{CFL} = 0.3$ assumed.

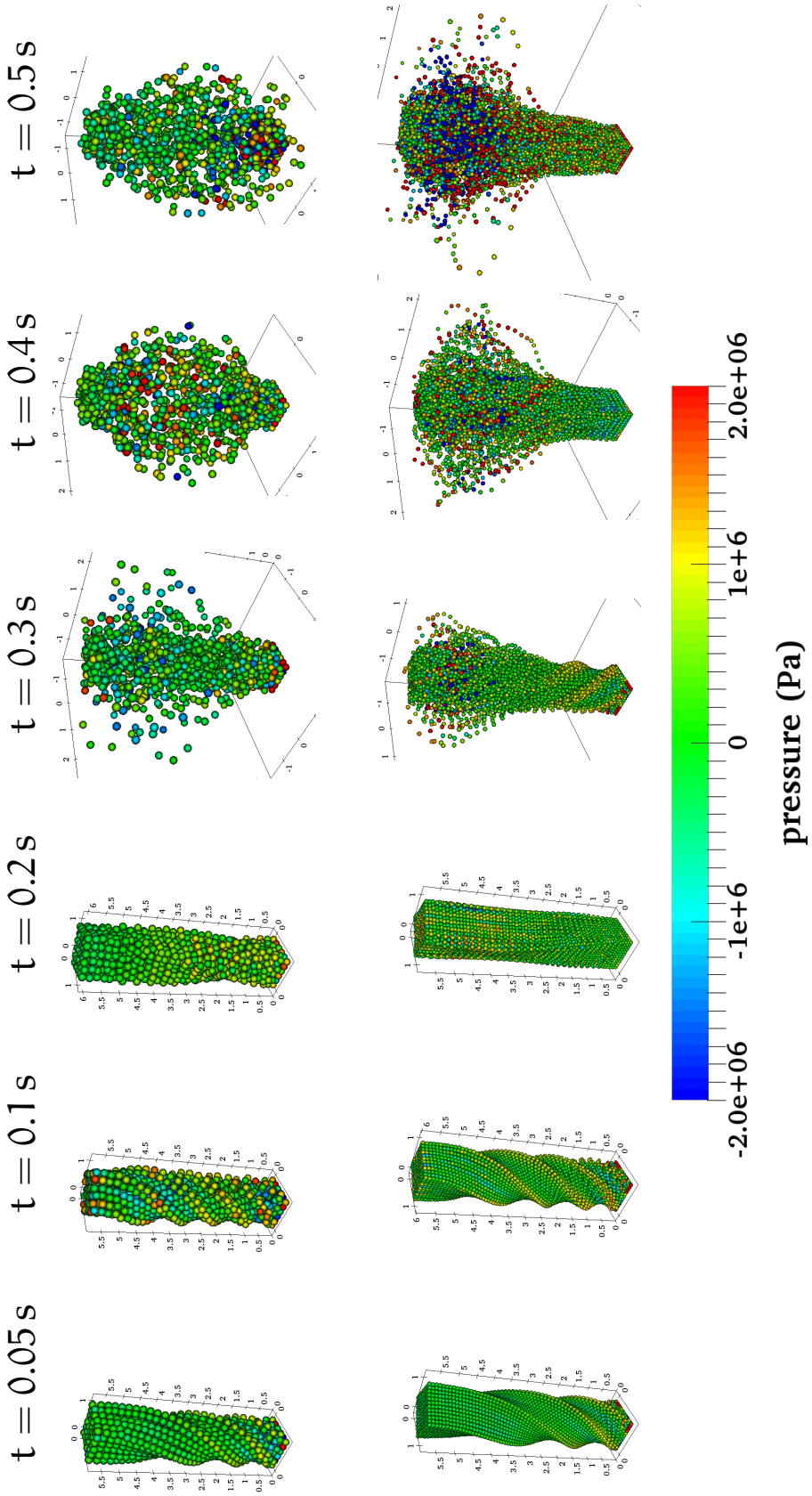

Figure 5.26: twisting column simulation, pressure contour plots obtained with the classic displacement-based SPH methodology, at different simulation times. The upper row shows a coarser mesh ($6 \times 6 \times 31 = 1116$ particles, as in figs. 5.23 to 5.25). A more refined mesh ($12 \times 12 \times 67 = 9648$ particles) is in the lower row. The simulations are run with the same parameters adopted in figs. 5.23 to 5.25.

Table 5.2: twisting column simulation, times to completion for analyses ending at $t_f = 0.25\,s$, expressed in relation to the first entry. Also reported are material properties that influence the time step length (ν and $c_{p\,max}$).

ν	mixed eq. set	wave speed $c_{p\,max}$ (m/s)	Δt_{min} (s)	total time steps	time elapsed
0.45	{**p**, **F**}	368.768	$1.627\,10^{-4}$	1331	1.000
0.45	{**p**, **F**, J}	373.270	$1.607\,10^{-4}$	1358	1.029
0.45	{**p**, **F**, **H**, J}	373.752	$1.602\,10^{-4}$	1365	1.051
0.495	{**p**, **F**}	1111.640	$5.397\,10^{-5}$	4005	2.920
0.495	{**p**, **F**, J}	1101.822	$5.390\,10^{-5}$	4038	2.961
0.495	{**p**, **F**, **H**, J}	1099.906	$5.351\,10^{-5}$	4075	3.022
0.4995	{**p**, **F**}	3431.208	$1.749\,10^{-5}$	12540	9.380
0.4995	{**p**, **F**, J}	3425.657	$1.691\,10^{-5}$	12890	9.388
0.4995	{**p**, **F**, **H**, J}	3424.597	$1.681\,10^{-5}$	13047	9.481

More in general, the hindering effect that a short time step length exerts on explicit time stepping simulations will resurface in the next section, covering plasticity problems.

5.2 PLASTICITY

5.2.1 *Taylor bar*

A common benchmark test for plastic deformation at high-speed is the classical Taylor bar impact problem [253], presented graphically in fig. 5.27.

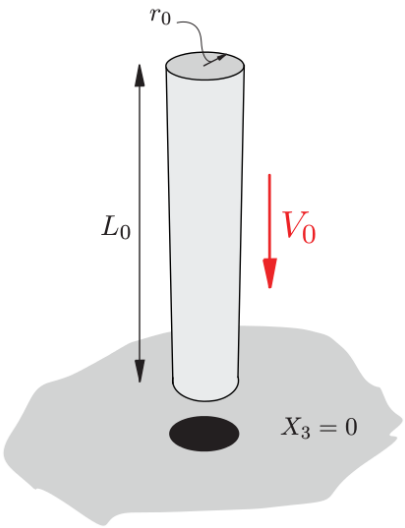

Figure 5.27: Taylor bar test, initial configuration.

The original test was performed on an aluminium cylinder, but work-hardening effects, essential in order to derive an acceptably realistic plastic flow model, are better demonstrated with copper. Elastic behaviour is governed by a stretch-based, hyperelastic energy function defined as [39]:

$$\Psi(\lambda_1, \lambda_2, \lambda_3, J) = \mu[(\ln \lambda_1)^2 + (\ln \lambda_2)^2 + (\ln \lambda_3)^2] + \frac{\lambda}{2}(\ln J)^2 \tag{5.5}$$

Equation (5.5) will be coupled with a standard von Mises plastic yield model with linear isotropic hardening. The material has the following properties: Young's modulus $E = 117$ GPa, Poisson ratio $\nu = 0.35$, yield stress $\bar{\tau}_y^0 = 0.4$ GPa, hardening modulus $H = 0.1$ GPa and density $\rho = 8930$ kg/m^3. The bar has initial height $h_0 = 32$ mm and radius $r_0 = 3.2$ mm, and is discretised as a set of 4131 particles arranged in a regular pattern, each being assigned a spherical subvolume k with radius $r_k = 0.32$ mm. The impact is frictionless and takes place at an initial speed $v_{0z} = -227$ m/s in the X_3 direction on a rigid wall in the plane normal to X_3. Due to extensive plastic dissipation, the JST stabilising term is set to a very low value. Figure 5.28 presents results of the Taylor bar simulation performed by JST-SPH.

In fig. 5.28, as expected [270], the plastic front is shown to remain close to the bottom wall in the early stages of the simulation (red contour regions). It then slowly climbs up, as more kinetic energy dissipates into plastic strain.

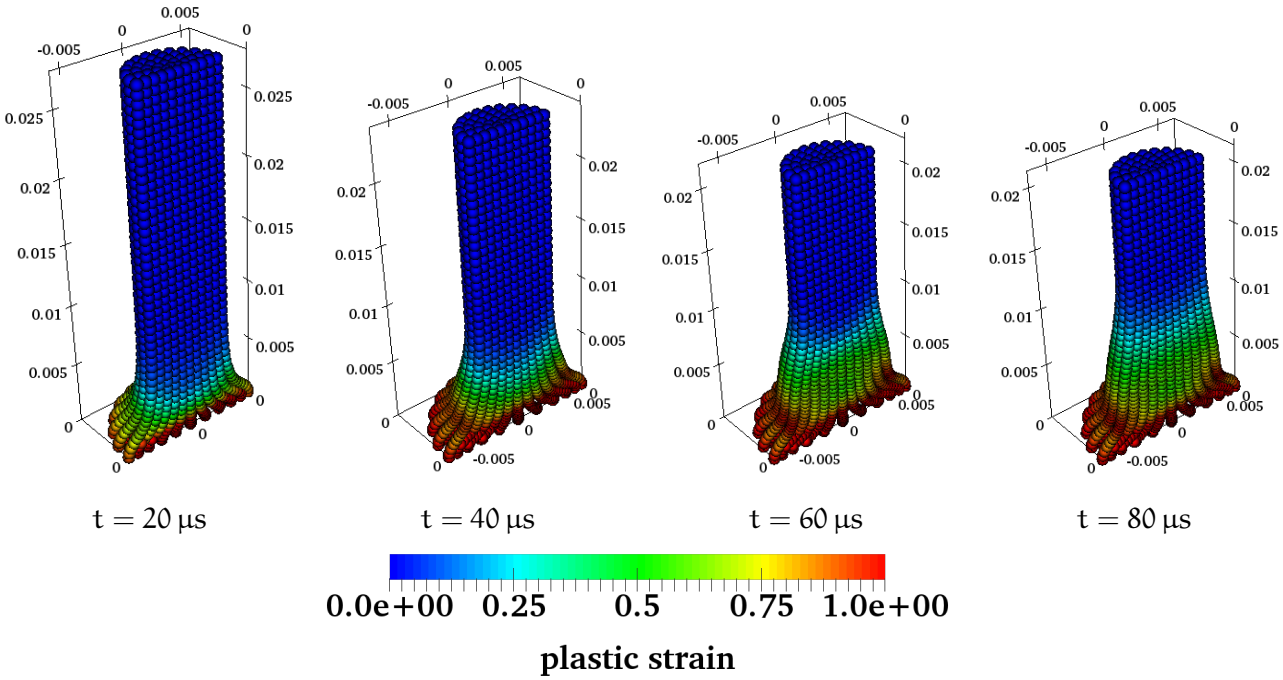

Figure 5.28: Taylor bar problem. The pictures show the cross sectional shape of the bar, and the plastic strain contour plot at various instants in the simulation. 4131 particles, $\{\mathbf{p}, \mathbf{F}\}$ JST-SPH employed, with smoothing length factor $\alpha_h = 2.2$, $k^{(4)}_{JST} = 1/4096$. The material chosen is copper, modelled as following isotropic hardening von Mises plasticity, with properties: Young's modulus $E = 117$ GPa, Poisson ratio $\nu = 0.35$, initial yield stress $\bar{\tau}^0_y = 0.4$ GPa, hardening parameter $H = 0.1$ GPa, density $\rho = 8930$ kg/m^3, initial velocity $v_{0z} = -227$ m/s.

In this case, a pressure contour plot would not reveal much of the state of tension in the structure. The deformation happening is in fact predominantly plastic, and therefore deviatoric in nature. The evolution of the von Mises equivalent stress would constitute a better gauge, and therefore is plotted in fig. 5.29.

In table 5.3, the radius of the bottom surface at $t_f = 80$ μs is compared to results of identical tests performed using different numerical techniques [1]. As can be seen from table 5.3, mixed formulation techniques, being locking-free, avoid the excessively rigid response of the structure given by FEM displacement-based analyses.

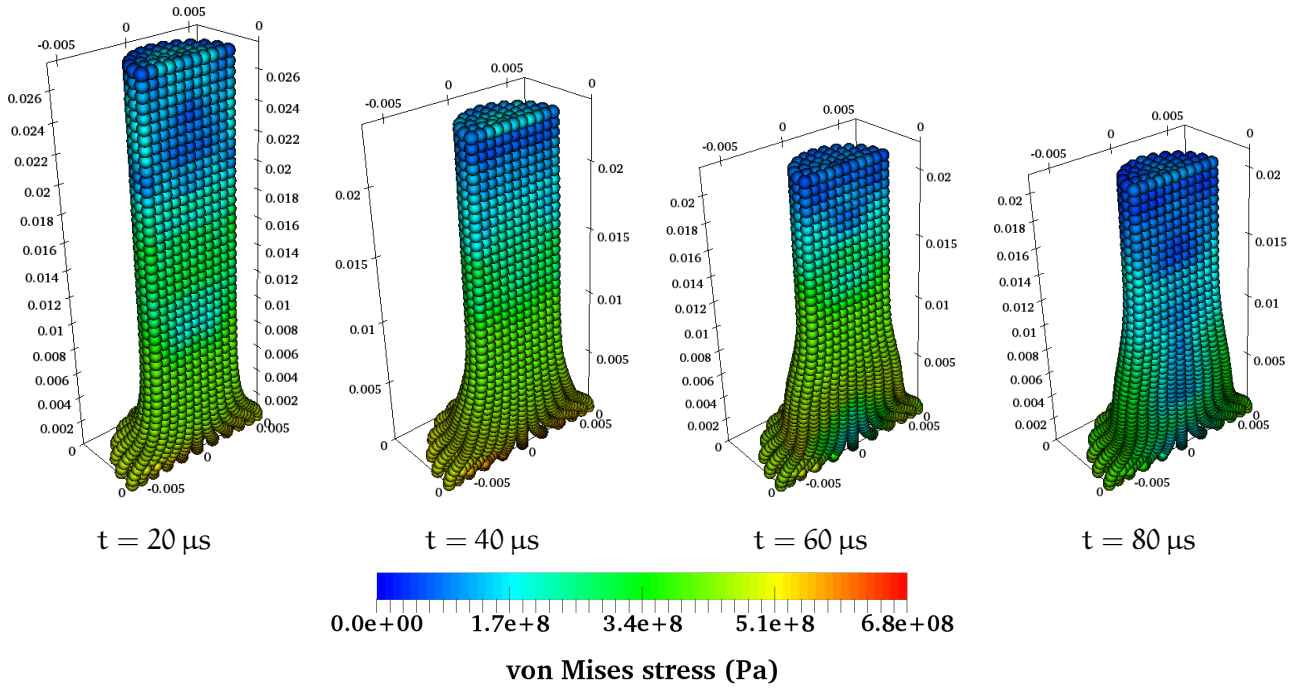

Figure 5.29: Taylor bar problem. The pictures show the cross sectional shape of the bar, and the von Mises stress contour plot at various instants in the simulation. 4131 particles, $\{\mathbf{p}, \mathbf{F}\}$ JST-SPH employed, with smoothing length factor $\alpha_h = 2.2$, $k^{(4)}_{JST} = 1/4096$. The material chosen is copper, modelled as obeying to isotropic hardening von Mises plasticity, with properties: Young's modulus $E = 117$ GPa, Poisson ratio $\nu = 0.35$, initial yield stress $\bar{\tau}^0_y = 0.4$ GPa, hardening parameter $H = 0.1$ GPa, density $\rho = 8930$ kg/m^3, initial velocity $v_{0z} = -227$ m/s.

Table 5.3: Taylor bar, radius of bottom face at $t_f = 80$ μs, obtained from different numerical methods.

numerical method	**final radius (mm)**
standard finite elements, hexahedra [30]	6.95
standard finite elements, tetrahedra [30]	5.55
mixed JST finite volumes, vertex-centred [1]	6.98
mixed JST-SPH	$6.66 + r_k = 6.98$

More to note, SPH particles station at the centre of their assigned spherical subvolumes, of radius r_k. Results in table 5.3 account for r_k in the JST-SPH case.

5.2.2 *Equal Channel Angular Extrusion (ECAE) process*

Numerous metallurgic techniques exploit the mechanics of plastic deformation, in order to attain smaller grain size – and thus better material standards – for metals and alloys. Amongst them, equal channel angular extrusion (ECAE) [217, 226] can guarantee high levels of shear strain for relatively low levels of external pressure, making it suitable for mass production. In the present setting, the ECAE process will be simulated in its 2-turns, 90°-channel variant, trying to replicate the results obtained in [217] using a commercial finite element software. In the same paper, these results were qualitatively validated through physical modelling. The test will showcase the robustness of the JST-SPH numerical setup, and indeed the overall adequacy of the CFD-inspired mixed formulation implementations, under a demanding dynamical regime where external energy is continuously introduced, generating very large distortions.

The analysis is performed in plane strain conditions, and is focused on a bar made of commercially pure aluminium (Al1100, $E = 69$ GPa, $\nu = 0.33$, $\rho_0 = 2800$ kg/m^3, width $l = 8$ mm) passing through a channel carved into a rigid die, of the same width of the bar. The right-angled corners are rounded, with 1.5 mm and 1 mm external and internal fillet radii. A sketch of the initial setup of the experiment is presented in fig. 5.30.

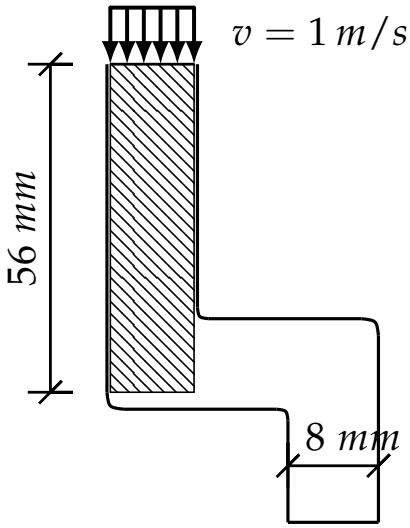

Figure 5.30: JST-SPH ECAE simulation, initial setup.

Simulations are run with a mesh of 400 particles disposed in 50 rows of 8, at a distance of 1.14 mm from each other, with each assigned a constant volume of $1.12\,\mathrm{mm}^2$. The CFL number governing the time stepping increments is 0.3.

Contact between bar and die is assumed lubricated, and is simulated firstly as frictionless, and afterwards in presence of a kinetic friction coefficient of $\mu = 0.05$, as adopted in [217]. However, a proper contact algorithm has not been developed; more simply, the contact is managed through a procedure based on the reflection of the velocity of SPH particles coming at, or crossing, a wall position. The reflection is calculated with respect to the perpendicular to that wall (see [110]). Friction is simulated by detracting momentum from the particles in contact with the straight walls of the die. In addition, a coefficient of restitution < 1 is imposed for reflections happening on the curvilinear angular regions of the channel die. Therefore, the simulation does not yield the contact forces exerted on the walls of the die.

Given that heavy plastic deformations are expected, it is useful to add numerical dissipation at the very first stages of the simulation, to prevent pressure instabilities that may happen before the base of the billet reaches the bottom wall of the channel. To this end, for each particle, the JST term $k^{(4)}$ was linked to the plastic strain $\epsilon_{(p)}$ in order to make it decrease linearly, as plastic dissipation gradually sets. This is accomplished by resorting to the following formula:

$$\begin{cases} k^{(4)} = \frac{1}{64} - 2\left(\frac{1}{64} - \frac{1}{4096}\right)\epsilon_{(p)} & \text{if } \epsilon_{(p)} \leqslant 0.5 \\ k^{(4)} = \frac{1}{4096} & \text{if } \epsilon_{(p)} > 0.5 \end{cases} \tag{5.6}$$

The hyperelastic-plastic material model used obeys to (5.5) and to the plastic isotropic hardening law:

$$\sigma^{Y}(\varepsilon_{(p)}) = 159\,(0.02 + \varepsilon_{(p)})^{0.27}\,\mathrm{MPa} \tag{5.7}$$

Equation (5.7) is solved for $\varepsilon_{(p)}$ numerically by employing the Newton-Raphson method.

Figures 5.31 and 5.32 graphically capture the deformation process of the billet at various instants in time, with the former plotting the pressure

distributions in the bar, and the latter doing the same for the plastic strains. These figures are obtained from the simulation in presence of friction; results for the frictionless analysis are substantially similar, given the relevance of plasticity as the main mechanism of energy dissipation. For the sake of comparison, in figs. 5.31 and 5.32 a second row of results is shown where tests are run with the FEM commercial solver Abaqus/Explicit, employing linear quadrilateral elements.

There is substantial agreement of figs. 5.31 and 5.32 with the FEM results, and with data presented in [217]. Irregularities in the particles distribution can be spotted near the upper angle of the first bend at later stages of the simulation. These can be attributed to difficulties in repositioning particles that have crossed the die wall, and in reassigning them a correct velocity. It can be observed that this generates a "boundary effect" that does not affect the quality of the solution outside of the two outer layers of particles. In fact, concerning the central part of the channel, deformation shapes and plastic strain contour plot in fig. 5.32 closely resemble the one presented in fig. 4 of [217]. Also, the mounting compressive stress shown in fig. 5.31 is proportional to the number of walls of the die coming to contact with the billet. Particularly evident are the sharp increments in plastic deformation – from blue ($\epsilon_{(p)} \approx 0$) to green ($\epsilon_{(p)} \approx 1$) to red ($\epsilon_{(p)} \approx 2$) – that happen when the bar reaches, fills and surpasses each one of the two bends.

In the future, to ameliorate this boundary problem, it could be useful to study and implement a penalty-type contact algorithm.

Analysis of the energy patterns throughout the simulation confirms that plasticity is the main mechanism of energy dissipation, being on average two orders of magnitude larger than the JST-related energy term when the latter is active. A comparison in time, between the energy released through plastic and JST dissipation, and the total internal energy of the bar is presented in fig. 5.33.

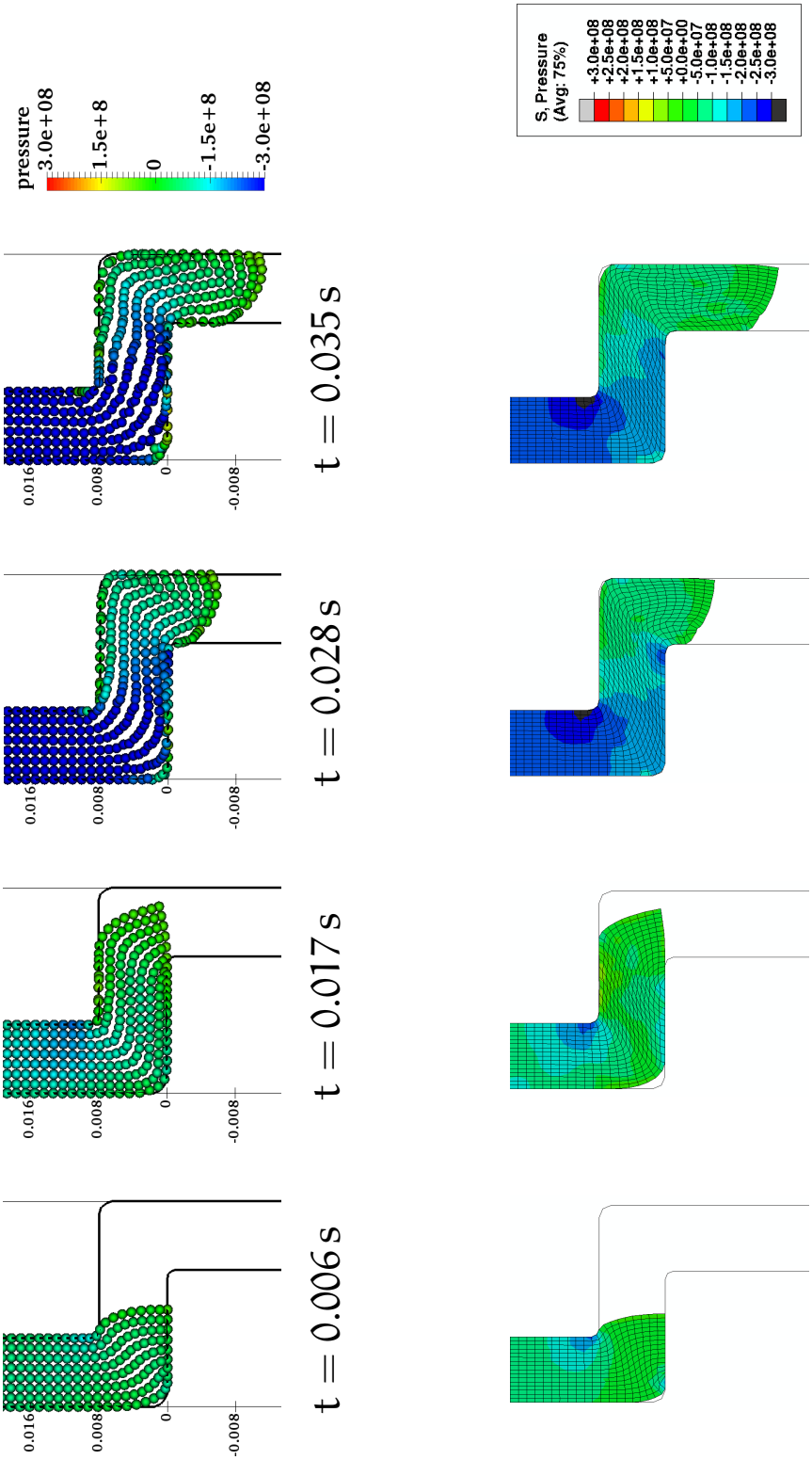

Figure 5.31: pressure p at various stages of the ECAE process. The billet being extruded is made of Al1100, with $E = 69$ GPa, $\nu = 0.33$, $\rho_0 = 2800$ kg/m^3 and plastic properties determined by (5.7); it is subjected to a velocity of $v = -1$ m/s. Top row, JST-SPH, discretised with 400 particles. Bottom row, FEM commercial solver Abaqus/Explicit, linear elements, no remeshing.

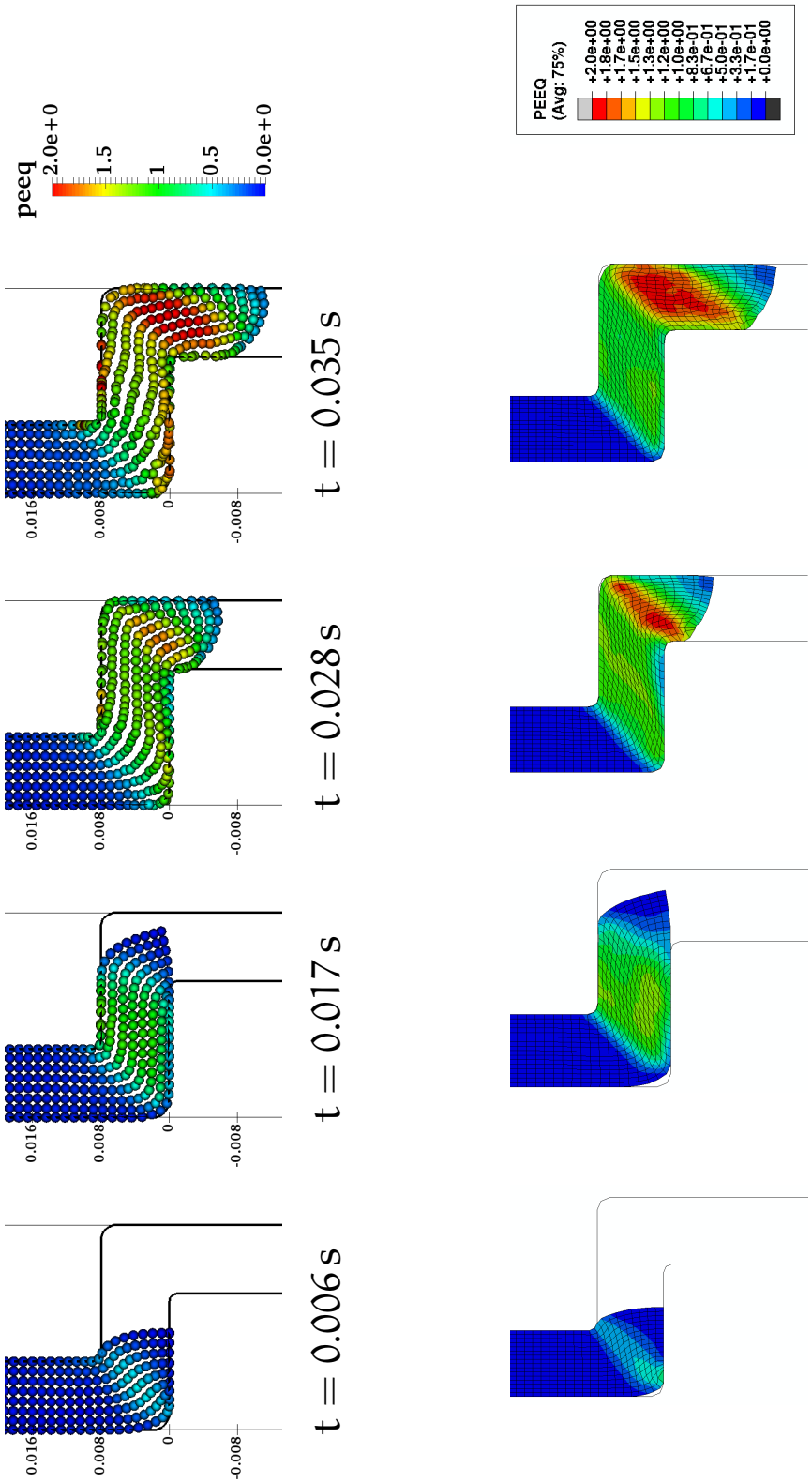

Figure 5.32: plastic strain (Peeq) $\epsilon_{(p)}$ at various stages of the ECAE process. Billet properties and simulation conditions are the same of fig. 5.31. Top row, JST-SPH, discretised with 400 particles. Bottom row, FEM commercial solver Abaqus/Explicit, linear elements, no remeshing.

The formulas employed to calculate the total internal energy U_{int}, the total plastic dissipation $W_{(p)}$ and the artificial JST dissipation $W_{(JST)}$ at each time step, are the following:

$$U_{int} = \sum_{a=1}^{N} \frac{\Delta t}{\rho_0} \|\mathbf{p}_a(\mathbf{X}, t)\| \cdot \|\mathbf{T}_a\| \tag{5.8a}$$

$$W_{(p)} = \sum_{a=1}^{N} J\|\boldsymbol{\sigma}_a\| \cdot \Delta\varepsilon_{(p)\,a} \tag{5.8b}$$

$$W_{(JST)} = \sum_{a=1}^{N} \frac{\Delta t}{\rho_0} \mathcal{D}_a^{JST}(\mathbf{p}_a) \qquad \text{for } a = 1, \dots, N \tag{5.8c}$$

It can be seen from fig. 5.33 that the total internal energy, and the total plastic dissipation, follow patterns that can be readily linked to the progress of the billet inside the die channel. Thus, a peak for both these types of energy near the beginning of the simulation, reaching their maxima around time 0.00142 s, implies contact of the bar with the mid-channel bottom wall. Starting from that same position, values of the energies begin to steeply decline, signifying that expansion in the mid-channel has begun. A similar, if less pronounced energy pattern can be found once the bar reaches, and then begins to flow into the second channel, with a peak around time 0.035 s. Noise levels for both types of energy increase with each channel intersection the bar is compressed against. They then gradually subside, once at a sufficient distance from these intersections.

For ease of visualisation, energies shown in fig. 5.33 are plotted separately in figs. 5.34a to 5.34c. In particular, fig. 5.34c shows more clearly the gradual decrease of JST with the onset of plastic deformation introduced with (5.6), and the low values of artificial dissipation needed.

In order to verify the accuracy of the simulation, a convergence study has been run, with the number of particles in the mesh acting as parameter.

The quantity under analysis is the amount of plasticity at instant 0.035 s, both in local (the maximum equivalent plastic strain $\max \varepsilon_{(p)}$ among particles) and in global (the plastic dissipation developed in the single time step leading to instant 0.035 s) terms. Other than the mesh of 400 particles used so far in other analyses, alternative meshes of 88, 216 and 640 particles were

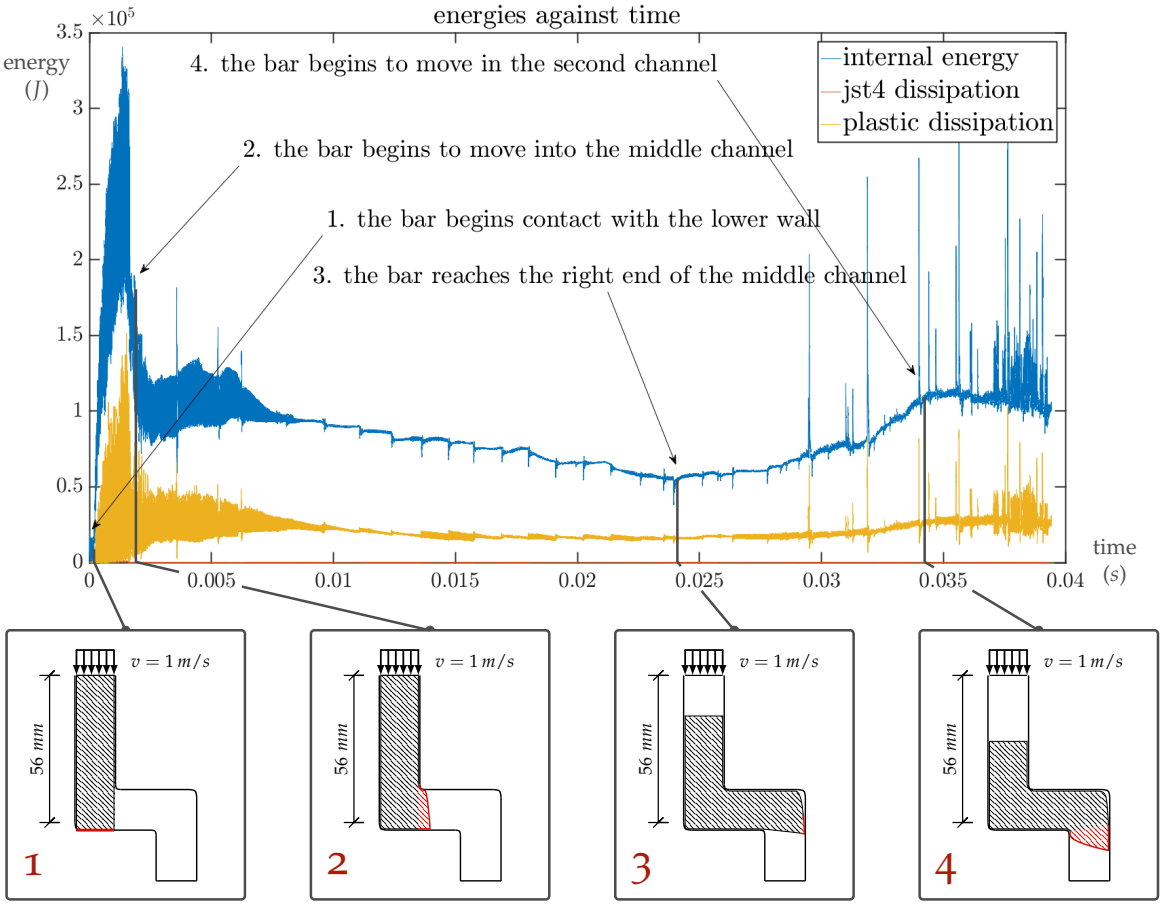

Figure 5.33: JST-SPH ECAE. Total values, summed over all particles, of the internal energy (blue line), plastic dissipation (yellow line) and JST artificial dissipation (red line) over the simulation time. The evolution of these quantities discloses information on various stages of the process.

employed. The results of the convergence analysis are listed in table 5.4 and plotted in fig. 5.35. Data on plastic deformation presented there show a tendency towards converging monotonically to a set value, as the investigated quantities increase less and less for each grid refinement (and hence as the ratio volume/particle decreases).

The 640 particles mesh has also been employed to check more accurately the degree of similarity of the JST-SPH ECAE test conducted here with the reference analysis found in [217]. To this end, the strain contour in the direction normal to movement has been investigated towards the end of the test, at simulation time $t = 0.04$ s. The two locations selected are "Section 1" positioned at the centre of the middle channel, and "Section 2" at 5 mm into

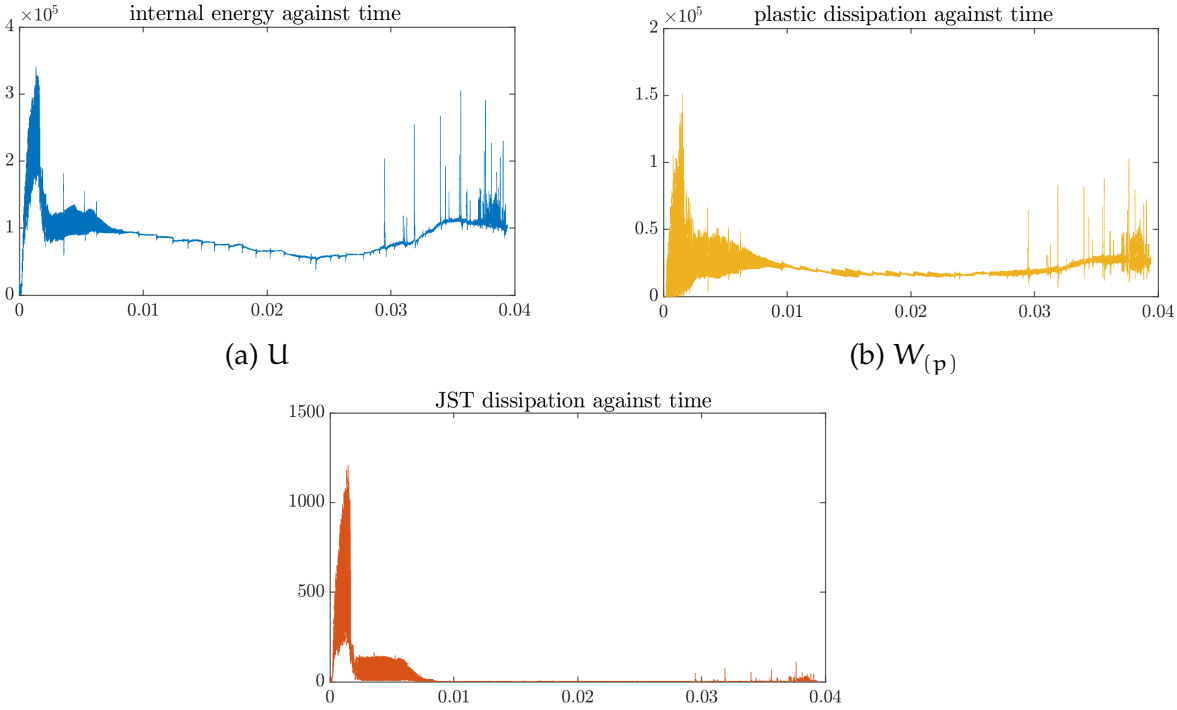

(a) U (b) $W_{(p)}$

(c) W_{JST}

Figure 5.34: JST-SPH ECAE. separate plots in time of the total internal energy U, the total plastic dissipation $W_{(p)}$, and the total JST dissipation W_{JST}.

Table 5.4: JST-SPH ECAE. Convergence analysis obtained on meshes populated with an increasing number of particles. Discretisation properties listed are the total number of particles in each grid, the number of particles composing a row of the discretised bar, the volume assigned to each particle, and the distance of particles from each other. Physical quantities listed are the total plastic dissipation $W_{(p)}$ of the bar in the single time step, and the maximum plastic strain so far accumulated, entering instant 0.035 s into the simulation.

total particles	**part./row**	**vol./part.** (mm^2)	**p. distance** (mm)	**max peeq** $\max \varepsilon_{(p)}$	**plastic** $W_{(p)}$ (J)
88	4	5.09	2.67	1.410	20497.80
216	6	2.07	1.60	2.028	24692.61
400	8	1.12	1.14	2.133	28049.84
640	10	0.70	0.89	2.197	28186.20

the output segment of the die. The same analysis can be found in fig. 5 of the reference [217], obtained through commercial FEM software.

Ten target positions have been chosen on the two sections of interest, disposed at regular intervals. Local values of the plastic strain $\varepsilon_{(p)}$ have been computed through SPH averaging over neighbouring particles. Results have been collected in fig. 5.36. Comparison of fig. 5.36 with fig. 5 in [217] reveals

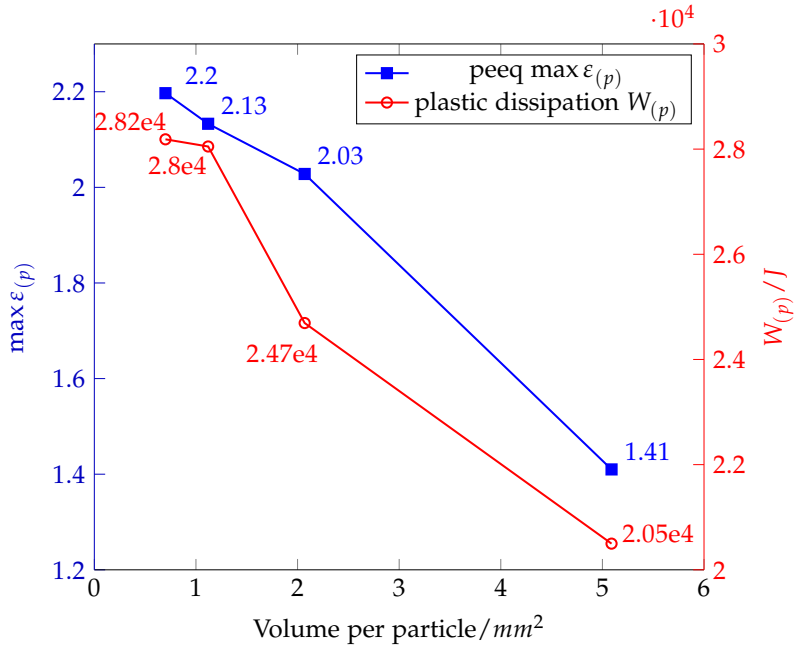

Figure 5.35: JST-SPH ECAE. Convergence plot of local maximum plastic strain $\varepsilon_{(p)}$ (in blue, left y-axis) and total dissipation $W_{(p)}$ due to plasticity (in red, right y-axis) at the time step entering 0.035 s in simulation time, based on data found in table 5.4.

that plastic strain patterns of the two tests match closely along Section 2, the main difference being that the JST-SPH analysis predictably presents a smoother curve. The same can be observed for Section 1, the two analyses showing qualitative agreement up to the control points near the upper wall, where there is a surge in plastic strain in JST-SPH. This inaccuracy is caused by being at the downstream of the previously mentioned boundary effect originating near the top side of first bend, and visible in fig. 5.32.

Parametric analyses conducted in [217] offered occasion for further checking on the validity of the results.

In [217], geometric properties of the die are modified in order to see if it was possible to enhance ECAE metallurgic performances. One of those parameters was the length of the middle die channel. From fig. 10 in [217] it can be noted that interesting deformed shapes develop, when the middle channel is shortened from 24 mm to 16 mm. The upper second bend has a large unfilled area, while the bar itself experiences more stress due to bending than due to shear. The effect is particularly strong around the inner region of the billet in the vicinity of the bottom second bend. Both these

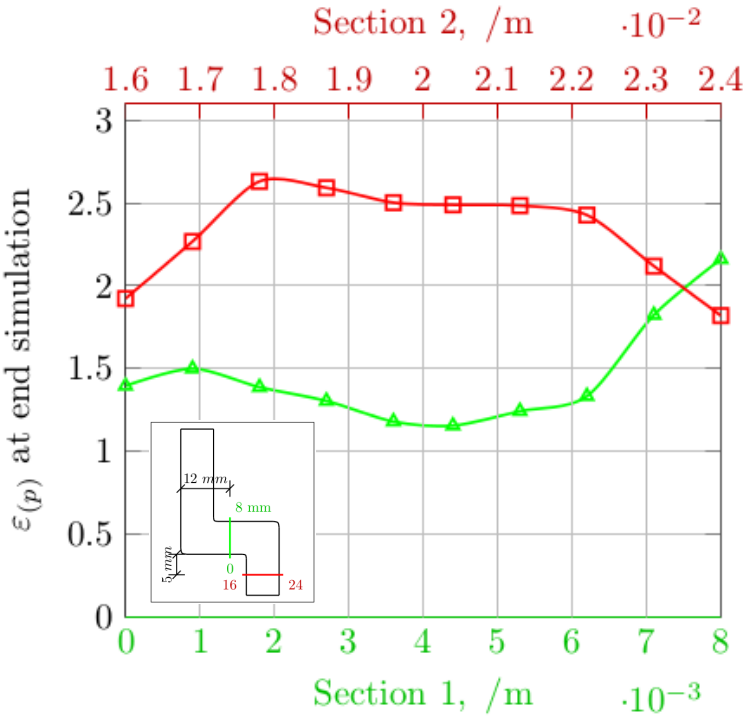

Figure 5.36: JST-SPH ECAE. Plastic strain $\varepsilon_{(p)}$ distribution across the billet sections labelled in colour at margin. Values obtained from SPH averaging of particles near the control points distributed over the sections, at the closing stages of the simulation, $t = 0.04\,s$. The mesh utilised had 640 particles in total, 10 per line. Compare to fig. 5 in [217].

aspects have been caught by an analogous simulation run with JST-SPH, as reported in fig. 5.37, taken at time $t = 0.027\,s$. Results obtained with the FEM commercial solver Abaqus/Explicit, employing linear quadrilateral elements, are also shown in fig. 5.37.

5.3 UNSTRUCTURED CONFIGURATIONS

In this section, some of the tests described in the previous sections will be run again, with the difference that this time the particles will be arranged in an irregular pattern across the domain.

For each test, the particles disposition has been generated via the default random generator algorithm (Mersenne twister, [174]) available within the Matlab computational software. This has been accomplished by inputting an array of random numbers as particles positions, and then using this array as the seed for a Voronoi tessellation [9] of the problem domain, in

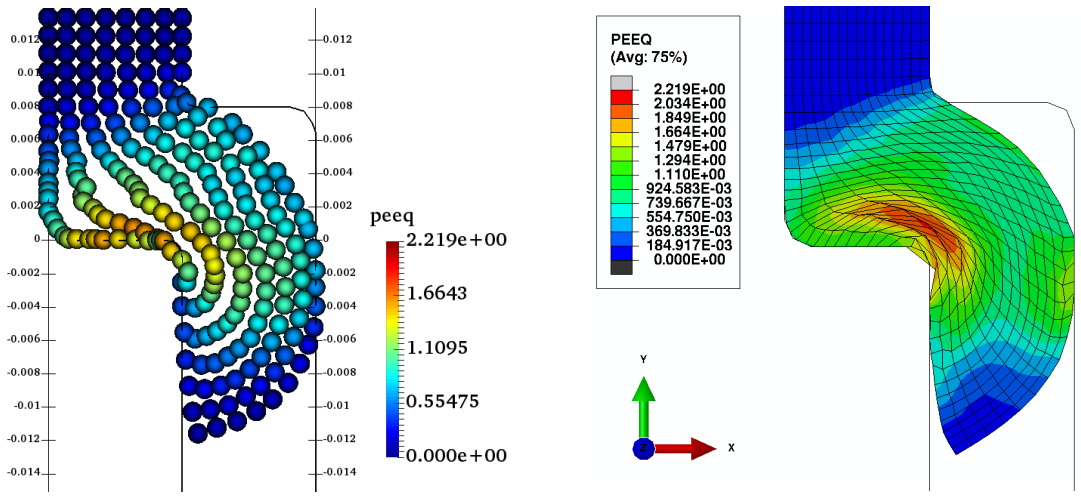

Figure 5.37: ECAE. On the left, contour plot obtained with JST-SPH at time $t = 0.027$ s of the equivalent plastic strain $\varepsilon_{(p)}$ distribution over a modified version of the die, with a shortened middle channel length. On the right, same result obtained on Abaqus/Explicit, with linear quadrilateral finite elements and no remeshing.

order to determine the subvolume attached to each particle. The vertices of the Voronoi volume cells so obtained are then used as the seed array for a second run of the Voronoi algorithm, to ensure particles are present at the boundaries of the structures.

These tests are undertaken in order to mimic particles arrangements that are needed for the discretisation of complex geometries. Application of SPH irregular particles clouds in the realm of solid dynamics has proven to be problematic in the past. In [34], for instance, it is seen that the corrected SPH displacement-based method does not give satisfying results for irregular dispositions of particles.

5.3.1 *Cube*

Previous analyses performed in section 5.1.3, involving a unit cube discretised with a regular arrangement of particles, are hereby run again, this time in a randomised configuration. Figure 5.38 shows the Voronoi tessellation, with evidence on the particles positions, and their assigned subvolumes.

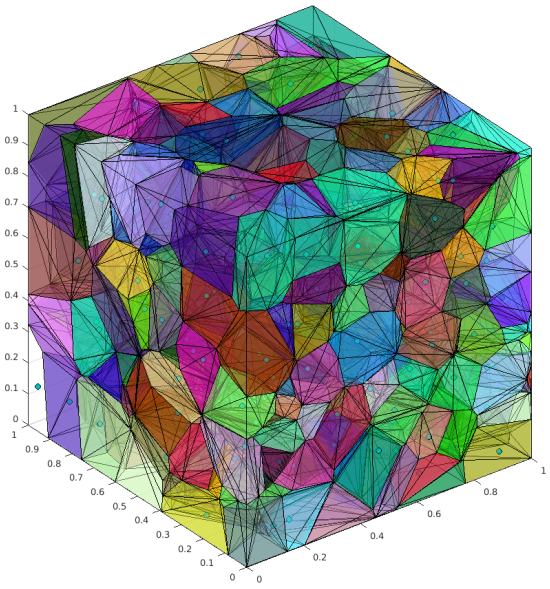

Figure 5.38: SPH discretisation of a unit cube, with particles arranged in a random pattern, and subsequent Voronoi tessellation. Particles are represented as blue dots, and their assigned subvolumes as Voronoi cells of different colours.

Next, the cube is set to receive an initial velocity field of $v_{y0} = 800 \cdot X_3$ m/s, and to be pinned to the ground, as in fig. 5.12. Material and discretisation properties are the same as those listed at page 202, with the exception that there are now 353 particles present. The simulation is run to check whether there are any important differences with the regular particles position case in section 5.1.3.

Figure 5.39 presents the time evolution of the simulation.

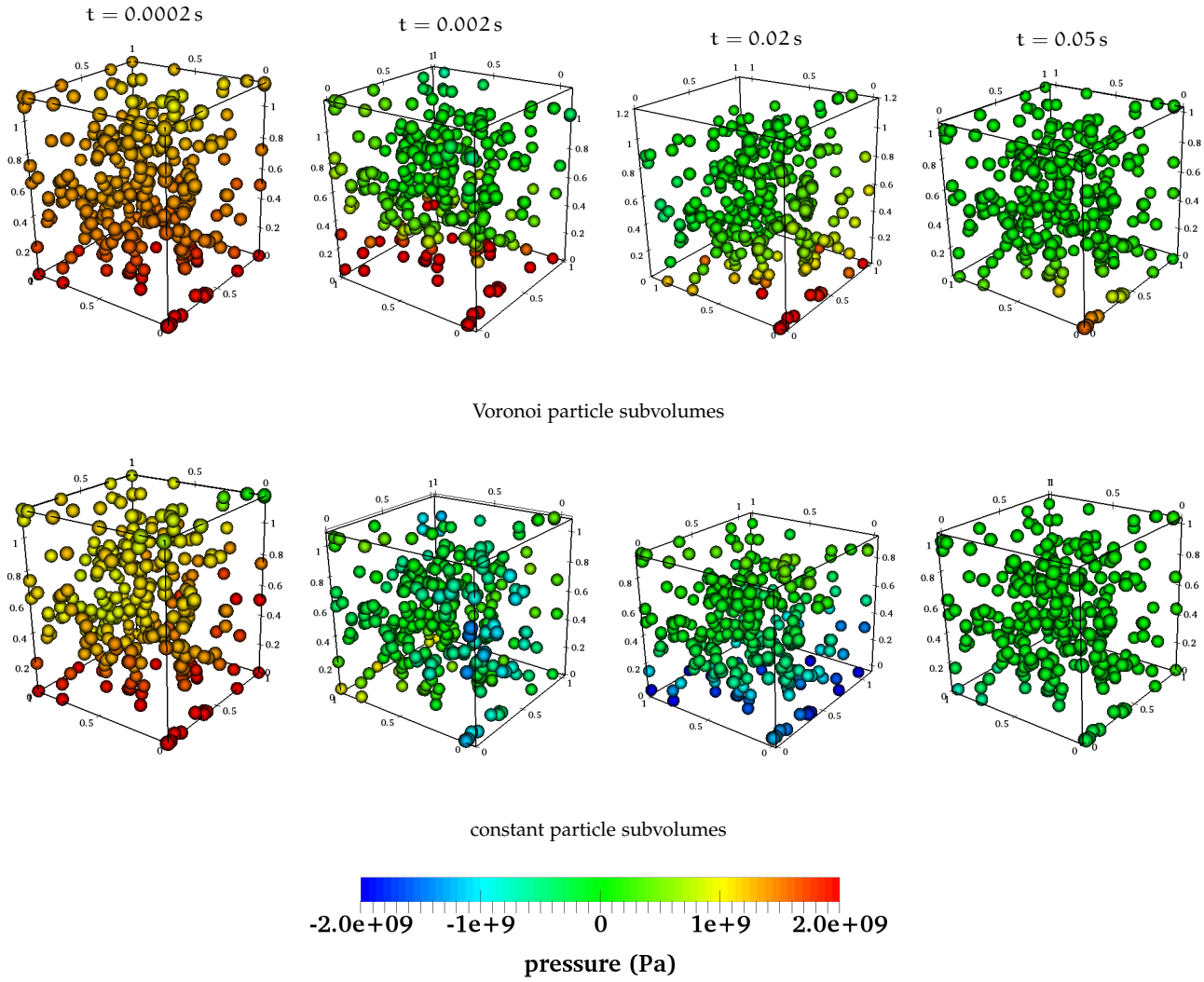

Figure 5.39: tensile cube simulation, pressure contour plot at various instants in time. {**p**, **F**} JST-SPH scheme employed. Results obtained assigning to each particle its Voronoi volume are in the first row; assigning the same constant subvolume to each, in the second. Simulation parameters: $1 \times 1 \times 1$ m^3, discretised with 353 particles, $k_{JST}^{(4)} = 1/8$; neo-Hookean hyperelastic material with density $\rho = 7000$ kg/m^3, Young's modulus $E = 21$ MPa, Poisson's ratio $\nu = 0.3$. Initial velocity field of $v_{0z} = 800 \cdot X_3$ m/s imposed only in the first time step. $\sigma_{CFL} = 0.3$ assumed.

Figure 5.40 plots in time the displacements of the particle at the top side corner position $(1, 1, 1)$ of the cube, in both the random and regular pattern simulations. It is clear that allowing a variable volume for each cell leads to different results, than having it preserving a constant volume. Some of the particles, in fact, also sway to the sides as a result of their random distribution inside the cube, that places them more at distance from the others, and, thus, less constrained in their motion.

The magnitude of side movements can be observed in fig. 5.41, where displacements in the X_1 direction are plotted for the corner particle at $(1, 1, 1)$. Moreover, it should be observed that allowing for a large variance in the values of volumes, can further shorten the time step, and hence further slow down the simulation.

5.3.2 *Taylor bar*

The Taylor bar experiment run in section 5.2.1 will be proposed again here, with a randomly disposed geometry of particles. As previously, a copper bar of identical shape and material properties to the one in section 5.2.1 is subjected to an initial vertical velocity of $v_{0z} = -227$ m/s, as pictured in fig. 5.27.

The SPH discretisation is composed of 373 particles disposed in a randomised pattern; other simulation parameters and properties are the same as those in section 5.2.1.

Results in fig. 5.42 show the simulation captured at a series of instants in time, for the case where a uniform value of the subvolume is assigned to each particle.

Figure 5.43, instead, represents a simulation where each particle gets assigned its own Voronoi subvolume.

What emerges from comparing fig. 5.42 with fig. 5.43 is that in the first instance, where densities and subvolumes are the same for each particle, the non-uniform distribution of particles in space determines deformation shapes substantially different from those of the Voronoi volume simulation, as well as from those of the regular case (see fig. 5.28). This can be explained by noting that there is no material matter assigned in regions where particles are more distanced from each other. As a consequence, particles simply fill the gap regions without exerting stress on their neighbours.

On the contrary, where particles tend to clump, their subvolumes overlap and create clusters where particles influence each other and behave as a group.

The analysis conducted with Voronoi particles subvolumes, in fig. 5.43, exhibits an even more marked lack of configuration symmetry. This time, forces and momenta computed by the JST-SPH solver depend on the assigned

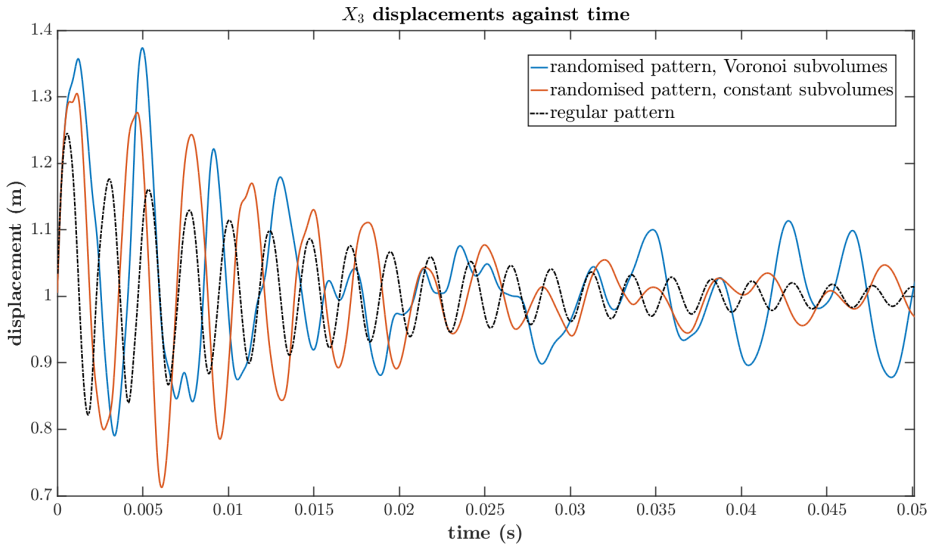

Figure 5.40: tensile cube simulation, time plot of displacements in the X_3 direction, for a particle at one of the upper face corners of the cube, obtained with the {**p**, **F**} JST-SPH formulation. Tests run with random arrangement of particles, each assigned Voronoi subvolumes (blue), each assigned constant subvolumes (red), and results from the regular patterned simulation (dashed black).

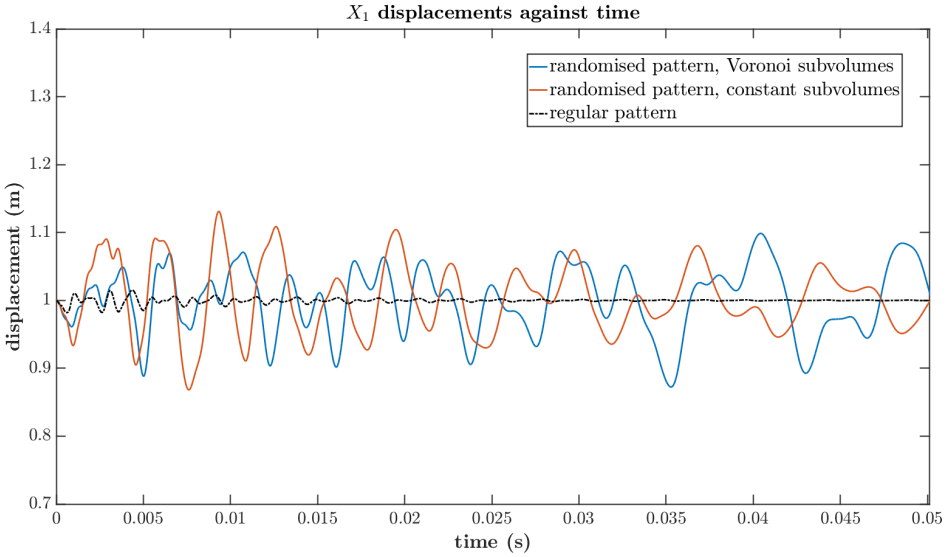

Figure 5.41: tensile cube simulation, time plot of displacements in the X_1 direction, for a particle at one of the upper face corners of the cube, obtained with the {**p**, **F**} JST-SPH formulation. Tests run with random arrangement of particles, each assigned Voronoi subvolumes (blue), each assigned constant subvolumes (red), and results from the regular patterned simulation (dashed black).

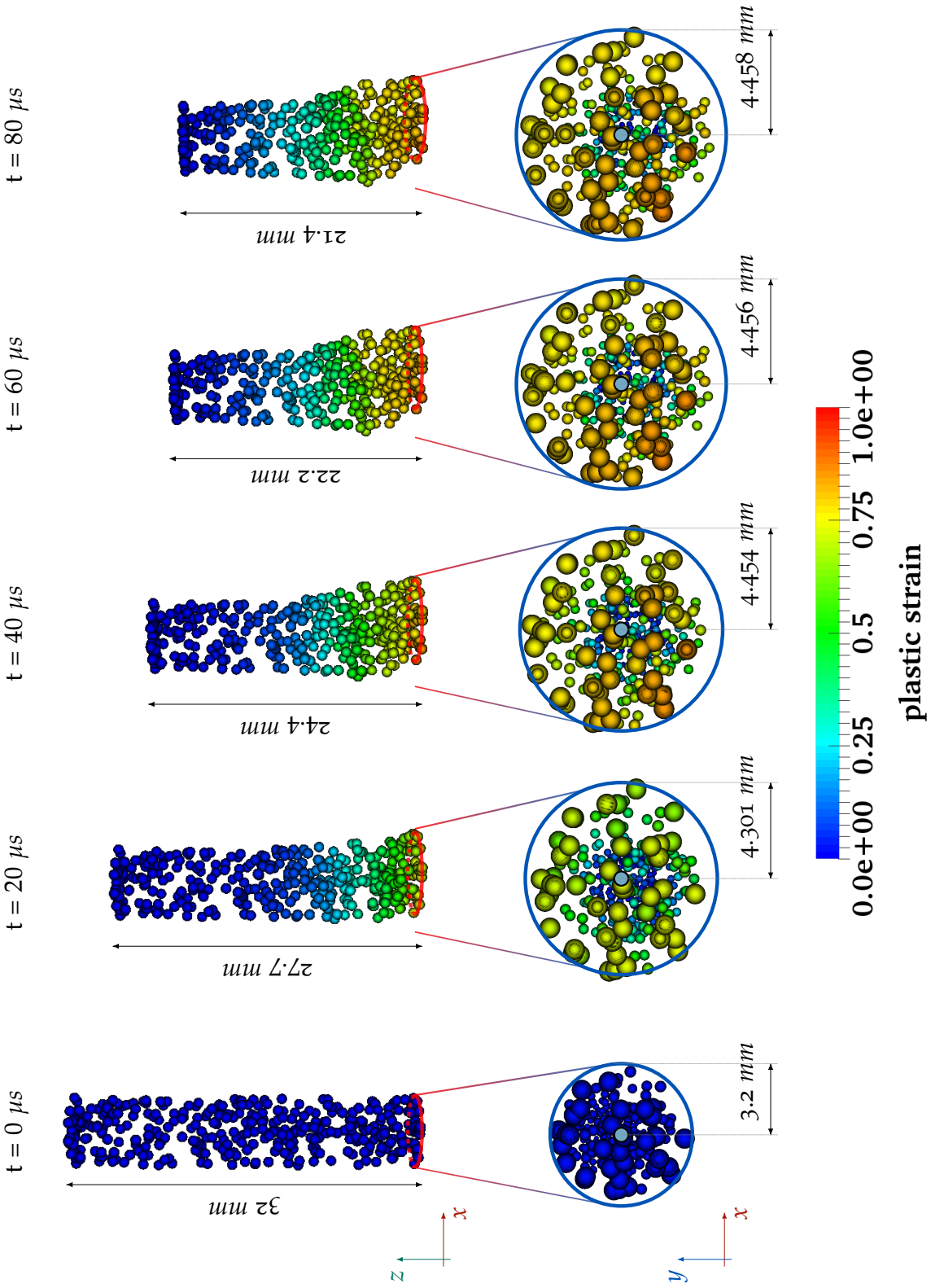

Figure 5.42: Taylor bar problem, with random particles distribution and constant particles subvolumes. $\{\mathbf{p}, \mathbf{F}\}$ JST-SPH scheme employed. Shapes of the bar, and plastic strain contour plots are shown in lateral view (top row) and from a bottom perspective (lower row), at various instants during the simulation. 373 particles, with smoothing length factor $\alpha_h = 2.2$, $k_{JST}^{(4)} = 1/4096$. A constant subvolume $V_k = 2.76\,10^{-9}\ m^3$ is assigned to each particle k. The material chosen is copper, modelled as following isotropic hardening von Mises plasticity, with properties: Young's modulus $E = 117$ GPa, Poisson ratio $\nu = 0.35$, initial yield stress $\bar{\tau}_y^0 = 0.4$ GPa, hardening parameter $H = 0.1$ GPa, density $\rho = 8930\ kg/m^3$, initial velocity $v_{0z} = -227$ m/s.

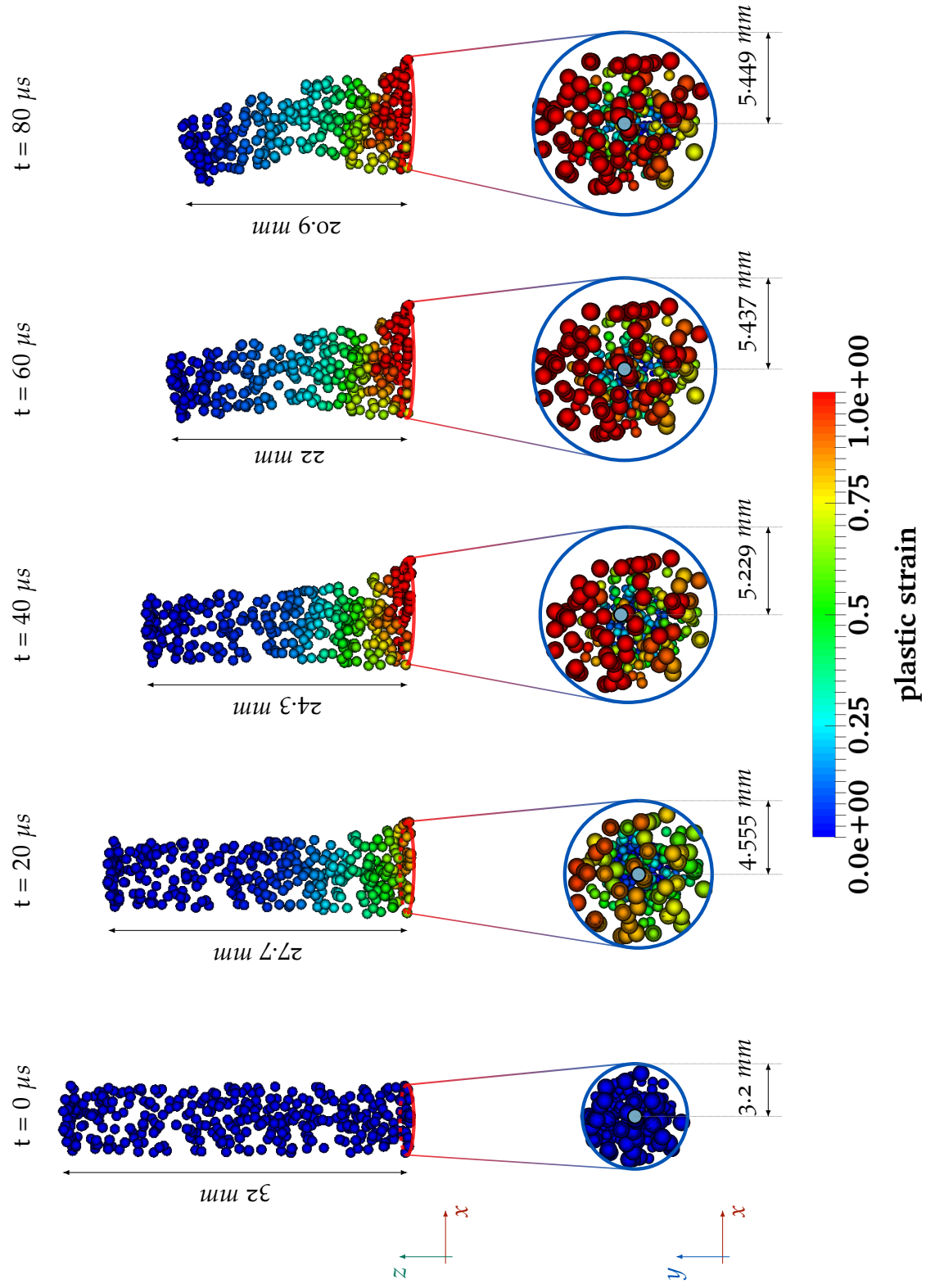

Figure 5.43: Taylor bar problem, with random particles distribution and Voronoi particles subvolumes. {**p**, **F**} JST-SPH scheme employed. Shapes of the bar, and plastic strain contour plots are shown in lateral view (top row) and from a bottom perspective (lower row), at various instants during the simulation. 373 particles, with smoothing length factor $\alpha_h = 2.2$, $k_{JST}^{(4)} = 1/4096$. The subvolume V_k assigned to each particle k is equal to the volume of the Voronoi cell of k. The material chosen is copper, modelled as following isotropic hardening von Mises plasticity, with properties: Young's modulus $E = 117$ GPa, Poisson ratio $\nu = 0.35$, initial yield stress $\bar{\tau}_y^0 = 0.4$ GPa, hardening parameter $H = 0.1$ GPa, density $\rho = 8930$ kg/m^3, initial velocity $v_{0z} = -227$ m/s.

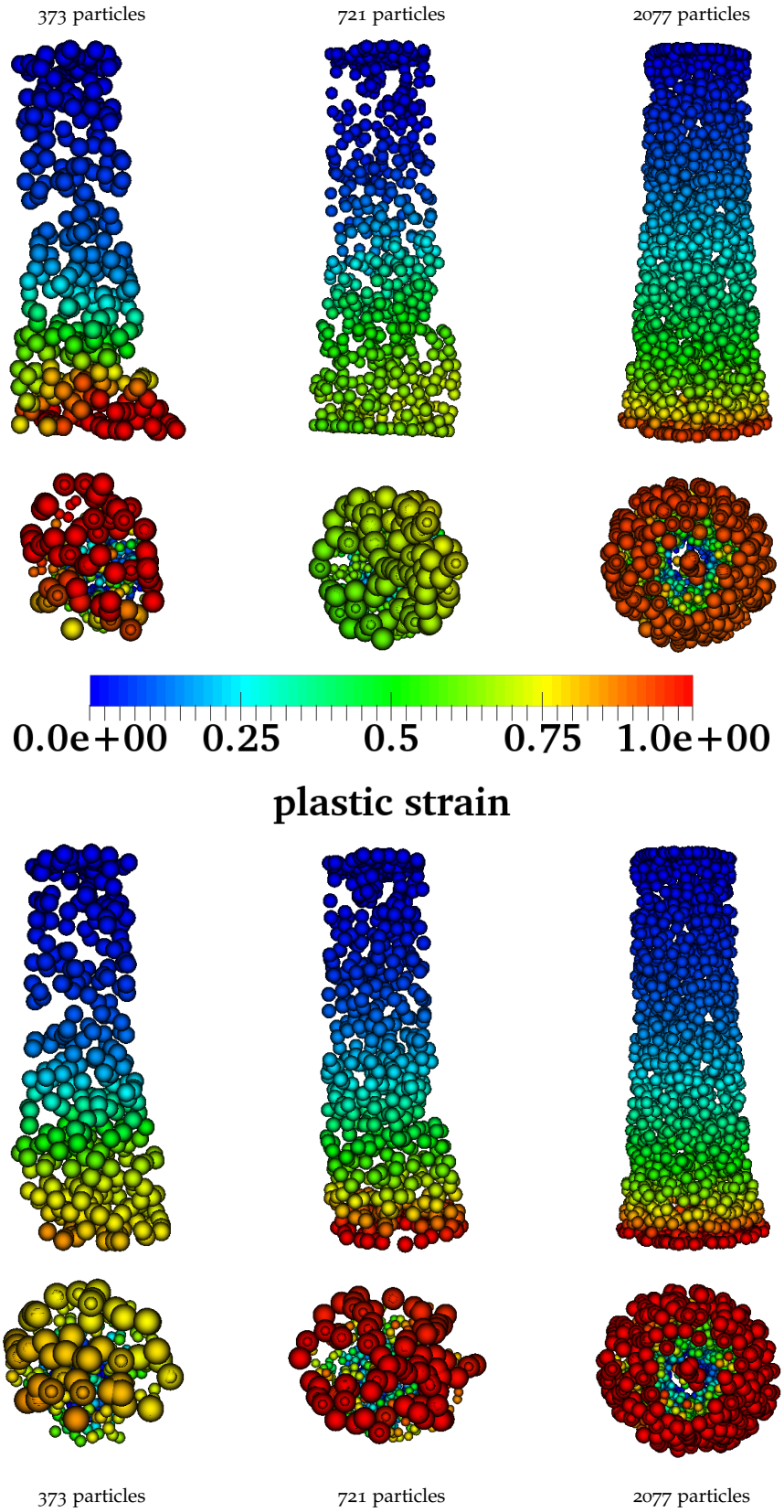

Figure 5.44: Taylor bar simulation, comparison of plastic strain distribution contours for meshes composed of different numbers of particles, at $t = 48$ μs into the simulation. Figures located above the legend refer to simulations run with Voronoi particle subvolumes, while figures below the legend refer to analyses in which constant particle subvolumes were used. For each of the simulations considered, views of the deformed cylinder are presented from the side, and from the bottom. Mixed {**p**, **F**} JST-SPH scheme employed. Simulation parameters are the same as those in figs. 5.42 and 5.43.

subvolumes, and are thus directly affected by their variance from particle to particle.

Figures 5.42 and 5.43 were obtained from simulations run with a smaller number of particles with respect to the Taylor bar simulation in section 5.2.1, that had a grid of regularly distributed particles.

In fig. 5.44, results obtained with increased particle mesh resolution (373 particles, as in figs. 5.42 and 5.43, 721 particles, and 2077 particles) at simulation time $t = 48\ \mu s$, are compared with each other. Clearly, the increase in number of particles leads to improved symmetry in both the deformed shape, and the plastic strain distribution.

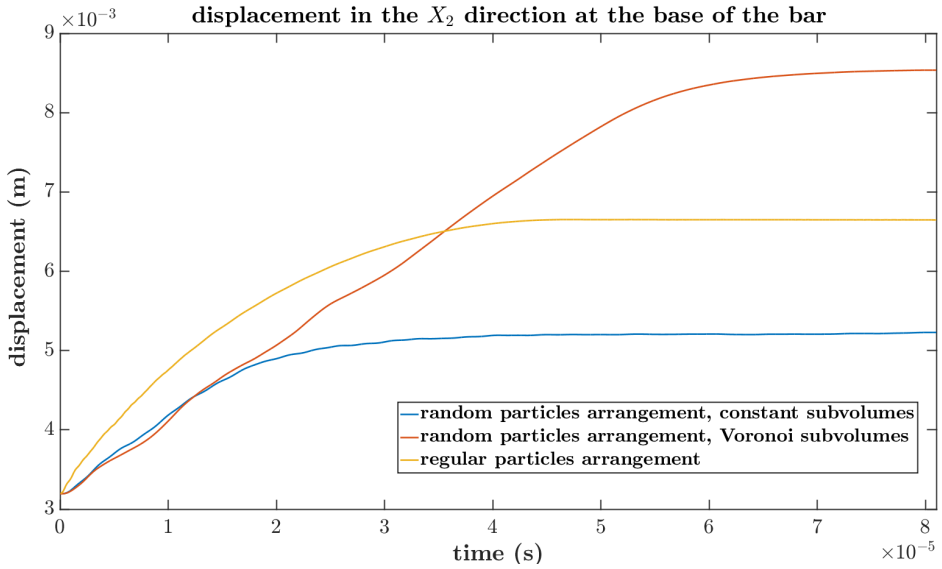

Figure 5.45: Taylor bar simulation, time plot of X_2 (radial) displacements of a particle at the edge of the bar bottom face, obtained from unstructured configurations, with constant particle subvolumes (blue line), Voronoi particles subvolumes (red line), and from the regular particles pattern (yellow line). The {**p**, **F**} JST-SPH formulation was used for all cases.

In fig. 5.45, the evolution of the radial displacement of a particle at the base of the bar is followed for both cases of variable or constant particles subvolumes. Results from the regular particles disposition are also reported. Confirming the previous observations, the simulation adopting constant particle subvolumes yields a reduced radius length, with respect to the other cases.

It may be worth reminding that the objective of running analyses with random particles dispositions is not to produce results comparable with

those obtained with particles arranged in an orderly manner, but to check the numeric feasibility of irregular distributions, in view of applying the method on complex geometries.

In this regard, the JST-SPH algorithm looks robust, as results obtained with unstructured simulations show a tendency to convergence towards results obtained with a regular patterned particles disposition, when the number of randomly-disposed particles is increased.

5.4 CONCLUDING REMARKS

The JST-SPH has been tested in a series of benchmark examples under various dynamic regimes, using different constitutive laws and patterns of particles disposition.

All in all, the method has been shown to perform well under a variety of circumstances. The novel techniques that have been introduced – such as the polyconvex full $\{\mathbf{p}, \mathbf{F}, \mathbf{H}, J\}$ mixed formulation, the JST dissipation from CFD, and the algorithm for preservation of total momenta presented in section 3.8 – have been proven to be dependable. The study of ECAE, an industrially relevant metallurgic process, has also shown the reliability of the method for use in more complex settings.

6 CONCLUSIONS

6.1 FINAL REMARKS

The research addressed in this thesis is set in the context of a more ample research effort [1, 2, 31, 86, 87, 99, 143–146], aimed at overcoming instabilities and improving the low orders of accuracy, that constitute current limitations in traditional linear tetrahedral finite elements in nonlinear solid dynamics modelling.

To accomplish this, a novel mixed-based formulation is adopted, where the linear momentum $\mathbf{p}$ and the three strain measures (of local fibre $\mathbf{F}$, area $\mathbf{H}$, and volume J) of a polyconvex material model are treated as independent variables, a move away from the displacement-based weak form commonly in use for other methods. It is well known from FEM literature [16, 115] that this is a general and robust approach to assume when modelling incompressible and nearly incompressible materials, for which adverse effects of volumetric locking are an issue.

Recently, this mixed approach in modelling the continuum has been coupled with an array of numerical discretisation techniques, spanning from FV [1, 2, 99, 143], to FE [31, 86, 87, 144], and to the SPH particle method (as explored in this thesis), and further expanded in recently published papers [145, 146].

Chapter 2 introduces the concept of systems of conservation laws in the context of solid mechanics. Balance equations are formulated for kinetic properties (mass, linear and angular momenta, and the total energy of a continuum) so that their total quantities are preserved over time. It is not guaranteed, however, that a system of PDEs derived from these conservation laws could yield real and distinct analytic solutions. In order to do so, such a system should have the property of hyperbolicity, which ensures the existence of real material elastic wave speeds.

Ball [13] and Dafermos [62] show that the property of polyconvexity of the material constitutive model guarantees a well posed system of PDEs. Polyconvexity, in fact, leads to ellipticity, that in turn establishes existence and uniqueness of solutions [13, 172]. According to the aforementioned literature, the strain energy of a polyconvex material is expressed in terms of the deformation gradient $\mathbf{F}$, its Jacobian J and the cofactors matrix $\mathbf{H}$.

Supplementary conservation laws are then elaborated for $\mathbf{F}$, J and $\mathbf{H}$. Together with the conservation of linear momentum $\mathbf{p}$, and a polyconvex constitutive model, these equations constitute a first order hyperbolic system of PDEs.

Chapter 2 provides a theoretical background relevant for the subsequent establishment of the JST-SPH computational method. Further, the eigenstructure of the system of equations with respect to standard hyperelastic materials are investigated. The eigenvalues of the system matrix represent the elastic wave speeds; real and distinct values would prove the soundness of the approach.

In addition to ensure the existence and uniqueness of solutions for the mixed $\{\mathbf{p}, \mathbf{F}, \mathbf{H}, J\}$ system of conservation laws, the established proof of hyperbolicity draws a direct parallel with the Euler equations that govern fluid dynamics [6, 107, 139], which are themselves a first order hyperbolic system of PDEs. This analogy with fluid dynamics allows the use of well-honed numerical dissipation techniques adopted from CFD for the mixed $\{\mathbf{p}, \mathbf{F}, \mathbf{H}, J\}$ system, in a fast solid dynamics context.

In depth, investigation of a numerical scheme to use for discretisation of the mixed $\{\mathbf{p}, \mathbf{F}, \mathbf{H}, J\}$ system is the object of the analysis performed in chapter 3, where the meshless SPH particle method is introduced and described. SPH is advantageous in a large deformation context because it does not need the concept of element, and hence does not require the use of a mesh to interpolate field variables [181, 243]. In fact, shape functions are instead directly built on the nodes (particles), with assistance from bell-shaped kernel functions. In a high-strain regime, the presence of a mesh would otherwise entail the risk of entanglements and excessive distortion of the finite elements that compose it [22].

Corrections, however, have to be introduced over the kernel functions and their derivatives, in order to help avoid irregularities at or near the

boundary of the physical domain. Moreover, SPH also suffers from the so-called tensile instability effect, which consists in particles clumping in pairs when subjected to a tensile stress. It is shown that tensile instability can be overcome by adopting a total Lagrangian approach.

One of the main novelties introduced in this thesis is the pairing of artificial dissipation with the SPH spatial discretisation. The JST artificial dissipation term is adopted directly from CFD, and is built on the Laplacians of the SPH kernel function acting as discontinuity sensors [119]. Coupled with an explicit, second order of accuracy, two stages TVD-RK time integrator, it forms the JST-SPH numerical discretisation framework.

Considering that (i) there is now no relation between the deformation gradient tensor $\mathbf{F}$ and the gradient of displacements $\nabla_0 \mathbf{x}$, as $\mathbf{F}$ is coopted as a primary unknown variable, and that (ii) the JST dissipation term is not symmetric due to corrections to the Laplacian of the kernel made to avoid boundary incompleteness, conservation of discrete linear and angular momenta has to be imposed on the system at each time step. An upwind scheme, as introduced in [146], would bypass the need of imposing momentum conservation for the artificial dissipation, but still, the cost of this added complexity for the JST-SPH methodology is paid back by its excellent stability, as is testified in the von Neumann analyses run in chapter 4.

Lastly, the viability of JST-SPH is demonstrated in practice by solving a range of numerical applications, as presented in chapter 5.

Chapter 5 also includes, amongst many examples, the simulation of a metallurgy process, ECAE, which will also be the focus of a journal paper that is currently being drafted. Chapter 5 concludes with a foray in applications run with an unstructured starting grid of particles, to assess the capability of the JST-SPH scheme to simulate the more complex body geometries characteristic of real world applications.

6.2 FUTURE WORK PERSPECTIVES

Possible avenues of future research based on the work carried out in this thesis are manifold. We list some ideas below, starting from the more straightforward, and proceeding towards the more difficult to implement.

- COMPLETION OF THE PROOF OF HYPERBOLICITY FOR THE OGDEN HYPERELASTIC MODEL: in order to fully bring closure to chapter 2, an eigenvalue analysis on system (2.186) should be performed, adopting the Ogden-type energy material potential Ψ_O expressed in (2.188). As a first step towards this result, the characteristic equation for Ψ_O has already been derived in (2.201). The resulting eigenvalues – the elastic wave speeds of the material – should come out real, positive and distinct, and consequently prove the hyperbolicity of the mixed system (2.162). This in turn will validate the treatment of nonlinear elastodynamics for Ogden-type materials, with discretisation techniques lifted from CFD, as described in chapter 3.

- ADOPTION OF AN IMPLICIT TIME INTEGRATION SCHEME: an explicit time stepping numerical approach can have hindering effects when in presence of large plastic deformations, as clearly seen in the case of the ECAE simulation in chapter 5. Indeed, the time step length of that simulation decreases considerably, as plastic deformation accumulates on the metal bar, with each 90°-turn in the ECAE cycle. This overextends the running time, to the point where the JST-SPH scheme loses its computational viability.

  As already described in section 3.7, this issue is caused by requirements on the minimum time step length, that are imposed by the limited stability of explicit RK time integrators.

  The CFL stability requirement on time step length Δt, (3.93), shows that Δt and the material sound wave speed c_p are inversely proportional. As c_p positively depends on the material current deformation state, it is clear that explicit time integration can considerably slow down analyses where large and rapid elasto-plastic deformations are involved. In addition, local high strains act as further limitation to the global Δt.

  Implicit methods are specifically designed with a stability region large enough to allow for large time step lengths, at the cost of a greater computational effort to solve singular steps, with respect to explicit methods. Therefore, it is speculated that the spatial JST-SPH discretising methodology, in conjunction with an implicit multistep method – such as the Crank-Nicholson method described in [57], the backward dif-

ferencing method [84], or any other type of multistep implicit method with at least second order of convergence such as those listed in [19] – can possibly improve the speed and efficacy of the ECAE simulations, as reported in chapter 5.

- MODELLING A NUMBER OF ADDITIONAL PHYSICAL MATERIAL BEHAVIOURS: the applications described in chapter 5 are simulations that have been conducted exclusively in the framework of isothermal nonlinear elastoplasticity. Considered the maturity of the theory [27, 79, 262], and its relevance in solid dynamics scenarios [17, 236], rate-dependent material behaviour (viscoelasticity and viscoplasticity) could constitute a valuable inclusion to the numerical model, and certainly a necessary one in view of simulating real world applications.

  In order to do so, the present $\{\mathbf{p}, \mathbf{F}, \mathbf{H}, J\}$ mixed formulation should be expanded to include thermal effects, by adding the total internal energy E to the set of unknowns. E would be made out of an internal mechanical energy component, and an additional component modelling the dependency from the temperature field.

  Assuming E as additional unknown of the system would also lead to a more efficient error estimation analysis, as the energy norms would be derived directly from an independent variable.

- EMPLOYMENT OF ALTERNATIVE MESHLESS METHODS TO SPH: as far as the spatial discretisation of the formulation is concerned, SPH was preferred over other meshfree methods because of the straightforward and physically meaningful correlation it creates between particles and material points, and its conceptual simplicity, that leads to ease of implementation and lower computational costs.

  However, these advantages are counteracted with numerical issues stemming in large part from nodal integration. These issues have been addressed by correction devices described at length in chapter 3.

  It would be interesting to verify whether the increase in computational expense that comes with the adoption of a meshless weak-form method requiring background quadrature cells, would constitute an acceptable trade-off for the absence of numerical stability issues, and for the

increased accuracy of those methods [50] with respect to SPH. Viable candidate models of this kind are the EFG method [23, 24], and the Max-Ent method [7, 204, 247]. In particular, as already mentioned in chapter 3, the latter has the peculiarity of enjoying the Kronecker delta property for nodes located at the boundary of the computational domain. This considerably simplifies the imposition of Dirichlet BCs with respect to what seen for other meshless methods, as SPH [77].

- INTRODUCTION OF A CONTACT ALGORITHM: the simulation of the ECAE process in chapter 5 has been carried out without detailed modelling of the interaction between the metal piece and the rigid walls of the die. A rebound algorithm was in place to adjust positions and velocities of the SPH particles composing the piece, in case they crossed the die walls. A more in-depth analysis of contact effects, such as magnitude of contact areas and pressures, would help to better define interaction properties like sliding mechanics and friction [131, 193].

  The implementation of a contact model is a fundamental step in order to progress towards fast solid dynamics analyses of a higher complexity, like high-velocity collisions, and ballistic tests [60].

- INTRODUCTION OF A FRACTURE MODEL: it has recently been observed [83] that a displacement-based, total Lagrangian SPH formulation coincides with a collocation-based meshless discretisation of the theory of Peridynamics, with few adaptations required. Peridynamics is a weak-statement extension of continuum mechanics, that does not need to set up jump conditions to treat discontinuities, and hence is frequently employed to simulate fracture and crack propagation.

  Models of material damage and failure have already been developed in the past using SPH, benefiting from the particle nature of the scheme. In fact, SPH, bridges the gap between the continuum and fragmentation in a natural way. A seminal study on the set-up of a SPH framework for brittle fracture (and subsequent fragmentation in damaged solids) has been firstly conducted by Benz and Asphaug [26], and later resumed by Owen [205], among others.

The SPH fracture model of Benz and Asphaug could, in our view, be implemented in the current JST-SPH methodology. It would constitute a useful addition, in view of investigating more complex fast solid dynamics phenomena.

- ATTEMPT MORE COMPLEX FAST SOLID DYNAMICS TESTS: should a contact algorithm and a fracture model be incorporated in our JST-SPH framework, it would then be theoretically possible to simulate more challenging fast solid dynamics applications. Among these are high-velocity ballistics and impacts involving complex geometry, industry relevant test cases and prototypes.

- CODE PARALLELISATION: open source, advanced performance SPH parallel codes are already at disposal of the CFD research community. Parallelisation offers optimised performances, with possibility to offload part of the computing effort to graphical processor units (GPUs), and capabilities to run common benchmark simulations (dam-breaking flows, flows around simply shaped obstacles, etc.) with up to several millions of particles in a reasonable time scale (hours). Most renown among these open-source platforms are SPHysics, written in Fortran [91, 92], and its off-shot Dual-SPHysics, written in the C++ and CUDA languages [58], and optimised for simulations requiring a high number of particles. Both are intended for local parallelism (OpenMP protocol).

  An expansion of either of these two powerful codebases, made to include a mixed formulation JST-SPH solver among pre-processing options, would equip SPHysics or Dual SPHysics with the capability to solve nonlinear solid dynamics problems. As a consequence, prototype testing, of the kind mentioned in the previous point, would be made computationally more affordable.

APPENDIX

A.1 REPRODUCING KERNEL PARTICLE METHODS

The RKPM was originally proposed in [159] and [163] as an improvement on SPH, capable to yield modified kernel functions $W_{RKPM}(\mathbf{x}-\mathbf{x}_b, \mathbf{x}, h)$ satisfying the discrete consistency conditions (3.39) across the whole problem domain, boundaries included.

The corrected kernels $W_{RKPM}(\mathbf{x}-\mathbf{x}_b, \mathbf{x}, h)$ are defined as

$$W_{RKPM}(\mathbf{x}-\mathbf{x}_b, \mathbf{x}, h) = C_{RKPM}(\mathbf{x}-\mathbf{x}_b, \mathbf{x})\, W(\mathbf{x}-\mathbf{x}_b, h) \tag{A.1}$$

with the correction function $C_{RKPM}(\mathbf{x}-\mathbf{x}_b, \mathbf{x})$ in (A.1) being

$$C_{RKPM}(\mathbf{x}-\mathbf{x}_b, \mathbf{x}) = \mathbf{P}^T\left(\frac{\mathbf{x}-\mathbf{x}_b}{h}\right)\boldsymbol{\alpha}(\mathbf{x}) \tag{A.2}$$

In (A.2), h is the smoothing length, used as dimension (*dilation* [163]) parameter of the kernel function, $\mathbf{x}_b$ are the neighbouring particles to target position $\mathbf{x}$, $\mathbf{P}(\mathbf{x})$ is the vectorial form for a complete set of polynomials in $\mathbf{x}$ up to order k, while $\boldsymbol{\alpha}(\mathbf{x})$ is the set of k unknown RKPM corrective parameters to be determined:

$$\mathbf{P}^T(\mathbf{x}) = \left(1, x, x^2, x^3, \ldots, x^k\right) \qquad \boldsymbol{\alpha}(\mathbf{x}) = \begin{pmatrix} a_0(\mathbf{x}) \\ a_1(\mathbf{x}) \\ a_2(\mathbf{x}) \\ a_3(\mathbf{x}) \\ \vdots \\ a_k(\mathbf{x}) \end{pmatrix} \tag{A.3}$$

The RKPM procedure then calls for finding the unknown parameters by solving a system made up of equations known as *moment equations* for the corrected kernel $W_{\text{RKPM}}(\mathbf{x}-\mathbf{x}_b,\mathbf{x},h)$:

$$\begin{aligned}
\sum_{b=1}^{n} V_b W_{\text{RKPM}}(\mathbf{x}-\mathbf{x}_b,\mathbf{x},h) &= 1 \\
\sum_{b=1}^{n} \frac{\mathbf{x}-\mathbf{x}_b}{h} V_b W_{\text{RKPM}}(\mathbf{x}-\mathbf{x}_b,\mathbf{x},h) &= 0 \\
\sum_{b=1}^{n} \left(\frac{\mathbf{x}-\mathbf{x}_b}{h}\right)^2 V_b W_{\text{RKPM}}(\mathbf{x}-\mathbf{x}_b,\mathbf{x},h) &= 0 \\
&\vdots \\
\sum_{b=1}^{n} \left(\frac{\mathbf{x}-\mathbf{x}_b}{h}\right)^k V_b W_{\text{RKPM}}(\mathbf{x}-\mathbf{x}_b,\mathbf{x},h) &= 0
\end{aligned} \tag{A.4}$$

Moment equations making up system (A.4) resemble discrete consistency conditions (3.39), except that they ensure up to the k^{th} order of polynomial reconstruction. This in turn guarantees a $(k+1)^{\text{th}}$ order of truncation error, as can be verified [160] if each term of the Taylor k^{th} order expansion of a function $f(\mathbf{x})$ from its value at point $\mathbf{x}_b$

$$\begin{aligned}
f(\mathbf{x}) = f(\mathbf{x}_b) + \frac{df(\mathbf{x})}{d\mathbf{x}}\left(\frac{\mathbf{x}-\mathbf{x}_b}{h}\right)h + \frac{1}{2!}\frac{d^2f(\mathbf{x})}{d\mathbf{x}^2}\left(\frac{\mathbf{x}-\mathbf{x}_b}{h}\right)^2 h^2 + \dots \\
\dots + \frac{1}{k!}\frac{d^kf(\mathbf{x})}{d\mathbf{x}^k}\left(\frac{\mathbf{x}-\mathbf{x}_b}{h}\right)^k h^k
\end{aligned}$$

is approximated with RKPM to obtain

$$\begin{aligned} f_{RKPM}(x) = \sum_{b=1}^{n} V_b f(x_b) W_{RKPM}(x - x_b, x, h) + \\ + \sum_{b=1}^{n} \left(\frac{x - x_b}{h}\right) V_b \frac{df(x)}{dx} W_{RKPM}(x - x_b, x, h)\, h + \\ + \frac{1}{2!} \sum_{b=1}^{n} \left(\frac{x - x_b}{h}\right)^2 V_b \frac{d^2 f(x)}{dx^2} W_{RKPM}(x - x_b, x, h)\, h^2 + \dots \\ \dots + \frac{1}{k!} \sum_{b=1}^{n} \left(\frac{x - x_b}{h}\right)^k V_b \frac{d^k f(x)}{dx^k} W_{RKPM}(x - x_b, x, h)\, h^k + \\ + \mathcal{O}\left(h^{k+1}\right) \end{aligned} \tag{A.5}$$

From the fulfilment of (A.4) follows that, for the approximated f_{RKPM} in (A.5), $\|f_{RKPM}(x) - f(x)\| = \mathcal{O}\left(h^{k+1}\right)$.

Substitution of (A.2) into (A.1) and then of (A.1) into the moment equations (A.4) leads to a system that can be solved for $\mathbf{a}(x)$:

$$\mathbf{M}(x, h)\, \mathbf{a}(x) = \mathbf{F}_0 \tag{A.6}$$

In (A.6), the matrix system $\mathbf{M}(x, h)$ assumes the form:

$$\mathbf{M}(x, h) = \begin{bmatrix} m_0(x) & m_1(x) & m_2(x) & \dots & m_n(x) \\ m_1(x) & m_2(x) & m_3(x) & \dots & m_{n+1}(x) \\ m_2(x) & m_3(x) & m_4(x) & \dots & m_{n+2}(x) \\ \vdots & & & \ddots & \vdots \\ m_n(x) & m_{n+1}(x) & m_{n+2}(x) & \dots & m_{2n}(x) \end{bmatrix} \tag{A.7}$$

with matrix components $m_i(x)$, $i = 1, \dots, n$ in (A.7) defined as

$$m_i(x) = \sum_{b=1}^{n} \left(\frac{x - x_b}{h}\right)^i V_b W(x - x_b, h) \tag{A.8}$$

In (A.8), $W(x - x_b, h)$ is the original SPH kernel function.

The vector of constant terms $\mathbf{F}_0$ in (A.6) is given as

$$\mathbf{F}_0 = \begin{pmatrix} 1 \\ 0 \\ 0 \\ \vdots \\ 0 \end{pmatrix} \tag{A.9}$$

It is worth noting that the moment matrix in (A.7) is symmetric and non-singular, as it is built out of a set of linearly independent bases $\left(\frac{x-x_b}{h}\right)^i$ and out of a positive function $W(x-x_b,h)$, with $i=1,\dots,2n$ and $b=1,\dots,n$ [51]. Hence, the solution of (A.6) can be found after inverting $\mathbf{M}(x,h)$ as

$$\boldsymbol{\alpha}(x) = \mathbf{M}^{-1}(x,h)\,\mathbf{F}_0 \tag{A.10}$$

In light of (A.10), correction function $C_{RKPM}(x-x_b,x)$ in (A.2) and modified kernel $W_{RKPM}(x-x_b,x,h)$ in (A.1) are obtained as

$$C_{RKPM}(x-x_b,x) = \mathbf{P}^T\left(\frac{x-x_b}{h}\right)\mathbf{M}^{-1}(x,h)\,\mathbf{F}_0 \tag{A.11}$$

$$W_{RKPM}(x-x_b,x,h) = \mathbf{P}^T\left(\frac{x-x_b}{h}\right)\mathbf{M}^{-1}(x,h)\,\mathbf{F}_0\,W(x-x_b,h) \tag{A.12}$$

In [163] a scaling factor $E(h)$, function of the smoothing length h, is used to maintain the RKPM consistency:

$$\sum_{b\in\Omega} E(h) W_{RKPM}(x-x_b,x,h)\,V_b = 1 \tag{A.13}$$

In (A.13), Ω is assumed to be the kernel support domain around position x.

Additional information on the RKPM can be found in [159, 160, 162, 163]; there is also a review paper [161]. Furthermore, see [51] for the first use of RKPM for solving explicit simulations of large, nonlinear deformations.

As opposed to unmodified SPH kernel functions, correction (A.12) can lead W_{RKPM} to break positivity condition (3.33).

This fact notwithstanding, RKPM succeeds in restoring consistency and completeness to SPH approximations up to a high order of choice at the problem boundaries, sparing the analyst of the need to resort to approaches like the mirror or ghost particles techniques mentioned in section 3.3. There is no verifiable manner, in fact, to measure the numerical accuracy of these latter ad-hoc methods.

In computational terms however, the improved consistency provided by RKPM does not come at a cheap cost. Clearly the need to assemble, and then invert system matrix $\mathbf{M}(\mathbf{x}, h)$ for every particle in order to obtain (A.11) is very absorbing, both in terms of time and computer resources. This is all the more true for simulations made in an Eulerian framework, where neighbours and connectivities, and hence RKPM system matrices $\mathbf{M}(\mathbf{x}, h)$, have to be recalculated for each particle at each time step.

BIBLIOGRAPHY

[1] M. Aguirre, A. Gil, J. Bonet, and A.A. Carreño. A Vertex Centred Finite Volume Jameson-Schmidt-Turkel Algorithm for a Mixed Conservation Formulation in Solid Dynamics. In: *Journal of Computational Physics* **259** (2014), pp. 672–699 (cit. on pp. 9, 15, 136, 137, 147, 222, 223, 245).

[2] M. Aguirre, A. Gil, J. Bonet, and C.H. Lee. An Upwind Vertex Centred Finite Volume Solver for Lagrangian Solid Dynamics. In: *Journal of Computational Physics* **300** (2015), pp. 387–422 (cit. on pp. 9, 15, 75, 245).

[3] C.D. Aliprantis and O. Burkinshaw. *Principles of Real Analysis*. 3rd edition. Academic Press, 1998 (cit. on pp. 66, 106).

[4] E. Anderson, Z. Bai, C. Bischof, S. Blackford, J. Demmel, J. Dongarra, J. Du Croz, A. Greenbaum, S. Hammarling, A. McKenney, and D. Sorensen. *Lapack Users' Guide*. 3rd edition. Society for Industrial and Applied Mathematics, 1999 (cit. on p. 154).

[5] J.D. Anderson. *Fundamentals of Aerodynamics*. McGraw-Hill, reprint, 1984 (cit. on p. 74).

[6] J.D. Anderson. *Computational Fluid Dynamics*. Computational Fluid Dynamics: The Basics with Applications. McGraw-Hill Education, 1995 (cit. on pp. 89, 142, 246).

[7] M. Arroyo and M. Ortiz. Local Maximum-Entropy Approximation Schemes: a Seamless Bridge between Finite Elements and Meshfree Methods. In: *International Journal for Numerical Methods in Engineering* **65**.13 (2006), pp. 2167–2202 (cit. on pp. 100, 250).

[8] S.N. Atluri and T. Zhu. A New Meshless Local Petrov-Galerkin (MLPG) Approach in Computational Mechanics. In: *Computational Mechanics* **22**.2 (1998), pp. 117–127 (cit. on pp. 100, 101).

[9] F. Aurenhammer. Voronoi Diagrams – a Survey of a Fundamental Geometric Data Structure. In: *ACM Computer Surveys (CSUR)* **23**.3 (1991), pp. 345–405 (cit. on p. 233).

[10] I. Babushka. The Finite Element Method with Lagrangian Multipliers. In: *Numerische Mathematik* **20**.3 (1973), pp. 179–192 (cit. on p. 6).

[11] I. Babushka and J.M. Melenk. The Partition of Unity Method. In: *International Journal for Numerical Methods in Engineering* **40**.4 (1997), pp. 727–758 (cit. on pp. 10, 101).

[12] M. Baker and J.L. Ericksen. Inequalities Restricting the Form of Stress Deformation Relations for Isotropic Elastic Solids and Reiner-Rivlin Fluids. In: *Journal of the Washington Academy of Sciences* **44**.2 (1954), pp. 33–35 (cit. on p. 37).

[13] J.M. Ball. Convexity Conditions and Existence Theorems in Nonlinear Elasticity. In: *Archive for Rational Mechanics and Analysis* **63**.4 (1977), pp. 337–403 (cit. on pp. 9, 34, 39, 40, 77, 246).

[14] J.M. Ball and Chen G-Q.G. Entropy and Convexity for Nonlinear Partial Differential Equations. In: *Philosophical Transactions of the Royal Society of London A: Mathematical, Physical and Engineering Sciences* **371**.2005 (2013) (cit. on p. 34).

[15] J.M. Ball and J.E. Marsden. Quasiconvexity at the Boundary, Positivity of the Second Variation and Elastic Stability. In: *Archive for Rational Mechanics and Analysis* **86** (1984), pp. 251–277 (cit. on p. 41).

[16] K.J. Bathe. *Finite Element Procedures*. 2nd edition. Prentice Hall, 2006 (cit. on pp. 4, 88, 245).

[17] R.C. Batra and C.H. Kim. Effect of Viscoplastic Flow Rules on the Initiation and Growth of Shear Bands at High Strain Rates. In: *Journal of the Mechanics and Physics of Solids* **38**.6 (1990), pp. 859–874 (cit. on p. 249).

[18] R.C. Batra and G.M. Zhang. Modified Smoothed Particle Hydrodynamics (MSPH) Basis Functions for Meshless Methods, and Their Application to Axisymmetric Taylor Impact Test. In: *Journal of Computational Physics* **227**.3 (2008), pp. 1962–1981 (cit. on p. 111).

[19] R.M. Beam and R.F. Warming. An Implicit Factored Scheme for the Compressible Navier-Stokes Equations. In: *AIAA Journal* **16**.4 (1978), pp. 393–402 (cit. on pp. 141, 142, 249).

[20] T. Belytschko, Y. Guo, W.K. Liu, and P.S. Xiao. A Unified Stability Analysis of Meshless Particle Methods. In: *International Journal for Numerical Methods in Engineering* **48**.9 (2000), pp. 1359–1400 (cit. on pp. 12, 13, 130).

[21] T. Belytschko, Y. Krongauz, J. Dolbow, and C. Gerlach. On the Completeness of Meshfree Particle Methods. In: *International Journal for Numerical Methods in Engineering* **43**.5 (1998), pp. 785–819 (cit. on p. 117).

[22] T. Belytschko, W.K. Liu, and B. Moran. *Nonlinear Finite Elements for Continua and Structures*. Wiley, 2000 (cit. on pp. 2, 33, 246).

[23] T. Belytschko, Y.Y. Lu, and L. Gu. Element-free Galerkin Methods. In: *International Journal for Numerical Methods in Engineering* **37**.2 (1994), pp. 229–256 (cit. on pp. 10, 100, 250).

[24] T. Belytschko, Y.Y. Lu, L. Gu, and M. Tabbara. Element-free Galerkin Methods for Static and Dynamic Fracture. In: *International Journal of Solids and Structures* **32**.17 (1995), pp. 2547–2570 (cit. on pp. 100, 250).

[25] W. Benz and E. Asphaug. Impact Simulations with Fracture. I. Method and Tests. In: *Icarus* **107**.1 (1994), pp. 98–116 (cit. on p. 11).

[26] W. Benz and E. Asphaug. Simulations of Brittle Solids Using Smooth Particle Hydrodynamics. In: *Computer Physics Communications* **87** (1995), pp. 253–265 (cit. on pp. 11, 250).

[27] J.S. Bergström and M.C. Boyce. Constitutive Modeling of the Large Strain Time-dependent Behavior of Elastomers. In: *Journal of the Mechanics and Physics of Solids* **46**.5 (1998), pp. 931–954 (cit. on p. 249).

[28] P. Betsch and P. Steinmann. Conservation Properties of a Time FE Method — part II: Time-stepping Schemes for Non-linear Elastodynamics. In: *International Journal for Numerical Methods in Engineering* **50**.8 (2001), pp. 1931–1955 (cit. on p. 147).

[29] D. Boffi, F. Brezzi, L. Gastaldi, L.F. Demkowicz, R.G. Duran, R.S. Falk, and M. Fortin. *Mixed Finite Elements, Compatibility Conditions, and Applications: Lectures given at the C.I.M.E. Summer School held in Cetraro, Italy, June 26 - July 1, 2006*. Lecture Notes in Mathematics. Springer Berlin Heidelberg, 2008 (cit. on p. 6).

[30] J. Bonet and A.J. Burton. A Simple Average Nodal Pressure Tetrahedral Element for Incompressible and Nearly Incompressible Dynamic Explicit Applications. In: *Communications in Numerical Methods in Engineering* **14**.5 (1998), pp. 437–449 (cit. on pp. 7, 223).

[31] J. Bonet, A. Gil, C.H. Lee, M. Aguirre, and R. Ortigosa. A First Order Hyperbolic Framework for Large Strain Computational Solid Dynamics. Part I: Total Lagrangian Isothermal Elasticity. In: *Computer Methods in Applied Mechanics and Engineering* **283** (2015), pp. 689–732 (cit. on pp. 9, 22, 61, 67, 245).

[32] J. Bonet, A. Gil, and R. Ortigosa. A Computational Framework for Polyconvex Large Strain Elasticity. In: *Computer Methods in Applied Mechanics and Engineering* **283** (2015), pp. 1061–1094 (cit. on pp. 9, 22, 61, 67, 132).

[33] J. Bonet, A. Gil, and R. Ortigosa. On a Tensor Cross Product based Formulation of Large Strain Solid Mechanics. In: *International Journal of Solids and Structures* **84** (2016), pp. 49–63 (cit. on pp. 9, 22, 64, 70, 71).

[34] J. Bonet and S. Kulasegaram. Correction and Stabilization of Smooth Particle Hydrodynamics Methods with Applications in Metal Forming Simulations. In: *International Journal for Numerical Methods in Engineering* **47**.6 (2000), pp. 1189–1214 (cit. on pp. 11, 13, 120, 127, 202, 206, 234).

[35] J. Bonet and S. Kulasegaram. Remarks on Tension Instability of Eulerian and Lagrangian Corrected Smooth Particle Hydrodynamics (CSPH) Methods. In: *International Journal for Numerical Methods in Engineering* **52**.11 (2001), pp. 1203–1220 (cit. on pp. 13, 112, 120, 130, 131, 202).

[36] J. Bonet and T.-S.L. Lok. Variational and Momentum Preservation Aspects of Smooth Particle Hydrodynamic Formulations. In: *Com-*

puter Methods in Applied Mechanics and Engineering **180**.1–2 (1999), pp. 97–115 (cit. on pp. 13, 112, 123, 125, 139, 146).

[37] J. Bonet, H. Marriott, and O. Hassan. An Averaged Nodal Deformation Gradient Linear Tetrahedral Element for Large Strain Explicit Dynamic Applications. In: *Communications in Numerical Methods in Engineering* **17**.8 (2001), pp. 551–561 (cit. on p. 7).

[38] J. Bonet and J. Peraire. An Alternating Digital Tree (ADT) Algorithm for 3D Geometric Searching and Intersection Problems. In: *International Journal for Numerical Methods in Engineering* **31**.1 (1991), pp. 1–17 (cit. on p. 155).

[39] J. Bonet and R.D. Wood. *Nonlinear Continuum Mechanics for Finite Element Analysis*. 2nd edition. Cambridge University Press, 2008 (cit. on pp. 2, 6, 28, 42, 44, 46, 49, 51, 52, 55, 56, 59, 61, 67, 71, 79, 80, 221).

[40] S. Bordas, T. Rabczuk, N.X. Hung, V.P. Nguyen, S. Natarajan, T. Bog, D.M. Quan, and V.H. Nguyen. Strain Smoothing in FEM and XFEM. In: *Computers and Structures* **88**.23 (2010), pp. 1419–1443 (cit. on p. 136).

[41] A.F. Bower. *Applied Mechanics of Solids*. CRC Press, 2009 (cit. on p. 5).

[42] M. Boyce and E.M. Arruda. Constitutive Models of Rubber Elasticity: a Review. In: *Rubber Chemistry and Technology* **73** (2000), pp. 504–523 (cit. on p. 42).

[43] S.P. Boyd and L. Vandenberghe. *Convex Optimization*. Cambridge University Press, 2004 (cit. on pp. 66, 127, 151).

[44] H. Brezis. *Functional Analysis, Sobolev Spaces and Partial Differential Equations*. Universitext. Springer New York, 2010 (cit. on p. 90).

[45] F. Brezzi. On the Existence, Uniqueness and Approximation of Saddle-point Problems Arising from Lagrangian Multipliers. In: *Revue Francaise d'Automatique, Informatique, Recherche Operationnelle. Analyse Numerique* **8**.R-2 (1974), pp. 129–151 (cit. on p. 6).

[46] T.J. Bridges and S. Reich. Numerical Methods for Hamiltonian PDEs. In: *Journal of Physics A: Mathematical and General* **39**.19 (2006), pp. 5287–5320 (cit. on p. 147).

[47] P.W. Bridgman. The Compression of Sixty-one Solid Substances to 25,000 kg/cm^2, Determined by a Rapid New Method. In: *Proceedings of the American Academy of Arts and Sciences* **76** (1945), pp. 9–24 (cit. on p. 48).

[48] D.E. Burton, T.C. Carney, N.R. Morgan, S.K. Sambasivan, and M.J. Shashkov. A Cell-centered Lagrangian Godunov-like Method for Solid Dynamics. In: *Computers and Fluids* **83** (2013), pp. 33–47 (cit. on p. 8).

[49] P. Cardiff, Z. Tukovic, P. De Jaeger, M. Clancy, and A. Ivankovic. A Lagrangian Cell-centred Finite Volume Method for Metal Forming Simulation. In: *International Journal for Numerical Methods in Engineering* **109**.13 (2016), pp. 1777–1803 (cit. on p. 8).

[50] J.S. Chen, M. Hillman, and S.W. Chi. Meshfree Methods: Progress Made after 20 Years. In: *Journal of Engineering Mechanics* **143**.4 (2017), p. 04017001 (cit. on pp. 10, 250).

[51] J.S. Chen, C. Pan, C.T. Wu, and W.K. Liu. Reproducing Kernel Particle Methods for Large Deformation Analysis of Non-linear Structures. In: *Computer Methods in Applied Mechanics and Engineering* **139**.1 (1996), pp. 195–227 (cit. on p. 256).

[52] J.S. Chen, C.T. Wu, S. Yoon, and Y. You. A Stabilized Conforming Nodal Integration for Galerkin Meshfree Methods. In: *International Journal for Numerical Methods in Engineering* **50**.2 (2001), pp. 435–466 (cit. on pp. 112, 136).

[53] J.S. Chen, S. Yoon, and C.T. Wu. Non-linear Version of Stabilized Conforming Nodal Integration for Galerkin Meshfree Methods. In: *International Journal for Numerical Methods in Engineering* **53**.12 (2002), pp. 2587–2615 (cit. on p. 112).

[54] B. Cockburn and C.W. Shu. The Runge-Kutta Discontinuous Galerkin Method for Conservation Laws V: Multidimensional Systems. In: *Journal of Computational Physics* **141**.2 (1998), pp. 199–224 (cit. on p. 144).

[55] J.A. Cottrell, T.J.R. Hughes, and Y. Bazilevs. *Isogeometric Analysis: toward Integration of CAD and FEA*. Wiley, 2009 (cit. on p. 4).

[56] R. Courant, K. Friedrichs, and H. Lewy. Über die Partiellen Differenzengleichungen der Mathematischen Physik. In: *Mathematische Annalen* **100** (1928), pp. 32–74 (cit. on p. 141).

[57] J. Crank and P. Nicolson. A Practical Method for Numerical Evaluation of Solutions of Partial Differential Equations of the Heat-Conduction Type. In: *Advances in Computational Mathematics* **6**.1 (1996), pp. 207–226 (cit. on p. 248).

[58] A.J.C. Crespo, J.M. Dominguez, B.D. Rogers, M. Gomez-Gesteira, S. Longshaw, R. Canelas, R. Vacondio, A. Barreiro, and O. Garcia-Feal. DualSPHysics: Open-source Parallel CFD Solver Based on Smoothed Particle Hydrodynamics (SPH). In: *Computer Physics Communications* **187** (2015), pp. 204–216 (cit. on p. 251).

[59] S.J Cummins and M. Rudman. An SPH Projection Method. In: *Journal of Computational Physics* **152**.2 (1999), pp. 584–607 (cit. on p. 116).

[60] A. Czekanski, N. El Abbasi, and S.A. Meguid. Optimal Time Integration Parameters for Elastodynamic Contact Problems. In: *Communications in Numerical Methods in Engineering* **17**.6 (2001), pp. 379–384 (cit. on p. 250).

[61] B. Dacorogna. *Introduction to the Calculus of Variations*. EBL-Schweitzer. Imperial College Press, 2004 (cit. on p. 39).

[62] C.M. Dafermos. *Hyperbolic Conservation Laws in Continuum Physics*. Grundlehren der mathematischen Wissenschaften. Springer Berlin Heidelberg, 1999 (cit. on pp. 9, 33, 34, 68, 72, 76, 246).

[63] C.M. Dafermos. Non-convex Entropies for Conservation Laws with Involutions. In: *Philosophical Transactions of the Royal Society of London A: Mathematical, Physical and Engineering Sciences* **371**.2005 (2013) (cit. on pp. 34, 36, 76).

[64] W. Dehnen and H. Aly. Improving Convergence in Smoothed Particle Hydrodynamics Simulations without Pairing Instability. In: *Monthly Notices of the Royal Astronomical Society* **425**.2 (2012), pp. 1068–1082 (cit. on pp. 13, 119–121).

[65] G.A. Dilts. Moving Least Squares Particle Hydrodynamics – I. Consistency and Stability. In: *International Journal for Numerical Methods in Engineering* **44**.8 (1999), pp. 1115–1155 (cit. on pp. 13, 112, 128).

[66] C.R. Dohrmann, M.W. Heinstein, J. Jung, S.W. Key, and W.R. Witkowski. Node-based Uniform Strain Elements for Three-node Triangular and Four-node Tetrahedral Meshes. In: *International Journal for Numerical Methods in Engineering* **47**.9 (2000), pp. 1549–1568 (cit. on p. 8).

[67] A. Dorfmann and A. Muhr, eds. *Constitutive Models for Rubber*. First european conference on constitutive models for rubber. Wien, Austria: A.A. Balkema Publishers, 1999 (cit. on p. 42).

[68] C.A. Duarte and J.T. Oden. H-p Clouds – an h-p Meshless Method. In: *Numerical Methods for Partial Differential Equations* **12**.6 (1996), pp. 673–705 (cit. on pp. 100, 101).

[69] F. Dunne and N. Petrinic. *Introduction to Computational Plasticity*. Oxford series on materials modelling. Oxford University Press, 2005 (cit. on p. 55).

[70] C.T. Dyka and R.P. Ingel. An Approach for Tension Instability in Smoothed Particle Hydrodynamics (SPH). In: *Computers and Structures* **57**.4 (1995), pp. 573–580 (cit. on pp. 13, 128).

[71] C.T. Dyka, P.W. Randles, and R.P. Ingel. Stress Points for Tension Instability in SPH. In: *International Journal for Numerical Methods in Engineering* **40**.13 (1998), pp. 2325–2341 (cit. on pp. 12, 13, 128).

[72] W. Elmer, J.S. Chen, M.A. Puso, and E. Taciroglu. A Stable, Mesh-free, Nodal Integration Method for Nearly Incompressible Solids. In: *Finite Elements in Analysis and Design* **51**.C (2012), pp. 81–85 (cit. on p. 136).

[73] A.C. Eringen. *Continuum Physics. Vol. II: Continuum Mechanics of Single-substance Bodies*. Academic Press, 1975 (cit. on p. 22).

[74] L.C. Evans. *Partial Differential Equations*. Graduate Studies in Mathematics. American Mathematical Society, 1998 (cit. on p. 34).

[75] L.C. Evans. A Survey of Entropy Methods for Partial Differential Equations. In: *Bulletin of the American Mathematical Society* **41**.4 (2004), pp. 409–439 (cit. on p. 34).

[76] E. Fermi. *Thermodynamics*. Dover books in physics and mathematical physics. Dover Publications, reprint, 1956 (cit. on pp. 31, 36).

[77] S. Fernandez-Mendez and A. Huerta. Imposing Essential Boundary Conditions in Mesh-Free Methods. In: *Computer Methods in Applied Mechanics and Engineering* **193**.12 (2004), pp. 1257–1275 (cit. on p. 250).

[78] D.A. Field. Laplacian Smoothing and Delaunay Triangulations. In: *Communications in Applied Numerical Methods* **4**.6 (1988), pp. 709–712 (cit. on p. 3).

[79] W.N. Findley, J.S. Lai, and K. Onaran. *Creep and Relaxation of Nonlinear Viscoelastic Materials: with an Introduction to Linear Viscoelasticity*. Dover Civil and Mechanical Engineering. Dover Publications, reprint, 1989 (cit. on p. 249).

[80] N.T. Frink. Recent Progress toward a Three-Dimensional Unstructured Navier-Stokes Flow Solver. In: *AIAA 32nd Aerospace Sciences Meeting*. Vol. 94-0061. 1994 (cit. on p. 137).

[81] D.A. Fulk and D.W. Quinn. An Analysis of 1-D Smoothed Particle Hydrodynamics Kernels. In: *Journal of Computational Physics* **126**.1 (1996), pp. 165–180 (cit. on pp. 117, 118).

[82] G.C. Ganzenmüller. An Hourglass Control Algorithm for Lagrangian Smooth Particle Hydrodynamics. In: *Computer Methods in Applied Mechanics and Engineering* **286** (2015), pp. 87–106 (cit. on pp. 12, 126).

[83] G.C. Ganzenmüller, S. Hiermaier, and M. May. On the Similarity of Meshless Discretizations of Peridynamics and Smooth-Particle Hydrodynamics. In: *ArXiv e-prints* (2014) (cit. on p. 250).

[84] G.W. Gear. *Numerical Initial Value Problems in Ordinary Differential Equations*. Automatic Computation. Prentice-Hall, 1971 (cit. on pp. 142, 143, 249).

[85] M.W. Gee, C.R. Dohrmann, S.W. Key, and W.A. Wall. A Uniform Nodal Strain Tetrahedron with Isochoric Stabilization. In: *International*

Journal for Numerical Methods in Engineering **78**.4 (2008), pp. 429–443 (cit. on p. 8).

[86] A. Gil, C.H. Lee, J. Bonet, and M. Aguirre. A Stabilised Petrov-Galerkin Formulation for Linear Tetrahedral Elements in Compressible, Nearly Incompressible and Truly Incompressible Fast Dynamics. In: *Computer Methods in Applied Mechanics and Engineering* **276** (2014), pp. 659–690 (cit. on pp. 9, 139, 245).

[87] A. Gil, C.H. Lee, J. Bonet, and R. Ortigosa. A First Order Hyperbolic Framework for Large Strain Computational Solid Dynamics. Part II: Total Lagrangian Compressible, Nearly Incompressible and Truly Incompressible Elasticity. In: *Computer Methods in Applied Mechanics and Engineering* **300** (2016), pp. 146–181 (cit. on pp. 9, 22, 245).

[88] R.A. Gingold and J.J. Monaghan. Smoothed Particle Hydrodynamics – Theory and Application to Non-Spherical Stars. In: *Monthly Notices of the Royal Astronomical Society* **181** (1977), pp. 375–389 (cit. on pp. 11, 99, 104).

[89] J. Glimm. Solutions in the Large for Nonlinear Hyperbolic Systems of Equations. In: *Communications on Pure and Applied Mathematics* **18** (1965), pp. 697–715 (cit. on p. 33).

[90] G.H. Golub and J.H. Welsch. Calculation of Gauss Quadrature Rules. In: *Mathematics of Computation* **23** (1968), pp. 221–230 (cit. on p. 95).

[91] M. Gomez-Gesteira, A.J.C. Crespo, B.D. Rogers, R.A. Dalrymple, J.M. Dominguez, and A. Barreiro. SPHysics – Development of a Free-Surface Fluid Solver – Part 2: Efficiency and Test Cases. In: *Computers and Geosciences* **48** (2012), pp. 300–307 (cit. on p. 251).

[92] M. Gomez-Gesteira, B.D. Rogers, A.J.C. Crespo, R.A. Dalrymple, M. Narayanaswamy, and J.M. Dominguez. SPHysics – Development of a Free-Surface Fluid Solver – Part 1: Theory and Formulations. In: *Computers and Geosciences* **48** (2012), pp. 289–299 (cit. on p. 251).

[93] O. Gonzalez. Exact Energy and Momentum Conserving Algorithms for General Models in Nonlinear Elasticity. In: *Computer Methods in Applied Mechanics and Engineering* **190**.13 (2000), pp. 1763–1783 (cit. on p. 147).

[94] O. Gonzalez and J.C. Simo. On the Stability of Symplectic and Energy-Momentum Algorithms for Non-linear Hamiltonian Systems with Symmetry. In: *Computer Methods in Applied Mechanics and Engineering* **134**.3 (1996), pp. 197–222 (cit. on p. 147).

[95] J.P. Gray, J.J. Monaghan, and R.P. Swift. SPH Elastic Dynamics. In: *Computer Methods in Applied Mechanics and Engineering* **190**.49–50 (2001), pp. 6641–6662 (cit. on pp. 12, 130).

[96] M. Gross, P. Betsch, and P. Steinmann. Conservation properties of a Time FE Method. Part IV: Higher Order Energy and Momentum Conserving Schemes. In: *International Journal for Numerical Methods in Engineering* **63**.13 (2005), pp. 1849–1897 (cit. on p. 147).

[97] M.E. Gurtin. *An Introduction to Continuum Mechanics*. Mathematics in Science and Engineering. Elsevier Science, 1982 (cit. on p. 28).

[98] J. Hadamard. Sur Quelques Questions de Calcul de Variations. In: *Bulletin de la Société Mathématique de France* **33** (1905), pp. 73–80 (cit. on pp. 40, 77).

[99] J. Haider, C.H. Lee, A. Gil, and J. Bonet. A First-Order Hyperbolic Framework for Large Strain Computational Solid Dynamics: an Upwind Cell Centred Total Lagrangian Scheme. In: *International Journal for Numerical Methods in Engineering* **109**.3 (2016), pp. 407–456 (cit. on pp. 9, 147, 148, 245).

[100] A. Harten. High Resolution Schemes for Hyperbolic Conservation Laws. In: *Journal of Computational Physics* **49**.3 (1983), pp. 357–393 (cit. on p. 144).

[101] A. Harten. On a Class of High Resolution Total-Variation-Stable Finite-Difference Schemes. In: *SIAM Journal on Numerical Analysis* **21**.1 (1984), pp. 1–23 (cit. on p. 144).

[102] S. Hartmann and P. Neff. Polyconvexity of Generalized Polynomial-type Hyperelastic Strain Energy Functions for Near–incompressibility. In: *International Journal of Solids and Structures* **40** (2003), pp. 2767–2791 (cit. on p. 42).

[103] D. Hibbitt, B. Karlsson, and P. Sorensen. *Abaqus Theory Manual: Version 6.15*. Dassault Systemes Simulia Corp., 2015 (cit. on pp. 3, 5).

[104] S. Hiermaier. *Structures Under Crash and Impact: Continuum Mechanics, Discretization and Experimental Characterization*. Springer US, 2007 (cit. on p. 114).

[105] F.B. Hildebrand. *Introduction to Numerical Analysis*. Dover books on advanced mathematics. Dover Publications, reprint, 1987 (cit. on pp. 95, 154).

[106] M. Hillman and J.S. Chen. An Accelerated, Convergent, and Stable Nodal Integration in Galerkin Meshfree Methods for Linear and Nonlinear Mechanics. In: *International Journal for Numerical Methods in Engineering* **107**.7 (2015), pp. 603–630 (cit. on p. 136).

[107] C. Hirsch. *Numerical Computation of Internal and External Flows: the Fundamentals of Computational Fluid Dynamics*. 2nd edition. Elsevier Science, 2007 (cit. on pp. 8, 27, 114, 136, 140, 142–144, 246).

[108] K. Hjelmstad. *Fundamentals of Structural Mechanics*. Springer, 2005 (cit. on p. 69).

[109] G.A. Holzapfel. *Nonlinear Solid Mechanics: A Continuum Approach for Engineering*. Wiley, 2000 (cit. on pp. 36, 41–43, 48, 52).

[110] B.P.B. Hoomans, J.A.M. Kuipers, W.J. Briels, and W.P.M. van Swaaij. Discrete Particle Simulation of Bubble and Slug Formation in a Two-dimensional Gas-fluidised Bed: A Hard-sphere Approach. In: *Chemical Engineering Science* **51**.1 (1996), pp. 99–118 (cit. on p. 225).

[111] F.Q. Hu, M.Y. Hussaini, and J.L. Manthey. Low-Dissipation and Low-Dispersion Runge-Kutta Schemes for Computational Acoustics. In: *Journal of Computational Physics* **124**.1 (1996), pp. 177–191 (cit. on p. 143).

[112] A. Huerta, Y. Vidal, and J. Bonet. Updated Lagrangian Formulation for Corrected Smooth Particle Hydrodynamics. In: *International Journal of Computational Methods* **3**.4 (2006), pp. 383–399 (cit. on p. 130).

[113] T.J.R. Hughes. Some Applications of Geometry in Continuum Mechanics. In: *Reports on Mathematical Physics* **12**.1 (1977), pp. 35–44 (cit. on p. 40).

[114] T.J.R. Hughes. Generalization of Selective Integration Procedures to Anisotropic and Nonlinear Media. In: *International Journal for Numerical Methods in Engineering* **15**.9 (1980), pp. 1413–1418 (cit. on p. 6).

[115] T.J.R. Hughes. *The Finite Element Method: Linear Static and Dynamic Finite Element Analysis*. Dover Civil and Mechanical Engineering. Dover Publications, reprint, 1987 (cit. on pp. 3, 6, 12, 39, 88, 89, 94, 95, 112, 148, 210, 245).

[116] T.J.R. Hughes. Multiscale Phenomena: Green's Functions, the Dirichlet-to-Neumann Formulation, Subgrid Scale Models, Bubbles and the Origins of Stabilized Methods. In: *Computer Methods in Applied Mechanics and Engineering* **127**.1 (1995), pp. 387–401 (cit. on p. 7).

[117] W. Hundsdorfer and J.G. Verwer. *Numerical Solution of Time–Dependent Advection–Diffusion–Reaction Equations*. Springer Series in Computational Mathematics. Springer Berlin Heidelberg, 2003 (cit. on p. 142).

[118] A. Iserles. *A First Course in the Numerical Analysis of Differential Equations*. 2nd edition. Cambridge Texts in Applied Mathematics. Cambridge University Press, 2009 (cit. on p. 89).

[119] A. Jameson. Solution of the Euler Equations for Two Dimensional Transonic Flow by a Multigrid Method. In: *Applied Mathematics and Computation* **13**.3 (1983), pp. 327–355 (cit. on pp. 144, 247).

[120] A. Jameson. Analysis and Design of Numerical Schemes for Gas Dynamics, 1: Artificial Diffusion, Upwind Biasing, Limiters and Their Effect on Accuracy and Multigrid Convergence. In: *International Journal of Computational Fluid Dynamics* **4**.3–4 (1995), pp. 171–218 (cit. on p. 144).

[121] A. Jameson, T. Baker, and N. Weatherill. Calculation of Inviscid Transonic Flow over a Complete Aircraft. In: *AIAA 24th Aerospace Sciences Meeting*. 86-0103. 1986 (cit. on pp. 136, 137, 139).

[122] A. Jameson, W. Schmidt, and E. Turkel. Solutions of the Euler Equations by Finite Volume Methods Using Runge-Kutta Time-Stepping Schemes. In: *AIAA 14th Fluid and Plasma Dynamic Conference*. 81-1259. 1981 (cit. on pp. 14, 136, 144).

[123] E.T. Jaynes. Information Theory and Statistical Mechanics. In: *Physical Review* **106**.4 (1957), pp. 620–630 (cit. on p. 100).

[124] F. John. Blow up of Solutions of Nonlinear Wave Equations in Three Space Dimensions. In: *Manuscripta Mathematica* **28**.1 (1979), pp. 235–268 (cit. on p. 33).

[125] C. Johnson. *Numerical Solution of Partial Differential Equations by the Finite Element Method*. Dover Books on Mathematics Series. Dover Publications, reprint, 1987 (cit. on pp. 39, 88, 94).

[126] G.R. Johnson and S.R. Beissel. Normalized Smoothing Functions for SPH Impact Computations. In: *International Journal for Numerical Methods in Engineering* **39**.16 (1996), pp. 2725–2741 (cit. on p. 13).

[127] C. Kane, J.E. Marsden, and M. Ortiz. Symplectic-Energy-Momentum Preserving Variational Integrators. In: *Journal of Mathematical Physics* **40**.7 (1999), pp. 3353–3371 (cit. on p. 147).

[128] E.J. Kansa. Multiquadrics – A Scattered Data Approximation Scheme with Applications to Computational Fluid-Dynamics – I Surface Approximations and Partial Derivative Estimates. In: *Computers and Mathematics with Applications* **19**.8 (1990), pp. 127–145 (cit. on p. 99).

[129] I.A. Karim, C.H. Lee, A. Gil, and J. Bonet. A Two-step Taylor-Galerkin Formulation for Fast Dynamics. In: *Engineering Computations* **31**.3 (2014), pp. 366–387 (cit. on p. 9).

[130] T. Kato. Quasi-linear Equations of Evolution with Applications to Partial Differential Equations. In: *Spectral Theory and Differential Equations*. Ed. by W.N. Everitt. Lecture Notes in Mathematics. Springer Berlin Heidelberg, 1975, pp. 25–70 (cit. on p. 33).

[131] N. Kikuchi and J.T. Oden. *Contact Problems in Elasticity: A Study of Variational Inequalities and Finite Element Methods*. Studies in Applied Mathematics. Society for Industrial and Applied Mathematics, 1988 (cit. on p. 250).

[132] G. Kluth and B. Despres. Discretization of Hyperelasticity on Unstructured Mesh with a Cell-centered Lagrangian Scheme. In: *Journal of Computational Physics* **229**.24 (2010), pp. 9092–9118 (cit. on p. 8).

[133] R.J. Knops and L.E. Payne. On Potential Wells and Stability in Nonlinear Elasticity. In: *Mathematical Proceedings of the Cambridge Philosophical Society* **84**.1 (1978), pp. 177–190 (cit. on p. 41).

[134] D. Komatitsch, J.P. Vilotte, R. Vai, J.M. Castillo-Covarrubias, and F.J. Sanchez-Sesma. The Spectral Element Method for Elastic Wave Equations - Application to 2-D and 3-D Seismic Problems. In: *International Journal for Numerical Methods in Engineering* **45**.9 (1999), pp. 1139–1164 (cit. on p. 147).

[135] S.K. Lahiri, J. Bonet, J. Peraire, and L. Casals. A Variationally Consistent Fractional Time-step Integration Method for Incompressible and Nearly Incompressible Lagrangian Dynamics. In: *International Journal for Numerical Methods in Engineering* **63**.10 (2005), pp. 1371–1395 (cit. on p. 193).

[136] J.D. Lambert. *Computational Methods in Ordinary Differential Equations*. Introductory Mathematics for Scientists and Engineers. Wiley, 1973 (cit. on p. 142).

[137] P. Lancaster and K. Salkauskas. Surfaces Generated by Moving Least Squares Methods. In: *Mathematics of Computation* **37**.155 (1981), pp. 141–158 (cit. on p. 100).

[138] L.D. Landau. *Theory of Elasticity*. 3rd English edition. Vol. 7. Course of Theoretical Physics series. Butterworth Heinemann, 1986 (cit. on pp. 41, 69).

[139] C.B. Laney. *Computational Gasdynamics*. Cambridge University Press, 1998 (cit. on pp. 8, 26, 34, 89, 114, 140, 142, 144, 246).

[140] P.D. Lax. Development of Singularities of Solutions of Nonlinear Hyperbolic Partial Differential Equations. In: *Journal of Mathematical Physics* **5** (1964), pp. 611–13 (cit. on p. 34).

[141] P.D. Lax and B. Wendroff. Systems of Conservation Laws. In: *Communications on Pure and Applied Mathematics* **13**.2 (1960), pp. 217–237 (cit. on p. 140).

[142] K. Ho-Le. Finite Element Mesh Generation Methods: a Review and Classification. In: *Computer-Aided Design* **20**.1 (1988), pp. 27–38 (cit. on p. 3).

[143] C.H. Lee, A. Gil, and J. Bonet. Development of a Cell Centred Upwind Finite Volume Algorithm for a New Conservation Law Formulation in Structural Dynamics. In: *Computers and Structures* **118** (2013), pp. 13–38 (cit. on pp. 9, 69, 147, 245).

[144] C.H. Lee, A. Gil, and J. Bonet. Development of a Stabilised Petrov-Galerkin Formulation for Conservation Laws in Lagrangian Fast Solid Dynamics. In: *Computer Methods in Applied Mechanics and Engineering* **268** (2014), pp. 40–64 (cit. on pp. 9, 245).

[145] C.H. Lee, A. Gil, G. Greto, S. Kulasegaram, and J. Bonet. A New JST Smooth Particle Hydrodynamics Algorithm for Large Strain Explicit Fast Dynamics. In: *Computer Methods in Applied Mechanics and Engineering* **311** (2016), pp. 71–111 (cit. on pp. 9, 127, 139, 148, 193, 245).

[146] C.H. Lee, A. Gil, O.I. Hassan, J. Bonet, and S. Kulasegaram. A Variationally Consistent Streamline Upwind Petrov-Galerkin Smooth Particle Hydrodynamics Algorithm for Large Strain Solid Dynamics. In: *Computer Methods in Applied Mechanics and Engineering* **318** (2017), pp. 514–536 (cit. on pp. 9, 148, 245, 247).

[147] R.J. LeVeque. *Numerical Methods for Conservation Laws*. 2nd edition. Lectures in Mathematics. Birkhäuser, 1992 (cit. on pp. 8, 26, 140).

[148] T. Levi-Civita and E. Persico. *Lezioni di Calcolo Differenziale Assoluto*. A. Stock, 1925 (cit. on pp. 22, 42, 66, 67).

[149] A. Lew, J.E. Marsden, M. Ortiz, and M. West. Asynchronous Variational Integrators. In: *Archive for Rational Mechanics and Analysis* **167**.2 (2003), pp. 85–146 (cit. on p. 147).

[150] A. Lew, J.E. Marsden, M. Ortiz, and M. West. Variational Time Integrators. In: *International Journal for Numerical Methods in Engineering* **60**.1 (2004), pp. 153–212 (cit. on p. 147).

[151] H. Li and S.S. Mulay. *Meshless Methods and Their Numerical Properties*. Taylor & Francis, 2013 (cit. on pp. 10, 89).

[152] S. Li and W.K. Liu. Moving Least-Square Reproducing Kernel Method Part II: Fourier Analysis. In: *Computer Methods in Applied Mechanics and Engineering* **139**.1 (1996), pp. 159–193 (cit. on pp. 120, 123).

[153] S. Li and W.K. Liu. *Meshfree Particle Methods*. Springer Berlin Heidelberg, 2007 (cit. on pp. 10–12, 105, 111, 114, 115).

[154] L.D. Libersky, A.G. Petschek, T.C. Carney, J.R. Hipp, and F.A. Allahdadi. High Strain Lagrangian Hydrodynamics a Three-Dimensional SPH Code for Dynamic Material Response. In: *Journal of Computational Physics* **109**.1 (1993), pp. 67–75 (cit. on p. 105).

[155] L.D. Libersky, P.W. Randles, T.C. Carney, and D.L. Dickinson. Recent Improvements in SPH Modeling of Hypervelocity Impact. In: *International Journal of Impact Engineering* **20**.6 (1997), pp. 525–532 (cit. on p. 114).

[156] T. Liszka and J. Orkisz. The Finite Difference Method at Arbitrary Irregular Grids and Its Application in Applied Mechanics. In: *Computers and Structures* **11**.1 (1980). Special Issue – Computational Methods in Nonlinear Mechanics, pp. 83–95 (cit. on p. 99).

[157] G.R. Liu. A Generalized Gradient Smoothing Technique and the Smoothed Bilinear Form for Galerkin Formulation of a Wide Class of Computational Methods. In: *International Journal of Computational Methods* **5**.2 (2008), pp. 199–236 (cit. on p. 136).

[158] G.R. Liu. *Meshfree Methods: Moving Beyond the Finite Element Method*. 2nd edition. CRC Press, 2009 (cit. on pp. 10, 106–108).

[159] W.K. Liu, J. Adee, S. Jun, and T. Belytschko. Reproducing Kernel Particle Methods for Elastic and Plastic Problems. In: *Advanced Computational Methods for Material Modeling*. Ed. by D.A. Siginer, W.E. VanArsdale, C.M. Altan, and A.N. Alexandrou. Vol. 180. Publ. by ASME, 1993, pp. 175–189 (cit. on pp. 13, 253, 256).

[160] W.K. Liu, Y. Chen, C.T. Chang, and T. Belytschko. Advances in Multiple Scale Kernel Particle Methods. In: *Computational Mechanics* **18**.2 (1996), pp. 73–111 (cit. on pp. 254, 256).

[161] W.K. Liu, Y. Chen, S. Jun, J.S. Chen, T. Belytschko, C. Pan, R.A. Uras, and C.T. Chang. Overview and Applications of the Reproducing Kernel Particle Methods. In: *Archives of Computational Methods in Engineering* **3**.1 (1996), pp. 3–80 (cit. on p. 256).

[162] W.K. Liu, S. Jun, S. Li, J. Adee, and T. Belytschko. Reproducing Kernel Particle Methods for Structural Dynamics. In: *International Journal for Numerical Methods in Engineering* **38**.10 (1995), pp. 1655–1679 (cit. on pp. 112, 256).

[163] W.K. Liu, S. Jun, and Y.F. Zhang. Reproducing Kernel Particle Methods. In: *International Journal for Numerical Methods in Fluids* **20**.8–9 (1995), pp. 1081–1106 (cit. on pp. 13, 117, 253, 256).

[164] W.K. Liu, S. Li, and T. Belytschko. Moving Least-Square Reproducing Kernel Methods (I) Methodology and Convergence. In: *Computer Methods in Applied Mechanics and Engineering* **143**.1 (1997), pp. 113–154 (cit. on p. 123).

[165] J. Lubliner. *Plasticity Theory*. 3rd edition. Dover Books on Engineering. Dover Publications, 2008 (cit. on pp. 56, 69).

[166] L.B. Lucy. A Numerical Approach to the Testing of the Fission Hypothesis. In: *Astronomical Journal* **82** (1977), pp. 1013–1024 (cit. on pp. 11, 99, 104).

[167] R.W. MacCormack. The Effect of Viscosity in Hypervelocity Impact Cratering. In: *AIAA 4th Aerodynamic Testing Conference*. 69-0354. 1969 (cit. on p. 140).

[168] D.S. Malkus. A Finite Element Displacement Model Valid for Any Value of the Compressibility. In: *International Journal of Solids and Structures* **12**.11 (1976), pp. 731–738 (cit. on p. 6).

[169] D.S. Malkus and T.J.R. Hughes. Mixed Finite Element Methods – Reduced and Selective Integration Techniques: a Unification of Concepts. In: *Computer Methods in Applied Mechanics and Engineering* **15**.1 (1978), pp. 63–81 (cit. on p. 6).

[170] A. Mani, J. Larsson, and P. Moin. Suitability of Artificial Bulk Viscosity for Large-Eddy Simulation of Turbulent Flows with Shocks. In: *Journal of Computational Physics* **228**.19 (2009), pp. 7368–7374 (cit. on p. 114).

[171] G. Marckmann and E. Verron. Comparison of Hyperelastic Models for Rubber-like Materials. In: *Rubber Chemistry and Technology* **79** (2006), pp. 835–858 (cit. on p. 42).

[172] J.E. Marsden and T.J.R. Hughes. *Mathematical Foundations of Elasticity*. Dover Civil and Mechanical Engineering. Dover Publications, reprint, 1983 (cit. on pp. 33, 34, 39–41, 76, 77, 246).

[173] J.E. Marsden and A. Tromba. *Vector Calculus*. W.H. Freeman, 2003 (cit. on p. 71).

[174] M. Matsumoto and T. Nishimura. Mersenne Twister: A 623-dimensionally Equidistributed Uniform Pseudo-random Number Generator. In: *ACM Transactions on Modeling and Computer Simulation (TOMACS)* **8**.1 (1998), pp. 3–30 (cit. on p. 233).

[175] R. von Mises. Mechanik der festen Körper im plastisch–deformablen Zustand. In: *Nachrichten von der Gesellschaft der Wissenschaften zu Göttingen, Mathematisch-Physikalische Klasse* (1913), pp. 582–592 (cit. on p. 56).

[176] J.J. Monaghan. Why Particle Methods Work. In: *SIAM Journal on Scientific and Statistical Computing* **3**.4 (1982), pp. 422–433 (cit. on p. 105).

[177] J.J. Monaghan. An Introduction to SPH. In: *Computer Physics Communications* **48**.1 (1988), pp. 89–96 (cit. on pp. 11, 12, 105, 125).

[178] J.J. Monaghan. Smoothed Particle Hydrodynamics. In: *Annual Review of Astronomy and Astrophysics* **30**.1 (1992), pp. 543–574 (cit. on pp. 11, 119, 125).

[179] J.J. Monaghan. Simulating Free Surface Flows with SPH. In: *Annual Review of Astronomy and Astrophysics* **110** (1994), pp. 399–406 (cit. on pp. 109, 116).

[180] J.J. Monaghan. SPH without a Tensile Instability. In: *Journal of Computational Physics* **159**.2 (2000), pp. 290–311 (cit. on pp. 13, 130).

[181] J.J. Monaghan. Smoothed Particle Hydrodynamics. In: *Reports on Progress in Physics* **68** (2005), pp. 1703–1759 (cit. on pp. 11, 246).

[182] J.J. Monaghan and R.A. Gingold. Shock Simulation by the Particle Method SPH. In: *Journal of Computational Physics* **52**.2 (1983), pp. 374–389 (cit. on pp. 114, 115, 136).

[183] J.J. Monaghan and J.C. Lattanzio. A Refined Particle Method for Astrophysical Problems. In: *Astronomy and Astrophysics* **149**.1 (1985), pp. 135–143 (cit. on p. 119).

[184] J.J. Monaghan and H. Pongracic. Artificial Viscosity for Particle Methods. In: *Applied Numerical Mathematics* **1**.3 (1985), pp. 187–194 (cit. on pp. 12, 14, 15).

[185] M. Mooney. A Theory of Large Elastic Deformation. In: *Journal of Applied Physics* **11** (1940), pp. 582–592 (cit. on p. 43).

[186] J.P. Morris. A Study of the Stability Properties of Smooth Particle Hydrodynamics. In: *Publications Astronomical Society of Australia* **13**.1 (1996), pp. 97–102 (cit. on p. 128).

[187] J.P. Morris, P.J. Fox, and Y. Zhu. Modeling Low Reynolds Number Incompressible Flows Using SPH. In: *Journal of Computational Physics* **136**.1 (1997), pp. 214–226 (cit. on p. 120).

[188] J.C. Nagtegaal, D.M. Parks, and J.R. Rice. On Numerically Accurate Finite Element Solutions in the Fully Plastic Range. In: *Computer Methods in Applied Mechanics and Engineering* **4**.2 (1974), pp. 153–177 (cit. on p. 6).

[189] B. Nayroles, G. Touzot, and P. Villon. Generalizing the Finite Element Method: Diffuse Approximation and Diffuse Elements. In: *Computational Mechanics* **10**.5 (1992), pp. 307–318 (cit. on p. 100).

[190] V.P. Nguyen, T. Rabczuk, S. Bordas, and M. Duflot. Meshless Methods: A Review and Computer Implementation Aspects. In: *Mathematics and Computers in Simulation* **79**.3 (2008), pp. 763–813 (cit. on pp. 10, 11).

[191] E. Noether. Invariante Variationsprobleme. In: *Nachrichten von der Gesellschaft der Wissenschaften zu Göttingen, Mathematisch-Physikalische Klasse* (1918), pp. 235–257 (cit. on p. 68).

[192] G.G. O'Brien, M.A. Hyman, and S. Kaplan. A Study of the Numerical Solution of Partial Differential Equations. In: *Journal of Mathematics and Physics* **29**.1–4 (1951), pp. 223–251 (cit. on p. 128).

[193] J.T. Oden and E.B. Pires. Nonlocal and Nonlinear Friction Laws and Variational Principles for Contact Problems in Elasticity. In: *Journal of Applied Mechanics* **50** (1983), pp. 67–73 (cit. on p. 250).

[194] R.W. Ogden. Large Deformation Isotropic Elasticity: on the Correlation of Theory and Experiment for Compressible Rubberlike Solids. In: *Proceedings of the Royal Society of London A: Mathematical, Physical and Engineering Sciences* **328**.1575 (1972), pp. 567–583 (cit. on p. 48).

[195] R.W. Ogden. Large Deformation Isotropic Elasticity – on the Correlation of Theory and Experiment for Incompressible Rubberlike Solids. In: *Proceedings of the Royal Society of London A: Mathematical, Physical and Engineering Sciences* **326**.1567 (1972), pp. 565–584 (cit. on p. 46).

[196] R.W. Ogden. *Non-Linear Elastic Deformations*. Dover Civil and Mechanical Engineering. Dover Publications, reprint, 1984 (cit. on pp. 2, 29, 42, 43, 83).

[197] B.J. Olson and S.K. Lele. Directional Artificial Bulk Viscosity for Shock Capturing on High Aspect Ratio Grids. In: *Computational Science and Discovery* **5**.1 (2012), p. 014008 (cit. on p. 114).

[198] P.J. Olver. Conservation Laws in Elasticity. I. General Results. In: *Archive for Rational Mechanics and Analysis* **85** (1984), pp. 111–129 (cit. on p. 68).

[199] P.J. Olver. Conservation Laws in Elasticity. II. Linear Homogeneous Isotropic Elastostatics. In: *Archive for Rational Mechanics and Analysis* **85** (1984), pp. 131–160 (cit. on p. 68).

[200] P.J. Olver. *Applications of Lie Groups to Differential Equations*. Graduate texts in mathematics. Springer New York, 1986 (cit. on p. 68).

[201] P.J. Olver. Conservation Laws in Continuum Mechanics. In: *Non-Classical Continuum Mechanics: Proceedings of the London Mathematical Society Symposium, Durham, July 1986*. Ed. by R.J. Knops, A.A. Lacey, and London Mathematical Society. Lecture note series 122. Cambridge University Press, 1987, pp. 96–107 (cit. on p. 68).

[202] P.J. Olver. Conservation Laws in Elasticity. III. Planar Linear Anisotropic Elastostatics. In: *Archive for Rational Mechanics and Analysis* **102** (1988), pp. 167–181 (cit. on p. 68).

[203] E. Onate, S. Idelsohn, O.C. Zienkiewicz, and R.L. Taylor. A Finite Point Method In Computational Mechanics. Applications to Convective Transport and Fluid Flow. In: *International Journal for Numerical Methods in Engineering* **39**.22 (1996), pp. 3839–3866 (cit. on p. 99).

[204] A. Ortiz, M.A. Puso, and N. Sukumar. Maximum-Entropy Meshfree Method for Incompressible Media Problems. In: *Finite Elements in Analysis and Design* **47**.6 (2011), pp. 572–585 (cit. on p. 250).

[205] J.M. Owen. ASPH Modeling of Material Damage and Failure. In: 5^{th} *International SPHERIC SPH Workshop*. 2010 (cit. on p. 250).

[206] S. Pirozzoli. Numerical Methods for High-Speed Flows. In: *Annual Review of Fluid Mechanics* **43**.1 (2011), pp. 163–194 (cit. on p. 8).

[207] M.A. Puso. A Highly Efficient Enhanced Assumed Strain Physically Stabilized Hexahedral Element. In: *International Journal for Numerical Methods in Engineering* **49**.8 (2000), pp. 1029–1064 (cit. on p. 136).

[208] M.A. Puso, J.S. Chen, E. Zywicz, and W. Elmer. Meshfree and Finite Element Nodal Integration Methods. In: *International Journal for Numerical Methods in Engineering* **74** (2008), pp. 416–446 (cit. on pp. 7, 112, 136).

[209] M.A. Puso and J. Solberg. A Stabilized Nodally Integrated Tetrahedral. In: *International Journal for Numerical Methods in Engineering* **67**.6 (2006), pp. 841–867 (cit. on p. 8).

[210] J. Ramboer, T. Broeckhoven, S. Smirnov, and C. Lacor. Optimization of Time Integration Schemes Coupled to Spatial Discretization for Use in CAA Applications. In: *Journal of Computational Physics* **213**.2 (2006), pp. 777–802 (cit. on p. 143).

[211] P.W. Randles and L.D. Libersky. Smoothed Particle Hydrodynamics: Some Recent Improvements and Applications. In: *Computer Methods in Applied Mechanics and Engineering* **139**.1–4 (1996), pp. 375–408 (cit. on pp. 13, 117, 202).

[212] P.W. Randles and L.D. Libersky. Normalized SPH with Stress Points. In: *International Journal for Numerical Methods in Engineering* **48**.10 (2000), pp. 1445–1462 (cit. on p. 12).

[213] O. Reynolds, A.W. Brightmore, and W.H. Moorby. *Papers on Mechanical and Physical Subjects*. Papers on Mechanical and Physical Subjects vol. 3. Cambridge University Press, 1903 (cit. on p. 71).

[214] L. Ridgway Scott. *Numerical Analysis*. Princeton University Press, 2011 (cit. on p. 95).

[215] M.C. Rivara. New Longest-Edge Algorithms for the Refinement and/or Improvement of Unstructured Triangulations. In: *International Journal for Numerical Methods in Engineering* **40**.18 (1997), pp. 3313–3324 (cit. on p. 3).

[216] R.S. Rivlin. Large Elastic Deformations of Isotropic Materials. IV. Further Developments of the General Theory. In: *Philosophical Transactions of the Royal Society of London A: Mathematical, Physical and Engineering Sciences* **241**.835 (1948), pp. 379–397 (cit. on p. 43).

[217] A. Rosochowski and L. Olejnik. Numerical and Physical Modelling of Plastic Deformation in 2-turn Equal Channel Angular Extrusion. In: *Journal of Materials Processing Technology* **125–126** (2002), pp. 309–316 (cit. on pp. 224–226, 230–233).

[218] S. Rossi, N. Abboud, and G. Scovazzi. Implicit Finite Incompressible Elastodynamics with Linear Finite Elements: A Stabilized Method in Rate Form. In: *Computer Methods in Applied Mechanics and Engineering* **311** (2016), pp. 208–249 (cit. on p. 7).

[219] J. Schröder and P. Neff. Invariant Formulation of Hyperelastic Transverse Isotropy based on Polyconvex Free Energy Functions. In: *International Journal of Solids and Structures* **40**.2 (2003), pp. 401–445 (cit. on pp. 41, 42, 46).

[220] W.J. Schroeder and M.S. Shephard. A Combined Octree/Delaunay Method for Fully Automatic 3-D Mesh Generation. In: *International Journal for Numerical Methods in Engineering* **29**.1 (1990), pp. 37–55 (cit. on p. 3).

[221] G. Scovazzi. Lagrangian Shock Hydrodynamics on Tetrahedral Meshes: A Stable and Accurate Variational Multiscale Approach. In: *Journal of Computational Physics* **231**.24 (2012), pp. 8029–8069 (cit. on p. 7).

[222] G. Scovazzi, B. Carnes, X. Zeng, and S. Rossi. A Simple, Stable, and Accurate Linear Tetrahedral Finite Element for Transient, Nearly, and Fully Incompressible Solid Dynamics: a Dynamic Variational Multiscale Approach. In: *International Journal for Numerical Methods in Engineering* **106**.10 (2015), pp. 799–839 (cit. on p. 7).

[223] G. Scovazzi, M.A. Christon, T.J.R. Hughes, and J.N. Shadid. Stabilized Shock Hydrodynamics: I. A Lagrangian Method. In: *Computer Methods in Applied Mechanics and Engineering* **196**.4 (2007), pp. 923–966 (cit. on p. 7).

[224] G. Scovazzi, J.N. Shadid, E. Love, and W.J. Rider. A Conservative Nodal Variational Multiscale Method for Lagrangian Shock Hydrodynamics. In: *Computer Methods in Applied Mechanics and Engineering* **199**.49 (2010), pp. 3059–3100 (cit. on p. 7).

[225] G. Scovazzi, T. Song, and X. Zeng. A Velocity/Stress Mixed Stabilized Nodal Finite Element for Elastodynamics: Analysis and Computations with Strongly and Weakly Enforced Boundary Conditions. In: *Computer Methods in Applied Mechanics and Engineering* **325** (2017), pp. 532–576 (cit. on p. 7).

[226] V.M. Segal. Materials Processing by Simple Shear. In: *Materials Science and Engineering A* **197**.2 (1995), pp. 157–164 (cit. on p. 224).

[227] J. Serrin. Mathematical Principles of Classical Fluid Mechanics. In: *Fluid Dynamics I / Strömungsmechanik I*. Ed. by C. Truesdell. Springer Berlin Heidelberg, 1959, pp. 125–263 (cit. on p. 33).

[228] C.E. Shannon. A Mathematical Theory of Communication. In: *Bell System Technical Journal* **27**.3 (1948), pp. 379–423 (cit. on p. 100).

[229] C.W. Shu and S. Osher. Efficient Implementation of Essentially non-Oscillatory Shock-Capturing Schemes. In: *Journal of Computational Physics* **77**.2 (1988), pp. 439–471 (cit. on p. 144).

[230] T.C. Sideris and B. Thomases. Global Existence for Three-dimensional Incompressible Isotropic Elastodynamics via the Incompressible Limit. In: *Communications on Pure and Applied Mathematics* **58**.6 (2005), pp. 750–788 (cit. on p. 41).

[231] T.C. Sideris and B. Thomases. Global Existence for Three-dimensional Incompressible Isotropic Elastodynamics. In: *Communications on Pure and Applied Mathematics* **60**.12 (2007), pp. 1707–1730 (cit. on pp. 9, 41).

[232] M. Silhavý. *The Mechanics and Thermodynamics of Continuous Media*. Theoretical and Mathematical Physics. Springer Berlin Heidelberg, 2013 (cit. on p. 42).

[233] J.G. Simmonds. *A Brief on Tensor Analysis*. 2nd edition. Undergraduate Texts in Mathematics. Springer New York, 2012 (cit. on p. 30).

[234] J.C. Simo. Algorithms for Static and Dynamic Multiplicative Plasticity that Preserve the Classical Return Mapping Schemes of the Infinitesimal Theory. In: *Computer Methods in Applied Mechanics and Engineering* **99**.1 (1992), pp. 61–112 (cit. on p. 147).

[235] J.C. Simo and T.J.R. Hughes. On the Variational Foundations of Assumed Strain Methods. In: *Journal of Applied Mechanics* **53**.1 (1986), pp. 51–54 (cit. on p. 6).

[236] J.C. Simo and T.J.R. Hughes. *Computational Inelasticity*. Interdisciplinary Applied Mathematics. Springer New York, 2000 (cit. on pp. 55, 59, 249).

[237] J.C. Simo and N. Tarnow. The Discrete Energy-Momentum Method. Conserving Algorithms for Nonlinear Elastodynamics. In: *Zeitschrift für angewandte Mathematik und Physik* **43**.5 (1992), pp. 757–792 (cit. on p. 146).

[238] J.C. Simo and N. Tarnow. A New Energy and Momentum Conserving Algorithm for the Non-linear Dynamics of Shells. In: *International Journal for Numerical Methods in Engineering* **37**.15 (1994), pp. 2527–2549 (cit. on p. 147).

[239] J.C. Simo, N. Tarnow, and K.K. Wong. Exact Energy-Momentum Conserving Algorithms and Symplectic Schemes for Nonlinear Dynamics. In: *Computer Methods in Applied Mechanics and Engineering* **100**.1 (1992), pp. 63–116 (cit. on p. 146).

[240] E.A. de Souza Neto, F.M. Andrade Pires, and D.R.J. Owen. F-bar-based Linear Triangles and Tetrahedra for Finite Strain Analysis of

Nearly Incompressible Solids. Part I: Formulation and Benchmarking. In: *International Journal for Numerical Methods in Engineering* **62**.3 (2005), pp. 353–383 (cit. on p. 7).

[241] E.A. de Souza Neto, D. Peric, M. Dutko, and D.R.J. Owen. Design of Simple Low Order Finite Elements for Large Strain Analysis of Nearly Incompressible Solids. In: *International Journal of Solids and Structures* **33**.20 (1996), pp. 3277–3296 (cit. on p. 7).

[242] A.J.M. Spencer. *Continuum Mechanics*. Longman Mathematical Texts Series. Addison-Wesley Longman, Limited, 1980 (cit. on pp. 29, 83).

[243] V. Springel. Smoothed Particle Hydrodynamics in Astrophysics. In: *Annual Review of Astronomy and Astrophysics* **48** (2010), pp. 391–430 (cit. on pp. 11, 136, 246).

[244] P. Steinmann, M. Hossain, and G. Possart. Hyperelastic Models for Rubber-like Materials: Consistent Tangent Operators and Suitability for Treloar's Data. In: *Archive of Applied Mechanics* **82** (2012), pp. 1183–1217 (cit. on pp. 42, 45, 46).

[245] F. Stoppelli. Un Teorema di Esistenza ed Unicità Relativo alle Equazioni dell'Elastostatica Isoterma per Deformazioni Finite. In: *Ricerche di Matematica* **3** (1954), pp. 247–267 (cit. on p. 40).

[246] A.H. Stroud and D. Secrest. *Gaussian Quadrature Formulas*. Prentice-Hall Series in Automatic Computation. Prentice-Hall, 1966 (cit. on p. 95).

[247] N. Sukumar. Construction of Polygonal Interpolants: a Maximum Entropy Approach. In: *International Journal for Numerical Methods in Engineering* **61**.12 (2004), pp. 2159–2181 (cit. on pp. 100, 250).

[248] J.W. Swegle, D.L. Hicks, and S.W. Attaway. Smoothed Particle Hydrodynamics Stability Analysis. In: *Journal of Computational Physics* **116**.1 (1995), pp. 123–134 (cit. on pp. 13, 128–130, 202).

[249] C.H. Tai, J.H. Sheu, and B. van Leer. Optimal Multistage Schemes for Euler Equations with Residual Smoothing. In: *AIAA Journal* **33**.6 (1995), pp. 1008–1016 (cit. on p. 144).

[250] C.H. Tai, J.H. Sheu, and P.Y. Tzeng. Improvement of Explicit Multistage Schemes for Central Spatial Discretization. In: *AIAA Journal* **34**.1 (1996), pp. 185–188 (cit. on p. 144).

[251] H. Takeda, S.M. Miyama, and M. Sekiya. Numerical Simulation of Viscous Flow by Smoothed Particle Hydrodynamics. In: *Progress of Theoretical Physics* **92**.5 (1994), pp. 939–960 (cit. on p. 117).

[252] N. Tarnow and J.C. Simo. How to Render Second Order Accurate Time-stepping Algorithms Fourth Order Accurate while Retaining the Stability and Conservation Properties. In: *Computer Methods in Applied Mechanics and Engineering* **115**.3 (1994), pp. 233–252 (cit. on p. 147).

[253] G.I. Taylor. The Use of Flat-ended Projectiles for Determining Dynamic Yield Stress. In: *Proceedings of the Royal Society of London A: Mathematical, Physical and Engineering Sciences* **194** (1948), pp. 289–299 (cit. on p. 220).

[254] S.H. Teng and C.W. Wong. Unstructured Mesh Generation: Theory, Practice, and Perspectives. In: *International Journal of Computational Geometry and Applications* **10**.3 (2000), pp. 227–266 (cit. on p. 3).

[255] S. Timoshenko. *Theory of Elasticity*. Engineering Societies Monographs. McGraw-Hill, 1951 (cit. on pp. 1, 69).

[256] E.F. Toro. *Riemann Solvers and Numerical Methods for Fluid Dynamics: A Practical Introduction*. 2nd edition. Applied mechanics: researchers and students. Springer, 1999 (cit. on p. 74).

[257] J.A. Trangenstein. A Second-order Godunov Algorithm for Two-dimensional Solid Mechanics. In: *Computational Mechanics* **13**.5 (1994), pp. 343–359 (cit. on p. 8).

[258] J.A. Trangenstein. *Numerical Solution of Elliptic and Parabolic Partial Differential Equations*. Cambridge University Press, 2013 (cit. on p. 8).

[259] J.A. Trangenstein and P. Colella. A Higher-order Godunov Method for Modeling Finite Deformation in Elastic-plastic Solids. In: *Communications on Pure and Applied Mathematics* **44**.1 (1991), pp. 41–100 (cit. on p. 8).

[260] J.A. Trangenstein and R.B. Pember. Numerical Algorithms for Strong Discontinuities in Elastic-plastic Solids. In: *Journal of Computational Physics* **103**.1 (1992), pp. 63–89 (cit. on p. 8).

[261] L.R.G. Treloar. Stress-strain Data for Vulcanised Rubber under Various Types of Deformation. In: *Transactions of the Faraday Society* **40** (1943), pp. 59–70 (cit. on pp. 43, 45–47).

[262] C. Truesdell and W. Noll. *The Non-linear Field Theories of Mechanics*. Springer–Verlag, 1965 (cit. on pp. 2, 46, 52, 72, 249).

[263] P.J. Van der Houwen. *Construction of Integration Formulas for Initial Value Problems*. North-Holland Series in Applied Mathematics and Mechanics. Elsevier Science, 1977 (cit. on p. 143).

[264] Y. Vidal, J. Bonet, and A. Huerta. Stabilized Updated Lagrangian Corrected SPH for Explicit Dynamic Problems. In: *International Journal for Numerical Methods in Engineering* **69**.13 (2007), pp. 2687–2710 (cit. on pp. 12, 130, 207).

[265] R. Vignjevic and J. Campbell. Review of Development of the Smooth Particle Hydrodynamics (SPH) Method. In: *Predictive Modeling of Dynamic Processes*. Ed. by S. Hiermaier. Springer US, 2009, pp. 367–396 (cit. on p. 11).

[266] R. Vignjevic, J. Campbell, and L. Libersky. A Treatment of Zero-energy Modes in the Smoothed Particle Hydrodynamics Method. In: *Computer Methods in Applied Mechanics and Engineering* **184** (2000), pp. 67–85 (cit. on p. 12).

[267] J. Von Neumann and R.D. Richtmyer. A Method for the Numerical Calculation of Hydrodynamic Shocks. In: *Journal of Applied Physics* **21** (1950), pp. 232–237 (cit. on p. 114).

[268] J.G. Wang and G.R. Liu. A Point Interpolation Meshless Method Based on Radial Basis Functions. In: *International Journal for Numerical Methods in Engineering* **54**.11 (2002), pp. 1623–1648 (cit. on p. 100).

[269] H. Wendland. Piecewise Polynomial, Positive Definite and Compactly Supported Radial Functions of Minimal Degree. In: *Advances in Computational Mathematics* **4**.1 (1995), pp. 389–396 (cit. on p. 120).

[270] M.L. Wilkins and M.W. Guinan. Impact of Cylinders on a Rigid Boundary. In: *Journal of Applied Physics* **44**.3 (1973), pp. 1200–1206 (cit. on p. 221).

[271] O.C. Zienkiewicz, R.L. Taylor, and J.Z. Zhu. *The Finite Element Method: Its Basis and Fundamentals*. 7th edition. The Finite Element Method. Elsevier Science, 2013 (cit. on p. 88).

D

E

F

G

H

I

J

K

L

M

Q

R

S

T

U

V

W

Y